Device-to-Device Communication and Wearable Networks: Harnessing Spatial Proximity

Geordie George

TESI DOCTORAL UPF / 2017

Director de la tesi

Dr. Angel Lozano Solsona
Wireless Communications Research Group
Dept. of Information and Communication Technologies

Wireless Communications Research Group (http://wicom.upf.edu/), Department of Information and Communication Technologies (http://www.upf.edu/etic), Universitat Pompeu Fabra (http://www.upf.edu), Barcelona, Spain

The doctoral defense was held on ..... at the Universitat Pompeu Fabra and scored as .....

Dr. Angel Lozano Solsona
(Thesis Supervisor)
Universitat Pompeu Fabra (UPF), Barcelona

Dr. Marco Di Renzo
(Thesis Committee Member)
CNRS / Paris-Saclay University, France

Dr. Olga Muñoz Medina
(Thesis Committee Member)
Universitat Politècnica de Catalunya (UPC), Barcelona

Dr. Nuria González Prelcic
(Thesis Committee Member)
Universidade de Vigo, Spain

In loving memory of my aunt Annamma Joseph

Acknowledgements

I would like to thank my thesis supervisor Prof. Angel Lozano for his valuable guidance, encouragement and patience. Working with him has been an incredible learning opportunity, I feel privileged and fortunate, therefore. Angel sets the bar high for students, by trying to inculcate a meticulous attitude towards research that is resolute in seeking pragmatic and pertinent solutions to engineering problems. He has always asserted the principle that relevance should take precedence over tractability, in the attempts to obtain analytical solutions to real-world problems. Co-authoring with Angel, who is an eloquent and fastidious writer, has greatly motivated me to strive for expressing ideas more lucidly and aesthetically.

My sincere gratitude goes to the thesis committee members, Prof. Marco Di Renzo, Prof. Olga Muñoz Medina, Prof. Nuria González-Prelcic, Prof. Boris Bellalta Jimenez, and Prof. Vanesa Daza Fernandez, for agreeing to serve on my committee, and for their insightful comments and feedback.

I am indebted to my collaborators, Dr. Ratheesh K. Mungara, Prof. Martin Haenggi, Prof. Robert Heath Jr. and Mr. Kiran Venugopal for their valuable contributions and for prompting me to hone my research skills. Especially, it was great to have a friendly colleague like Ratheesh, with whom I had the opportunity to engage in enriching collaborations.

I gratefully acknowledge the sources of financial support for the work presented in this dissertation, namely, the doctoral fellowship from DTIC (UPF), the Intel/Verizon University Research Program: "5G: Transforming the Wireless User Experience", Project

TEC2015-66228-P by the Spanish Ministry of Economy and Competitiveness (MINECO) and the European Fund for Regional Development (FEDER), and the European Research Council under the H2020 Framework Programme/ERC grant agreement 694974. I would like to thank the DTIC Secretariat as well as the research staff service unit of the Human Resources Department at UPF for all their help.

I am very thankful to my dear parents, Kuttiyamma and George, for their endless love and support, and for having always nurtured my interests. Thanks are due to my beloved brothers, Joph and Fredie, for their care and encouragement.

Lastly and foremostly, I am deeply grateful to my best friend and amazing life partner, Princy, for her compassion, support and wisdom, and—not least—for patiently bearing the brunt of living with me all along my thesis work; I couldn't have accomplished this without her.

Abstract

Spatially proximal devices wanting to exchange information are expected to become more prevalent in wireless networks, rendering the option for direct device-to-device (D2D) communication increasingly important. On the one hand, within networks where communication via infrastructure has been the convention, enabling such an option for short-range and single-hop communication between co-located devices might potentially bring about performance benefits on several accounts. On the other hand, in the realm of networks where direct interaction between devices has been an obvious option, there is a growing demand for supporting extreme-data-rate applications and much denser deployments of simultaneous transmissions. This dissertation explores these aspects by addressing two main problems: (*i*) analyzing the performance benefits of D2D communication integrated into cellular mobile networks, and (*ii*) investigating the feasibility of mmWave (millimeter wave) frequencies for personal networks of wearable (body-born) devices in enclosed settings.

Under sufficient spatial locality in wireless traffic within cellular networks, the D2D mode of communication can be leveraged to employ a denser spectral reuse, thereby achieving very high area spectral efficiencies (bits/s/Hz per unit area). Enabling D2D entails a reshaping of the network topology comprising the sources of useful signal and harmful interference from the vantage of each receiver, which is a factor that delimits network performance fundamentally. Therefore, to gauge the performance gains of D2D and to identify the challenges thereof, it is essential to model D2D communication in a large multicellular setting, without missing key features of the ensuing interference environment. In this regard, we develop a robust analytical framework, utilizing tools from stochastic geometry.

The dissertation propounds a novel approach to the application of stochastic geometry that is shown to improve the simplicity, accuracy, and generality of wireless network analysis. The performance evaluation conducted using the framework, while demonstrating the potential of D2D, also indicates the need for managing the interference surge. Prompted by this, and to illustrate the flexibility of the framework, we further extended it to incorporate interference protection schemes based on exclusion regions and the benefits thereof are assessed.

The presence of multiple wearable networks—each comprising several on-body device-pairs worn by people—in proximity might result in an extreme density of simultaneous wireless transmissions. Such a scenario is expected to become commonplace in enclosed settings, e.g., commuter trains, subways, airplanes, airports or offices, and be further challenging due to an increasing demand for data-rate-intensive wireless applications in wearable technology. This combination of very-short-range communication, high-data-rate applications, and dense spectral reuse seems to render operation at mmWave frequencies a suitable candidate; add to that the possibility of accommodating antenna arrays within devices for directional beamforming. Hence, we investigate the feasibility of enclosed mmWave wearable networks, with a particular focus on appropriately modeling the impact of propagation mechanisms at these frequencies. In the propagation modeling, specular reflections off surfaces are explicitly accounted for, as they are expected to contribute useful signal power while, at the same time, intensify the interference. Recognizing the increased prominence of blocking by obstacles, body-blockages in the direct and reflected propagation paths are also modeled. The impact of these mechanisms on the spectral efficiency of the network is evaluated, aided by the application of stochastic geometry and random shape theory. Under relevant indoor settings, and in the plausible absence of strong direct signal, the reliability of surface reflections in providing useful signal power for efficient communication is investigated and the need for directional antennas is established.

Resumen

Se espera que los dispositivos espacialmente proximales que desean intercambiar información se vuelvan más frecuentes en redes inalámbricas, lo que hace cada vez más importante la opción de comunicación directa dispositivo-a-dispositivo (D2D). Por un lado, dentro de las redes en las que la comunicación a través de la infraestructura ha sido la convención, permitir tal opción para la comunicación de corto alcance y single-hop entre dispositivos ubicados conjuntamente podría potencialmente generar beneficios de rendimiento en varios aspectos. Por otro lado, en el ámbito de las redes en las que la interacción directa entre dispositivos ha sido una opción obvia, existe una demanda creciente de soportar aplicaciones de velocidad extrema de datos e despliegues mucho más densas de transmisiones simultáneas. Esta disertación explora dichos aspectos abordando dos problemas principales: (*i*) analizando los beneficios de rendimiento de la comunicación D2D integrada en las redes móviles celulares, y (*ii*) investigando la viabilidad de las frecuencias de mmWave (ondas milimétricas) para redes personales de dispositivos wearables (usado en el cuerpo) en entornos cerrados.

Bajo suficiente localidad espacial en el tráfico inalámbrico en redes celulares, el modo de comunicación D2D puede ser apalancado para emplear una reutilización espectral más densa, logrando así eficiencias espectrales de área muy alta (bits/s/Hz por unidad de área). La habilitación de D2D implica una remodelación de la topología de red que comprende las fuentes de señal útil e interferencia perjudicial desde la vista de cada receptor, lo cual es un factor que delimita el funcionamiento de la red de manera fundamental. Por tanto, para medir las ganancias de rendimiento de D2D y para identificar los retos de la misma, es esencial para modelar la comunicación D2D en un gran ajuste multicelular, sin faltar las características

clave del entorno de interferencia resultante. En este sentido, se desarrolla un sólido marco analítico, utilizando herramientas de geometría estocástica. La disertación propone un nuevo enfoque para la aplicación de la geometría estocástica para mejorar la simplicidad, precisión y generalidad del análisis de redes inalámbricas. La evaluación realizada utilizando dicho enfoque, al mismo tiempo que demuestra el potencial de D2D, también indica la necesidad de manejar la oleada de interferencia. Impulsado por estos resultados, y para ilustrar la flexibilidad del marco, también se amplía para incorporar esquemas de protección contra interferencias basados en regiones de exclusión y se evaluán sus los beneficios.

La presencia de redes wearables múltiples—cada una de las cuales comprende varios pares de dispositivos en el cuerpo desgastados por personas—en proximidad puede dar como resultado una densidad extrema de transmisiones inalámbricas simultáneas. Se espera que este escenario se convierta habitual en entornos cerrados, por ejemplo, trenes de cercanías, subterráneos, aviones, aeropuertos u oficinas, y será un desafío adicional debido a la creciente demanda de aplicaciones inalámbricas intensivas en datos en tecnología wearable. Esta combinación de comunicaciones de muy corto alcance, en aplicaciones de alta velocidad de datos y de reutilización espectral densa parece hacer que la operación en las frecuencias mmWave sea un candidato adecuado; se añade la posibilidad de alojar conjuntos de antenas dentro de dispositivos para el beamforming direccionales. Por tanto, también se investiga la viabilidad de las redes wearables mmWave cerradas, con especial énfasis en modelar apropiadamente el impacto de los mecanismos de propagación en estas frecuencias. En el modelado de propagación, las reflexiones especulares de las superficies se explican explícitamente, ya que se espera que contribuyan a la potencia de la señal útil, mientras que, al mismo tiempo, intensificar la interferencia. Reconociendo la mayor prominencia del bloqueo por obstáculos, también se modelan los bloqueos corporales en los caminos de propagación directa y reflejada. El impacto de estos mecanismos en la eficiencia espectral de la red se evalúa, ayudado por la aplicación de la geometría estocástica y la teoría de la forma aleatoria. Bajo configuraciones internas relevantes, y en la ausencia plausible de señal directa fuerte, se investiga la fiabilidad de las reflexiones superficiales proporcionando potencia de señal útil para una comunicación eficiente y se establece la necesidad de antenas direccionales.

Acronyms, Notation, and Symbols

Acronyms

3GPP	3rd Generation Partnership Project
5G	5th Generation
ARQ	Automatic Repeat reQuest
BPP	Binomial Point Process
BS	Base Station
CDF	Cumulative Distribution Function
CCDF	Complementary CDF
CSMA	Carrier Sense Multiple Access
D2D	Device-to-Device
IEEE	Institute of Electrical and Electronics Engineers
IID	Independent and Identically Distributed
MAC	Medium Access Control
MANET	Mobile Ad hoc Networks
MIMO	Multiple-Input Multiple-Output
mmWave	Millimeter Wave
PDF	Probability Density Function
PPP	Poisson Point Process
ProSe	Proximity-based Services
RX	Receiver
SD	Standard Deviation
SINR	Signal-to-Interference-plus-Noise Ratio
SIR	Signal-to-Interference Ratio
TX	Transmitter

UPA	Uniform Planar Array
WLAN	Wireless Local Area Network

Notation

a, A	Scalars
$\boldsymbol{a}$	Column vector
$\boldsymbol{A}$	Matrix variable
$\lvert a \rvert$	Magnitude of a
$\lVert \boldsymbol{a} \rVert$	Euclidean norm of $\boldsymbol{a}$
$\binom{A}{a}$	Binomial coefficient
$\mathcal{A}(a, b)$	Annular region with inner radius a and outer radius b
$\mathbb{C}$	Complex numbers
$\mathbb{C}^n$	n-dimensional complex space
$\mathrm{ci}(\cdot)$	Cosine integral
$\mathrm{erf}(\cdot)$	Error function
$\mathbb{E}[\cdot]$	Expectation operator
$\mathbb{E}_A[\cdot]$	Expectation over A
$E_n(\cdot)$	Exponential integral
$f_A(\cdot)$	PDF of A
$F_A(\cdot)$	CDF of A
$F_A^{\mathrm{c}}(\cdot)$	CCDF of A
$\mathcal{G}(\cdot, \cdot)$	Antenna gain pattern
$\Gamma(\cdot)$	Gamma function
$\Gamma(\cdot, \cdot)$	Upper incomplete gamma function
$\bar{\Gamma}(\cdot, \cdot)$	Lower incomplete gamma function
$\mathit{\Gamma}(\cdot)$	Reflection coefficient as a function of angle of incidence
$I(a; b)$	Mutual information of a and b
$\mathcal{L}_{F_A}(\cdot)$	Laplace transform of the CDF of A
$\mathcal{N}_{\mathbb{C}}(\mu, \sigma^2)$	Complex Gaussian distribution with mean μ and variance σ^2
$\mathbb{P}[\cdot]$	Probability of an event
$\mathbb{R}$	Real numbers
$\mathbb{R}^n$	n-dimensional real space
$\Re(a)$	Real part of a
$\sim$	Distributed as
$\mathrm{si}(\cdot)$	Sine integral
$\mathcal{U}(a, b)$	Uniform distribution from a to b

Common Symbols

$a_{\mathrm{c},k}$	Normalized $r_{\mathrm{c},k}$
a_{d}	Normalized r_{d}
$a_{\mathrm{d},j}$	Normalized $r_{\mathrm{d},j}$
a_{ex}	Normalized r_{ex}
α_k	Polarization angle of the direct path from X_k
$\alpha_{i,k}$	Polarization angle of the ith reflected path from X_k
B	Bandwidth
$\mathcal{B}(0,R)$	Averaging circle of radius R, centered at a receiver
β_k	Binary blockage variable in direct path
$\beta_{i,k}$	Binary blockage variable in the ith reflected path
$\upbeta$	Parameter appertaining to D2D link distance
C	Spectral efficiency under Gaussian-distributed aggregate interference
$\bar{C}$	Average of C
$\bar{\mathcal{C}}$	Average area spectral efficiency
C_{c}	Spectral efficiency of cellular uplink
$\bar{C}_{\mathrm{c}}$	Average of C_{c}
C_{d}	Spectral efficiency of D2D link
$\bar{C}_{\mathrm{d}}$	Average of C_{d}
$\bar{\mathcal{C}}_{\mathrm{d}}$	Average area spectral efficiency of D2D links
$\bar{\mathcal{C}}_{\mathrm{d}}^{\star}$	Optimum $\bar{\mathcal{C}}_{\mathrm{d}}(\lambda_{\mathrm{d}},\updelta)$, maximized over $\updelta$
$\bar{\mathcal{C}}_{\mathrm{d}}^{\star\star}$	Optimum $\bar{\mathcal{C}}_{\mathrm{d}}(\lambda_{\mathrm{d}},\updelta)$, maximized over λ_{d} and $\updelta$
C_{exact}	Spectral efficiency under arbitrarily distributed aggregate interference
$\bar{C}_{\mathsf{exact}}$	Average of C_{exact}
C_{ub}	Upper bound to C_{exact}
$\bar{C}_{\mathsf{ub}}$	Average of C_{ub}
Δ	Surface thickness
$\updelta$	Ratio of exclusion region radius to D2D link distance
$\updelta^{\star}$	Value of $\updelta$ that gives $\bar{\mathcal{C}}_{\mathrm{d}}^{\star}$
$\mathcal{D}$	Diameter of a cylinder modeling human body
$\updelta_{\mathrm{I}}$	Value of $\updelta$ that gives $\bar{\mathcal{C}}_{\mathrm{d}}^{\star\star}$, in type I channelization
$\updelta_{\mathrm{II}}$	Value of $\updelta$ that gives $\bar{\mathcal{C}}_{\mathrm{d}}^{\star\star}$, in type II channelization
$\Delta\phi_{i,k}$	Phase difference of direct path and ith reflected path
η	Path loss exponent
η_{c}	Path loss exponent of user-to-BS link
η_{d}	Path loss exponent of user-to-user link
F_{N}	Receiver noise figure
g	Side-lobe gain
G	Main-lobe gain

G_k	Large-scale gain of the kth link
$\mathcal{G}_k^{\mathrm{r}}$	Receive antenna gain in direct path
$\mathcal{G}_{i,k}^{\mathrm{r}}$	Receive antenna gain in the ith reflected path
$\mathcal{G}_k^{\mathrm{t}}$	Transmit antenna gain in direct path
$\mathcal{G}_{i,k}^{\mathrm{t}}$	Transmit antenna gain in the ith reflected path
Γ_{high}	High reflection coefficient
Γ_{low}	Low reflection coefficient
$\Gamma_{\parallel}$	Reflection coefficient of parallel polarization
$\Gamma_{\perp}$	Reflection coefficient of perpendicular polarization
$\boldsymbol{\Gamma}_{i,k}$	Reflection coefficient matrix in the ith reflected path
H	Height of a rectangular cuboid
H_k	Small-scale fading coefficient of the kth link
$\boldsymbol{H}_k$	Fading channel matrix of the kth link
$H_{\mathrm{c},k}$	Fading of the link from kth cellular uplink user
$H_{\mathrm{d},j}$	Fading of the link from jth D2D transmitter
h_{u}	Height of the cylinder modeling human body
j	Imaginary unit
K	Number of interferers
K	Average number of D2D links per cell
K'	Number of D2D transmitters in $\mathcal{B}(0,R)$
K''	Number of cellular uplink users in $\mathcal{B}(0,R)$
$\varkappa$	Parameter distinguishing overlay and underlay
L	Path loss at one meter
L	Length of a rectangular region/cuboid
λ	Wavelength
λ	Density of the PPP Φ
λ_{c}	Density of the PPP Φ_{c}
λ_{d}	Density of the PPP Φ_{d}
$\tilde{\lambda}_{\mathrm{d}}$	Average number of co-channel links per unit area
$\tilde{\lambda}_{\mathrm{d}}^{\star}$	Value of $\tilde{\lambda}_{\mathrm{d}}$ corresponding to $\bar{\mathcal{C}}_{\mathrm{d}}^{\star}$
m	$\min(\mathsf{N}_{\mathrm{t}}, \mathsf{N}_{\mathrm{r}})$
m	Random mark of D2D links in type II channelization
μ	Ratio of D2D and cellular user transmit powers
n	$\max(\mathsf{N}_{\mathrm{t}}, \mathsf{N}_{\mathrm{r}})$
n	Complex refractive index
N	Number of codeword symbols
N	Number of antennas
N_0	Noise power spectral density
N_{t}	Number of transmit antennas
N_{r}	Number of receive antennas
Ω	Antenna beamwidth

P	Transmit power
p_{c}	Ratio of exclusion area (around BS) to cell area
P_{c}	Power at one meter from cellular uplink transmitter
p_{d}	Probability of selecting a co-channel D2D link
P_{d}	Power at one meter from D2D transmitter
$\boldsymbol{p}_k$	Polarization unit vector of the direct path from X_k
$\boldsymbol{p}_{i,k}$	Polarization unit vector of the ith reflection from X_k
p_{t}	Probability of X_0^{r} falling in the main-lobe of X_k
$\Phi_{\mathcal{A}}$	Points on the annular region $\mathcal{A}(\cdot,\cdot)$
Φ	Poisson point process
Φ_{c}	PPP corresponding to cellular user locations
Φ_{d}	PPP corresponding to D2D transmitter locations
$\tilde{\Phi}_{\mathrm{d}}$	PPP with density $\tilde{\lambda}_{\mathrm{d}}$
Φ_{d}	PPP with density $p_{\mathrm{c}}\lambda_{\mathrm{d}}$
$\psi_0^{\mathrm{a}}, \psi_0^{\mathrm{e}}$	Azimuth and elevation of the main-lobe of X_0^{r}
$\psi_k^{\mathrm{a}}, \psi_k^{\mathrm{e}}$	Azimuth and elevation of the main-lobe of X_k
$\psi_{i,k}^{\mathrm{a}}, \psi_{i,k}^{\mathrm{e}}$	Azimuth and elevation of the main-lobe of $X_{i,k}$
R	Cell radius
r_{d}	Parameter appertaining to D2D link distance
r_k	Distance to the kth transmitter
$r_{i,k}$	Distance to the ith image of the kth transmitter
$r_{\mathrm{c},k}$	Distance to the kth cellular uplink transmitter
r_{d}	Parameter appertaining to D2D link distance
$r_{\mathrm{d},j}$	Distance to the jth D2D transmitter
r_{ex}	Exclusion region around BS
R_{i}	Inner radius
R_{o}	Outer radius
r_{w}	Distance between a wearable and its body
ρ	Local-average SINR
ρ_{c}	Local-average SIR of cellular uplink
ρ_{d}	Local-average SIR of D2D link
SINR	Instantaneous SINR
SIR	Instantaneous SIR
$\mathsf{SIR}_{\mathrm{c}}$	Instantaneous SIR of cellular uplink
$\mathsf{SIR}_{\mathrm{d}}$	Instantaneous SIR of D2D link
s_k	Transmit signal
$s_{\mathrm{c},k}$	Transmit signal from cellular uplink user
$s_{\mathrm{d},j}$	Transmit signal from D2D transmitter
σ_{N}^2	Noise variance
σ_{c}^2	Aggregate interference power at BS receiver
$\sigma_{\mathrm{c,in}}^2$	Part of σ_{c}^2 emanating from inside $\mathcal{B}(0,R)$

$\sigma^2_{\mathrm{c,out}}$	Part of σ^2_{c} emanating from outside $\mathcal{B}(0,R)$
$\overline{\sigma^2}_{\mathrm{c,out}}$	Average of $\sigma^2_{\mathrm{c,out}}$
σ^2_{d}	Aggregate interference power at D2D receiver
$\sigma^2_{\mathrm{d,in}}$	Part of σ^2_{d} emanating from inside $\mathcal{B}(0,R)$
$\sigma^2_{\mathrm{d,out}}$	Part of σ^2_{d} emanating from outside $\mathcal{B}(0,R)$
$\overline{\sigma^2}_{\mathrm{d,out}}$	Average of $\sigma^2_{\mathrm{d,out}}$
$\varsigma^{\mathrm{a}}_k, \varsigma^{\mathrm{e}}_k$	Azimuth and elevation of the orientation of X_k with respect to X^{r}_0
θ	Angle of incidence
$\theta_{i,k}$	Angle of incidence on the ith surface
v	AWGN
W	Width of a rectangular region/cuboid
$\boldsymbol{\mathcal{X}}_0$	Horizontal plane containing X^{r}_0
X_k	Location of the kth transmitter
X'_k	Projection of X_k onto $\boldsymbol{\mathcal{X}}_0$
$X_{i,k}$	Image of X_k across the ith surface
X^{r}_0	Reference receiver location
$(\mathsf{x}_k, \mathsf{y}_k, \mathsf{z}_k)$	Cartesian coordinates of X_k
$(\mathsf{x}_{i,k}, \mathsf{y}_{i,k}, \mathsf{z}_{i,k})$	Cartesian coordinates of $X_{i,k}$
$(\mathsf{x}^{\mathrm{r}}_0, \mathsf{y}^{\mathrm{r}}_0, \mathsf{z}^{\mathrm{r}}_0)$	Cartesian coordinates of X^{r}_0
y	Observation at the receiver
y_{c}	Observation at BS receiver
y_{d}	Observation at D2D receiver
z	Received aggregate interference
z_{c}	Aggregate interference at BS receiver
z_{d}	Aggregate interference at D2D receiver

Contents

Abstract ix

Resumen xi

Acronyms, Notation, and Symbols xiii

List of Figures xxiii

List of Tables xxvi

1 Introduction 1
- 1.1 Motivation . . . 1
  - 1.1.1 Towards 5G . . . 2
  - 1.1.2 D2D Communication in Cellular Networks . . . 3
  - 1.1.3 A Stochastic Geometry-based Analytical Framework . . . 7
  - 1.1.4 Enclosed mmWave Wearable Networks . . . 9
  - 1.1.5 Summary of Motivation . . . 12
- 1.2 Contribution and Organization . . . 13

2 A Novel Approach for Spectral Efficiency Analysis 19
- 2.1 Background . . . 19
- 2.2 Network Modeling . . . 20
  - 2.2.1 Separation of Scales . . . 20
  - 2.2.2 Large-scale Modeling . . . 21
  - 2.2.3 Small-scale Modeling . . . 22
- 2.3 Interference Modeling . . . 23
  - 2.3.1 Ergodic Spectral Efficiency . . . 23

2.3.2 Local Distribution of Interference 25
2.3.3 Characterization of the Ergodic Spectral Efficiency 26
2.4 Distribution of the Local-Average SINR 30
2.4.1 Application of Stochastic Geometry 31
2.5 Distribution of the Spectral Efficiency 38
2.5.1 Contrast with Conventional Approach 39
2.6 Spatial Average of the Spectral Efficiency 41
2.6.1 Contrast with Conventional Approach 42
2.7 System-level Performance of Unbounded Networks . 43
2.7.1 Area Spectral Efficiency 45
2.8 Summary 45

3 D2D Communication in Cellular Networks 47
3.1 Background 47
3.2 Network Modeling 48
3.2.1 User Locations 48
3.2.2 Large-scale Modeling 50
3.2.3 Small-scale Modeling 51
3.3 Interference Modeling 52
3.3.1 Gaussian Modeling of the Local Distribution 52
3.3.2 Classification of the Interference Terms . . . 53
3.4 SIR 55
3.4.1 Cellular Uplink 55
3.4.2 D2D Link 58
3.5 Ergodic Spectral Efficiency 59
3.5.1 Specific Network Geometry 59
3.5.2 Distribution over All Geometries 60
3.5.3 Spatial Average 62
3.6 Benefits of D2D 65
3.6.1 Overlay D2D 65
3.6.2 Underlay D2D 69
3.7 Summary 70

4 Exclusion Regions for Interference Protection in D2D Networks 71
4.1 General Considerations 71
4.2 Underlay D2D with Exclusion Regions 72
4.2.1 Background 72
4.2.2 Network Geometry 72
4.2.3 Interference Modeling 72
4.2.4 SIR 75

4.2.5 Ergodic Spectral Efficiency . . . 76
4.2.6 Summary . . . 80
4.3 Overlay D2D with Exclusion Regions . . . 81
4.3.1 Background . . . 81
4.3.2 Network Geometry . . . 81
4.3.3 Channelization Schemes . . . 82
4.3.4 Interference Modeling . . . 84
4.3.5 SIR . . . 85
4.3.6 Ergodic Spectral Efficiency . . . 86
4.3.7 Area Spectral Efficiency . . . 89
4.3.8 Exclusion Region Size Optimization . . . 89
4.3.9 Summary . . . 96

5 Enclosed mmWave Wearable Networks 97
5.1 Background . . . 97
5.2 Network Modeling . . . 98
5.2.1 Network Geometry . . . 99
5.2.2 Surface Reflections . . . 100
5.2.3 Body Blockages . . . 103
5.3 Antenna Arrays . . . 106
5.4 Propagation Model . . . 108
5.4.1 Intended Signal Power . . . 108
5.4.2 Interference Power . . . 109
5.5 SINR . . . 109
5.6 Stochastic Modeling . . . 110
5.6.1 Random Network Geometry . . . 110
5.6.2 Stochastic Blockage Model . . . 112
5.6.3 Stochastic Model for the Antenna Gains . . . 117
5.7 Impact of Reflections and Blockages . . . 118
5.8 Impact of Antenna Arrays . . . 121
5.9 Summary . . . 123

6 Conclusion 125
6.1 Summary of Conclusions . . . 125
6.1.1 Application of Stochastic Geometry to Wireless Network Analysis . . . 125
6.1.2 Benefits of D2D in Cellular Networks . . . 125
6.1.3 Enclosed mmWave Wearable Networks: Feasibility and Performance . . . 126
6.2 Future Research . . . 127
6.2.1 D2D in Cellular Networks . . . 127
6.2.2 Enclosed mmWave Wearable Networks . . . 128

A Appendix to Chapter 2 **129**
A.1 Computation of C_{exact} in Eq. (2.6) 129
A.2 Derivation of Eq. (2.9) 130

B Appendix to Chapter 3 **131**
B.1 Proof of Proposition 3.1 131
B.2 Proof of Proposition 3.2 132
B.3 Proof of Proposition 3.3 133
B.4 Proof of Proposition 3.4 134
B.5 Proof of Proposition 3.5 135
B.6 Proof of Proposition 3.6 135

C Appendix to Chapter 4 **137**
C.1 Proof of Lemma 4.1 137
C.2 Proof of Lemma 4.2 138
C.3 Proof of Lemma 4.3 138

D Appendix to Chapter 5 **141**
D.1 Coordinates of Image Transmitters and Angles of Incidence 141
D.2 Polarization Angles 142
D.3 Algorithm to Determine Blockages 143
D.3.1 Direct Interference Paths and Wall Reflections 143
D.3.2 Ceiling-Reflected Interference Path 144
D.4 Antenna Gains 144
D.5 Derivation of Blockage Probability 145
D.5.1 Direct Interference Paths 145
D.5.2 Wall-Reflected Interference Paths 146
D.5.3 Ceiling-Reflected Interference Paths 147
D.5.4 Wall-Reflected Signal Path 148

Bibliography **151**

List of Figures

1.1 The modes of communication between two devices in a D2D integrated cellular system. 3
1.2 An illustration of the interference environment in a D2D integrated cellular network. 5
1.3 Cellular topology vs. D2D topology 7
1.4 Examples of wearable devices. 9
1.5 A wearable network on a person, coordinated via a hub. 10
1.6 An illustration of several users with their respective wearable networks inside a train car. 10
1.7 An illustration of reflections from interior surfaces and blockages. 12

2.1 A receiver, its intended transmitter and four interferers. 22
2.2 Variation of large-scale gains, small-scale fading and spectral efficiency over several codewords. 24
2.3 Ergodic spectral efficiency vs. the intended link distance. 29
2.4 A receiver with intended transmitter r_0 away and interfering transmitters in an annulus. 33
2.5 CDF of the local-average SIR. 35
2.6 Receiver with intended transmitter r_0 away and interferers distributed as a BPP inside a rectangular region. . . 37
2.7 CDF of the ergodic spectral efficiency. 38
2.8 Spatially averaged spectral efficiency as a function of η. 43
2.9 Depiction of the links in an overlay D2D network, distributed as per a Poisson dipole model. 44

3.1 Cellular uplink with D2D. 49
3.2 CDF of the local-average SIR ρ_c, with shadowing. . . . 57

3.3 The three situations considered in Example 3.2. 60
3.4 D2D link spectral efficiency in an overlay system as function of the normalized link distance $a_{d,0}$. 61
3.5 CDFs of C_c and C_d. 62
3.6 Spatially average spectral efficiencies of uplink and D2D link for varying η_c and η_d with overlay. 65
3.7 Contour plot for the relationship in (3.42). 66
3.8 CDFs of cellular and D2D link spectral efficiencies in an overlay system. 67
3.9 Average area spectral efficiency in an overlay system. . . 68
3.10 Average area spectral efficiency of underlay D2D. 69

4.1 Cellular uplink with no underlay D2D transmitters allowed in circular exclusion regions. 73
4.2 Asymmetric voids inside the averaging circle around a co-channel D2D receiver. 75
4.3 CDF of ergodic spectral efficiency in an underlay system with exclusion regions. 77
4.4 Average area spectral efficiency of the underlaying D2D links. 79
4.5 With $\nu = 0.8$, achievable average area spectral efficiency of the underlay D2D links. 80
4.6 Co-channel links under type I and type II channelization schemes performed on the same pool of available links. . 82
4.7 CDF of spectral efficiency for $\lambda_d = 40$ links/km^2, $r_d = 40$ m and path loss exponent $\eta_d = 4.5$. 86
4.8 Average spectral efficiency as function of λ_d with $r_d = 40$ m and $\eta_d = 4.5$. 88
4.9 Average area spectral efficiency (bits/s/Hz/km^2) as function of λ_d, for $r_d = 40$ m and $\eta_d = 4.5$, with optimized δ. 90
4.10 Optimum δ as function of λ_d for $r_d = 40$ m and $\eta_d = 4.5$. 91
4.11 Average number of co-channel links per km^2 as function of λ_d, for $r_d = 40$ m and $\eta_d = 4.5$, with optimized δ. . . 92
4.12 CDF of spectral efficiency for $\lambda_d = 246.46$ links/km^2, $r_d = 40$ m, path loss exponent $\eta_d = 4.5$. 96

5.1 Co-channel wearable devices on people. 99
5.2 Reflected links from a transmitter to a receiver, off two walls. 100
5.3 Low (Γ_{low}) and high (Γ_{high}) reflection coefficients as functions of the angle of incidence. 102

5.4 Illustrations of unblocked and blocked propagation paths. 104
5.5 A cone shaped blockage zone (shaded), formed by a circular blockage, from the vantage of the receiver. 104
5.6 An instance of the interferers (unblocked/blocked) to the reference receiver located at the center of $\boldsymbol{\mathcal{X}}_0$. 104
5.7 Ceiling-reflected link from transmitter X_k to receiver X_0^{r}. 105
5.8 Antenna gain pattern, rotationally symmetric about the broadside direction. 107
5.9 The horizontal plane $\boldsymbol{\mathcal{X}}_0$ containing the reference receiver X_0^{r}. 111
5.10 Large-scale gain G_k vs. (direct) link distance r_k, under high reflectivity (Γ_{high}) surfaces and omnidirectional ($\mathsf{N} = 1$) antennas. 113
5.11 Average blockage probabilities of the direct interference path and the reflected paths. 117
5.12 CDFs of SINR with the reference receiver located at the center, $\mathsf{r}_{\mathrm{w}} = 10$ cm and isotropic antennas ($\mathsf{N} = 1$). . . . 119
5.13 Spatially averaged spectral efficiency (bits/s/Hz) with high-reflectivity surfaces (Γ_{high}) and isotropic antennas ($\mathsf{N} = 1$). 120
5.14 CDFs of spectral efficiency (bits/s/Hz) with the reference receiver located at the center, blocked on-body link ($\beta_0 = 0$), $K = 40$ and $\mathsf{r}_{\mathrm{w}} = 10$ cm. 121
5.15 Difference between the average spectral efficiencies considered in Example 5.9. 122

C.1 Two neighboring D2D links under type II channelization scheme. 139

D.1 Polarization of a ray from a transmitter (TX). 142
D.2 A blockage (X_j^{c}) in the direct path between X_k' and X_0^{r}. 144
D.3 A direct interferer path. The link intersects any circle with center inside the 2-D capsule. 145
D.4 A reflected interferer link off a wall. The link intersects any circle with center inside the folded 2-D capsule depicted with solid lines. 146
D.5 A direct interferer link. The corresponding ceiling reflection intersects any circle with center inside any of the two 2-D capsules. 147
D.6 A reflected signal link off a wall. The link intersects any circle with center inside the folded 2-D capsule depicted with solid lines. 149

List of Tables

4.1 Typical values of δ_{I} and $\kappa_{\mathrm{I}}(\eta_{\mathrm{d}})$ for type I 93
4.2 Typical values of δ_{II} and $\kappa_{\mathrm{II}}(\eta_{\mathrm{d}})$ for type II 95

5.1 Array Settings 108
5.2 Settings 112

Chapter 1

Introduction

1.1 Motivation

The ever growing mobile data traffic is surmised to get propelled substantially, fueled by an explosion in the number of wirelessly connected devices and the unceasing emergence of extreme-data-rate demanding applications [1]. The expanding demand for wireless connectivity is expected to be constituted by a variety of entities, ranging from personal mobile devices—hand-held or body-born, and possibly multiple of them per person—to autonomous (mobile or fixed) machines [2–6]. Importantly, this disruption in wireless connectivity might be augmented by some radical reshaping of the topology of the data traffic [1, 2].

In voice-centric systems, it was implicitly accepted that two users trying to establish a phone call were far apart, the basic premise under which the (infrastructure-based) cellular communication systems had been designed. Come the age of data, this is not always the case, as co-located devices might want to share content or interact wirelessly. Cellular systems have been progressively evolving over the past decades, making significant advances in efficiently handling the communication between mobile devices that are far apart. The conventional mode of communicating via the uplink and downlink, however, is arguably not the most efficient way to handle the wireless traffic between co-located devices. All the same, having mobile devices autonomously discover traffic locality and establish direct communication links by themselves, in an ad hoc fashion, is known to be very taxing, due to several design roadblocks [7]. There is, therefore, a lot of interest in leveraging the availability

of infrastructure assistance to control and manage *device-to-device* communication (*D2D*, in short), i.e., to enable such provision within the cellular systems to efficiently handle proximal wireless traffic.

The foreseen avalanche of new smart devices in conjunction with the emergence of extreme-data-rate applications might trigger distinct challenges in the communication between proximal wireless devices. Namely, scenarios that warrant significant engineering effort might occur, even when the locality of the communicating devices is rather predictable within a limited ambit, e.g., a wireless personal area network [8], such that the coordination of simultaneous transmissions is easier in contrast to the generic D2D setting between mobiles in a (wide area) cellular network. A prime example of such a specific challenge is the coexistence of multiple personal networks of wireless *wearable* devices—each formed by several body-born devices—in close vicinity, resulting in an unprecedented density of simultaneous wireless transmissions.

1.1.1 Towards 5G

In the ongoing evolution to the 5th-generation (5G) of wireless networks [9], one of the major engineering requirements—arguably the primary driving force behind this evolution—is the enhancement of the mobile broadband. Specifically, by achieving extremely high data rates [10]: roughly 1000× increase in aggregate data rate (bit/s per unit area) and 100× increase in edge-rate (minimum bit/s achieved by 95% of users).

The key 5G technology directions that are expected to enable this unprecedented leap in communication performance are broadly classified as [9, 10]:

1) Extreme densification and offloading for enhancing of the area spectral efficiency, i.e., more active transceivers per unit area and Hz.

2) Increased bandwidth, mainly by moving towards and into the mmWave (millimeter wave) spectrum, i.e., more Hz.

3) Increased spectral efficiency via massive MIMO (multiple-input-multiple-output), i.e., more bits/s/Hz per node.

The investigations that culminated in this dissertation are in the realm of the first and the second 5G technology directions:

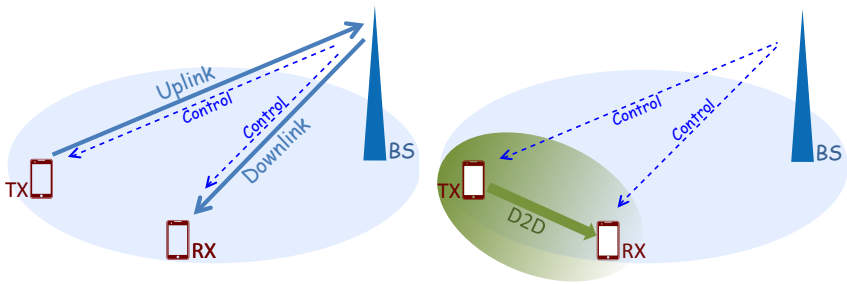

(a) Cellular mode. (b) D2D mode.

Figure 1.1: The modes of communication between two devices (TX and RX) in a D2D integrated cellular system. In both modes, the communication is managed by the infrastructure via control signaling from the base stations (BSs).

- Spectral efficiency analysis of D2D communication in cellular networks, wherein the potential of D2D for enabling densification to boost the bits/s/Hz per unit area is gauged.

- Establishing the feasibility of operation at mmWave frequencies for personal networks of wireless wearable devices in indoor settings, wherein multiple high-data-rate applications are required to coexist in close vicinity.

1.1.2 D2D Communication in Cellular Networks

D2D communication, currently being touted as a potential ingredient of 5G cellular networks [9–13], allows users in close proximity to establish direct communication, replacing two long hops via the BS (base station or radio-head) with a single shorter hop (cf. Fig. 1.1). Provided there is sufficient spatial locality in the wireless traffic, this can bring about several benefits: reduced power consumption, lower end-to-end latency, reduced backhaul loads, and especially a much higher spectral efficiency thanks to the shorter range and denser spectral reuse. While implementing smaller cells is indeed the primary densification approach in 5G [10], accounting for the expenditure of energy and other costs incurred in building more infrastructure, arguably, the desification enabled by D2D has the advantage of being more scalable.

The 3rd Generation Partnership Project (3GPP) is in the process of studying and standardizing D2D communication, under the name proximity-based services (ProSe), for cellular networks [14–16] while

several problems associated with D2D have been identified and are being explored by academia [17–28].

Infrastructure Assistance is Key

While D2D results in more complex and irregular (ad hoc like) topologies, an integrated D2D system can benefit from the infrastructure assistance for control functionalities, unlike in traditional mobile ad hoc networks (MANETs) which had very limited success notwithstanding the immense effort in research and development [7]. Most of the design roadblocks in MANETs, such as the extreme overheads incurred in control functions like user discovery, synchronization, session setup, channelization and interference management, can be greatly alleviated in D2D, thanks to the infrastructure assistance. Moreover, in situations when the communicating devices move apart from sufficient spatial proximity rendering direct (single-hop) communication non-beneficial, D2D has the option of falling back to the cellular mode, whereas a MANET cannot avoid inefficient long hops or multiple hops that would affect the performance severely [16].

Spectrum Sharing Options: Underlay vs. Overlay

There are two modes of spectrum sharing options in D2D:

- *Underlay* mode, wherein the D2D communication reuses cellular (uplink or downlink) signaling resources.
- *Overlay* mode, wherein a swath of spectrum is reserved for the D2D communication.

While the spectral reuse in the underly mode is relatively more aggressive, it comes at a price by causing undesired mutual interference between the cellular and D2D transmissions, which is avoided in the overlay mode at the expense of prohibiting cellular transmissions in a share of the resources. Note, however, that in both the options, D2D can potentially alleviate the backhaul load.

Further, in underlay D2D, reusing the cellular uplink resources is preferred over the downlink for several reasons [16]. The primary basis for this choice is that, in the uplink, the BS receiver can better handle the interference from D2D transmissions, as it may be more advanced than the mobile receiver, e.g., a massive MIMO BS

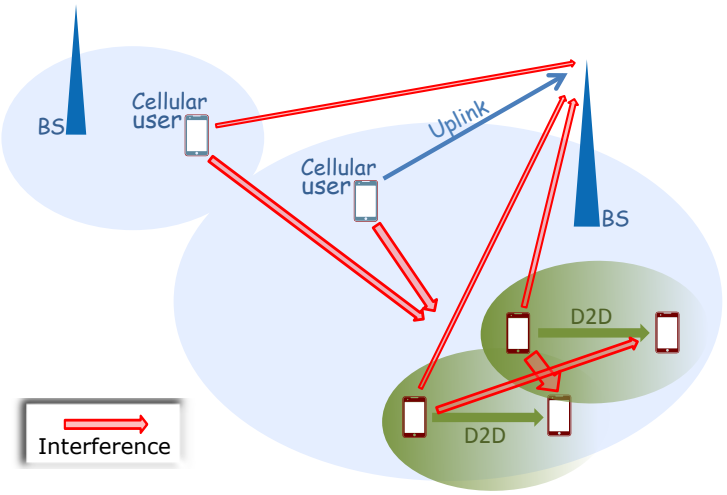

Figure 1.2: An illustration of the interference environment in a D2D integrated cellular network. The mutual interference between the cellular and D2D transmissions is absent in the overlay mode.

receiver [29]. Also, the downlink typically carries some essential signaling like control and pilots that must be protected from D2D interference with high priority and thereby necessitating complicated designs.

Interference Management

Obviously, the integration of D2D exacerbates the complexity of the interference environment in a cellular system, more so in underlay, with the mutual interference between cellular and D2D transmissions in addition to the inter-D2D interference under the irregular topology. There are several approaches to manage the surge of harmful interference between close-by transceivers reusing same signaling resource in wireless networks

The approaches for tackling the surge of harmful interference between close-by transceivers reusing a signaling resource in wireless networks can be categorized as follows:

- Transmit power control to regulate the interference seen at the receivers [30, 31].
- Smart channelization to carefully select the transceivers reusing a given time-frequency channel such that close-by interference is avoided [32, 33].

- Advanced signal processing at the transmitters and/or receivers to mitigate the interference [34–36].

Indeed, as indicated, the availability of infrastructure assistance aids D2D networks in applying the aforementioned interference management techniques. Nevertheless, these techniques differ significantly regarding complexity and the share of resources that needs to be expended as overhead. Therefore, the efficacy of such techniques in providing performance gains must be carefully gauged and contrasted with each other, without missing to account for the essential overheads and real-world constraints. For instance, in practice, transmit powers and channelization decisions are updated far less frequently, based on the large-scale variations in the wireless channel, compared to the advanced signal processing techniques which often require tracking of the small-scale channel fluctuations incurring much higher overheads, i.e., to learn and exchange the essential side-information between devices [37].

Understanding how the complex interference environment in a large D2D system fundamentally delimits the communication performance is pivotal. An important factor that renders interference more severe in D2D is the ensuing irregular topology, which is essentially different from the downlink and uplink of a cellular only network, irrespective of how dense the spatial reuse (number of BSs per unit area) is or how irregular the BS positions are. Namely, as each cellular user is typically associated with the BS from which it receives the strongest signal, a natural interference protection is easily established by ensuring that the interferers are always outside the coverage region of the desired BS. Specifically, from the vantage of a cellular user, no individual downlink interferer is stronger than the desired signal, while no uplink transmission reaches an unintended (BS) receiver with higher power than the desired one. On the contrary, this natural interference protection provided by the cellular structure is completely absent when the transmitter-receiver pairs with D2D traffic are allowed to establish direct communication links. To understand this better, if we consider that the strongest signal is received from the closest transmitter, under BSs uniformly distributed on $\mathbb{R}^2$, the cellular links are always confined within the geometric cellular tessellations formed by the BS positions (cf. Fig. 1.3a), providing the aforementioned interference protection. In comparison, considering a D2D network formed by transmitters distributed identically as the aforesaid BSs, their in-

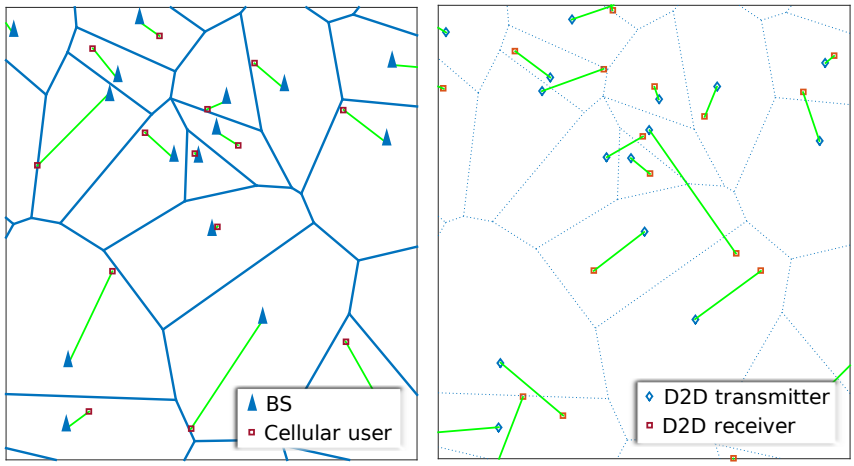

(a) Cellular links confined to cells. (b) D2D links distributed abritrarily.

Figure 1.3: Cellular topology vs. D2D topology

tended receivers need not be confined to such tessellations (cf. Fig. 1.3b), and the ensuing network geometry has the D2D links distributed rather independently.

The foregoing feature of the D2D networks indicates that a simple transmit power control would not be enough to regulate interference efficiently and smart channelization [32, 33] might be necessary, which could be complemented with power control to enhance the performance [38]. Also, D2D networks need not satisfy the property of cellular networks that the user performance is preserved with densification [39], i.e., with shrinking cell sizes, as long as the power-law path loss models hold [40]. Specifically, in D2D networks, this might depend on whether and how the D2D link lengths would vary with user density, which in turn might be application-dependent.

1.1.3 A Stochastic Geometry-based Analytical Framework

Most of the initial work that investigated the system level benefits of D2D had relied on simulations [17–28, 32, 33, 38]. Though simulations have long been the workhorse of wireless network design, they are often tedious, less general and difficult to glean insights from.

Lately, stochastic geometry is becoming an indispensable instrument

in wireless network analysis [41–63]. By mapping the empirical distribution of transmitter and receiver locations to appropriate point processes, it becomes possible to apply a powerful and expanding toolkit of mathematical results. This offers a complement, and increasingly even an outright alternative, to Monte-Carlo simulations. Due to its amenability to analytical treatment and suitability for the spatial behavior of D2D users, recent work on D2D [30, 31, 64–68] also have applied stochastic geometry tools.

As the performance metric for the networks considered in this dissertation, we focus squarely on the *ergodic* spectral efficiency, arguably the most operationally relevant quantity in contemporary systems [69, 70]. In this respect, however, we identify that most of the existing stochastic geometry-based analyses of D2D networks [30, 31, 64–68] and wireless networks, in general, [42–61] are not comprehensive and have some pitfalls.

The favorite analytical outcomes in conventional stochastic geometry literature are: (*i*) the distribution of the *instantaneous* SINR (signal-to-interference-plus-noise ratio) computed over all possible network geometries as well as the small-scale fading fluctuations, which is often presented as the *coverage probability*, and (*ii*) the spectral efficiency averaged over all possible network geometries. While the average spectral efficiency is indeed a useful quantity to gauge system-level benefits, the distribution of instantaneous SINR is not representative of performance in modern systems where the network coverage is oblivious to small-scale fading. Explicitly, in contemporary systems, since codewords span many fading realizations across frequency (because of the wide bandwidths) and time (because of hybrid ARQ), and also over space if multiple antennas are featured, network coverage is not associated with any instantaneous metric. The quantity that should be obtained in place of such instantaneous metric is the ergodic spectral efficiency averaged over the small-scale fading; its distribution over the (stochastic) network geometry provides a complete description of the user performance in the system. For instance, this distribution is essential to correctly gauge the edge-rate—recall from the 5G requirements in Section 1.1.1—whereas assessing the same from the instantaneous metric would be misleading. All the same, the conventional analytical approach renders such distribution of the ergodic spectral efficiency unwieldy. We rectify this shortcoming via a novel modeling approach for the interference that is propounded in the dissertation.

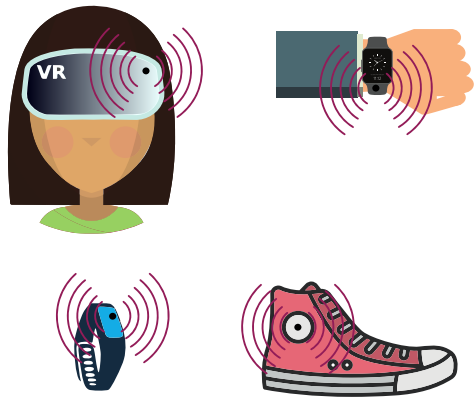

Figure 1.4: Examples of wearable devices: virtual reality gears, smart watches, fitness trackers and smart shoes.

1.1.4 Enclosed mmWave Wearable Networks

The expanding market for wearable computing devices (in short, *wearables*) bespeaks of a tomorrow where the sight of people with multiple body-born wearables connected wirelessly (cf. Fig. 1.4) might become commonplace [71, 72]. Such wireless devices can have a wide range of data rate requirements: from low-rate activity trackers to high-rate virtual/augmented-reality devices [73–75]. The disruptive changes in the wearable device market pose wireless communication challenges in two different aspects: (*i*) providing *wire-like* connectivity for the truly demanding applications such as augmented reality, some of which are yet to be unyoked [75, 76], and (*ii*) handling the high density of concurrent wireless transmissions, which is predicted to intensify with the proliferation of these devices.

The communication among wearables is expected to be highly proximal (cf. Fig. 1.5), in the form of small body area networks composed of very-short-range on-body links [77]. The presence of several wearable networks, one per person, in close vicinity creates a very high density of simultaneous wireless transmissions. Such scenarios are very likely in enclosed settings (cf. Fig. 1.6) like commuter trains, subways, airplanes, airports, or offices.

The existing short-range connectivity solutions, such as the WLAN (wireless local area network) interface based on IEEE 802.11 technology that employs random medium access control (MAC) protocols like carrier sense multiple access (CSMA), become very ineffi-

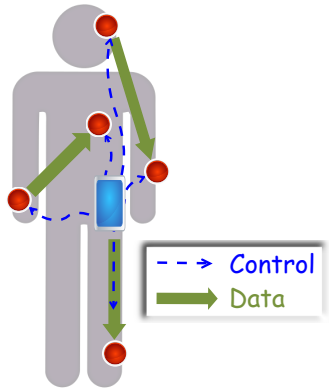

Figure 1.5: A wearable network on a person, coordinated via a hub (eg. smartphone).

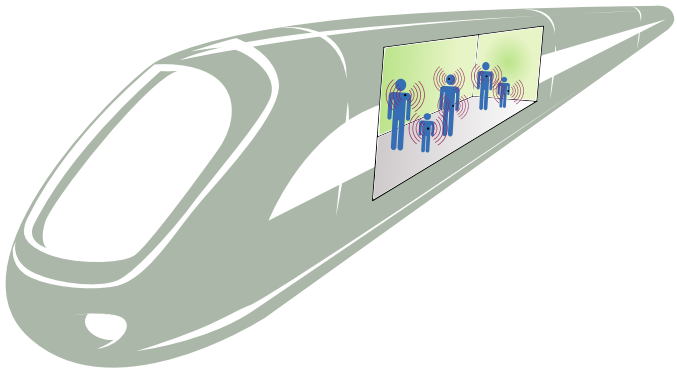

Figure 1.6: An illustration of several users with their respective wearable networks inside a train car.

cient when faced with the extremely high density of wireless transmissions [78]. While transmissions within each wearable network can be orthogonalized by means of coordination via a hub (cf. Fig. 1.5), interference from other wearable networks is very likely, as coordination between people can be challenging in practice. Understanding the ensuing complex interference environment as well as the on-body wireless channel is crucial for assessing the communication performance of such networks.

mmWave Frequencies are Appealing

Operation at mmWave frequencies seems promising for wearable networks due to inherent characteristics of these frequencies [8, 79, 80], namely:

- The availability of bandwidth (e.g., in the 60 GHz unlicensed band) so that wires can be replaced for high data rate applications.
- The suitability for short-range communication and dense spectral reuse due to the relatively better isolation from interference.
- The practicality of implementing directional antenna arrays within small devices, which can potentially boost the useful signal while reducing interference.

MmWave communication for indoor applications is becoming a reality thanks to standards such as WirelessHD [81] and IEEE 802.11ad [82]. These standards or the proposed D2D communication modes in mmWave-based 5G systems [9, 10, 83] could potentially be employed for wearable networks. There is, therefore, interest in establishing the feasibility of deploying very dense mmWave wearable networks, chiefly in enclosed settings [78, 84–87].

One of the early studies on wearable networks in indoor settings [78] that contrasted the operation at 5 GHz with 60 GHz—in terms of the number of transmissions that feature in the collision domain of random access protocols—indicated that the mmWave frequency provides relatively better isolation than the lower frequency, yet, interference from close-by networks are significant.

Feasibility and Performance

At mmWave frequencies, signals exhibit reduced scattering and minimal diffraction around blocking obstacles, but strong specular reflections off surfaces [88–95]. Measurement studies have reported that the reflections off the superstructure—i.e., walls, ceiling, and floor—dominate while the influence of details such as tables and cabinets as reflectors is insignificant [90]. As the blocking by obstacles (including people themselves) results in huge propagation losses [95–97], surface reflections are expected to play a major role in the performance of enclosed mmWave networks, by contributing additional signal and interference powers. Note that direct and reflected propagation paths can get blocked by people's bodies and it can occur in both signal as well as the interference paths. And there can be *self-body* blockages [98], i.e., situations where the body wearing a transceiver blocks the propagation from/to it.

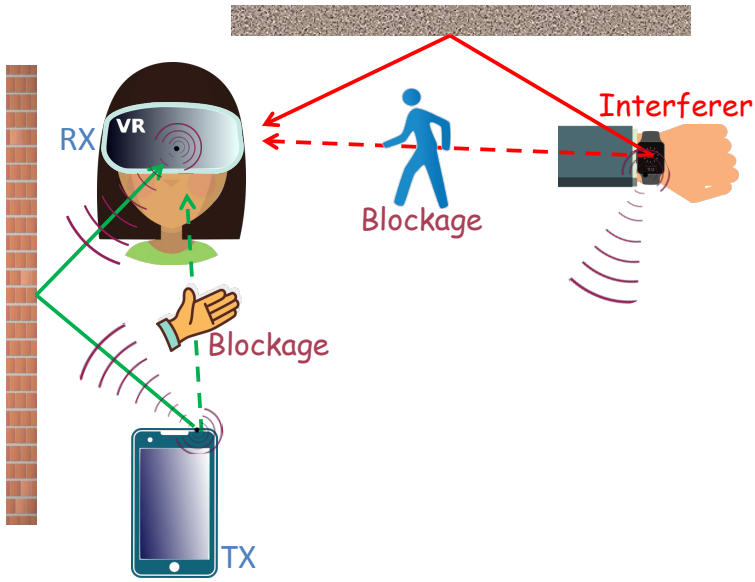

Figure 1.7: An illustration of reflections from interior surfaces (wall, ceiling, or floor) and blockages in the signal and interference propagation paths. Directional beams at the transceivers are also depicted, which gather useful signal while reducing unwanted interference.

In order to assess the feasibility and to evaluate the performance of such networks, it is crucial to model the interplay of reflections and blockages in relevant enclosed settings with high user densities. All the same, the possibility of directional beamforming [80, 99] must also be taken into account, by means of which wearables can gather useful signal from intended directions while reducing some of the unwanted interference incoming from other directions. In this regard, however, the models adopted by related work [78, 85, 86, 100] fall short of adequacy, and hence, significant advancement is needed to address relevant research questions. Recognizing this, in this dissertation, we set out to assemble the essential ingredients of mmWave propagation into a model that is tailored to the indoor setting with people wearing networks on them. Employing the propagation model, we investigate the feasibility and evaluate the spectral efficiency achievable by the communication links in these networks.

1.1.5 Summary of Motivation

The benefits of D2D communication under proximal wireless traffic in cellular networks—chiefly brought about by the denser spectral

reuse—must be gauged under a system model that incorporates the essential features of the ensuing complex interference environment in a large multicellular setting. Further, the performance gains provided by interference management techniques over the raw potential of D2D must be carefully contrasted, under reasonable assumptions. For such performance evaluations, a flexible and extensible analytical framework, which enable characterizing the spectral efficiency of the network, can serve as a powerful tool. The literature on stochastic geometry-based analysis sets the stage for devising such a framework; nonetheless, a significant rethinking of the existing modeling approaches is required to make the analysis more relevant to contemporary systems.

The extreme density of concurrent wireless transmissions that might ensue due to the coexistence of multiple wearables networks in indoor settings is predicted to be way beyond what the existing solutions for short-range communication can handle; add to that the increasing demand for data-rate-intensive wearable applications to go wireless. While operation at mmWave frequencies seems suitable for such demanding situations (dense spectral reuse coupled with very-short-range high data rate applications), its feasibility needs to be investigated. Impact of the propagation mechanisms at mmWave frequencies might differ radically from what is encountered at the conventional microwave frequencies. Appropriate propagation modeling, therefore, is crucial to address pertinent research questions such as the reliability of surface reflections in providing useful signal for efficient communication in the absence of a strong direct signal.

1.2 Contribution and Organization

Our investigations based on the foregoing motivation are expounded in Chapters 2 to 5; the technical contributions are briefed below:

- **A Novel Approach for Spectral Efficiency Analysis:** Chapter 2 introduces the general modeling principles that we follow for the spectral efficiency analysis of wireless networks throughout the dissertation. In particular, the application of stochastic geometry to the analysis of wireless networks is shown to be substantially facilitated by (*i*) a clean separation of time scales, (*ii*) the abstraction of small-scale effects via ergodicity, and (*iii*) an interference model reflecting

the receiver's lack of knowledge of how individual interference terms are faded. These steps render the analysis simpler and more precise, and more amenable to extensions incorporating advanced features. The improved analytical potency of this novel approach, in accurately computing the ergodic spectral efficiency—including its distribution over the network locations and the average thereof—and in rightly inferring the coverage, is contrasted with the conventional approach. While the exposition is conducted under arbitrary network geometry and propagation model, a number of examples pertinent to the scenarios that shall arise in the following chapters are provided.

- **D2D Communication in Cellular Networks:** Chapter 3 presents a framework that enables characterizing analytically the spectral efficiency achievable by D2D communication integrated with a cellular network. This framework is based on a stochastic geometry formulation that applies the aforesaid analytical approach while furthering the interference modeling to enable a controllable degree of spatial averaging that helps to yield approximate yet simpler characterizations, without noticeable loss in accuracy. Utilizing the framework, which engulfs both the underlay and overlay options, several examples are provided to illustrate its capability and to gauge the raw benefits of D2D, without any smart channelization of simultaneous D2D transmissions. These examples, while confirming the potential of D2D in situations of strong traffic locality, indicates the need for managing the interference surge suffered by a share of D2D receivers and particularly the BS receiver in the underlay mode.

- **Exclusion Regions for Interference Protection in D2D Networks:** Chapter 4 addresses the benefits of introducing exclusion regions around the receivers for interference protection in D2D networks. Specifically, the D2D links are selected to reuse a given time/frequency channel based on some channelization scheme that ensures the desired exclusion regions around the receivers. By extending the foregoing analytical framework, the underlay and overlay options are addressed separately, so as to incorporate exclusion regions—wherein no D2D transmitters are active—around, respectively, the BS receivers and the D2D receivers. Such exclusion regions offer

protection from interference at the expense of a sparser spatial reuse of spectrum, bringing about a tradeoff whose resolution entails optimizing the size of the exclusion regions as function of relevant system parameters. This optimization is carried out for the overlay case, with our figure of merit being the spectral efficiency, altogether establishing the major benefits of incorporating suitably sized exclusion regions in the applicable scheduling algorithms.

- **Enclosed mmWave Wearable Networks:** Chapter 5 investigates the feasibility of mmWave frequencies for personal networks of wireless wearable devices in enclosed settings. At these frequencies, specular reflections off surfaces are expected to contribute intended signal power and, simultaneously, to aggravate the interference at the receivers. Meanwhile, blockages by obstacles and people—including the individuals wearing the devices—are expected to shield receivers from interference. Considering people with wearable networks on them in an enclosed space, signal and interference propagations are modeled, accounting for reflections off the interior surfaces (walls/ceiling/floor), body blockages in the direct and reflected paths and directional antenna gains. Employing the propagation model and with the aid of stochastic geometry and random shape theory, we assess the interplay of surface reflections and blockages on the spectral efficiency achievable by wearable networks equipped with directional antenna arrays under dense deployments in relevant indoor settings.

List of Publications

Journal Articles

- G. George, R. K. Mungara, A. Lozano and M. Haenggi, "Ergodic Spectral Efficiency in MIMO Cellular Networks", *IEEE Transactions on Wireless Communications*, vol. 16, no. 5, May 2017.

- G. George, K. Venugopal, A. Lozano and R. W. Heath Jr., "Enclosed mmWave Wearable Networks: Feasibility and Performance", *IEEE Transactions on Wireless Communications*, vol. 16, no. 4, Apr. 2017.

- G. George, R. K. Mungara and A. Lozano, "An Analytical framework for Device-to-Device Communication in Cellular Networks", *IEEE Transactions on Wireless Communications*, vol. 14, no. 11, Nov. 2015.

- R. K. Mungara, G. George and A. Lozano, "Overhead and Spectral Efficiency of Pilot-Assisted Interference Alignment in Time-Selective Fading Channels", *IEEE Transactions on Wireless Communications*, vol. 13, no. 9, Sep. 2014.

Conference Papers

- G. George, R. K. Mungara, A. Lozano and M. Haenggi, "A Novel Approach for Spectral Efficiency Analysis in MIMO Cellular Networks", *accepted in IEEE Int'l Conference on Communications*, Paris, France, May 2017.

- G. George and A. Lozano, "Impact of Reflections in Enclosed mmWave Wearable Networks", *IEEE Int'l Workshop on Computational Advances in Multi-Sensor Adaptive Processing*, Cancun, Mexico, Dec. 2015.

- G. George, R. K. Mungara and A. Lozano, "Optimum Exclusion Regions for Interference Protection in Device-to-Device Wireless Networks", *Int'l Symposium on Modeling and Optimization in Mobile, Ad Hoc, and Wireless Networks (WiOpt)*, Mumbai, India, May 2015.

- G. George, R. K. Mungara and A. Lozano, "Overlaid Device-to-Device Communication in Cellular Networks", *IEEE Global Telecommunications Conference*, Austin, USA, Dec. 2014.

- R. K. Mungara, G. George and A. Lozano, "Pilot-Assisted Interference Alignment in Time-Selective Fading Channels", *IEEE Global Telecommunications Conference*, Atlanta, USA, Dec. 2013.

- R. K. Mungara, G. George and A. Lozano, "System-level Performance of Distributed Cooperation", *Asilomar Conference on Signals, Systems and Computers*, Pacific Grove, CA, USA, Nov. 2012.

Chapter 2

A Novel Approach for Spectral Efficiency Analysis

2.1 Background

An essential basis of this dissertation is the spectral efficiency analysis of wireless networks. To this end, we devise a novel modeling approach that takes us on a different route from the established one in stochastic geometry-based analyses [42–61]. This proves decidedly advantageous because it yields solutions that are both simpler and more precise than previous ones, and, most importantly, because it opens the door to accommodating key ingredients which have hitherto been out of reach. The modeling approach that unlocks new analytical possibilities is not arbitrary but rather based on sound arguments:

1. A clean decoupling of the small- and large-scale channel features, recognizing that the phenomena that engender these effects are separate.

2. A resolute adoption of ergodic performance metrics with respect to the small-scale features, recognizing that such small-scale ergodicity reflects well the operating conditions of contemporary wireless systems [69, 70].

3. The acknowledgment that each receiver, while being privy to the fading of its intended signal, does not track the fading of each interference term.

Enabled by local ergodicity, the impact of small-scale features on user performance can be abstracted out to focus the stochastic geometry analysis where it makes a difference, i.e., on the large-scale aspects.Thereby, as indicated, the analysis is advanced on all fronts: tractability, accuracy, and generality.

The dissertation addresses single-user communication involving single data stream transmissions under wireless channels with interference from concurrent transmissions; the transceivers have either a single antenna or multiple antennas employed for directional beamforming (cf. Chapter 5). Although the investigations in the dissertation are done under single-stream communication, our modeling approach renders the analysis amenable to extensions incorporating advanced features. For instance, MIMO spatial multiplexing can be easily included (a glimpse of which will be exemplified in the chapter), as we have demonstrated in a recent work [101] in the context of a downlink cellular network, along with the details presented in this chapter.

2.2 Network Modeling

The exposition in this chapter is conducted under an arbitrary network geometry. Specifically, the spatial distribution of the *co-channel* transmitter-receiver pairs—the ones simultaneously communicating via a given time-frequency channel—is arbitrary. All the same, we provide many examples pertinent to the particular network geometries that shall arise in the scenarios considered in the following chapters.

2.2.1 Separation of Scales

Established via extensive propagation measurements, the separation between large- and small-scale propagation phenomena has long been instrumental in the study of wireless networks, thereby enabling characterizations that would otherwise be unwieldy [102]. This separation relies on the premise that, over suitably small distances (tens to hundreds of wavelengths), the large-scale phenomena remain virtually unchanged and only small-scale fluctuations ensue. Accordingly, within local neighborhoods delineated around transmitters and receivers, the small-scale channel behavior conforms to a stationary random process whose distribution is dictated by the large-scale features. This space-domain random process then maps

to a time-domain process, through the user velocity. Further, this time-domain process is ergodic, following the very mild condition that the Doppler spectrum remains free of delta functions.

As the dwell time in a local neighborhood is far longer than the span of signal codewords, for frequencies and velocities in the widest possible range of interest the large-scale features can be deemed fixed over an individual codeword. Alternatively, the small-scale fading may or may not remain fixed over a codeword, depending on the coherence of such fading and on how codewords are arranged in time and/or frequency. This dichotomy gives rise to two classic information-theoretic idealizations of the channel over the horizon of a codeword:

- *Nonergodic.* Fading random, but fixed over the codeword.
- *Ergodic.* Fading random and manifesting amply many values to essentially unveil its distribution over the codeword.

In turn, these idealizations map respectively to outage and ergodic definitions for the spectral efficiency. Albeit both being useful, the ergodic definition is the most characteristic of modern systems where codewords can be interspersed over very wide bandwidths, across hybrid-ARQ repetitions, and possibly over multiple antennas, and they can be subject to scheduling and link adaptation. These mechanisms, as asserted in [69, 70], are indeed best abstracted by ergodic spectral efficiencies involving expectations over the small-scale fading, with the large-scale features held fixed. Conversely, since the large-scale features barely change over the extent of individual codewords, no averaging over these features has significance. Stochastic geometry should enter the analysis at this point when the small-scale variations are abstracted out, so as to undertake the randomization over the large-scale ones.

2.2.2 Large-scale Modeling

We focus on the communication between a given transmitter-receiver pair in the network (cf. Fig. 2.1) where the co-channel transmitters, comprising the intended one and K other interferers, have a fixed transmit power P. Let us index the intended transmitter with $k = 0$ while the interferers with $k = 1, \ldots, K$. The transmission

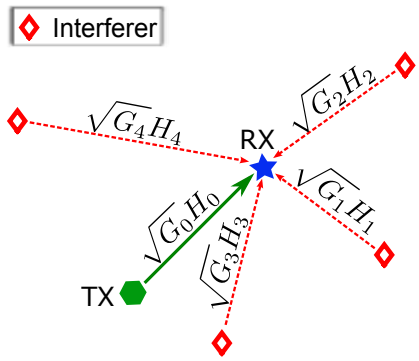

Figure 2.1: A receiver (RX), its intended transmitter (TX) and four interferers.

from the kth transmitter reaches the receiver with the *local-average*[1] power modeled as $P\,G_k$, where G_k denotes the large-scale gain that abstracts the propagation losses and the (transmit and receive) antenna gains.

The gains $\{G_k\}$ are constituted by the dominant propagation mechanisms (line-of-sight or/and non-line-of-sight) that emerge through the propagation environment, which in turn depend on the network geometry and the frequency of operation. Generally, G_k can be abstracted as a function of a few parameters whose variations beyond the local neighborhood are modeled via appropriate stochastic processes; the relative positions of the receiver and transmitter, within the space occupied by the co-channel links, are central among these parameters.

In this chapter, $\{G_k\}_{k=0}^{K}$ are kept arbitrary, while we invoke appropriate models for exemplifications at different stages of the exposition.

2.2.3 Small-scale Modeling

The observation of the receiver at symbol n is expressed as

$$y[n] = \sqrt{P\,G_0}\,H_0[n]\,s_0[n] + z[n] \tag{2.1}$$

[1]The term "local-average" indicates averaging over the small-scale fading only.

where the leading term is the intended signal received from the paired transmitter while

$$z[n] = \sum_{k=1}^{K} \sqrt{P\,G_k}\,H_k[n]\,s_k[n] + v[n] \tag{2.2}$$

is the aggregate interference received from the K undesired co-channel transmitters plus the thermal noise v. In turn, $\{s_k\}$ are the transmit signals and $\{H_k\}$ the associated small-scale fading coefficients.

The fading coefficients $\{H_k\}_{k=0}^{K}$ are independent and of unit power, but otherwise arbitrarily distributed, while $v \sim \mathcal{N}_{\mathbb{C}}(0, \sigma_{\mathrm{N}}^2)$. The transmit signal is distributed as $s_k \sim \mathcal{N}_{\mathbb{C}}(0, 1)$, a choice that is justified later.

Note that, when antenna arrays are featured at the transceivers for directional beamforming (cf. Chapter 5), the relationship in (2.1) is the post-array-processing received signal, with G_k subsuming the (transmit and receive) array gains and H_k being the effective fading coefficient that models the small-scale fluctuations.

Conditioned on the large-scale gains $\{G_k\}_{k=0}^{\infty}$, which are fixed as far as the small-scale fading is concerned, the instantaneous SINR at symbol n is

$$\mathsf{SINR}[n] = \frac{G_0\,H_0[n]}{\sum_{k=1}^{K} G_k\,H_k[n] + \sigma_{\mathrm{N}}^2/P}. \tag{2.3}$$

2.3 Interference Modeling

As indicated, the key differentiating feature of our framework is the interference modeling, motivated and presented in this section.

2.3.1 Ergodic Spectral Efficiency

Assuming that $H_0[1], \ldots, H_0[N]$ are known at the receiver, the mutual information (in bits/symbol) over codewords spanning N symbols is

$$\frac{1}{N} I\Big(s_0[1], \ldots, s_0[N]; y[1], \ldots, y[N] | H_0[1], \ldots, H_0[N], \{G_k\}_{k=0}^{K}\Big) \tag{2.4}$$

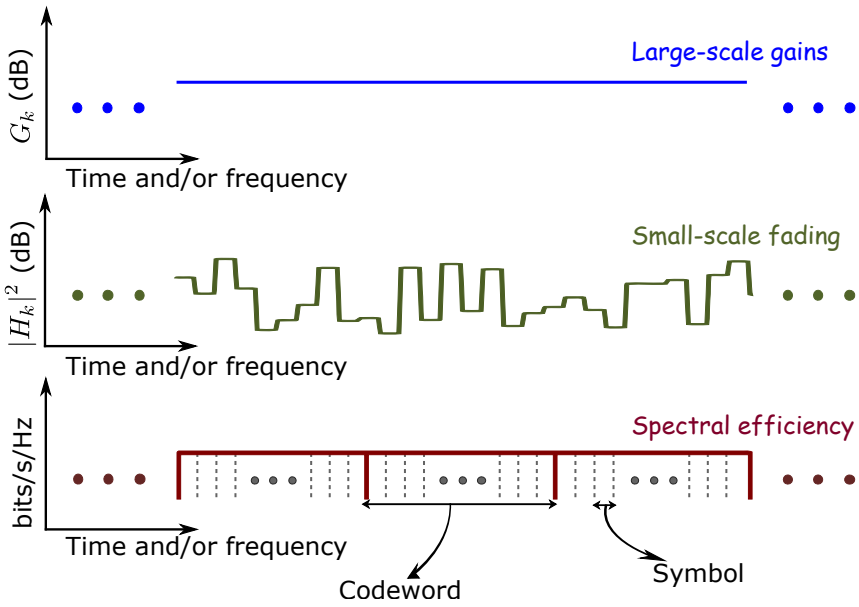

Figure 2.2: An Illustration of the variation of the large-scale gains, small-scale fading and the ergodic spectral efficiency over several codewords—consisting of symbols arranged in time and/or frequency—spanning the dwell time in a local neighborhood.

which, with IID (independent and identically distributed) codeword symbols, becomes

$$\frac{1}{N}\sum_{n=1}^{N} I\big(s_0[n]; y[n]\,|H_0[n], \{G_k\}_{k=0}^{K}\big). \tag{2.5}$$

With spans of a few thousand symbols, codewords are nowadays long enough and arranged in such a way—interspersed in time, frequency, and increasingly across antennas—to experience sufficiently many fading swings for an effective averaging of the mutual information to take place over the small-scale fading (cf. Fig. 2.2). From the stationarity and ergodicity of the small-scale fading over the codeword, the averaging in (2.5) becomes an expectation and bestows the significance of the ergodic spectral efficiency (in bits/s/Hz)

$$C_{\mathsf{exact}} = \mathbb{E}_{H_0}\Big[I\big(s_0; y\,|H_0, \{G_k\}_{k=0}^{K}\big)\Big] \tag{2.6}$$

$$= \mathbb{E}_{H_0}\Big[I\Big(s_0; \sqrt{P\,G_0}\,H_0\,s_0 + z\,\Big|H_0, \{G_k\}_{k=0}^{K}\Big)\Big]. \tag{2.7}$$

This quantity, a baseline in the sequel, does not admit explicit expressions. Rather, the evaluation of C_{exact} requires computation-

ally very intensive simulations involving lengthy Monte-Carlo histograms (cf. Appendix A.1).

2.3.2 Local Distribution of Interference

Let us examine the local distribution of the interference-plus-noise z as defined in (2.2), for some given $\{G_k\}_{k=0}^K$. Note that, without further conditioning on $\{H_k\}_{k=1}^K$, i.e., without the receiver knowing the fading coefficients from *all* interferers, the distribution of z over the local neighborhood is generally not Gaussian. Conditioned only on $\{G_k\}_{k=1}^K$, the distribution of z is actually highly involved; in Rayleigh fading, for instance, it involves products of Gaussians. While the non-Gaussianity of z is irrelevant to the SINR, since only the variance of z matters in that respect, it is relevant to information-theoretic derivations and chiefly that of the spectral efficiency, which does depend on the distribution of z.

Conventional Modeling Approach

Conventionally, C_{exact} is analyzed in the form it would have if the fading coefficients $\{H_k\}_{k=1}^K$ were actually known by the receiver and z were consequently Gaussian, namely the form

$$C_{\mathsf{ub}} = \mathbb{E}_{\{H_k\}_{k=0}^K}\left[\log_2\left(1+\frac{G_0\,|H_0|^2}{\sum_{k=1}^K G_k\,|H_k|^2+\sigma_{\mathrm{N}}^2/P}\right)\right] \tag{2.8}$$

where the tacit redefinition of z as Gaussian—although rarely made explicit—is unmistakable from $I(s_0;\sqrt{\gamma}\,s_0+z)=\log_2(1+\gamma)$, which is applicable only when s_0 and z are Gaussian. Besides being analytically convenient, a Gaussian modeling of z turns out to be sensible because, if a decoder is designed for Gaussian interference-plus-noise (either by design or because the distribution thereof is unknown), then the spectral efficiency is precisely as if the interference-plus-noise were indeed Gaussian [103], regardless of its actual distribution. Note that, once z is taken to be Gaussian, the capacity-achieving signal distribution is also Gaussian, validating our choice for s_0. At the same time, the gifting of $\{H_0\}_{k=1}^K$ as extra side information to the receiver renders (2.8) an upper bound to C_{exact}, hence the denomination C_{ub}.

Although much more tractable than C_{exact}, the form of C_{ub} has the issue of depending not only on H_0, but further on $\{H_k\}_{k=1}^K$; this still clutters its analysis considerably.

Example 2.1. With Rayleigh fading in all the links (intended and interfering), i.e., $H_k \sim \mathcal{N}_{\mathbb{C}}(0,1)$ for $k = 0, \ldots, K$, C_{ub} becomes (cf. Appendix A.2)

$$C_{\mathsf{ub}} = \log_2 e \int_0^{\infty} \frac{e^{-x \frac{\sigma_{\mathrm{N}}^2}{PG_0}}}{1+x} \prod_{k=1}^{K} \frac{1}{1+x\,G_k/G_0}\,\mathrm{d}x. \tag{2.9}$$

A Novel Modeling Approach

Alternatively, we propound to go one step further in the Gaussian modeling of z, by forgoing the small-scale variations in its power, i.e., to use

$$z \sim \mathcal{N}_{\mathbb{C}}\left(0, \sum_{k=1}^{K} P\,G_k + \sigma_{\mathrm{N}}^2\right). \tag{2.10}$$

The closeness between this distribution for z and its original counterpart in (2.2) has been tightly bounded [104, 105].

The virtue of rendering z Gaussian without the strain of granting the receiver with $\{H_k\}_{k=1}^K$ results in gratifying analytical benefits. (Some contexts, other than the D2D one that we focus in this dissertation, where this has been tested include [62, 63, 101, 106].)

2.3.3 Characterization of the Ergodic Spectral Efficiency

With z as in (2.10), the instantaneous SINR then becomes

$$\mathsf{SINR} = \frac{G_0\,|H_0|^2}{\sum_{k=1}^{K} G_k + \sigma_{\mathrm{N}}^2/P} \tag{2.11}$$

and the corresponding ergodic spectral efficiency is

$$C = \mathbb{E}_{H_0}\left[\log_2\left(1 + \frac{G_0|H_0|^2}{\sum_{k=1}^{K} G_k + \sigma_{\mathrm{N}}^2/P}\right)\right] \tag{2.12}$$

which is the quantity we shall work with.

Since, with Gaussian codewords and a given variance for z, the mutual information is minimized when z is Gaussian [107], we have that $C \leq C_{\mathsf{exact}}$. The similarity between C and C_{exact}, with the former characterized analytically and the latter obtained through Monte-Carlo simulation, is illustrated in the examples that follow.

Contrasting the instantaneous SINR expressions in (2.3) and (2.11), the analytical virtues of our model for z become evident once we rewrite the latter as $\mathsf{SINR} = \rho\,|H_0|^2$ where

$$\rho = \frac{G_0}{\sum_{k=1}^{K} G_k + \sigma_{\mathrm{N}}^2/P} \tag{2.13}$$

is the local-average SINR at the receiver, fixed over any entire codeword and cleanly separated from the fluctuant term $|H_0|^2$; this reflects the decoupling between the large- and small-scale dependences. Conditioned on the large-scale gains $\{G_k\}_{k=0}^{K}$, ρ becomes determined and the conditional distribution of the instantaneous SINR is then given directly by that of $|H_0|^2$, i.e., by the CDF (cumulative distribution function)

$$F_{|H_0|^2}(\zeta) = \mathbb{P}\left[|H_0|^2 < \zeta\right],$$

while the ergodic spectral efficiency of a link with local-average SINR ρ is

$$C(\rho) = \mathbb{E}_{H_0}\left[\log_2\left(1 + \rho\,|H_0|^2\right)\right] \tag{2.14}$$

$$= \int_0^\infty \log_2(1+\rho\,\zeta)\,\mathrm{d}F_{|H_0|^2}(\zeta) \tag{2.15}$$

which, through ρ, sets the stage for further computations involving the geometry of the network, via the distributions that model the large-scale gains $\{G_k\}_{k=0}^{K}$, while being undistracted by lingering small-scale terms.

Example 2.2. In Rayleigh fading,

$$F_{|H_0|^2}(\zeta) = 1 - e^{-\zeta}, \tag{2.16}$$

from which

$$C(\rho) = e^{1/\rho}\,E_1\!\left(\frac{1}{\rho}\right)\log_2 e, \tag{2.17}$$

where $E_n(x) = \int_1^\infty \mathsf{t}^{-n} e^{-x\,\mathsf{t}}\,\mathrm{d}\mathsf{t}$ is an exponential integral.

For fading distributions other than Rayleigh, or with MIMO (spatial multiplexing) or other features, corresponding forms can be obtained for $C(\rho)$, always with the key property of these being a function of ρ and not of the instantaneous fading coefficients as demonstrated in the following examples in this section.

Example 2.3. Under Nakagami-m fading ($m \geq 1/2$),

$$F_{|H_0|^2}(\zeta) = 1 - \frac{1}{\Gamma(m)}\Gamma(m, m\,\zeta), \tag{2.18}$$

with $\Gamma(u) = \int_0^\infty \mathsf{t}^{u-1}\, e^{-u}\, \mathrm{d}\mathsf{t}$ and $\Gamma(u, v) = \int_v^\infty \mathsf{t}^{u-1}\, e^{-u}\, \mathrm{d}\mathsf{t}$ being, respectively, the gamma function and the upper incomplete gamma function. Using (2.18) in (2.15), the ergodic spectral efficiency becomes [108]

$$C(\rho) = \left(\frac{m}{\rho}\right)^m \mathcal{I}_m\left(\frac{m}{\rho}\right) \frac{\log_2 e}{\Gamma(m)} \tag{2.19}$$

with $\mathcal{I}_n(u) = \int_0^\infty \mathsf{t}^{n-1}\, \log_e(1+\mathsf{t})\, e^{-u\,\mathsf{t}}\, \mathrm{d}\mathsf{t}$. Note that, setting $m = 1$ in (2.19) returns (2.17).

Example 2.4. Consider MIMO spatial multiplexing wherein an $\mathsf{m} \times 1$ signal vector $\boldsymbol{s}_0$—in place of s_0—is communicated from the transmitter to the receiver via an $\mathsf{N_r} \times \mathsf{N_t}$ channel matrix $\boldsymbol{H}_0$—replacing H_0—having IID Rayleigh-faded entries, then [109]

$$C(\rho) = e^{\mathsf{N_t}/\rho} \sum_{i=0}^{\mathsf{m}-1} \sum_{j=0}^{i} \sum_{\ell=0}^{2j} \left\{ \binom{2\,i - 2\,j}{i-j} \binom{2\,j + 2\,\mathsf{n} - 2\,\mathsf{m}}{2\,j - \ell} \right.$$
$$\left. \cdot\, \frac{(-1)^\ell\, (2\,j)!\, (\mathsf{n} - \mathsf{m} + \ell)!}{2^{2i-\ell}\, j!\, \ell!\, (\mathsf{n} - \mathsf{m} + j)!} \sum_{q=0}^{\mathsf{n}-\mathsf{m}+\ell} E_{q+1}\left(\frac{\mathsf{N_t}}{\rho}\right) \right\} \log_2 e \tag{2.20}$$

with $\mathsf{m} = \min(\mathsf{N_t}, \mathsf{N_r})$ and $\mathsf{n} = \max(\mathsf{N_t}, \mathsf{N_r})$.

Before proceeding further, let us validate $C(\rho)$ as in the foregoing examples by contrasting them with the corresponding C_{exact} as per (2.6), which—recall—is computed as detailed in Appendix A.1.

Example 2.5. Consider a transmitter-receiver pair (cf. Fig. 2.1) with the receiver suffering interference from $K = 10$ unintended co-channel transmitters. Let the large-scale gain be modeled by the following distance dependent path loss function

$$G_k = L\, r_k^{-\eta} \tag{2.21}$$

where r_k is the distance between the kth transmitter and the receiver, $\eta > 2$ is the path loss exponent and L is the path loss at 1 meter. Further, assuming interference-limited conditions ($\sigma_{\mathrm{N}}^2/P \to 0$),

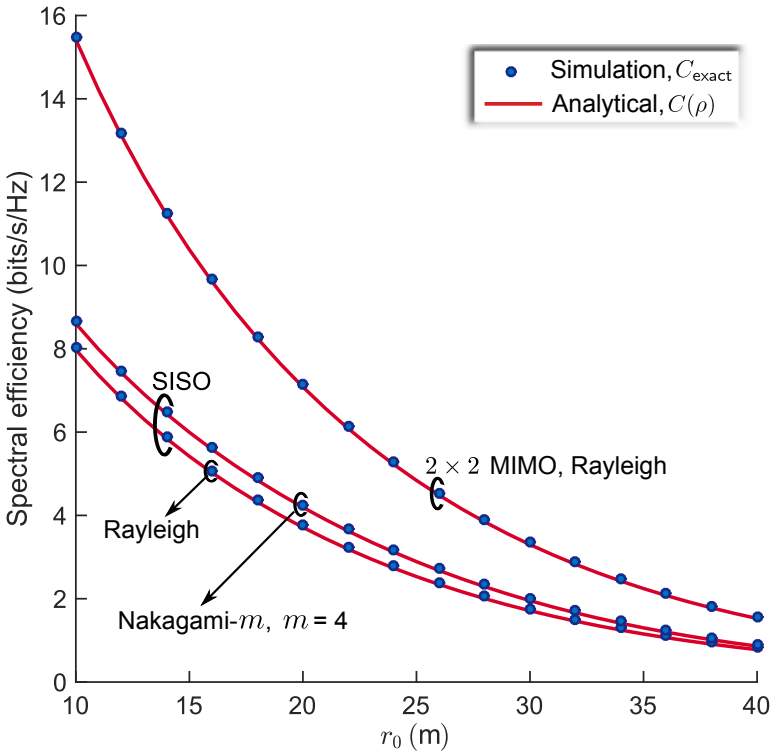

Figure 2.3: Ergodic spectral efficiency vs. the intended link distance r_0, under the large-scale gain model in (2.21) with path loss exponent $\eta = 4$, interference-limited conditions ($\sigma_{\text{N}}^2/P \to 0$), and $K = 10$ interferers with link distances $r_k = 45 + 5\,k$ m, for $k = 1, \ldots, 10$.

the local-average SIR can be expressed as

$$\rho = \frac{r_0^{-\eta}}{\sum_{k=1}^{10} r_k^{-\eta}} \tag{2.22}$$

following (2.13). In Fig. 2.3, $C(\rho)$ is contrasted with C_{exact} by setting the interfering link distances to $r_k = 45 + 5\,k$ m, for $k = 1, \ldots, 10$, and the path loss exponent to $\eta = 4$, for different values of the intended link distance $r_0 \in [10, 40]$. Specifically, for SISO, the comparison is given under fading coefficients distributed as Rayleigh and Nakagami-m (with $m = 4$), while for MIMO, it is done with $\mathsf{N}_{\text{t}} = \mathsf{N}_{\text{r}} = 2$ while the channel matrices $\{\boldsymbol{H}_k\}_{k=0}^{10}$ have IID Rayleigh-faded entries.

The spectral efficiency C obtained via our analytical approach is not only an accurate lower bound to C_{exact}, but arguably more operationally relevant because it is unlikely that the receiver can learn

the exact distribution of such interference and, even if it could, a standard decoder for Gaussian noise might be featured.

In contrast to our approach, the conventional way of dealing with C_{ub} renders extensions (in SISO) to fading distributions other than Rayleigh fading (which itself returned the complicated integral form in (2.9)) and incorporation of MIMO unwieldy.

2.4 Distribution of the Local-Average SINR

As yet, we have established that with the large-scale gains $\{G_k\}_{k=0}^K$ conditioned upon, the local-average SINR ρ determines the spectral efficiency C, averaged over the small-scale fading. Once the conditioning on $\{G_k\}_{k=0}^K$ is released, ρ becomes itself a random variable, signifying the variations beyond the local neighborhood, essentially induced by the random network geometry. The ensuing distribution of the local-average SINR, given by the CDF

$$F_\rho(\xi) = \mathbb{P}\left[\frac{G_0}{\sum_{k=1}^K G_k + \sigma_{\mathrm{N}}^2/P} < \xi\right], \tag{2.23}$$

is a central ingredient in the subsequent analysis of the ergodic spectral efficiency. This function can be computed via Monte-Carlo simulations, as it is done conventionally by system designers, based on the stochastic modeling of the large-scale propagation features that dictate $\{G_k\}_{k=0}^K$, for the network under consideration.

Before moving ahead, it is worth pondering what the randomization of ρ signifies, concerning our narrative thus far; recall, we have been focusing on a receiver, its intended transmitter and the K co-channel interferers. For instance, if the receiver position is held fixed, the CDF $F_\rho(\cdot)$ computed over the distribution of $\{G_k\}_{k=0}^K$, induced by the random transmitter positions and the large-scale features that transpire consequently, gives a complete description of the local-average SINR enjoyed by a receiver at that particular position within the space occupied by the network. The conditioning on the receiver location may further be released, possibly letting $F_\rho(\cdot)$ encompass more situations within the network. This, however, turns out to be immaterial for several network scenarios that will be addressed in the dissertation (cf. Section 2.7).

2.4.1 Application of Stochastic Geometry

Stochastic geometry serves as a potent analytical tool for wireless network analysis. Under several scenarios of practical relevance, simulations can be replaced outrightly, with easy-to-evaluate analytical expressions for $F_\rho(\cdot)$, as will be seen in the sequel.

Generally, direct and exact analytical forms are not yielded for $F_\rho(\cdot)$. Nonetheless, we will demonstrate, in the following chapter, that by introducing prudent modeling assumptions fitted to the network geometry of interest, approximate characterizations may be obtained, without significant loss in accuracy.

Characterization of $F_{1/\rho}(\cdot)$ in the Laplace Domain

Alternatively, the difficulty in computing $F_\rho(\cdot)$ may be skirted by resorting to an approach that obtains $F_{1/\rho}(\cdot)$ in the Laplace domain, namely,

$$\mathcal{L}_{F_{1/\rho}}(\mathsf{s}) = \frac{1}{\mathsf{s}}\,\mathbb{E}_\rho\Big[e^{-\mathsf{s}/\rho}\Big] \tag{2.24}$$

$$= \frac{1}{\mathsf{s}}\,\mathbb{E}_{\{G_k\}_{k=0}^K}\left[e^{-\mathsf{s}\frac{\sigma_{\mathrm{N}}^2/P+\sum_{k=1}^K G_k}{G_0}}\right] \tag{2.25}$$

$$= \frac{1}{\mathsf{s}}\,\mathbb{E}_{\{G_k\}_{k=0}^K}\left[e^{-\mathsf{s}\frac{\sigma_{\mathrm{N}}^2/P}{G_0}}\prod_{k=1}^K e^{-\mathsf{s}\,G_k/G_0}\right] \tag{2.26}$$

which, under several relevant models for the large-scale gains and the network geometry, admits analytical solutions. Once an applicable expression for $\mathcal{L}_{F_{1/\rho}}(\cdot)$ is derived, a numerical inversion thereof—using the *Abate and Whitt algorithm* [110]—yields an approximation for $F_{1/\rho}(\cdot)$, and subsequently for $F_\rho(\cdot)$, in a series form that is accurate with only a few terms, as couched in the following Lemma.

Lemma 2.1. The CDF of the local-average SINR ρ is

$$F_\rho(\xi) \approx 1 - \xi\,\frac{e^{A/2}}{2^{\mathsf{B}}}\sum_{b=0}^{\mathsf{B}}\binom{\mathsf{B}}{b}\sum_{q=0}^{\mathsf{Q}+b}\frac{(-1)^q}{D_q}\,\Re\Big\{\mathcal{L}_{F_{1/\rho}}(\xi\,t)\Big\} \tag{2.27}$$

where $t = (A + \mathrm{j}2\pi q)/2$ while $D_0 = 2$ and $D_q = 1$ for $q \geq 1$. In turn, the parameters A, B and Q control the accuracy of the approximation. Suggested values for numerical Laplace transform inversions with many digits of precision are $A = 18.4$, $\mathsf{B} = 11$ and

$\mathsf{Q} = 15$ [110]. Following the recommendations of [111] for a 4-digit accuracy, a more relaxed—but still plentiful for our purposes—precision target, we obtain $A = 9.21$ and $\mathsf{B} = 5$, with Q as large as possible; as it turns out, moderate values of Q suffice to yield error levels that are negligible.

Proof. The CDF of ρ can be expressed as

$$F_\rho(\xi) = \mathbb{P}\left[\rho < \xi\right] \tag{2.28}$$
$$= \mathbb{P}\left[1/\rho > 1/\xi\right] \tag{2.29}$$
$$= 1 - F_{1/\rho}(1/\xi). \tag{2.30}$$

The numerical inversion of $\mathcal{L}_{F_{1/\rho}}(\cdot)$, as per [110, Eq. (15)], gives the approximation for $F_{1/\rho}(\cdot)$, which, plugged into (2.30) completes the proof. ■

Apart from aiding the computation of $F_\rho(\cdot)$, the function $\mathcal{L}_{F_{1/\rho}}(\cdot)$ also serves as an ingredient in the characterization of the spatially averaged spectral efficiency, a quantity we shall define later in Section 2.6, under Rayleigh fading: our recourse in the derivation of many essential results in the forthcoming chapters.

Let us exemplify the aforementioned steps for computing $F_\rho(\cdot)$, under a setting that shall become applicable in the sequel.

Example 2.6. Let the receiver and all the co-channel transmitters be located on $\mathbb{R}^2$, (cf. Fig. 2.4) in such a way that, from the vantage of the receiver, the intended transmitter is located at a (fixed) distance r_0 away (at an arbitrary angle). In turn, the interferer locations, modeled via a point process $\Phi_{\mathcal{A}} \subset \mathbb{R}^2$, are within an annular region $\mathcal{A}(R_{\mathsf{i}}, R_{\mathsf{o}})$ centered at the receiver location with the inner radius R_{i} and the outer radius R_{o}. Further, assuming the large-scale gain model in (2.21), the CDF $F_{1/\rho}(\cdot)$ in the Laplace domain becomes

$$\mathcal{L}_{F_{1/\rho}}(\mathsf{s}) = \frac{e^{-\mathsf{s}\frac{\sigma_{\mathrm{N}}^2 r_0^\eta}{L P}}}{\mathsf{s}} \mathbb{E}_{\Phi_{\mathcal{A}}}\left[\prod_{k=1}^{K} e^{-\mathsf{s}\, r_0^\eta\, r_k^{-\eta}}\right] \tag{2.31}$$

where the expectation is over the random interfering link distances $\{r_k\}_{k=1}^K$, whose distribution can be modeled via an appropriate point process for $\Phi_{\mathcal{A}}$.

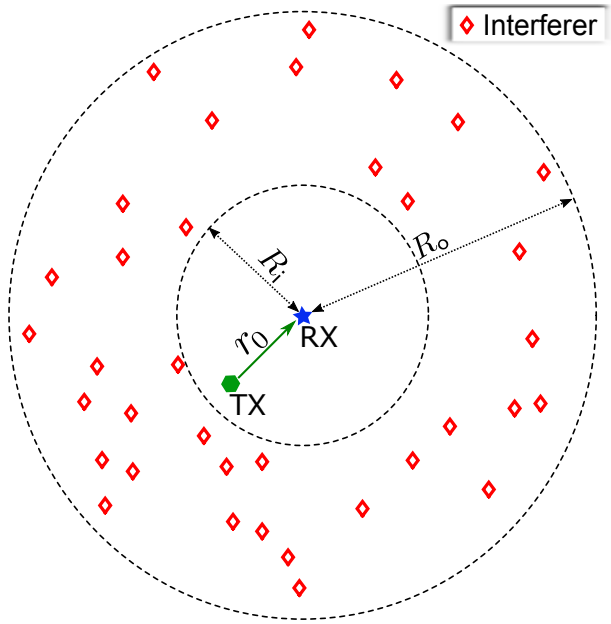

Figure 2.4: A receiver (RX) with intended transmitter (TX) r_0 away and interfering transmitters located within an annulus with inner and outer radii denoted respectively by R_i and R_o.

Note that, provided a distribution for the desired link r_0, (2.31) can be expected over the same. As we keep r_0 fixed for the ease of expounding the modeling approach, it is also convenient to assume interference-limited conditions ($\sigma_N^2/P \to 0$) to have

$$\mathcal{L}_{F_{1/\rho}}(\mathsf{s}) = \frac{1}{\mathsf{s}}\,\mathbb{E}_{\Phi_{\mathcal{A}}}\left[\prod_{k=1}^{K} e^{-\mathsf{s}\, r_0^{\eta}\, r_k^{-\eta}}\right] \tag{2.32}$$

for some of the following exemplifications.

Let us invoke a couple of specific distributions for $\Phi_{\mathcal{A}}$ that shall be encountered under the network scenarios addressed in subsequent chapters.

Poisson Point Process (PPP)

Example 2.7. Reconsider Example 2.6 and let the points in $\Phi_{\mathcal{A}}$ conform to those points in a homogeneous PPP $\Phi \subset \mathbb{R}^2$ with density λ, i.e, $\Phi_{\mathcal{A}} = \Phi \cap \mathcal{A}(R_i, R_o)$. In other words, there are K interferers on $\mathcal{A}(R_i, R_o)$ where K is a Poisson random variable with mean

$\lambda\,\pi\,(R_{\mathsf{o}}^2 - R_{\mathsf{i}}^2)$, such that for a given K, the points are distributed independently and uniformly. Under this Poisson modeling of $\Phi_{\mathcal{A}}$, (2.32) simplifies to

$$\mathcal{L}_{F_{1/\rho}}(\mathsf{s}) = \frac{1}{\mathsf{s}} \exp\left\{-2\pi\lambda \int_{R_{\mathsf{i}}}^{R_{\mathsf{o}}} \left(1 - e^{-\mathsf{s}\, r_0^{\eta}\, x^{-\eta}}\right)\, x\, \mathrm{d}x\right\} \tag{2.33}$$

$$= \frac{1}{\mathsf{s}}\, e^{-\pi\lambda\left\{R_{\mathsf{o}}^2 - R_{\mathsf{i}}^2 + r_0^2\, \mathsf{s}^{2/\eta}\, \frac{2}{\eta}\left[\Gamma\left(\frac{-2}{\eta}, \mathsf{s}\, r_0^{\eta}\, R_{\mathsf{i}}^{-\eta}\right) - \Gamma\left(\frac{-2}{\eta}, \mathsf{s}\, r_0^{\eta}\, R_{\mathsf{o}}^{-\eta}\right)\right]\right\}} \tag{2.34}$$

$$= \frac{1}{\mathsf{s}}\, e^{-\pi\lambda\left\{R_{\mathsf{o}}^2 - R_{\mathsf{i}}^2 + \frac{2}{\eta}\left[R_{\mathsf{i}}^2\, E_{\frac{2+\eta}{\eta}}\left(\mathsf{s}\, r_0^{\eta}\, R_{\mathsf{i}}^{-\eta}\right) - R_{\mathsf{o}}^2\, E_{\frac{2+\eta}{\eta}}\left(\mathsf{s}\, r_0^{\eta}\, R_{\mathsf{o}}^{-\eta}\right)\right]\right\}} \tag{2.35}$$

where (2.33) follows from the definition of the probability generating functional (PGFL) of the PPP [41] and the solution of the integration can be expressed, in terms of either the upper incomplete gamma functions as in (2.34) or the exponential integrals as in (2.35). Also of interest are the limiting cases that we shall encounter later on, i.e., when $R_{\mathsf{i}} \to 0$ and/or $R_{\mathsf{o}} \to \infty$. Specifically, with $R_{\mathsf{i}} \to 0$, i.e., when the Poisson-distributed interferers are confined to a circle of radius R_{o} around the receiver

$$\lim_{R_{\mathsf{i}} \to 0} \mathcal{L}_{F_{1/\rho}}(\mathsf{s}) = \frac{1}{\mathsf{s}}\, e^{-\pi\lambda\left\{R_{\mathsf{o}}^2 - r_0^2\, \mathsf{s}^{2/\eta}\, \frac{2}{\eta}\, \Gamma\left(-2/\eta, \mathsf{s}\, r_0^{\eta}\, R_{\mathsf{o}}^{-\eta}\right)\right\}} \tag{2.36}$$

$$= \frac{1}{\mathsf{s}}\, e^{-\pi\lambda\, R_{\mathsf{o}}^2\left\{1 - \frac{2}{\eta}\, E_{\frac{2+\eta}{\eta}}\left(\mathsf{s}\, r_0^{\eta}\, R_{\mathsf{o}}^{-\eta}\right)\right\}} \tag{2.37}$$

With $R_{\mathsf{o}} \to \infty$, i.e., when the Poisson-distributed interferers are excluded from a circle of radius R_{i} around the receiver

$$\lim_{R_{\mathsf{o}} \to \infty} \mathcal{L}_{F_{1/\rho}}(\mathsf{s}) = \frac{1}{\mathsf{s}}\, e^{\pi\lambda\left[R_{\mathsf{i}}^2 + r_0^2\, \mathsf{s}^{2/\eta}\, \frac{2}{\eta}\, \bar{\Gamma}\left(-2/\eta, \mathsf{s}\, r_0^{\eta}\, R_{\mathsf{i}}^{-\eta}\right)\right]} \tag{2.38}$$

where $\bar{\Gamma}(\cdot,\cdot)$ is the lower incomplete gamma function; also, note that $K \to \infty$. Finally, when $R_{\mathsf{i}} \to 0$ and $R_{\mathsf{o}} \to \infty$, i.e., when the interferer locations conform to all the points in the homogeneous PPP and $\Phi_{\mathcal{A}} = \Phi$, (2.33) reduces to

$$\lim_{R_{\mathsf{i}} \to 0,\, R_{\mathsf{o}} \to \infty} \mathcal{L}_{F_{1/\rho}}(\mathsf{s}) = \frac{1}{\mathsf{s}}\, e^{-\pi\lambda\, r_0^2\, \mathsf{s}^{2/\eta}\, \Gamma(1-2/\eta)}. \tag{2.39}$$

While the Laplace functionals derived above can be utilized to compute $F_{\rho}(\cdot)$ via the approximation in Lemma 2.1, for the case when

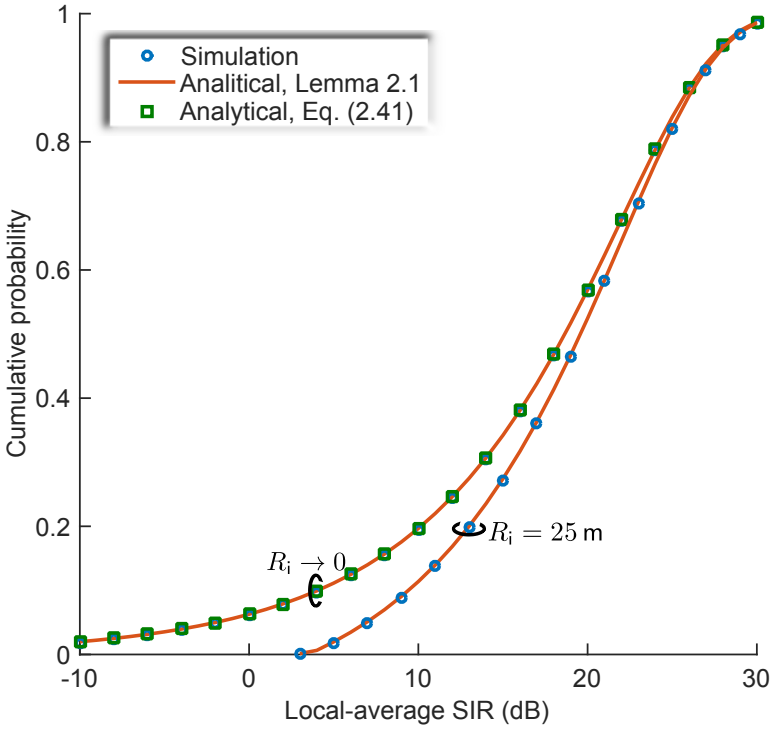

Figure 2.5: CDF of the local-average SIR $F_\rho(\cdot)$ with $r_0 = 20$ m, $\lambda = 50$ links/km^2 and $\eta = 4$. The application of $\mathcal{L}_{F_{1/\rho}}(\cdot)$ as per (2.38) into Lemma 2.1 is contrasted for $R_i = 25$ and $R_i \to 0$.

$\Phi_{\mathcal{A}} = \Phi$ corresponding to (2.39), alternately, a direct expression can be derived (cf. Proposition 3.3) in the following infinite series form

$$F_\rho(\xi) = \frac{1}{\pi} \sum_{u=1}^{\infty} \left[\pi\, \xi^{2/\eta}\, r_0^2\, \lambda\, \Gamma\left(1 - 2/\eta\right)\right]^u \frac{\Gamma\left(2\,u/\eta\right)}{u!} \sin\left[u\,\pi\,(1 - 2/\eta)\right] \tag{2.40}$$

which for $\eta = 4$ reduces to

$$F_\rho(\xi) = \operatorname{erf}\left(\sqrt{\xi}\,\pi^{3/2}\, r_0^2\, \lambda/2\right) \tag{2.41}$$

where $\operatorname{erf}(\nu) = \frac{2}{\sqrt{\pi}} \int_0^\nu e^{-\mathrm{t}^2} \mathrm{dt}$ is the error function.

Example 2.8. Setting $r_0 = 20$ m, $\lambda = 50$ interferers/km^2, and $\eta = 4$, the CDF $F_\rho(\cdot)$ corresponding to (2.38) under $R_i = 25$ m, and (2.39), obtained via Lemma 2.1 is contrasted with its counterpart obtained via Monte-Carlo in Fig. 2.5. For the one corresponding to

(2.39), by comparing with the exact form for $F_\rho(\xi)$ in (2.41), which is also plotted in Fig. 2.5, we have verified that the absolute error of the approximation in Lemma 2.1 is below 10^{-4} for $\xi \geq -10$ dB, with the parameters set to $A = 9.21$, $\mathsf{B} = 5$ and $\mathsf{Q} = 8$.

Binomial Point Process (BPP)

Example 2.9. Reconsider Example 2.6, but now letting $\Phi_{\mathcal{A}}$ be distributed as per a BPP with K points on $\mathcal{A}(R_{\mathsf{i}}, R_{\mathsf{o}})$. Namely, there are K interferers independently and uniformly distributed on $\mathcal{A}(R_{\mathsf{i}}, R_{\mathsf{o}})$ where K is deterministic. Then, the Laplace transform in (2.32) becomes

$$\mathcal{L}_{F_{1/\rho}}(\mathsf{s}) = \frac{1}{\mathsf{s}} \left(\mathbb{E}_{r_k} \left[e^{-\mathsf{s}\, r_0^{\eta}\, r_k^{-\eta}} \right] \right)^K \tag{2.42}$$

$$= \frac{1}{\mathsf{s}} \left(\frac{2 \int_{R_{\mathsf{i}}}^{R_{\mathsf{o}}} e^{-\mathsf{s}\, r_0^{\eta}\, x^{-\eta}}\, x \, \mathrm{d}x}{R_{\mathsf{o}}^2 - R_{\mathsf{i}}^2} \right)^K \tag{2.43}$$

$$= \frac{1}{\mathsf{s}} \left\{ \frac{r_0^2\, \mathsf{s}^{2/\eta}\, \frac{2}{\eta} \left[\Gamma\left(\frac{-2}{\eta},\, s\, r_0^{\eta}\, R_{\mathsf{o}}^{-\eta} \right) - \Gamma\left(\frac{-2}{\eta},\, s\, r_0^{\eta}\, R_{\mathsf{i}}^{-\eta} \right) \right]}{R_{\mathsf{o}}^2 - R_{\mathsf{i}}^2} \right\}^K \tag{2.44}$$

which, when $R_{\mathsf{i}} \to 0$, simplifies to

$$\mathcal{L}_{F_{1/\rho}}(\mathsf{s}) = \frac{1}{\mathsf{s}} \left[\frac{2\, r_0^2\, \mathsf{s}^{2/\eta}}{\eta\, R_{\mathsf{o}}^2}\, \Gamma\left(-2/\eta,\, s\, r_0^{\eta}\, R_{\mathsf{o}}^{-\eta} \right) \right]^K . \tag{2.45}$$

Next, let us consider another finite sized network, also modeled via a BPP, but in a differently shaped region. This example, where the distance distributions get complicated and the analysis is rendered cumbersome, is relevant to the topic of Chapter 5.

Example 2.10. Consider a network confined to a rectangular region of length L, along the x-axis and width W along the y-axis (cf. Fig. 2.6), with the origin $(0, 0)$ made to coincide with the center of the rectangle. Focus on a receiver located at an arbitrary location inside the rectangle, with coordinates $(\mathsf{x}^{\mathrm{r}}, \mathsf{y}^{\mathrm{r}})$ where $-\mathsf{L}/2 \leq \mathsf{x}_0^{\mathrm{r}} \leq \mathsf{L}/2$ and $-\mathsf{W}/2 \leq \mathsf{y}_0^{\mathrm{r}} \leq \mathsf{W}/2$, and with its intended transmitter located at a (fixed) distance r_0. In turn, let the K interferers be distributed as a BPP within the rectangular region, i.e., as K independent and uniformly distributed points. In other words, for $k = 1, \ldots, K$, location of the kth interferer has coordinates $(\mathsf{x}_k, \mathsf{y}_k)$ with $\mathsf{x}_k \sim \mathcal{U}(-\mathsf{L}/2, \mathsf{L}/2)$

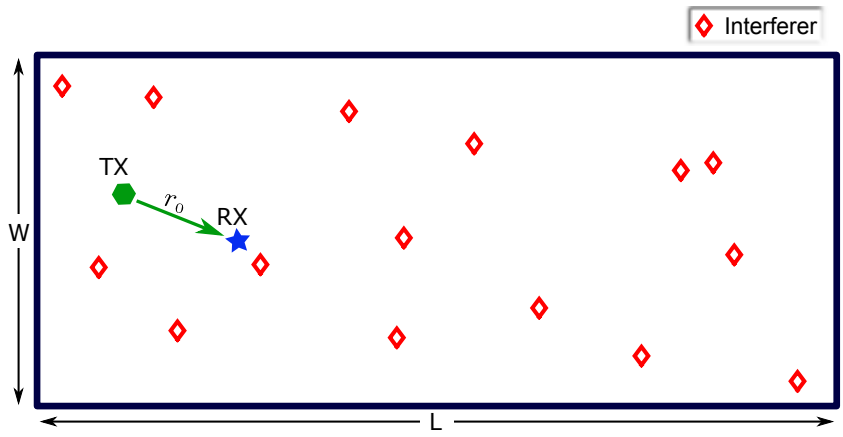

Figure 2.6: Receiver (RX) with intended transmitter (TX) r_0 away and interferers distributed as a BPP inside a rectangular region.

and $\mathsf{y}_k \sim \mathcal{U}(-\mathsf{W}/2, \mathsf{W}/2)$. Under the large-scale gains modeled as in (2.21), the Laplace transform in (2.31) becomes

$$\mathcal{L}_{F_{1/\rho}}(\mathsf{s}) = \frac{1}{\mathsf{s}}\, e^{-\mathsf{s}\frac{\sigma_{\mathrm{N}}^2 r_0^\eta}{P\,L}}\, \mathbb{E}_{\{r_k\}_{k=1}^K}\left[\prod_{k=1}^{K} e^{-\mathsf{s}\, r_0^\eta\, r_k^{-\eta}}\right] \tag{2.46}$$

$$= \frac{1}{\mathsf{s}}\, e^{-\mathsf{s}\frac{\sigma_{\mathrm{N}}^2 r_0^\eta}{P\,L}}\, \left(\mathbb{E}_{\{\mathsf{x}_k,\mathsf{y}_k\}}\left[e^{-\mathsf{s}\, r_0^\eta\, [(\mathsf{x}_k-\mathsf{x}^{\mathrm{r}})^2+(\mathsf{y}_k-\mathsf{y}^{\mathrm{r}})^2]^{-\eta/2}}\right]\right)^K \tag{2.47}$$

$$= \frac{1}{\mathsf{s}}\, e^{-\mathsf{s}\frac{\sigma_{\mathrm{N}}^2 r_0^\eta}{P\,L}}\, \left(\int_{\frac{-\mathsf{L}}{2}}^{\frac{\mathsf{L}}{2}} \int_{\frac{-\mathsf{W}}{2}}^{\frac{\mathsf{W}}{2}} \frac{e^{-\mathsf{s}\, r_0^\eta\, [(\mathsf{x}-\mathsf{x}^{\mathrm{r}})^2+(\mathsf{y}-\mathsf{y}^{\mathrm{r}})^2]^{-\eta/2}}}{\mathsf{L}\,\mathsf{W}}\, \mathrm{d}\mathsf{x}\, \mathrm{d}\mathsf{y}\right)^K \tag{2.48}$$

which can be plugged into (2.27) to evaluate $F_\rho(\cdot)$ numerically.

Such integral forms, which can sometimes be made slightly simpler via appropriate distance distributions replacing the coordinates [112], do admit numerical evaluations that serve as an alternative to Monte-Carlo. However, when faced with more involved models for G_k in combination with such radially asymmetrical network geometry, as we shall encounter in Chapter 5 (in the context of indoor mmWave communication), replacing simulations entirely becomes difficult.

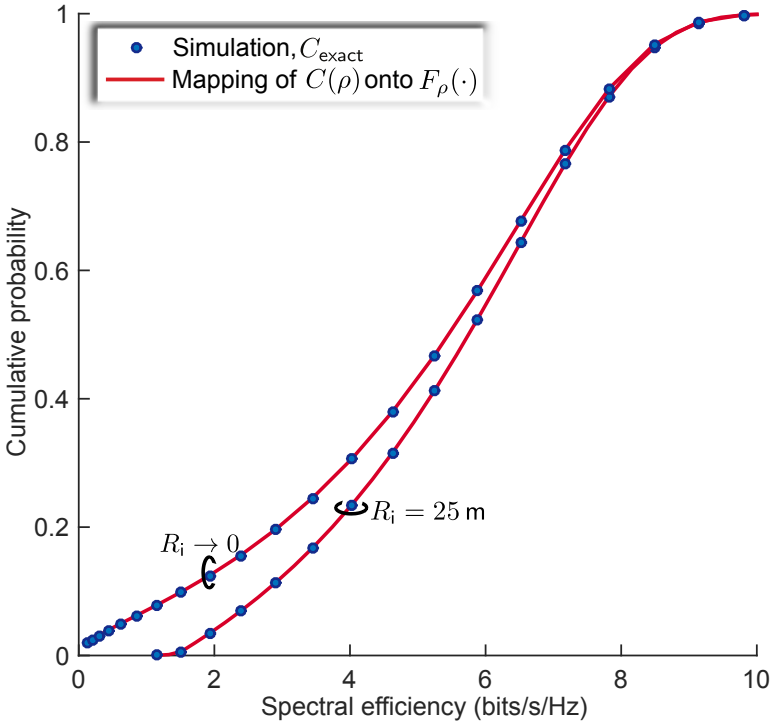

Figure 2.7: CDF of the ergodic spectral efficiency $F_C(\cdot)$ with $r_0 = 20$ m, $\lambda = 50$ links/km^2 and $\eta = 4$.

2.5 Distribution of the Spectral Efficiency

The randomness that ρ acquires once the large-scale features are randomized is then inherited by $C(\rho)$, and the corresponding CDF provides a complete description of the ergodic spectral efficiency achievable by the receiver, over all possible values of $\{G_k\}_{k=0}^{K}$. Provided that an invertible form for $C(\cdot)$ is available, the CDF of C is simply

$$F_C(\gamma) = F_\rho\left[C^{-1}(\gamma)\right]. \tag{2.49}$$

Alternatively, by mapping the applicable function $C(\rho)$ onto the expression for $F_\rho(\cdot)$, such as the ones put forth in the previous section, $F_C(\cdot)$ is readily characterized.

Example 2.11. Reconsider the settings in Example 2.8, and further assume that the links are Rayleigh-faded such that C is given by (2.17). The CDF $F_C(\cdot)$ computed by mapping $C(\rho)$ onto $F_\rho(\cdot)$ are plotted in Fig. 2.7, alongside the corresponding Monte-Carlo coun-

terparts, namely, the large-scale distribution of C_{exact} computed as detailed in Appendix A.1.

Again, note that similar mapping can be applied to any applicable forms of $C(\rho)$, e.g., the one in (2.19) for SISO Nakagami-m fading or the one in (2.20) under a MIMO channel with Rayleigh-faded entries.

2.5.1 Contrast with Conventional Approach

In contrast to $F_C(\cdot)$, which is easily computed as illustrated above, without the interference modeling that we propound the spatial distribution of the spectral efficiency is far more inaccessible. Specifically, a counterpart CDF is not easily obtainable for the upper bound C_{ub} in (2.8), i.e., the computation of $F_{C_{\mathsf{ub}}}(\cdot)$ is not easy, as made clear by the following example.

Example 2.12. Under the large-scale gain model in (2.21), the result with Rayleigh-faded links from Example 2.1 is

$$C_{\mathsf{ub}} = \log_2 e \int_0^\infty \frac{e^{-x\,\sigma_{\mathrm{N}}^2\, r_0^\eta/(P\,L)}}{1+x} \prod_{k=1}^{K} \frac{1}{1+x\,(r_0/r_k)^\eta}\,\mathrm{d}x. \tag{2.50}$$

Note that, C_{ub}—unlike C in (2.17)—is no longer a function of singly ρ, whose distribution could be characterized as demonstrated in the previous section; rather, (2.50) is a more involved function of $\{r_k\}_{k=0}^K$ that does not offer an clear way of disentangling these dependences, so as to characterize $F_{C_{\mathsf{ub}}}(\cdot)$ over the distribution of a given point process that models the transmitter locations.

Faced with such difficulty, some authors choose to instead characterize the distribution of

$$\log_2\left(1+\frac{G_0|H_0|^2}{\sum_{k=1}^K G_k\,|H_k|^2+\sigma_{\mathrm{N}}^2/P}\right)$$

over $\{H_k\}_{k=0}^K$ as well as $\{G_k\}_{k=0}^K$, namely, the CDF of instantaneous spectral efficiency obtained as [113][52, Sec. VII.A]

$$\mathbb{P}\left[\log_2(1+\mathsf{SINR})<\gamma\right] = F_{\mathsf{SINR}}(2^\gamma-1) \tag{2.51}$$

where SINR—recall from (2.3)—is the instantaneous SINR. While this quantity becomes tractable under Rayleigh fading, the mixing

of small- and large-scale variations within it clutters potential observations. Moreover, the generalization to more involved settings, say MIMO, becomes arduous or outright hopeless.

Particularly, it is worth highlighting the issue of inferring the *coverage* from such instantaneous metrics: a common recourse in stochastic geometry literature [43, 52, 64].

Coverage

Although the full CDF of ergodic spectral efficiency is relevant from a network-design perspective, the lower tail is of particular significance as it defines the coverage, i.e., the share of geometries in which a minimum level of service can be provided. The shape of the lower tail, in particular, reveals the change in coverage with a diminishing service demand or, equivalently, the sacrifice in coverage that is essential to ensure a better minimum service. For instance, reconsidering the cases in Example 2.11, the spectral efficiency achievable in 99% of the possible network geometries—i.e., the values that the curves in Fig. 2.7 maps to, at 1%—are, 0.62 bits/s/Hz when $R_{\mathsf{i}} \to 0$ and 2.15 bits/s/Hz when $R_{\mathsf{i}} = 25$ m.

Since coverage is not gained or lost in reference to small-scale fades, which are highly localized in space, time and frequency, care must be exercised not to infer coverage from the distribution of instantaneous SINR $F_{\mathsf{SINR}}(\cdot)$ or of instantaneous spectral efficiency in (2.51), both of which are dominated by small-scale fading. This is a major differentiating aspect of our results in comparison to the majority of stochastic geometry literature where coverage is wrongly inferred from the spatial distributions of the instantaneous metrics. For example, as counterparts of the cases considered above in reference to Example 2.11, the values inferred via $F_{\mathsf{SINR}}(\cdot)$, which becomes [114]

$$F_{\mathsf{SIR}}(\xi) = 1 - e^{-\pi r_0^2 \lambda \sqrt{\xi} \left(\pi/2 - \arctan \frac{R_{\mathsf{i}}^2}{\sqrt{\xi} r_0^2} \right)}, \tag{2.52}$$

are 0.015 bits/s/Hz when $R_{\mathsf{i}} \to 0$ and 0.36 bits/s/Hz when $R_{\mathsf{i}} = 25$ m. Note that these are drastically off from what the distribution of C_{exact} gives as we verified in Fig. 2.7. It is, therefore, important to glean coverage from the ergodic spectral efficiency, which is impervious to small-scale fluctuations, rather than from quantities subject to those fluctuations.

2.6 Spatial Average of the Spectral Efficiency

It might be useful, sometimes, to condense $F_C(\cdot)$ down to a single quantity, and in that case, the average is the logical choice. The spatially averaged quantities thus obtained—albeit being less informative—are preferred outcomes in stochastic geometry, because they allow calibrating system-level benefits which are often desirable in many scenarios, as we shall see in the next section and in following chapters. Here again, our modeling approach proves advantageous. For any setting for which applicable expressions for $C(\rho)$ and $F_\rho(\cdot)$ are available, we can compute

$$\bar{C} = \mathbb{E}_\rho[C(\rho)] = \int_0^\infty C(\xi)\,\mathrm{d}F_\rho(\xi). \tag{2.53}$$

Although the application of $C(\rho)$ and $F_\rho(\cdot)$ in (2.53) may not always yield a simplification, numerical evaluations can be easily carried out via standard software packages (such as Matlab, Octave, Maple or Mathematica), thereby circumventing large-scale Monte-Carlo simulations.

In some cases, rewriting (2.53) as follows may yield simpler solutions

$$\bar{C} = \mathbb{E}_\rho\left\{\mathbb{E}_{H_0}\left[\log_2\left(1+\rho\,|H_0|^2\right)\right]\right\} \tag{2.54}$$

$$= \mathbb{E}_\rho\left\{\int_0^\infty \mathbb{P}\left[\log_2\left(1+\rho\,|H_0|^2\right) > \gamma \,|\, \rho\right]\,\mathrm{d}\gamma\right\} \tag{2.55}$$

$$= \log_2(e)\int_0^\infty \frac{1}{1+x}\,\mathbb{E}_\rho\left[F^{\mathrm{c}}_{|H_0|^2}\left(x/\rho\right)\right]\,\mathrm{d}x \tag{2.56}$$

where $F^{\mathrm{c}}_{|H_0|^2}(\cdot)$ is the CCDF (complementary cumulative distribution function) of $|H_0|^2$. This approach is particularly beneficial under Rayleigh fading, as (2.56) can be expressed in terms of the Laplace transform $\mathcal{L}_{F_{1/\rho}}(\cdot)$ in (2.24); as indicated, this is a key recourse in the sequel.

Lemma 2.2. In Rayleigh fading, the spatial average of ergodic spectral efficiency is

$$\bar{C} = \log_2(e)\int_0^\infty \frac{x}{1+x}\,\mathcal{L}_{F_{1/\rho}}(x)\,\mathrm{d}x. \tag{2.57}$$

Proof. The result follows by substituting $F^{\mathrm{c}}_{|H_0|^2}(\zeta) = e^{-\zeta}$ in (2.56) and further recalling (2.24). ■

Example 2.13. Again, reconsider Example (2.7) and assume that all the links are Rayleigh-faded. The spatially averaged ergodic spectral efficiency, under $\Phi_{\mathcal{A}} = \Phi$, obtained by applying (2.39) in (2.2) is

$$\bar{C} = \log_2(e) \int_0^\infty \frac{1}{1+x}\, e^{-\pi\lambda\, r_0^2\, x^{2/\eta}\, \Gamma(1-2/\eta)}\, \mathrm{d}x \tag{2.58}$$

which for $\eta = 4$ reduces to (cf. Proposition 3.6)

$$\bar{C} = 2\left[\sin\left(\pi^{3/2}\, r_0^2\, \lambda\right) \mathrm{si}\left(\pi^{3/2}\, r_0^2\, \lambda\right) - \cos\left(\pi^{3/2}\, r_0^2\, \lambda\right) \mathrm{ci}\left(\pi^{3/2}\, r_0^2\, \lambda\right)\right] \log_2 e \tag{2.59}$$

where the trigonometric integrals $\mathrm{si}(\cdot)$ and $\mathrm{ci}(\cdot)$ are respectively given by

$$\mathrm{si}(x) = \int_x^\infty \frac{\sin(\mathsf{t})}{\mathsf{t}} \mathrm{d}\mathsf{t}$$

and

$$\mathrm{ci}(x) = -\int_x^\infty \frac{\cos(\mathsf{t})}{\mathsf{t}} \mathrm{d}\mathsf{t}.$$

Interestingly, in this case, $C(\rho)$ as in (2.17) integrated, as per (2.53), over the closed form of $F_\rho(\cdot)$ as in (2.41), also yields the same result, with $\eta = 4$.

2.6.1 Contrast with Conventional Approach

Once again, let us contrast our approach with the existing analyses. As indicated earlier, the spatially averaged spectral efficiency is the favorite outcome in stochastic geometry, however, it is usually characterized as [43, 51]

$$\bar{C}_{\mathsf{ub}} = \mathbb{E}_{\{H_k\},\{G_k\}}[C_{\mathsf{ub}}]. \tag{2.60}$$

Example 2.14. Reconsidering Example 2.13, the upper bound of the average spectral efficiency [43, 114] is

$$\bar{C}_{\mathsf{ub}} = \log_2(e) \int_0^\infty \frac{1}{1+x}\, e^{-\pi\lambda\, r_0^2\, x^{2/\eta}/\mathrm{sinc}\,(2/\eta)}\, \mathrm{d}x. \tag{2.61}$$

Let us now compare $\bar{C}$ and $\bar{C}_{\mathsf{ub}}$ in terms of their closeness to $\bar{C}_{\mathsf{exact}}$, the spatial average of C_{exact}.

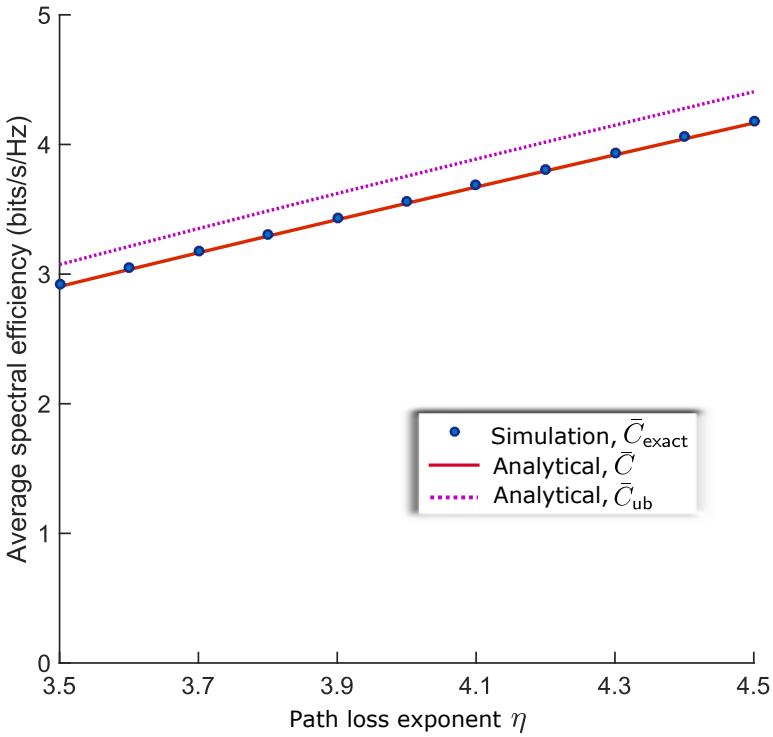

Figure 2.8: Spatially averaged spectral efficiency as a function of η.

Example 2.15. Setting $r_0 = 20$ m and $\lambda = 50$ interferers/km^2, Fig. 2.8 contrasts $\bar{C}$ as per (2.58), $\bar{C}_{\text{ub}}$ as per (2.61) and the corresponding $\bar{C}_{\text{exact}}$ computed via Monte-Carlo (cf. Appendix A.1), by varying $\eta \in [3.5, 4.5]$.

Thus, the spatial average $\bar{C}$ that we characterize is not only a lower bound to $\bar{C}_{\text{exact}}$, but also more precise than the upper bound $\bar{C}_{\text{ub}}$, as evidenced by the above example.

2.7 System-level Performance of Unbounded Networks

Thus far, we have focused on the perspective of a receiver at a given position in the network, in terms of the distribution of the ergodic spectral efficiency and the average thereof, evaluated over all possible realizations of large-scale propagation features.

For an unbounded network model—i.e., with the network area and

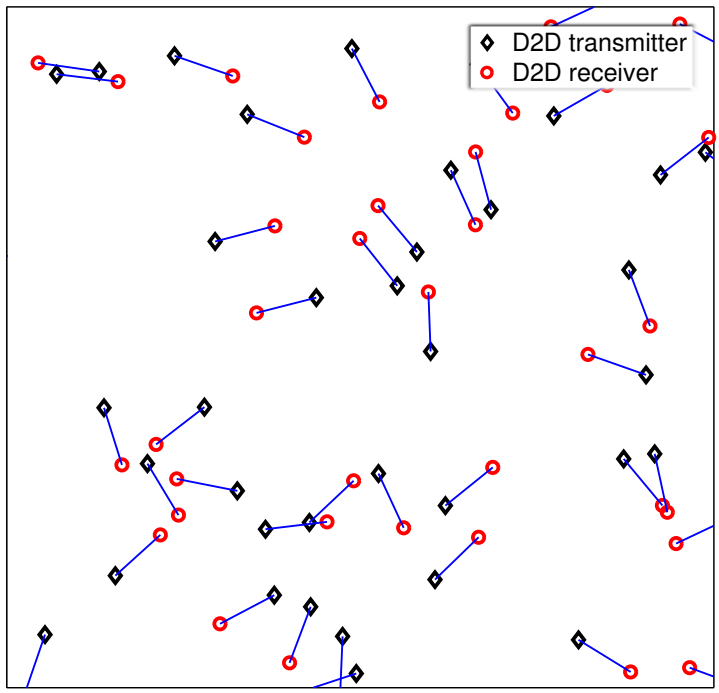

Figure 2.9: Depiction of the links in an overlay D2D network, distributed as per a Poisson dipole model.

the number of co-channel communication links going to infinity—if the point process that models the random network geometry is such that a randomly picked receiver (and held fixed) has the same distribution for $\{G_k\}_{k=0}^{\infty}$ from its vantage, it becomes the *typical* receiver [41] under expectation over $\{G_k\}_{k=0}^{\infty}$, without loss of generality. Therefore, $F_C(\cdot)$ and $\bar{C}$ computed for the typical receiver become representative of the whole network, describing the network performance in bits/s/Hz *per link*.

For instance, consider an overlay D2D network where the co-channel D2D transmitters are distributed as the homogeneous PPP $\Phi \subset \mathbb{R}^2$ with density λ: implying that on average there are λ available links per unit area. Further, assume that each D2D receiver is distributed in such a way that all D2D pairs have a link distance r_0, which is either fixed or IID. Under this model, also termed as the Poisson dipole model [41], from the typical D2D receiver's vantage, the interferer locations behave as a homogeneous PPP [41]. This implies that, when r_0 is fixed, the results that follow from the setting $\Phi_{\mathcal{A}} = \Phi$ in Example 2.7—e.g., (2.38), (2.40) and (2.58)—are rep-

resentative of the network. Additionally, under spatial ergodicity, which holds for the PPP and many other point processes [41], $\bar{C}$ also represents the average value of all the links in the network, under a given realization.

2.7.1 Area Spectral Efficiency

Scaling $\bar{C}$ of the typical receiver with the number of co-channel links per unit area gives the average *area spectral efficiency* in bits/s/Hz/ per unit area, a key performance metric that we shall employ in Chapters 3 and 4. For example, for the foregoing overlay D2D network modeled via the Poisson dipole model with λ links per unit area and with a fixed r_0, the area spectral efficiency under interference limited conditions and the large-scale gain model in (2.21) equals

$$\bar{\mathcal{C}} = \lambda \bar{C} \tag{2.62}$$

$$= \lambda \log_2(e) \int_0^\infty \frac{1}{1+x} e^{-\pi\lambda r_0^2 x^{2/\eta} \Gamma(1-2/\eta)} \, \mathrm{d}x \tag{2.63}$$

which follows from (2.58).

2.8 Summary

The chapter established that the ergodic spectral efficiency of a wireless network can be better abstracted with the aid of a Gaussian model for the aggregate interference. First, the spectral efficiency of a given communication link in the network is characterized conditioned on the locations of the receiver, its intended transmitter, and the interfering transmitters, i.e., under a specific network geometry that determines the large-scale features. Then, the variabilities induced by random network geometry are taken into account, by releasing the conditioning on the transmitter positions (while holding the receiver location fixed), namely, to compute the distribution of the ergodic spectral efficiency enjoyed by the receiver over all possible transmitter locations, emphasizing on the application of stochastic geometry theory for gaining analytical tractability. Further, the computation of the spatially averaged spectral efficiency is demonstrated, which can be employed to compute the area spectral efficiency (bits/s/Hz/unit area), as a measure of the system-level performance in unbounded networks.

Chapter 3

D2D Communication in Cellular Networks

3.1 Background

Many initial investigations on D2D had relied on simulations [17–19, 21–26, 28] that render system-level performance evaluations arduous. More recent works [64, 65, 115] have modeled the user locations via PPP distributions and analytically tackled D2D communication.

In this dissertation, we proceed down the path of [64], but applying the novel modeling approach expounded in Chapter 2 and further the interference model by introducing a controllable degree of spatial averaging that enables obtaining simpler analytical solutions. Besides, we allow the length of the D2D links to depend on the user density, altogether developing a robust and extensible framework that enables characterizing in simpler form—sometimes even in closed form—the spectral efficiencies achievable with D2D communication. The framework accommodates both underlay or overlay options.

The chapter provides several examples in order to illustrate how this framework can be employed to assess the benefits of D2D, answering questions such as:

- How often does direct D2D outperform the conventional cellular mode involving two hops (uplink-downlink) via the BS?

- How many co-channel D2D links can be activated in each cell, without debilitating the spectral efficiencies of those D2D links (bits/s/Hz) or that of the cellular links in that cell?

- How much better is the area spectral efficiency (bits/s/Hz per cell or bits/s/Hz per unit area) given the denser spectral reuse?

3.2 Network Modeling

We consider an interference-limited cellular network where the BSs are regularly placed on a hexagonal grid.[1] At each BS, cellular transmissions are orthogonalized while multiple D2D links share each time-frequency channel. Transmitters and receivers have a single antenna, and each receiver knows the fading of only its own link, be it cellular or D2D. Our focus is on a given time-frequency channel, where one cellular uplink and/or (underlay/overlay) multiple co-channel D2D links are active in each cell.

3.2.1 User Locations

The locations of the transmitters, both cellular and D2D, are modeled relative to the location of a given receiver under consideration. For the *cellular uplink*, the receiver under consideration is a BS whereas, for the *D2D link*, it is a user. In either case, and without loss of generality, we place such receiver at the origin and index the intended transmitter with zero. All other transmitters (interferers) are indexed in order of increasing distance within each class (cellular and D2D). For a cellular uplink, the intended transmitter is always the closest cellular transmitter while, for a D2D link, the intended transmitter need not be the closest D2D transmitter.

Cellular Uplink

To study this link, we place a receiving BS at the origin and locate an intended cellular transmitter uniformly within the cell associated with that BS (cf. Fig. 3.1), which is circular with radius R and denoted by $\mathcal{B}(0, R)$. There is one and only one cellular transmitter within $\mathcal{B}(0, R)$, and its distance to the BS at the origin is denoted by $r_{\mathrm{c},0}$.

[1] It would also be possible to model the BS locations stochastically, but in any event, the emphasis in our framework is on the location of the D2D users.

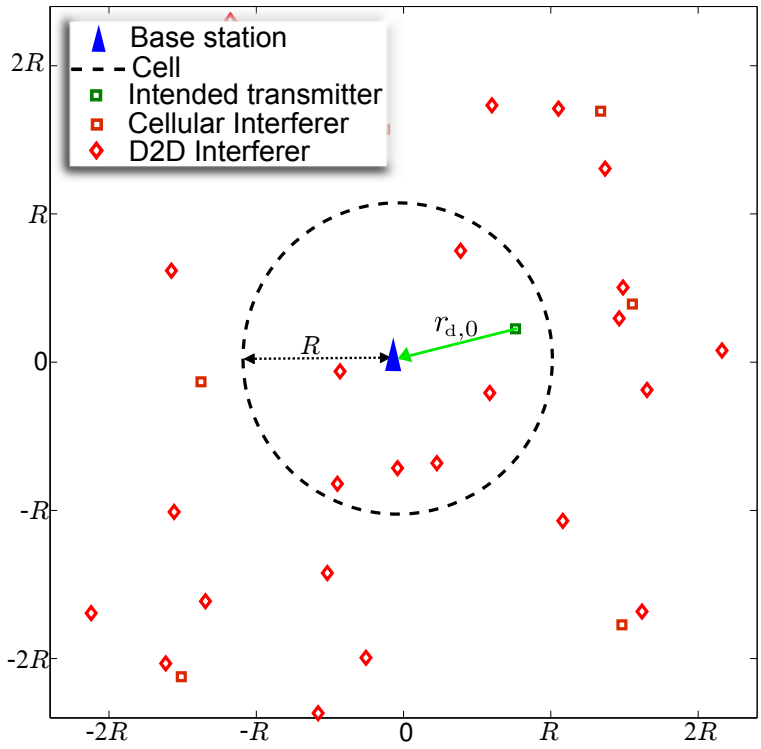

Figure 3.1: Cellular uplink with D2D. Located at the origin is a receiving BS and shown with a square marker in the surrounding circle is its intended cellular transmitter; shown with square markers outside the circle are the cellular interferers; shown with diamond markers are the D2D interferers.

The cellular interferers from other cells are outside $\mathcal{B}(0,R)$, modeled via a PPP Φ_c with density $\lambda_c = \frac{1}{\pi R^2}$. Specifically, they belong to $\Phi_c \backslash \mathcal{B}(0,R)$, i.e, those points in Φ_c which fall outside $\mathcal{B}(0,R)$. With this density made to coincide with the number of BSs per unit area, this has been shown to be a fine model for the uplink, in a network with one cellular transmitter per cell, formed by BSs placed on a hexagonal grid [64, 116].

The D2D interferer locations form another independent PPP Φ_d with density $\lambda_d = \mathsf{K}\lambda_c$ such that there are, on average, K active D2D links per cell.[2]

[2]The results in this chapter are presented in terms of the number of D2D links per cell K, under arbitrary cell radius R. It is worth noting that, under a cell radius $R = 564$ m, as the cell area becomes 1 km^2, K can be interpreted as the number of D2D links per km^2, i.e., $\mathsf{K} = \lambda_d$ links/km^2, which would be useful for contrasting the results in this chapter with some of the results presented (in terms of λ_d in links/km^2) in Chapter 4.

D2D Link

To study this link, we place a D2D receiver at the origin and locate its intended D2D transmitter at a distance $r_{\mathrm{d},0}$. Given the absence of empirical data on whether and how the length of the intended links depends on the user density, we adopt the rather general model

$$r_{\mathrm{d},0} = \frac{\mathsf{r}_{\mathrm{d}}}{\mathsf{K}^{\beta}}$$

with $\mathsf{r}_{\mathrm{d}} > 0$ and $\beta \geq 0$. For strictly positive β, the link length shrinks as the user density intensifies—a behavior that is intuitively reasonable—whereas, for $\beta = 0$, we obtain $r_{\mathrm{d},0} = \mathsf{r}_{\mathrm{d}}$ independently of the user density.

The cellular and D2D interferers conform to Φ_{c} and Φ_{d}, respectively. Note that there may be cellular interferers arbitrarily close to a D2D receiver, a point whose implications are discussed later.

3.2.2 Large-scale Modeling

Unit-gain antennas are featured at the users while the BS antenna gain is immaterial to the cellular uplink because, in interference-limited conditions, it affects signal and interference equally. Thus, the large-scale gains are modeled via distance dependent path loss function as in (2.21), with different exponents for the user-to-BS and user-to-user links, respectively, $\eta_{\mathrm{c}} > 2$ and $\eta_{\mathrm{d}} > 2$. And, we denote by P_{c} and P_{d} the (fixed) signal powers, respectively, of cellular and D2D users, both measured at 1 m from the transmitter (thereby subsuming the path loss intercept) and with their ratio being

$$\mu = \frac{P_{\mathrm{d}}}{P_{\mathrm{c}}}.$$

Interlude: Effect of Shadowing

In large-scale modeling, we do not explicitly account for shadowing. Note, however, that shadowing can be easily incorporated for the D2D link, as long as it is uncorrelated and identically distributed across all the links from each PPP (Φ_{c} and Φ_{d}) to the receiver with a condition that its fractional moment, for $2/\eta$, exists. Specifically, for the aggregate interference, as shown in [117], supposing the transmitter positions are agnostic to the radio propagation, an abstraction involving a mere scaling—depending on the type and strength of the shadowing—of the PPP densities suffices. Then, what remains to be accounted for is the shadowing in the intended signal,

which features only as an extra random variable in the large-scale gain.

Although such a straightforward extension is not applicable for the cellular uplink due to the placement of BSs on a regular grid as we consider, a stochastic modeling of the BS positions via a PPP would implicitly capture the effect of shadowing. With Poisson-distributed BSs, analysis would be possible for the uplink, as it is done under the conventional modeling approach [118]. We will numerically verify this possibility for the cellular uplink (cf. Example 3.1) to contrast with an analytical result derived in this dissertation and motivated by the recent findings from downlink cellular network analysis [119, 120] that an increasing shadowing standard deviation (SD) renders the network progressively PPP-like from the vantage of any given user, regardless of what those BS positions are (under only a very mild homogeneity condition).

3.2.3 Small-scale Modeling

In order to present the results in the most general fashion, we define a binary parameter $\varkappa \in \{0, 1\}$ that distinguishes between underlay and overlay as follows:

$$\begin{cases} \varkappa = 1 & \text{underlay} \\ \varkappa = 0 & \text{overlay.} \end{cases}$$

Cellular Uplink

The BS at the origin observes

$$y_{\mathrm{c}} = \sqrt{P_{\mathrm{c}}\, r_{\mathrm{c},0}^{-\eta_{\mathrm{c}}}}\, H_{\mathrm{c},0}\, s_{\mathrm{c},0} + z_{\mathrm{c}} \tag{3.1}$$

where the first term is the signal from the intended cellular user while the second term represents the interference

$$z_{\mathrm{c}} = \sum_{k=1}^{\infty} \sqrt{P_{\mathrm{c}}\, r_{\mathrm{c},k}^{-\eta_{\mathrm{c}}}}\, H_{\mathrm{c},k}\, s_{\mathrm{c},k} + \varkappa \sum_{j=1}^{\infty} \sqrt{P_{\mathrm{d}}\, r_{\mathrm{d},j}^{-\eta_{\mathrm{c}}}}\, H_{\mathrm{d},j}\, s_{\mathrm{d},j} \tag{3.2}$$

whose first summation spans the other-cell cellular users in $\Phi_{\mathrm{c}} \backslash \mathcal{B}(0, R)$ and whose second summation spans all the D2D transmitters in Φ_{d}. In turn, $r_{\mathrm{c},k}$ represents the distance between the kth cellular transmitter and the BS at the origin, $H_{\mathrm{c},k} \sim \mathcal{N}_{\mathbb{C}}(0, 1)$ denotes the corresponding fading, and $s_{\mathrm{c},k} \sim \mathcal{N}_{\mathbb{C}}(0, 1)$ is the symbol transmitted by the kth cellular transmitter. Similarly, $r_{\mathrm{d},j}$ represents the distance

between the jth D2D transmitter and the BS at the origin, $H_{\mathrm{d},j} \sim \mathcal{N}_{\mathbb{C}}(0,1)$ denotes the corresponding fading and $s_{\mathrm{d},j} \sim \mathcal{N}_{\mathbb{C}}(0,1)$ is the symbol transmitted by the jth D2D transmitter.

D2D Link

To analyze this link, we shift the origin to the D2D receiver of interest, which observes

$$y_{\mathrm{d}} = \sqrt{P_{\mathrm{d}}\, r_{\mathrm{d},0}^{-\eta_{\mathrm{d}}}}\, H_{\mathrm{d},0}\, s_{\mathrm{d},0} + z_{\mathrm{d}} \tag{3.3}$$

where the first term is the signal from the intended D2D transmitter while the second term is the interference

$$z_{\mathrm{d}} = \varkappa \sum_{k=1}^{\infty} \sqrt{P_{\mathrm{c}}\, r_{\mathrm{c},k}^{-\eta_{\mathrm{d}}}}\, H_{\mathrm{c},k}\, s_{\mathrm{c},k} + \sum_{j=1}^{\infty} \sqrt{P_{\mathrm{d}}\, r_{\mathrm{d},j}^{-\eta_{\mathrm{d}}}}\, H_{\mathrm{d},j}\, s_{\mathrm{d},j} \tag{3.4}$$

received from the D2D transmitters in Φ_{d} and the cellular transmitters in Φ_{c}. Note that for these user-to-user signals have a different path loss exponent.

Although the analysis is limited to single-user SISO communication and Rayleigh-faded links—recall—our modeling approach allows easily extensions to incorporate other fading distributions or single-user MIMO.

3.3 Interference Modeling

3.3.1 Gaussian Modeling of the Local Distribution

The first step is to invoke the Gaussian modeling of interference, as propounded in Section 2.3, by forgoing the small-scale variations in the power of z_{c} and z_{d}, i.e., they are modeled as

$$z_{\mathrm{c}} \sim \mathcal{N}_{\mathbb{C}}\left(0, \sigma_{\mathrm{c}}^2\right) \tag{3.5}$$

where

$$\sigma_{\mathrm{c}}^2 = \sum_{k=1}^{\infty} P_{\mathrm{c}}\, r_{\mathrm{c},k}^{-\eta_{\mathrm{c}}} + \varkappa \sum_{j=1}^{\infty} P_{\mathrm{d}}\, r_{\mathrm{d},j}^{-\eta_{\mathrm{c}}} \tag{3.6}$$

and

$$z_{\mathrm{d}} \sim \mathcal{N}_{\mathbb{C}}\left(0, \sigma_{\mathrm{d}}^2\right) \tag{3.7}$$

where

$$\sigma_{\mathrm{d}}^2 = \varkappa \sum_{k=1}^{\infty} P_{\mathrm{c}}\, r_{\mathrm{c},k}^{-\eta_{\mathrm{d}}} + \sum_{j=1}^{\infty} P_{\mathrm{d}}\, r_{\mathrm{d},j}^{-\eta_{\mathrm{d}}}. \tag{3.8}$$

3.3.2 Classification of the Interference Terms

Further, identifying that both (3.6) and (3.8) comprise an infinite number of terms, of which a handful mostly dominate the total interference power because of the distance-dependent path loss, we propose an extra step of approximation. Specifically, we condition on the interferer locations within a circle centered at the receiver of interest and replace the aggregate interference emanating from outside that circle with its expected—over the interferer locations—value. As we shall see, this expected value is representative of most instances of the interference outside the circle (by virtue of the law of large numbers) and, thanks to the potency of stochastic geometry, this expected value can be computed explicitly. By introducing the averaging circle, the number of variables retained in the formulation is reduced without the significant loss of information brought about by a complete spatial averaging, which is a typical recourse in stochastic geometry analyses. This allows establishing the performance for specific locations of the users within the circle, which are the dominant interferers, and not only the average performance over all such locations. Thus, the radius of the averaging circle is a modeling parameter that needs to be chosen to balance simplicity (the smaller the circle, the fewer interferers that are explicitly retained) and accuracy (the smaller the circle, the less fidelity in representing interference instances outside the circle with their average). Remarkably, an averaging circle encompassing very few interferers suffices, something that is illustrated in Example 3.2 and Fig. 3.4: conditioning on the location of the three closest interferes suffices to capture the specificity of various situations, and the rest of the interference can be replaced by its spatial average with hardly any loss in fidelity. For each specific in-circle situation in the example, simulation results for 10 different snapshots of the out-of-circle interference are shown, and all are tightly clustered around the analytical result involving their spatial averages; in fact, for some of the situations it is utterly impossible to tell that multiple snapshots are overlapped. With an averaging circle that encompassed more than 3 interferers, the accuracy would increase even further.

A natural and very safe choice is to have the size of the circle coincide with that of a cell, $\mathcal{B}(0, R)$. Unless otherwise stated such is the size of the averaging circle, whereby the interference power in (3.6) can

be rewritten as

$$\sigma_{\mathrm{c}}^2 = \underbrace{\varkappa \sum_{j=1}^{\mathsf{K}'} P_{\mathrm{d}}\, r_{\mathrm{d},j}^{-\eta_{\mathrm{c}}}}_{\sigma_{\mathrm{c,in}}^2} + \underbrace{\varkappa \sum_{j=\mathsf{K}'+1}^{\infty} P_{\mathrm{d}}\, r_{\mathrm{d},j}^{-\eta_{\mathrm{c}}} + \sum_{k=1}^{\infty} P_{\mathrm{c}}\, r_{\mathrm{c},k}^{-\eta_{\mathrm{c}}}}_{\sigma_{\mathrm{c,out}}^2} \tag{3.9}$$

where $\sigma_{\mathrm{c,in}}^2$ corresponds to the K' D2D transmitters in $\Phi_{\mathrm{d}} \cap \mathcal{B}(0,R)$ for the given network realization whereas $\sigma_{\mathrm{c,out}}^2$ corresponds to the transmitters in $\Phi_{\mathrm{d}} \backslash \mathcal{B}(0,R)$ and $\Phi_{\mathrm{c}} \backslash \mathcal{B}(0,R)$. Recalling that $\mathbb{E}[\mathsf{K}'] = \mathsf{K}$, the expectation of $\sigma_{\mathrm{c,out}}^2$ over the PPPs equals

$$\overline{\sigma^2}_{\mathrm{c,out}} = \varkappa \mathbb{E}_{\Phi_{\mathrm{d}}}\left[\sum_{j=\mathsf{K}'+1}^{\infty} P_{\mathrm{d}}\, r_{\mathrm{d},j}^{-\eta_{\mathrm{c}}}\right] + \mathbb{E}_{\Phi_{\mathrm{c}}}\left[\sum_{k=1}^{\infty} P_{\mathrm{c}}\, r_{\mathrm{c},k}^{-\eta_{\mathrm{c}}}\right] \tag{3.10}$$

$$= \varkappa \int_R^{\infty} 2\pi \mathsf{K} \lambda_{\mathrm{c}}\, P_{\mathrm{d}}\, r^{1-\eta_{\mathrm{c}}} \mathrm{d}r + \int_R^{\infty} 2\pi \lambda_{\mathrm{c}}\, P_{\mathrm{c}}\, r^{1-\eta_{\mathrm{c}}} \mathrm{d}r \tag{3.11}$$

$$= \frac{2\left(\varkappa \mathsf{K}\, P_{\mathrm{d}} + P_{\mathrm{c}}\right)}{\left(\eta_{\mathrm{c}} - 2\right) R^{\eta_{\mathrm{c}}}} \tag{3.12}$$

where (3.11) follows from Campbell's theorem [41, Theorem 4.1] and (3.12) is obtained by evaluating the integrals and substituting $\lambda_{\mathrm{c}} = \frac{1}{\pi R^2}$. Then, we may approximate the interference power at the BS receiver as

$$\sigma_{\mathrm{c}}^2 \approx \sigma_{\mathrm{c,in}}^2 + \overline{\sigma^2}_{\mathrm{c,out}}. \tag{3.13}$$

Similarly, for the D2D link, considering $\mathcal{B}(0,R)$ around the D2D receiver at the origin, the interference power in (3.8) can be rewritten as

$$\sigma_{\mathrm{d}}^2 = \underbrace{\sum_{j=1}^{\mathsf{K}'} P_{\mathrm{d}}\, r_{\mathrm{d},j}^{-\eta_{\mathrm{d}}} + \varkappa \sum_{k=1}^{\mathsf{K}''} P_{\mathrm{c}}\, r_{\mathrm{c},k}^{-\eta_{\mathrm{d}}}}_{\sigma_{\mathrm{d,in}}^2} + \underbrace{\sum_{j=\mathsf{K}'+1}^{\infty} P_{\mathrm{d}}\, r_{\mathrm{d},j}^{-\eta_{\mathrm{d}}} + \varkappa \sum_{k=\mathsf{K}''+1}^{\infty} P_{\mathrm{c}}\, r_{\mathrm{c},k}^{-\eta_{\mathrm{d}}}}_{\sigma_{\mathrm{d,out}}^2} \tag{3.14}$$

where $\sigma_{\mathrm{d,in}}^2$ corresponds to the K' D2D transmitters in $\Phi_{\mathrm{d}} \cap \mathcal{B}(0,R)$ and the K'' cellular uplink transmitters in $\Phi_{\mathrm{c}} \cap \mathcal{B}(0,R)$, whereas $\sigma_{\mathrm{d,out}}^2$ corresponds to the transmitters in $\Phi_{\mathrm{d}} \backslash \mathcal{B}(0,R)$ and $\Phi_{\mathrm{c}} \backslash \mathcal{B}(0,R)$.

Noting that $\mathbb{E}[\mathsf{K}'] = \mathsf{K}$ and $\mathbb{E}[\mathsf{K}''] = 1$, the expectation of $\sigma^2_{\mathrm{d,out}}$ over the PPPs, computed by applying steps similar to (3.10) to (3.12), is

$$\overline{\sigma^2}_{\mathrm{d,out}} = \frac{2\left(\mathsf{K}\,P_{\mathrm{d}} + \varkappa\,P_{\mathrm{c}}\right)}{\left(\eta_{\mathrm{d}} - 2\right)R^{\eta_{\mathrm{d}}}} \tag{3.15}$$

to approximate the interference power at the BS receiver as

$$\sigma^2_{\mathrm{d}} \approx \sigma^2_{\mathrm{d,in}} + \overline{\sigma^2}_{\mathrm{d,out}}. \tag{3.16}$$

As we shall see, in some cases, especially in computing some quantities expected over all the transmitter locations, it is beneficial to make the averaging circle bigger, even to enclose the entire network. Specifically, in this chapter, we make the radius of the averaging circle either equal to R or take it to infinity, to enclose the whole network.

3.4 SIR

3.4.1 Cellular Uplink

Under the redefinition of the interference distribution as in (3.5), the instantaneous SIR of the cellular uplink becomes,

$$\mathsf{SIR}_{\mathrm{c}} = \frac{P_{\mathrm{c}}\,r_{\mathrm{c},0}^{-\eta_{\mathrm{c}}}\,|H_{\mathrm{c},0}|^2}{\sigma^2_{\mathrm{c}}} = \rho_{\mathrm{c}}\,|H_{\mathrm{c},0}|^2 \tag{3.17}$$

with the local-average SIR

$$\rho_{\mathrm{c}} = \frac{r_{\mathrm{c},0}^{-\eta_{\mathrm{c}}}}{\sum_{k=1}^{\infty} r_{\mathrm{c},k}^{-\eta_{\mathrm{c}}} + \varkappa\,\mu\sum_{j=1}^{\infty} r_{\mathrm{d},j}^{-\eta_{\mathrm{c}}}} \tag{3.18}$$

$$\approx \frac{r_{\mathrm{c},0}^{-\eta_{\mathrm{c}}}}{\varkappa\mu\sum_{j=1}^{\mathsf{K}'} r_{\mathrm{d},j}^{-\eta_{\mathrm{c}}} + \frac{2(\varkappa\mu\mathsf{K}+1)}{(\eta_{\mathrm{c}}-2)R^{\eta_{\mathrm{c}}}}} \tag{3.19}$$

$$= \frac{a_{\mathrm{c},0}^{-\eta_{\mathrm{c}}}}{\varkappa\mu\sum_{j=1}^{v'} a_{\mathrm{d},j}^{-\eta_{\mathrm{c}}} + \frac{2(\varkappa\mu\mathsf{K}+1)}{(\eta_{\mathrm{c}}-2)}} \tag{3.20}$$

where the approximation in (3.19) follows from the application of (3.13) while (3.20) is obtained by normalizing all the terms with $R^{-\eta_{\mathrm{c}}}$ and with $a_{\mathrm{c},0} = \frac{r_{\mathrm{c},0}}{R}$, $a_{\mathrm{c},k} = \frac{r_{\mathrm{c},k}}{R}$ and $a_{\mathrm{d},j} = \frac{r_{\mathrm{d},j}}{R}$ being the normalized distances. Indeed, our formulation is interference-limited and therefore invariant to the absolute scale of the network.

Local-Average SIR Distribution

The large-scale distribution of ρ_c, induced by the PPPs Φ_c and Φ_d (the transmitter locations), do not admit an exact and direct analytical form. Recall that, however, following the results in Example 2.7, the distribution can be characterized in the Laplace domain, in the form $\mathcal{L}_{F_{1/\rho_c}}(\cdot)$, which in turn can be applied in Lemma 2.1 to compute the CDF $F_{\rho_c}(\cdot)$.

Alternatively, leveraging the approximation in (3.19), we obtain direct characterizations for $F_{\rho_c}(\cdot)$, as presented next, separately for the underlay and overlay options. Though the analytical form of the distribution is unwieldy for underlay ($\varkappa = 1$) and arbitrary η_c, it takes the following closed form for underlay with $\eta_c = 4$.

Proposition 3.1. With underlay and $\eta_c = 4$, the CDF of ρ_c is

$$F_{\rho_c}(\xi) \approx \begin{cases} \dfrac{e^{\kappa^2}\left[\operatorname{erf}(\kappa) - \operatorname{erf}\left(\frac{\kappa}{\sqrt{1-\xi}}\right)\right]}{\sqrt{\xi}} & \\ \qquad + \operatorname{erf}\left(\dfrac{\kappa\sqrt{\xi}}{\sqrt{1-\xi}}\right) & 0 < \xi < 1 \\ 1 - \frac{e^{\kappa^2}}{\sqrt{\xi}} \operatorname{erfc}(\kappa) & \xi \geq 1 \end{cases} \tag{3.21}$$

where $\kappa = \frac{\sqrt{\pi\mu}\,\mathsf{K}}{2}$, $\operatorname{erf}(\nu) = \frac{2}{\sqrt{\pi}} \int_0^\nu e^{-t^2} \mathrm{d}t$ is the error function and $\operatorname{erfc}(\nu) = 1 - \operatorname{erf}(\nu)$.

Proof. See Appendix B.1. ■

For overlay ($\varkappa = 0$), a form that is both simpler and general in η_c can be obtained.

Proposition 3.2. With overlay, the CDF of ρ_c is

$$F_{\rho_c}(\xi) \approx 1 - \left(\frac{\eta_c - 2}{2\,\xi}\right)^{\frac{2}{\eta_c}} \qquad \xi \geq \frac{\eta_c - 2}{2} \tag{3.22}$$

Proof. See Appendix B.2. ■

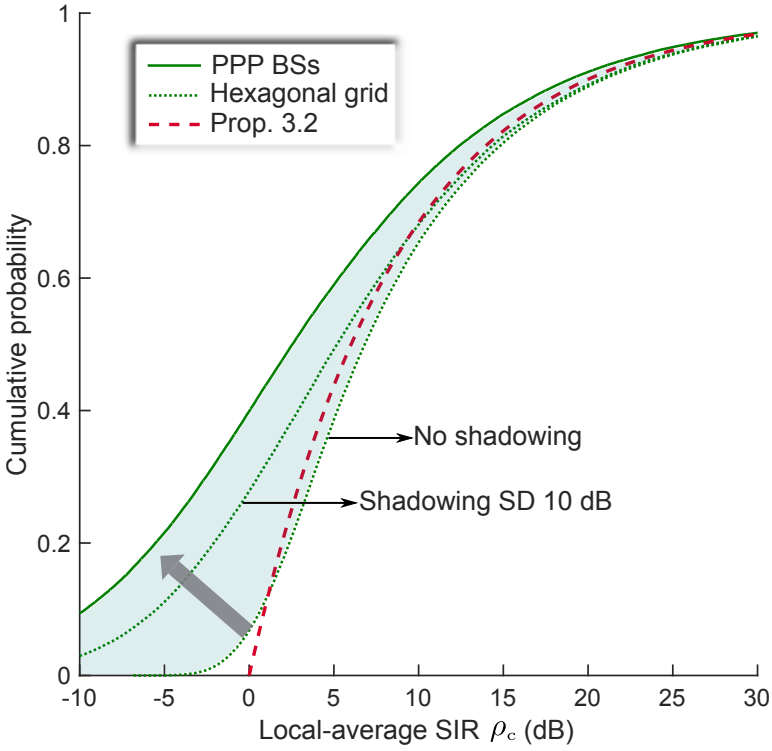

Figure 3.2: CDF of the local-average SIR ρ_c, with shadowing.

Interlude: Shadowing and Poisson-distributed BSs

At this point, let us examine the effect of shadowing in the cellular uplink, to contrast with the foregoing result and to verify the claim made earlier about the possible abstraction via Poisson-distributed BSs.

Example 3.1. Setting $\eta = 4$, CDFs of the local-average SIR of the cellular uplink are contrasted Fig. 3.2. Specifically, $F_{\rho_c}(\cdot)$ as in Prop. 3.2 is compared with numerically computed CDFs: two of them under a hexagonal grid model with no shadowing and with 10 dB shadowing SD, and another one computed under Poisson-distributed BSs.

As expected, strong shadowing renders the cellular network more PPP-like, in the uplink as well, indicating that shadowing could be implicitly incorporated into the uplink analysis via a Poisson modeling of the BS locations. All the same, such an uplink analysis under

the modeling approach we propound—focusing on the local-average metric, i.e., the ergodic spectral efficiency—is an open problem.

Note that the approximation in Prop. 3.2 is optimistic in comparison to the results with shadowing (cf. Fig. 3.2). However, this does not affect any conclusions made in this dissertation regarding the performance benefits of D2D or its impact on the cellular performance.

3.4.2 D2D Link

For the D2D link, the instantaneous SIR is

$$\mathsf{SIR}_{\mathrm{d}} = \frac{P_{\mathrm{d}}\, r_{\mathrm{d},0}^{-\eta_{\mathrm{d}}}\, |H_{\mathrm{d},0}|^2}{\sigma_{\mathrm{d}}^2} = \rho_{\mathrm{d}}\, |H_{\mathrm{d},0}|^2 \tag{3.23}$$

with the local-average SIR

$$\rho_{\mathrm{d}} = \frac{r_{\mathrm{d},0}^{-\eta_{\mathrm{d}}}\, |H_{\mathrm{d},0}|^2}{\frac{\varkappa}{\mu} \sum_{k=1}^{\infty} r_{\mathrm{c},k}^{-\eta_{\mathrm{d}}} + \sum_{j=1}^{\infty} r_{\mathrm{d},j}^{-\eta_{\mathrm{d}}}} \tag{3.24}$$

$$\approx \frac{r_{\mathrm{d},0}^{-\eta_{\mathrm{d}}}}{\sum_{j=1}^{\mathsf{K}'} r_{\mathrm{d},j}^{-\eta_{\mathrm{d}}} + \frac{\varkappa}{\mu} \sum_{k=1}^{\mathsf{K}''} r_{\mathrm{c},k}^{-\eta_{\mathrm{d}}} + \frac{2(\mathsf{K}+\varkappa/\mu)}{(\eta_{\mathrm{d}}-2)R^{\eta_{\mathrm{d}}}}} \tag{3.25}$$

$$= \frac{\left(\frac{\mathsf{a}_{\mathrm{d}}}{\mathsf{K}^{\beta}}\right)^{-\eta_{\mathrm{d}}}}{\sum_{j=1}^{\mathsf{K}'} a_{\mathrm{d},j}^{-\eta_{\mathrm{d}}} + \frac{\varkappa}{\mu} \sum_{k=1}^{\mathsf{K}''} a_{\mathrm{c},k}^{-\eta_{\mathrm{d}}} + \frac{2(\mathsf{K}+\varkappa/\mu)}{\eta_{\mathrm{d}}-2}} \tag{3.26}$$

where the approximation in (3.25) follows from the application of (3.16) and (3.26) is obtained by normalizing all the terms with $R^{-\eta_{\mathrm{c}}}$ and with $\frac{\mathsf{a}_{\mathrm{d}}}{\mathsf{K}^{\beta}} = a_{\mathrm{d},0} = \frac{r_{\mathrm{d},0}}{R}$, $a_{\mathrm{c},k} = \frac{r_{\mathrm{c},k}}{R}$ and $a_{\mathrm{d},j} = \frac{r_{\mathrm{d},j}}{R}$ are normalized distances.

Local-Average SIR Distribution

Remarkably, the large-scale distribution of ρ_{d} can be characterized in closed form, even without the need for the approximation in (3.25). Once again, while recalling—from Example 2.7—that $\mathcal{L}_{F_{1/\rho_{\mathrm{d}}}}(\cdot)$ also admits remarkably simple forms due to the interferers conforming to independent and homogeneous PPPs, our preference here is to present a direct expression for $F_{\rho_{\mathrm{d}}}(\cdot)$.

Proposition 3.3. The CDF of ρ_{d} is

$$F_{\rho_{\mathrm{d}}}(\xi) = \frac{1}{\pi}\sum_{k=1}^{\infty}\left[\frac{\xi^{2/\eta_{\mathrm{d}}}\,\mathsf{a}_{\mathrm{d}}^2}{\mathsf{K}^{2\beta}}\left(\mathsf{K}+\frac{\varkappa}{\mu^{2/\eta_{\mathrm{d}}}}\right)\Gamma\left(1-\frac{2}{\eta_{\mathrm{d}}}\right)\right]^k \cdot\frac{\Gamma\left(\frac{2k}{\eta_{\mathrm{d}}}\right)}{k!}\sin\left[k\pi\left(1-\frac{2}{\eta_{\mathrm{d}}}\right)\right] \quad (3.27)$$

which for $\eta_{\mathrm{d}} = 4$, reduces to

$$F_{\rho_{\mathrm{d}}}(\xi) = \operatorname{erf}\left[\frac{\sqrt{\pi\,\xi}\,\mathsf{a}_{\mathrm{d}}^2}{2\,\mathsf{K}^{2\beta}}\left(\mathsf{K}+\frac{\varkappa}{\sqrt{\mu}}\right)\right]. \quad (3.28)$$

Proof. See Appendix B.3. ■

3.5 Ergodic Spectral Efficiency

We now turn our attention to the ergodic spectral efficiency, the performance metric of our interest.

3.5.1 Specific Network Geometry

Under a specific network geometry, i.e., conditioned on the transmitter locations, the local-average SIR becomes determined and since we assume Rayleigh fading, the result in Example 2.2 is applied for the ergodic spectral efficiency.

For given ρ_{c}, the spectral efficiency of the corresponding cellular uplink, is

$$C_{\mathrm{c}}(\rho_{\mathrm{c}}) = e^{1/\rho_{\mathrm{c}}}E_1\left(\frac{1}{\rho_{\mathrm{c}}}\right)\log_2 e. \quad (3.29)$$

Similarly, for given ρ_{d}, the spectral efficiency of the corresponding D2D link equals

$$C_{\mathrm{d}}(\rho_{\mathrm{d}}) = e^{1/\rho_{\mathrm{d}}}E_1\left(\frac{1}{\rho_{\mathrm{d}}}\right)\log_2 e. \quad (3.30)$$

Example 3.2. Consider a D2D link in an overlay system with $\mathsf{K} = 3$ links per cell on average, with $\beta = 0$ (i.e., with link lengths that are independent of the user density) and with the path loss exponent $\eta_{\mathrm{d}} = 4.5$. Draw around the receiver an averaging circle of size R such that only the locations of the inner interferers are conditioned

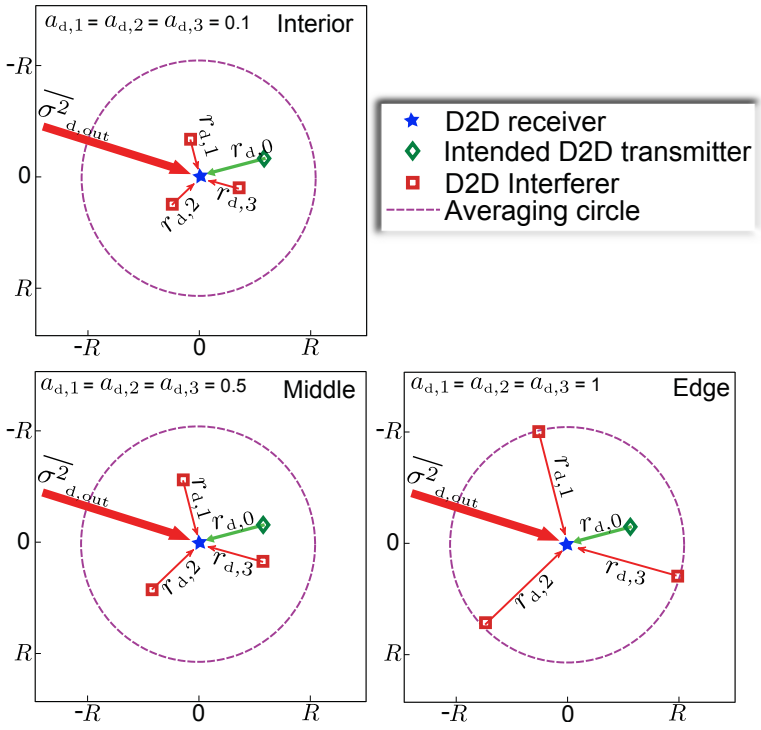

Figure 3.3: The three situations considered in Example 3.2.

on. Compared in Fig. 3.4 are the spectral efficiency in (3.30) and the exact mutual information under the non-Gaussian interference z_d, averaged over many fading realizations—recall C_{exact} as in (2.6)—computed numerically as per Appendix A.1, for many snapshots of the interferer locations outside the averaging circle. Three different situations are considered, with the interferers placed at the interior, middle and edge of the averaging circle (cf. Fig. 3.3). Excellent matches are observed, supporting our interference modeling approach.

Similarly good agreements are observed for other overlay settings and also for underlay settings.

3.5.2 Distribution over All Geometries

Moving beyond the specific placements in Example 3.2, the spatial distribution of the transmitters induces, through ρ_c and ρ_d, distributions of their own for C_c and C_d. Provided $F_{\rho_c}(\cdot)$ and $F_{\rho_d}(\cdot)$, the distributions of C_c and C_d can be evaluated via numerical mapping,

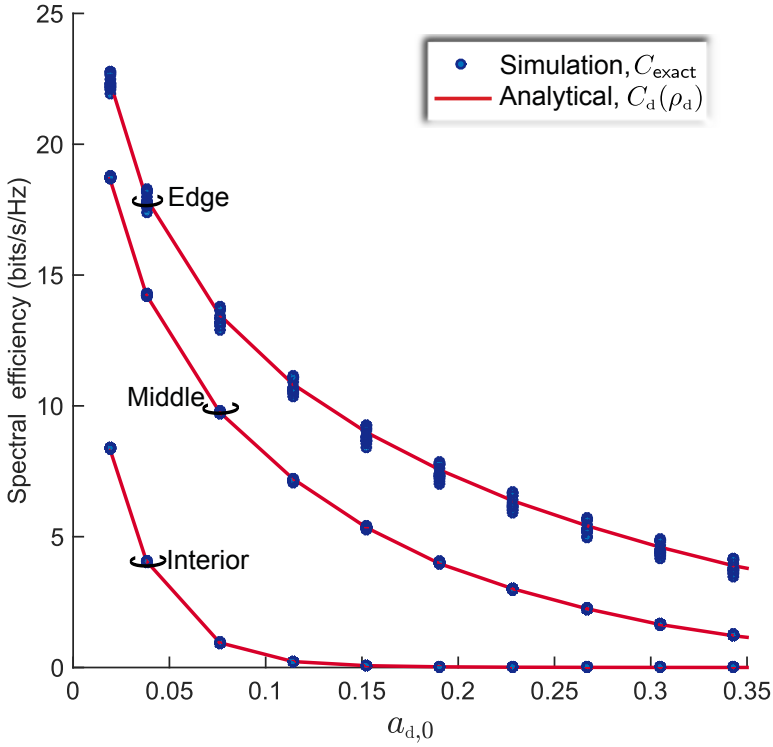

Figure 3.4: D2D link spectral efficiency in an overlay system as function of the normalized link distance $a_{\text{d},0}$ with $\beta = 0$ and $\mathsf{K} = 3$: analysis with our interference model vs. simulation with the interference modeled as per (3.4). The path loss exponent $\eta_{\text{d}} = 4.5$.

using (3.29) and (3.30), for given values of the parameters. However, characterizing them analytically appears challenging because of the exponential integral function in the spectral efficiency expressions. Alternatively, invoking [121]

$$e^{\nu} E_1(\nu) \log_2 e \approx 1.4 \log_e \left(1 + \frac{0.82}{\nu}\right) \tag{3.31}$$

we can approximate the CDFs of C_{c} and C_{d} as

$$F_{C_{\text{c}}}(\gamma) \approx F_{\rho_{\text{c}}} \left(\frac{e^{\frac{\gamma}{1.4}} - 1}{0.82}\right) \tag{3.32}$$

$$F_{C_{\text{d}}}(\gamma) \approx F_{\rho_{\text{d}}} \left(\frac{e^{\frac{\gamma}{1.4}} - 1}{0.82}\right). \tag{3.33}$$

Example 3.3. In Fig. 3.5, the approximated CDFs in (3.32) and (3.33) are contrasted against the ones obtained numerically by means

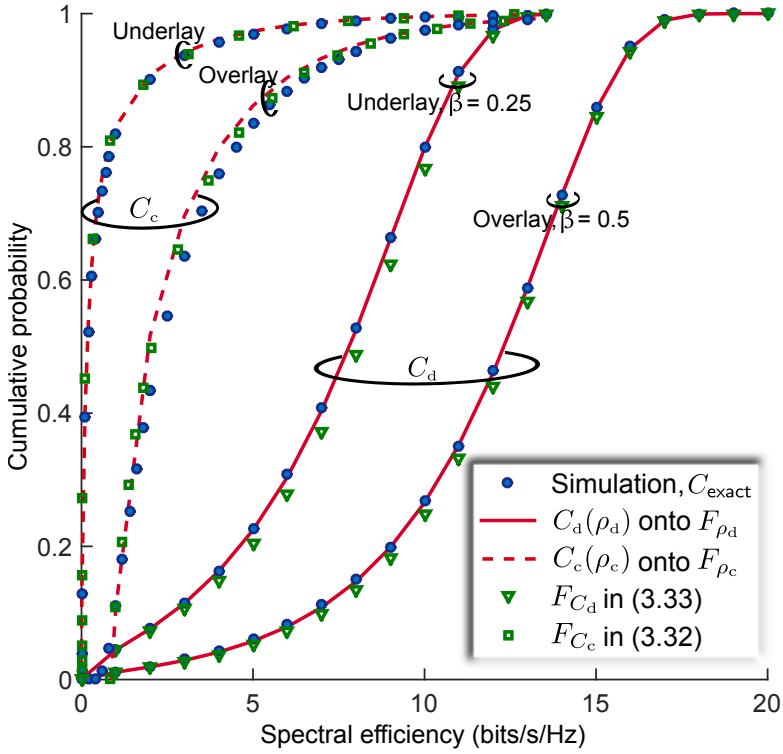

Figure 3.5: CDFs of C_c and C_d for $\mathsf{K} = 10$, $\mathsf{a}_d = 0.1$, $\eta_c = 4$, $\eta_d = 4.5$ and $\mu = -10$ dB.

of the corresponding local-average SIR CDFs (Props. 3.1, 3.2 and 3.3) and the link spectral efficiency equations, and the ones obtained completely through Monte-Carlo. Setting $\mathsf{K} = 10$, $\mathsf{a}_d = 0.1$, $\eta_c = 4$, $\eta_d = 4.5$ and $\mu = -10$ dB, underlay with $\beta = 0.25$ and overlay with $\beta = 0.5$ are considered. Very good agreements are observed, again validating our interference modeling approach.

3.5.3 Spatial Average

To effect the spatial averaging, slightly different approaches are computationally more convenient in our framework depending on the type of link (cellular/D2D) and on the case (underlay/overlay). Hence, each is separately presented next, with the details relegated to the Appendix.

Cellular Uplink

Proposition 3.4. With underlay, the cellular uplink spectral efficiency averaged over all network geometries is

$$\bar{C}_{\mathrm{c}} \approx 2 \int_0^{\infty} \frac{\log_2 e}{\gamma+1} \int_0^1 a\, e^{-\gamma \frac{2\, a^{\eta_{\mathrm{c}}}}{\eta_{\mathrm{c}}-2} - (\gamma\mu)^{\frac{2}{\eta_{\mathrm{c}}}} a^2\, \mathsf{K}\, \Gamma\left(1-\frac{2}{\eta_{\mathrm{c}}}\right)} \mathrm{d}a\, \mathrm{d}\gamma \tag{3.34}$$

which, for $\eta_{\mathrm{c}} = 4$, simplifies to

$$\bar{C}_{\mathrm{c}} = \frac{\sqrt{\pi} e^{-\pi\mu\mathsf{K}^2/4}}{2\, \log_e 2} \int_0^{\infty} \frac{\mathrm{erf}\left(\sqrt{\gamma} + \frac{\sqrt{\pi\mu}\mathsf{K}}{2}\right) - \mathrm{erf}\left(\frac{\sqrt{\pi\mu}\mathsf{K}}{2}\right)}{\sqrt{\gamma}\,(1+\gamma)} \mathrm{d}\gamma$$

Proof. See Appendix B.4. ∎

With overlay ($\varkappa = 0$), a compact result involving only the Meijer-G function

$$G_{p,q}^{m,n}\left(z \,\middle|\, \begin{matrix} a_1, ..., a_n, a_{n+1}, ..., a_p \\ b_1, ..., b_m, b_{m+1}, ..., b_q \end{matrix}\right) \tag{3.35}$$

and the cellular path loss exponent η_{c} is obtained.

Proposition 3.5. With overlay, the cellular uplink average spectral efficiency over all network geometries is

$$\bar{C}_{\mathrm{c}} = \frac{2 \log_2 e}{\eta_{\mathrm{c}}}\, G_{2,3}^{2,2}\left(\frac{2}{\eta_{\mathrm{c}}-2} \,\middle|\, \begin{matrix} 0, \frac{\eta_{\mathrm{c}}-2}{\eta_{\mathrm{c}}} \\ 0, 0, \frac{-2}{\eta_{\mathrm{c}}} \end{matrix}\right). \tag{3.36}$$

Proof. See Appendix B.5. ∎

The versatility of our interference modeling approach is in full display here, facilitating a closed form expression for a quantity that had previously been obtained only in integral form.

D2D Link

Proposition 3.6. The D2D link spectral efficiency averaged over all network geometries equals

$$\bar{C}_{\mathrm{d}} = \int_0^{\infty} \frac{\log_2 e}{\gamma+1}\, e^{-\gamma^{2/\eta_{\mathrm{d}}} \frac{\mathsf{a}_{\mathrm{d}}^2}{\mathsf{K}^2\beta} \left(\mathsf{K} + \frac{\varkappa}{\mu^{2/\eta_{\mathrm{d}}}}\right) \Gamma\left(1-\frac{2}{\eta_{\mathrm{d}}}\right)} \mathrm{d}\gamma \tag{3.37}$$

which, for $\eta_{\mathrm{d}} = 4$, reduces to

$$\bar{C}_{\mathrm{d}} = 2\left[\sin\left(\mathcal{K}\,\mathsf{a}_{\mathrm{d}}^2\right)\mathrm{si}\left(\mathcal{K}\,\mathsf{a}_{\mathrm{d}}^2\right) - \cos\left(\mathcal{K}\,\mathsf{a}_{\mathrm{d}}^2\right)\mathrm{ci}\left(\mathcal{K}\,\mathsf{a}_{\mathrm{d}}^2\right)\right]\log_2 e \tag{3.38}$$

where

$$\mathcal{K} = \frac{\sqrt{\pi}}{\mathsf{K}^{2\beta}}\left(\mathsf{K} + \frac{\varkappa}{\sqrt{\mu}}\right)$$

while the trigonometric integrals $\mathrm{si}(\cdot)$ and $\mathrm{ci}(\cdot)$ are respectively given by

$$\mathrm{si}(x) = \int_x^\infty \frac{\sin \mathsf{t}}{\mathsf{t}}\mathrm{d}\mathsf{t}$$

and

$$\mathrm{ci}(x) = -\int_x^\infty \frac{\cos \mathsf{t}}{\mathsf{t}}\mathrm{d}\mathsf{t}.$$

Proof. See Appendix B.6. ■

A particularly interesting special case arises when $\beta = 1/2$, as then the D2D link length is $a_{\mathrm{d},0} \propto 1/\sqrt{\mathsf{K}}$ and the interferer link distances $\{a_{\mathrm{d},j}\}_{j=1}^{\infty}$ to the points in the PPP Φ_{d} satisfy [114]

$$\mathbb{E}[a_{\mathrm{d},j}] \propto 1/\sqrt{\mathsf{K}}.$$

Intuitively, one would expect the dependence on the user density to vanish, and that is indeed the case with overlay.

Corollary 3.1. With overlay and $\beta = 1/2$, the D2D link spectral efficiency averaged over all network geometries is

$$\bar{C}_{\mathrm{d}} = \int_0^\infty \frac{\log_2 e}{\gamma + 1}\, e^{-\gamma^{2/\eta_{\mathrm{d}}}\,\mathsf{a}_{\mathrm{d}}^2\,\Gamma\left(1-\frac{2}{\eta_{\mathrm{d}}}\right)}\,\mathrm{d}\gamma \tag{3.39}$$

which, for $\eta_{\mathrm{d}} = 4$, reduces to

$$\bar{C}_{\mathrm{d}} = 2\left[\sin\left(\sqrt{\pi}\,\mathsf{a}_{\mathrm{d}}^2\right)\mathrm{si}\left(\sqrt{\pi}\,\mathsf{a}_{\mathrm{d}}^2\right) - \cos\left(\sqrt{\pi}\,\mathsf{a}_{\mathrm{d}}^2\right)\mathrm{ci}\left(\sqrt{\pi}\,\mathsf{a}_{\mathrm{d}}^2\right)\right]\log_2 e. \tag{3.40}$$

Example 3.4. For an overlay system ($\varkappa = 0$) with $\mathsf{a}_{\mathrm{d}} = 0.1$ and $\mathsf{K} = 10$, Fig. 3.6 shows the spatial average of spectral efficiencies in (3.36) and (3.37) alongside the respective $\bar{C}_{\mathsf{exact}}$, the Monte-Carlo average of C_{exact}, i.e., with z_{c} as in (3.2) and z_{d} as in (3.4). The match is excellent, once again evincing the goodness of our interference modeling approach.

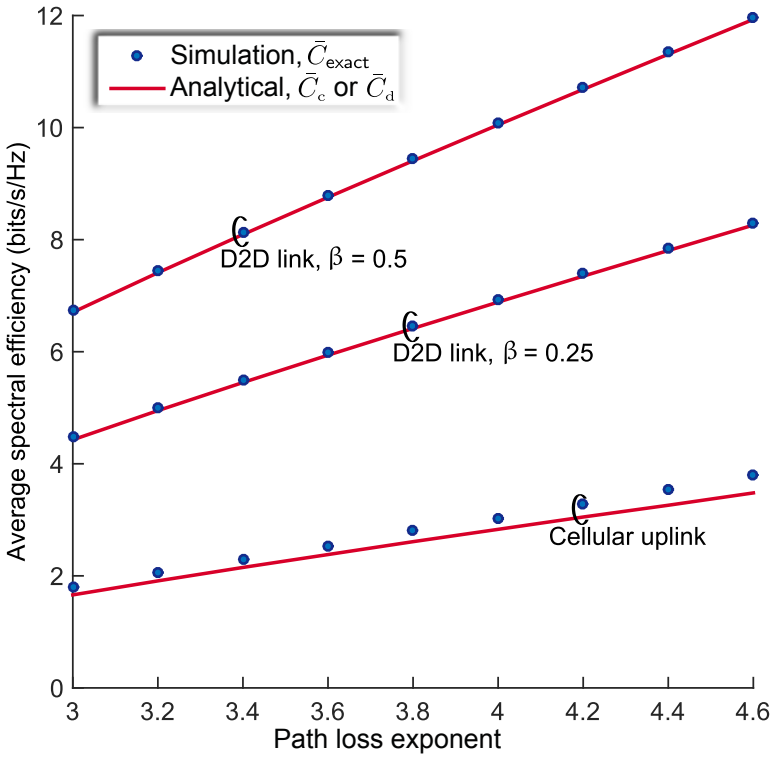

Figure 3.6: Spatially average spectral efficiencies of uplink and D2D link for varying η_{c} and η_{d} with overlay.

3.6 Benefits of D2D

In order to gauge the benefits of D2D and to demonstrate the usefulness of the framework developed in earlier sections, we next provide some examples. Unless otherwise specified, the path loss exponents are $\eta_{\text{c}} = 3.5$ and $\eta_{\text{d}} = 4.5$.

3.6.1 Overlay D2D

Example 3.5. Consider an overlay system with fixed D2D link distance $a_{\text{d},0} = \mathsf{a}_{\text{d}}$ (i.e., with $\beta = 0$) and with an average of $\mathsf{K} = 10$ D2D links per cell. To render the system as typical as possible, K' is set to its expected value and, for $j = 1, \ldots, \mathsf{K}'$, $a_{\text{d},j}$ is set to the expected value of the normalized distance to the jth nearest neighboring point in a PPP with density λ_{d} [114]. In such a setup,

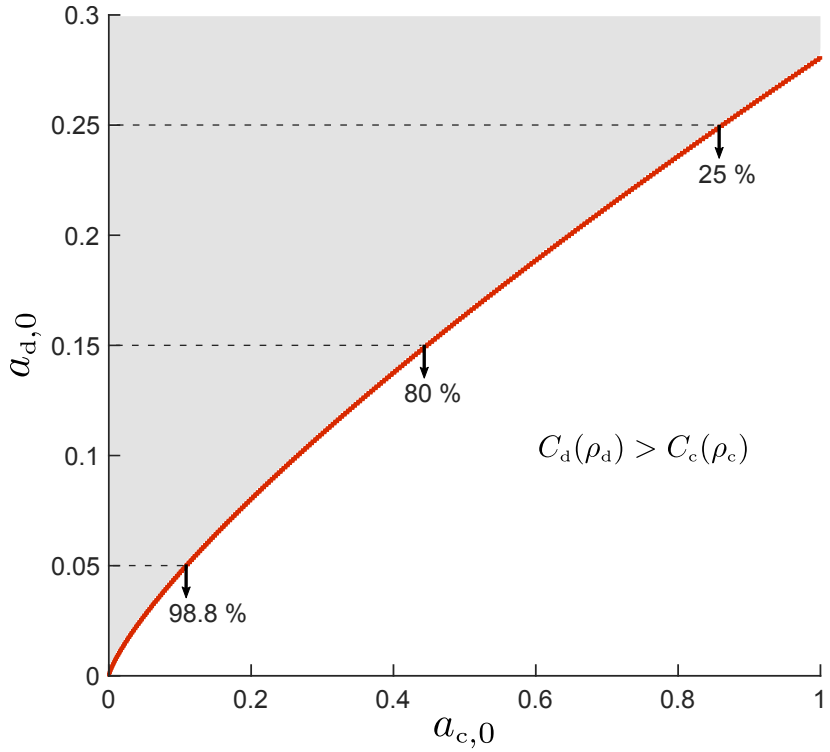

Figure 3.7: Contour plot for the relationship in (3.42). Within the unshaded region, $C_{\mathrm{d}}(\rho_{\mathrm{d}}) > C_{\mathrm{c}}(\rho_{\mathrm{c}})$.

equating the link spectral efficiencies $C_{\mathrm{c}}(\rho_{\mathrm{c}})$ and $C_{\mathrm{d}}(\rho_{\mathrm{d}})$ we obtain

$$\frac{(3.5-2)\, a_{\mathrm{c},0}^{-3.5}}{2} = \frac{a_{\mathrm{d},0}^{-4.5}}{\sum_{j=1}^{10} \left(\frac{\Gamma(0.5+j)}{\sqrt{10}\,\Gamma(j)}\right)^{-4.5} + \frac{2\cdot 10}{4.5-2}} \tag{3.41}$$

which simplifies into

$$a_{\mathrm{c},0} = 5.12\, a_{\mathrm{d},0}^{\frac{4.5}{3.5}} \tag{3.42}$$

for which a contour plot is shown in Fig. 3.7. Within the unshaded region, the D2D link has a better spectral efficiency than a corresponding uplink transmission from the same user would have, and thus D2D is advantageous. The share of geometries for which $C_{\mathrm{d}}(\rho_{\mathrm{d}}) > C_{\mathrm{c}}(\rho_{\mathrm{c}})$ for a given $a_{\mathrm{d},0}$ is

$$\mathbb{P}[a_{\mathrm{c},0} > x] = 1 - x^2$$

where x is the corresponding x-axis value of the contour. Some such shares are displayed, e.g., for $a_{\mathrm{d},0} = 0.15$ D2D is preferable in 80% of situations.

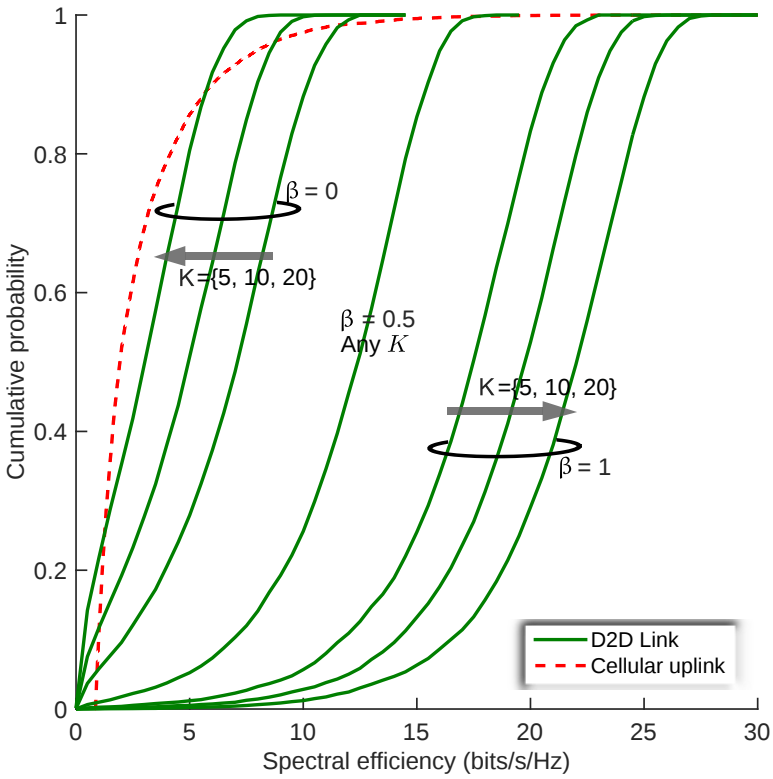

Figure 3.8: CDFs of cellular and D2D link spectral efficiencies in an overlay system with $\mathsf{a}_\mathrm{d} = 0.1$ and different β.

Example 3.5 shows how, from a link vantage, D2D is very often preferable to communicating via the BS *even if only the uplink is considered*. With the resource costs of both uplink and downlink considered, the appeal of D2D would increase even further.

Example 3.6. Considering overlay and $\mathsf{a}_\mathrm{d} = 0.1$, CDFs of $C_\mathrm{c}(\rho_\mathrm{c})$ and $C_\mathrm{d}(\rho_\mathrm{d})$ are plotted in Fig. 3.8 for various β and K. Even for high densities K, with the system brimming with D2D interference, thanks to their short range many D2D links enjoy higher spectral efficiencies than the corresponding cellular uplink. We observe the following from the CDFs of $C_\mathrm{d}(\rho_\mathrm{d})$:

- When $\beta < 1/2$, $C_\mathrm{d}(\rho_\mathrm{d})$ worsens with increasing K.
- When $\beta = 1/2$, $C_\mathrm{d}(\rho_\mathrm{d})$ is independent of K.
- When $\beta > 1/2$, $C_\mathrm{d}(\rho_\mathrm{d})$ improves with increasing K.

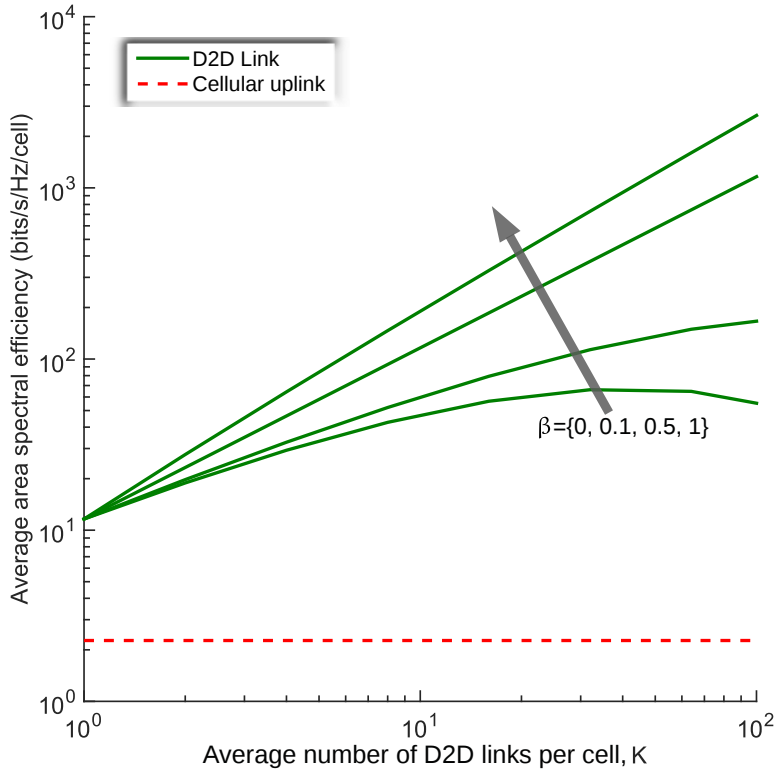

Figure 3.9: Average area spectral efficiency in an overlay system with $\mathsf{a}_\mathrm{d} = 0.1$.

The above conforms with intuition as the interferer distances $\{a_{\mathrm{d},j}\}$, for $j = 1, \ldots, \infty$, shrink with K, on average $\mathbb{E}[a_{\mathrm{d},j}] \propto 1/\sqrt{\mathsf{K}}$. When $\beta < 1/2$, $C_\mathrm{d}(\rho_\mathrm{d})$ decreases with K as $a_{\mathrm{d},0}$ shrinks slower than the interferer distances while, when $\beta > 1/2$, $C_\mathrm{d}(\rho_\mathrm{d})$ increases with K as $a_{\mathrm{d},0}$ shrinks faster than the interferer distances.

The number of D2D links that can coexist on a given signaling resource is large, although a small share of links suffer from close-by interference. To better appreciate the benefits of such dense spectral reuse we next turn our attention to the area spectral efficiency which reflects the benefits of this reuse.

Example 3.7. Since there are K active D2D links per cell on average, the average area spectral efficiency of the D2D traffic is $\mathsf{K}\bar{C}_\mathrm{d}$ whereas, for the cellular uplink, the average area spectral efficiency is $\bar{C}_\mathrm{c}$ as there is only one active cellular user per cell. Shown in Fig. 3.9 is the comparison of these quantities as function of K, for various β. As K grows beyond the range of values shown in the plot,

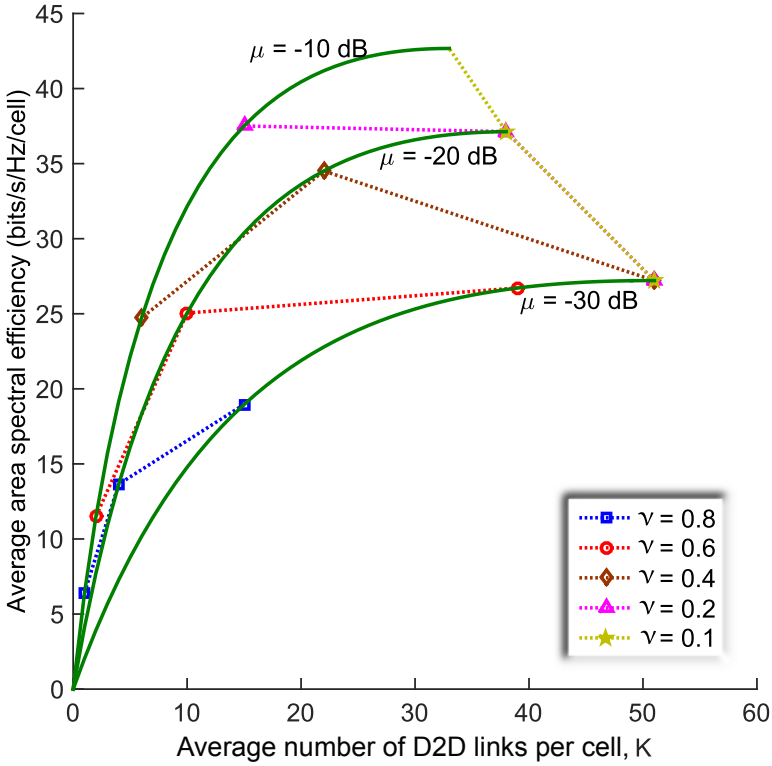

Figure 3.10: Average area spectral efficiency of underlay D2D with $\mathsf{a}_\mathrm{d} = 0.12$ and $\beta = 0$ for different values of K, μ and ν.

the D2D link curves for $\beta = 0$ and $\beta = 0.1$ eventually fall below the cellular uplink curve. The following is observed for a variety of such settings:

- For each $\beta < 1/2$, there is an optimum "load" K.
- When $\beta \geq 1/2$, the D2D system spectral efficiency increases monotonically with K.
- Even when not monotonic in K, the D2D system spectral efficiency is generally *much* higher than its cellular counterpart.

3.6.2 Underlay D2D

Example 3.8. In Fig. 3.10, the average area spectral efficiency (bits/s/Hz per cell) achieved by underlay D2D with $a_{\mathrm{d},0} = 0.12$ is plotted until its peak value by varying K, for different values of μ. Suppose that we want the average uplink area spectral efficiency to

satisfy $\bar{C}_c \geq \nu \bar{C}_c|_{K=0}$ where $\bar{C}_c|_{K=0}$ denotes its value without D2D and $\nu > 0$ parametrizes its degradation; for instance, $\nu = 0.8$ means less than 20% degradation. The maximum average area spectral efficiencies of D2D for different values of ν are indicated in the figure.

The strong dependence on ν in Example 3.8 indicates that, with underlay, the cellular uplink spectral efficiency is severely affected by D2D interference, which was also evidenced by the CDF $F_{C_c}(\cdot)$ plotted in Fig. 3.5. This encourages us to look into ways for protecting the cellular uplink from the D2D interferers, as we do in the next chapter.

3.7 Summary

The framework presented in this chapter enables analytical characterizations of the ergodic spectral efficiency of a D2D integrated cellular network; the characterizations are provided for the cellular uplinks and the D2D links, incorporating both the underlay and overlay options. It allows a controllable degree of spatial averaging so as to reduce the complexity in gauging the benefits of D2D under specific geometries and to yield easy-to-evaluate expressions—that in some cases are even in closed form—for the distribution and spatial average of the spectral efficiency.

From these expressions, and the various supporting examples, we can distill the following answers to the questions posed in the beginning of the chapter (cf. Section 3.1):

- For local traffic, direct D2D is better than uplink-downlink communication in a vast majority of situations, upwards of 80% for relatively long D2D links (15% of cell radius) and upwards of 98% for shorter D2D links (5% of cell radius).
- Tens of D2D links can be packed on each cell with acceptable mutual interference, for a large share of the links; however, a significant share of D2D links and particularly the cellular uplink in the underlay mode greatly suffer from the increased interference.
- For local traffic, the average system spectral efficiency with D2D can be between one and three orders of magnitude larger than without D2D.

Chapter 4

Exclusion Regions for Interference Protection in D2D Networks

In this chapter, we generalize the analytical framework developed in Chapter 3 to incorporate exclusion regions around the receivers and investigate their efficacy in alleviating the increased interference due to the co-channel D2D transmissions. The underlay and overlay options are examined separately, namely, to address the problems of: (*i*) the interference seen at the BS from the underlay D2D links and (*ii*) the interference between the overlay D2D links.

4.1 General Considerations

In both underlay and overlay, only a subset of the *available* D2D links are selected to be the co-channel D2D links, i.e., to reuse a common time-frequency channel, based on some selection criteria to avoid nearby interference. In the absence of such selection, all of the available links are co-channel, as they were in Chapter 3. We focus only on these co-channel links and the spectral efficiency thereof. The unselected available links with potential D2D traffic (whose performance we do not investigate) may operate in D2D mode, possibly reusing a different channel or in an orthogonalized fashion, or may resort to the conventional two-hop cellular mode.

Note that, except for the distinction in the network geometry, i.e., the distinct spatial distribution of the co-channel D2D links, the network modeling in this chapter matches that in Section 3.2.

4.2 Underlay D2D with Exclusion Regions

4.2.1 Background

Recall the cellular uplink results in underlay D2D, e.g., the CDFs of spectral efficiency in Fig. 3.5 and the area spectral efficiency plots in Fig. 3.10 corresponding to Example 3.8; it is seen that the performance is often severely affected by D2D interference. One way to reduce the interference seen in the uplink is to have exclusion regions around the BSs wherein no co-channel D2D transmitters are allowed. This idea has been explored in [122] under a simplistic single-cell model and in [123] by characterizing the success probability of transmissions in meeting fixed SIR thresholds. Alternatively, we set out to analyze the ergodic spectral efficiency of the cellular uplinks and D2D links by incorporating such exclusion regions into the multicell framework presented in Chapter 3.

4.2.2 Network Geometry

Let us consider circular exclusion regions of radius r_{ex} (cf. Fig. 4.1) and normalized radius $a_{\mathrm{ex}} = \frac{r_{\mathrm{ex}}}{R}$, wherein no co-channel D2D transmitter is present. As indicated earlier, with the introduction of such exclusion regions, the locations of the ensuing co-channel D2D transmitters no longer conform to a homogeneous PPP. Specifically, unlike in Chapter 3 where the D2D interferer locations from the vantage of any given receiver (be it in the cellular uplink or the D2D link) conformed to the same PPP Φ_{d}, here we encounter different spatial distributions thereof. And, particularly for the co-channel D2D links, a randomly picked one—and held fixed—is not the *typical* D2D link, because the distribution of the D2D interferer locations seen by the receiver varies, depending on its position relative to the exclusion regions (as the BS positions are fixed). To overcome the analytical roadblocks that arise due to the changed network geometry, we shall introduce some approximations in the interference modeling as expounded next.

4.2.3 Interference Modeling

Local Distribution

As established in Chapter 3, given the interfering link distances, the local distribution of the interference seen at the BS and D2D receiver are respectively modeled as $z_{\mathrm{c}} \sim \mathcal{N}_{\mathbb{C}}(0, \sigma_{\mathrm{c}}^2)$ and $z_{\mathrm{d}} \sim \mathcal{N}_{\mathbb{C}}(0, \sigma_{\mathrm{d}}^2)$.

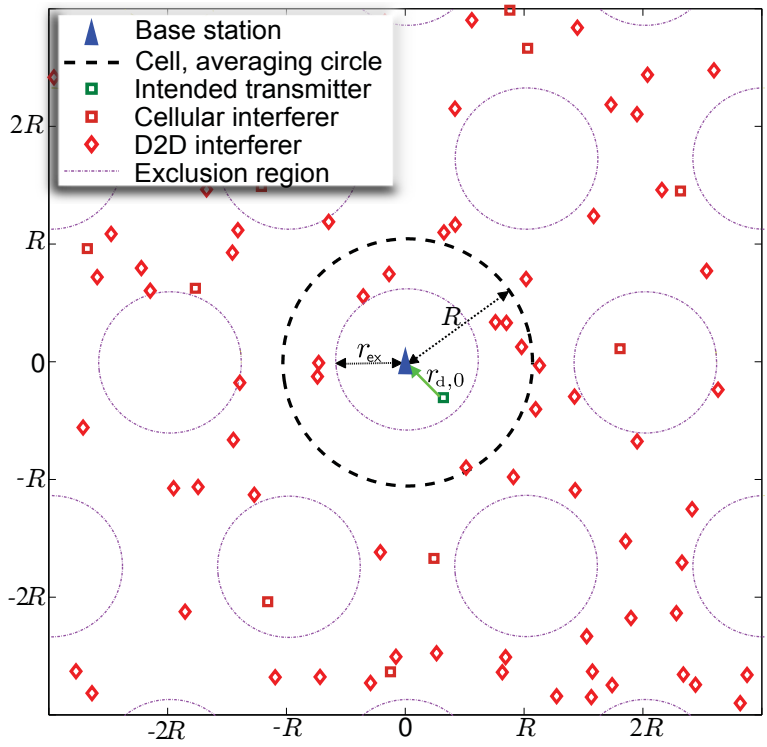

Figure 4.1: Cellular uplink with no underlay D2D transmitters allowed in circular exclusion regions of radius r_{ex} around the BSs. At the origin is a receiving BS and shown with a square marker within the circle of radius R is its intended cellular transmitter; shown with square markers outside the circle are the cellular interferers; shown with diamond markers are the D2D interferers.

Interferer Locations

Recalling (3.9) and (3.14), i.e., the interference power seen at the receiver at origin, for the underlay system ($\alpha = 0$) under consideration, we have for the cellular uplink

$$\sigma_{\mathrm{c}}^2 = \underbrace{\varkappa \sum_{j=1}^{\mathsf{K}'} P_{\mathrm{d}}\, r_{\mathrm{d},j}^{-\eta_{\mathrm{c}}}}_{\sigma_{\mathrm{c,in}}^2} + \underbrace{\sum_{j=\mathsf{K}'+1}^{\infty} P_{\mathrm{d}}\, r_{\mathrm{d},j}^{-\eta_{\mathrm{c}}} + \sum_{k=1}^{\infty} P_{\mathrm{c}}\, r_{\mathrm{c},k}^{-\eta_{\mathrm{c}}}}_{\sigma_{\mathrm{c,out}}^2} \tag{4.1}$$

and for the D2D link

$$\sigma_{\mathrm{d}}^2 = \underbrace{\sum_{j=1}^{\mathsf{K}'} P_{\mathrm{d}}\, r_{\mathrm{d},j}^{-\eta_{\mathrm{d}}} + \sum_{k=1}^{\mathsf{K}''} P_{\mathrm{c}}\, r_{\mathrm{c},k}^{-\eta_{\mathrm{d}}}}_{\sigma_{\mathrm{d,in}}^2} + \underbrace{\sum_{j=\mathsf{K}'+1}^{\infty} P_{\mathrm{d}}\, r_{\mathrm{d},j}^{-\eta_{\mathrm{d}}} + \sum_{k=\mathsf{K}''+1}^{\infty} P_{\mathrm{c}}\, r_{\mathrm{c},k}^{-\eta_{\mathrm{d}}}}_{\sigma_{\mathrm{d,out}}^2} \tag{4.2}$$

where, as indicated earlier, the D2D interferers locations are now distributed differently.

Firstly, recognizing that the average number of co-channel D2D links is $p_{\mathrm{c}}\lambda_{\mathrm{d}}$, with $p_{\mathrm{c}} = 1 - a_{\mathrm{ex}}^2$, we propose to model the D2D interferer locations outside $\mathcal{B}(0,R)$, i.e., the ones constituting $\sigma^2_{\mathrm{c,out}}$ or $\sigma^2_{\mathrm{d,out}}$, as belonging to an independent homogeneous PPP Φ_{d} with a scaled-down density $p_{\mathrm{c}}\lambda_{\mathrm{d}}$. Then, the interference power emanating from outside $\mathcal{B}(0,R)$ can be averaged over the locations of those interferers, which for the cellular uplink gives

$$\overline{\sigma^2}_{\mathrm{c,out}} \approx \frac{2\,(p_{\mathrm{c}}\,\mathsf{K}\,P_{\mathrm{d}} + P_{\mathrm{c}})}{(\eta_{\mathrm{c}} - 2)R^{\eta_{\mathrm{c}}}} \tag{4.3}$$

and for the D2D link gives

$$\overline{\sigma^2}_{\mathrm{d,out}} \approx \frac{2\,(p_{\mathrm{c}}\,\mathsf{K}\,P_{\mathrm{d}} + P_{\mathrm{c}})}{(\eta_{\mathrm{d}} - 2)R^{\eta_{\mathrm{d}}}} \tag{4.4}$$

following similar steps as in the derivation of (3.10) and (3.15).

In modeling the D2D interferer locations inside $\mathcal{B}(0,R)$, the cases of cellular uplink and D2D link require separate treatment.

For the cellular uplink, the interference power from the transmitters inside $\mathcal{B}(0,R)$ is

$$\sigma^2_{\mathrm{c,in}} = \sum_{j=1}^{\mathcal{K}'} P_{\mathrm{d}}\, r_{\mathrm{d},j}^{-\eta_{\mathrm{c}}} \tag{4.5}$$

where the $\mathcal{K}'$ D2D transmitters are located within an annulus with inner radius r_{ex} and outer radius R denoted by $\mathcal{A}(r_{\mathrm{ex}},R)$. The locations of the D2D transmitters within $\mathcal{A}(r_{\mathrm{ex}},R)$ conform to the points of the PPP Φ_{d} with density λ_{d}.

Shifting the focus to the D2D link, from the receiver's perspective, the interference power from the transmitters inside $\mathcal{B}(0,R)$

$$\sigma^2_{\mathrm{d,in}} = \sum_{j=1}^{\mathcal{K}''} P_{\mathrm{d}}\, r_{\mathrm{d},j}^{-\eta_{\mathrm{d}}} + \sum_{k=1}^{\mathsf{K}''} P_{\mathrm{c}}\, r_{\mathrm{c},k}^{-\eta_{\mathrm{d}}} \tag{4.6}$$

where the K'' cellular interferer locations conform to the points of the PPP Φ_{c} falling inside $\mathcal{B}(0,R)$ while the $\mathcal{K}''$ D2D interferer locations are difficult to model in general due to the asymmetry of the voids in $\mathcal{B}(0,R)$ caused by exclusion regions (cf. Fig. 4.2).

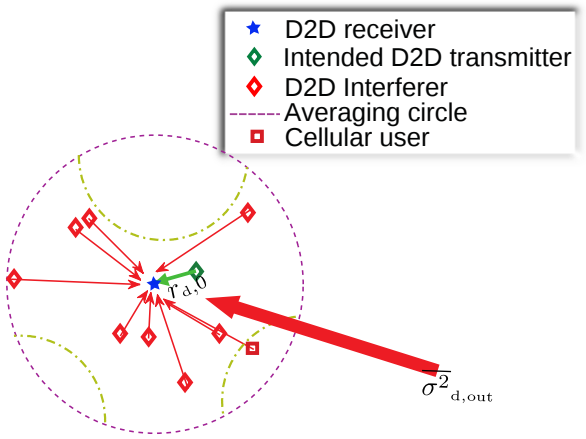

Figure 4.2: Asymmetric voids inside the averaging circle $\mathcal{B}(0,R)$ around a co-channel D2D receiver.

Therefore, in an attempt to obtain a lower bound on the average spectral efficiency, i.e., the performance averaged over all possible D2D receiver locations within a cell, we propose to upper-bound the interference power. Specifically, we fill the voids inside $\mathcal{B}(0,R)$ and regard the D2D interferers as conforming to a PPP with density λ_{d} within $\mathcal{B}(0,R)$, which can only increase the amount of interference.

The aforementioned assumption implies that a randomly picked co-channel D2D receiver sees D2D interferers in

$$[\Phi_{\mathrm{d}} \cap \mathcal{B}(0,R)] \cup [\Phi_{\mathrm{d}} \backslash \mathcal{B}(0,R)],$$

and thereby it is taken to be the typical receiver. The expectation is that the distributions and the spatial averages obtained for this typical D2D receiver become close approximations to the corresponding exact results, obtained via simulations and evaluated over all possible receiver locations in a cell; we shall verify this later.

4.2.4 SIR

Recalling (3.18) and (3.24) from the previous chapter, the local-average SIRs of the cellular uplink and the D2D link under the foregoing interference model are, respectively,

$$\rho_{\mathrm{c}} \approx \frac{a_{\mathrm{c},0}^{-\eta_{\mathrm{c}}}}{\mu \sum_{j=1}^{\mathcal{K}'} a_{\mathrm{d},j}^{-\eta_{\mathrm{c}}} + \frac{2(\mu p_{\mathrm{c}} \mathsf{K}+1)}{\eta_{\mathrm{c}}-2}} \tag{4.7}$$

and

$$\rho_{\mathrm{d}} \approx \frac{\left(\frac{\mathsf{a}_{\mathrm{d}}}{\mathsf{K}^{\beta}}\right)^{-\eta_{\mathrm{d}}}}{\sum_{j=1}^{\mathsf{K}''} a_{\mathrm{d},j}^{-\eta_{\mathrm{d}}} + \frac{1}{\mu}\sum_{k=1}^{\mathsf{K}''} a_{\mathrm{c},k}^{-\eta_{\mathrm{d}}} + \frac{2(p_{\mathrm{c}}\mathsf{K}+1/\mu)}{\eta_{\mathrm{d}}-2}}. \tag{4.8}$$

Local-Average SIR distribution

Although direct expressions are unwieldy, we characterize the large-scale distributions local-average SIRs in the Laplace domain, which may be applied in Lemma 2.1 for computing compute $F_{\rho_{\mathrm{c}}}(\cdot)$ and $F_{\rho_{\mathrm{d}}}(\cdot)$, without the need for Monte-Carlo simulations.

Lemma 4.1. In underlay D2D, with normalized exclusion regions of radius a_{ex} around each BS, the CDF $F_{1/\rho_{\mathrm{c}}}(\cdot)$ in the Laplace domain is

$$\mathcal{L}_{F_{1/\rho_{\mathrm{c}}}}(\mathsf{s}) \approx \frac{2}{\mathsf{s}\, e^{p_{\mathrm{c}}\mathsf{K}}} \int_0^1 a\, e^{-\mathsf{s}\, a^{\eta_{\mathrm{c}}}\, \frac{2(\mu p_{\mathrm{c}}\mathsf{K}+1)}{\eta_{\mathrm{c}}-2}} \cdot e^{-\frac{2\mathsf{K}}{\eta_{\mathrm{c}}}\left[a_{\mathrm{ex}}^2 E_{\frac{2+\eta_{\mathrm{c}}}{\eta_{\mathrm{c}}}}\left(\mathsf{s}\,\mu\,\frac{a^{\eta_{\mathrm{c}}}}{a_{\mathrm{ex}}^{\eta_{\mathrm{c}}}}\right) - E_{\frac{2+\eta_{\mathrm{c}}}{\eta_{\mathrm{c}}}}(\mathsf{s}\,\mu\, a^{\eta_{\mathrm{c}}})\right]} \mathrm{d}a. \tag{4.9}$$

Proof. See Appendix C.1. ∎

Lemma 4.2. In underlay D2D, with normalized exclusion regions of radius a_{ex} around each BS, the CDF $F_{1/\rho_{\mathrm{d}}}(\cdot)$ in the Laplace domain is

$$\mathcal{L}_{F_{1/\rho_{\mathrm{d}}}}(\mathsf{s}) \approx \frac{1}{\mathsf{s}} e^{\frac{2}{\eta_{\mathrm{d}}}\left[\mathsf{K}\, E_{\frac{2+\eta_{\mathrm{d}}}{\eta_{\mathrm{d}}}}\left(\frac{\mathsf{s}\,\mathsf{a}_{\mathrm{d}}^{\eta_{\mathrm{d}}}}{\mathsf{K}^{\eta_{\mathrm{d}}}\beta}\right) + E_{\frac{2+\eta_{\mathrm{d}}}{\eta_{\mathrm{d}}}}\left(\frac{\mathsf{s}\,\mathsf{a}_{\mathrm{d}}^{\eta_{\mathrm{d}}}}{\mu\mathsf{K}^{\eta_{\mathrm{d}}}\beta}\right)\right]} \cdot e^{-\mathsf{s}\,\frac{\mathsf{a}_{\mathrm{d}}^{\eta_{\mathrm{d}}}}{\mathsf{K}^{\eta_{\mathrm{d}}}\beta}\,\frac{2(p_{\mathrm{c}}\mathsf{K}+1/\mu)}{\eta_{\mathrm{d}}-2} - \mathsf{K} - 1}. \tag{4.10}$$

Proof. See Appendix C.2. ∎

4.2.5 Ergodic Spectral Efficiency

Specific Network Geometry

Under specific network geometry, i.e., for given ρ_{c} and ρ_{d}, ergodic spectral efficiencies—recall from (2.17)—are

$$C_{\mathrm{c}}(\rho_{\mathrm{c}}) = e^{1/\rho_{\mathrm{c}}}\, E_1\left(\frac{1}{\rho_{\mathrm{c}}}\right) \log_2 e \tag{4.11}$$

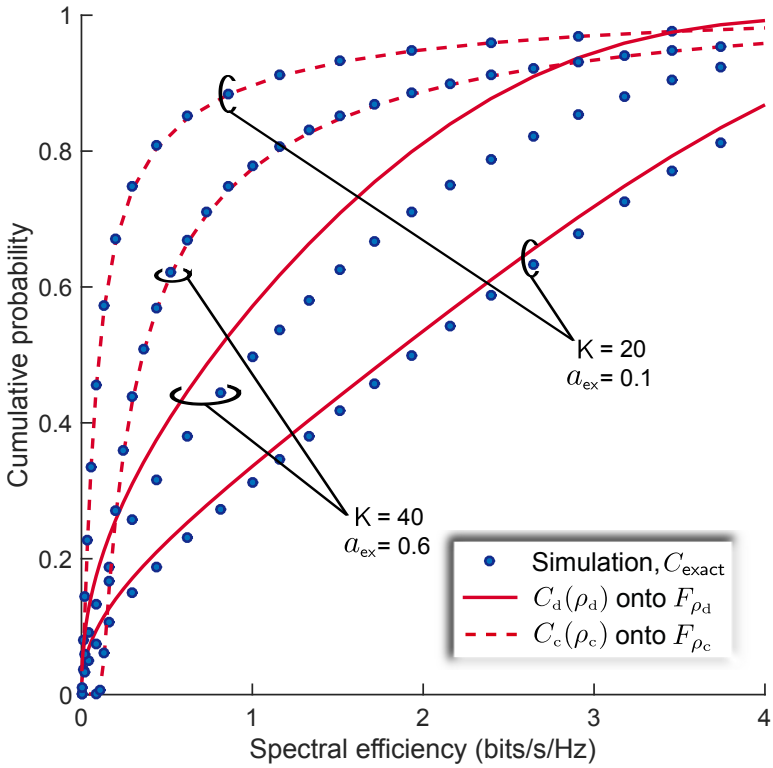

Figure 4.3: CDF of ergodic spectral efficiency in an underlay system with co-channel D2D transmitters present outside exclusion regions of radius a_{ex}.

and

$$C_d(\rho_d) = e^{1/\rho_d} E_1\left(\frac{1}{\rho_d}\right) \log_2 e. \tag{4.12}$$

Distribution over All Geometries

The CDFs of ergodic spectral efficiency are obtained by mapping $C_c(\rho_c)$ and $C_d(\rho_d)$ respectively onto $F_{\rho_c}(\cdot)$ and $F_{\rho_d}(\cdot)$.

Example 4.1. Plotted in Fig. 4.3 are the CDFs of the ergodic spectral efficiency, obtained as described above (under the foregoing approximate interference model), contrasted against the exact counterparts computed via Monte-Carlo, without any approximation. Setting $\beta = 0$, $a_d = 0.12$, $\eta_c = 3.5$, $\eta_d = 4.5$ and $\mu = -10$ dB, comparisons are provided under $K = 20$ (available) D2D links per cell with normalized exclusion radius $a_{ex} = 0.1$ and under $K = 20$ with $a_{ex} = 0.6$.

For the cellular uplink, the values obtained with our interference modeling are more accurate in comparison with the D2D link, because, for the former the modeling of the (close-by) in-circle interferers is exact, while the latter involves the coarse approximation with more interferers than in reality (due to the filling of the voids).

Spatial Average

The ergodic spectral efficiency can be further averaged over the locations of the interferers inside the averaging circle, leading to the results that follow.

Proposition 4.1. In underlay, with normalized exclusion regions of radius a_{ex} around each BS, the cellular uplink spectral efficiency averaged over all geometries is

$$\bar{C}_{\mathrm{c}} \approx \frac{2}{e^{p_{\mathrm{c}}\mathsf{K}}} \int_0^\infty \frac{\log_2 e}{\gamma+1} \int_0^1 a\, e^{-\gamma\, a^{\eta_{\mathrm{c}}}\, \frac{2(\mu p_{\mathrm{c}}\mathsf{K}+1)}{\eta_{\mathrm{c}}-2}} \cdot e^{-\frac{2\mathsf{K}}{\eta_{\mathrm{c}}}\left[a_{\mathrm{ex}}^2 E_{\frac{2+\eta_{\mathrm{c}}}{\eta_{\mathrm{c}}}}\left(\gamma\,\mu\,\frac{a^{\eta_{\mathrm{c}}}}{a_{\mathrm{ex}}^{\eta_{\mathrm{c}}}}\right) - E_{\frac{2+\eta_{\mathrm{c}}}{\eta_{\mathrm{c}}}}(\gamma\,\mu\,a^{\eta_{\mathrm{c}}})\right]} \mathrm{d}a\,\mathrm{d}\gamma. \quad (4.13)$$

Proof. The result follows from the application of $\mathcal{L}_{F_{1/\rho_{\mathrm{c}}}}(\cdot)$ from Lemma 4.1 in Lemma 2.2. ■

Proposition 4.2. In an underlay system with normalized exclusion regions of radius a_{ex} and with a given $a_{\mathrm{d},0}$,

$$\bar{C}_{\mathrm{d}} \geq \frac{1}{e^{\mathsf{K}+1}} \int_0^\infty \frac{\log_2 e}{\gamma+1} \cdot e^{-\gamma\, \frac{\mathsf{a}_{\mathrm{d}}^{\eta_{\mathrm{d}}}}{\mathsf{K}^{\eta_{\mathrm{d}}}\beta}\, \frac{2(p_{\mathrm{c}}\mathsf{K}+1/\mu)}{\eta_{\mathrm{d}}-2} + \frac{2}{\eta_{\mathrm{d}}}\left[\mathsf{K}\, E_{\frac{2+\eta_{\mathrm{d}}}{\eta_{\mathrm{d}}}}\left(\frac{\gamma\,\mathsf{a}_{\mathrm{d}}^{\eta_{\mathrm{d}}}}{\mathsf{K}^{\eta_{\mathrm{d}}}\beta}\right) + E_{\frac{2+\eta_{\mathrm{d}}}{\eta_{\mathrm{d}}}}\left(\frac{\gamma\,\mathsf{a}_{\mathrm{d}}^{\eta_{\mathrm{d}}}}{\mu\mathsf{K}^{\eta_{\mathrm{d}}}\beta}\right)\right]} \mathrm{d}\gamma. \quad (4.14)$$

Proof. The result follows from the application of $\mathcal{L}_{F_{1/\rho_{\mathrm{d}}}}(\cdot)$ from Lemma 4.2 in Lemma 2.2. ■

Note that (4.14) is a lower bound, for the reasons stated in Section 4.2.3, goodness of which is verified next.

Example 4.2. With exclusion regions around the BSs, the average area spectral efficiency (bits/s/Hz per cell) of the underlay D2D links becomes $p_{\mathrm{c}}\,\mathsf{K}\,\bar{C}_{\mathrm{d}}$. In Fig. 4.4, the analytical lower-bound on such average area spectral efficiency is contrasted against the exact

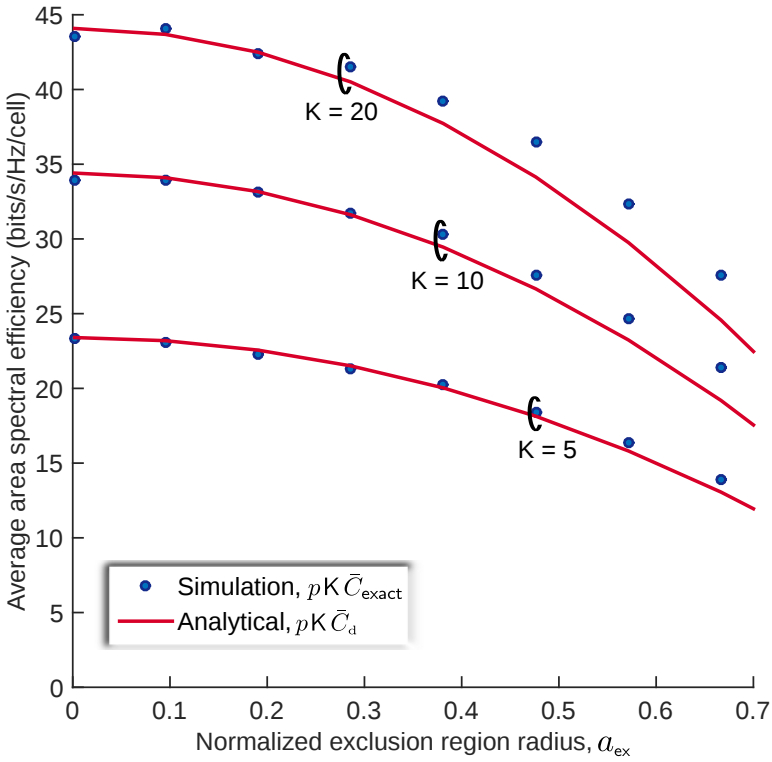

Figure 4.4: Average area spectral efficiency of the underlaying D2D links. The analytical lower bound and exact simulation results are contrasted for different values of K.

results obtained via Monte-Carlo for $\mathsf{a}_{\mathrm{d}} = 0.12$, $\beta = 0$, $\mu = 0.1$ and $\eta_{\mathrm{d}} = 4.5$.

Our final example in this section aims at illustrating the effectiveness of the exclusion regions.

Example 4.3. With a constraint of less than 20% degradation for the average uplink spectral efficiency, parametrized by $\nu = 0.8$ in the relationship $\bar{C}_{\mathrm{c}} \geq \nu \bar{C}_{\mathrm{c}}|_{\mathsf{K}=0}$, the achievable average area spectral efficiency (bits/s/Hz per cell) of the underlay D2D links $p_{\mathrm{c}}\,\mathsf{K}\,\bar{C}_{\mathrm{d}}$ computed utilizing the analytical lower-bound in (4.14) is plotted in Fig. 4.5, against the number of underlay D2D links per cell, $p_{\mathrm{c}}\,\mathsf{K}$, for different values of a_{ex} and μ. As in Example 3.8, we set $\mathsf{a}_{\mathrm{d}} = 0.12$, $\beta = 0$, $\eta_{\mathrm{c}} = 3.5$ and $\eta_{\mathrm{d}} = 4.5$.

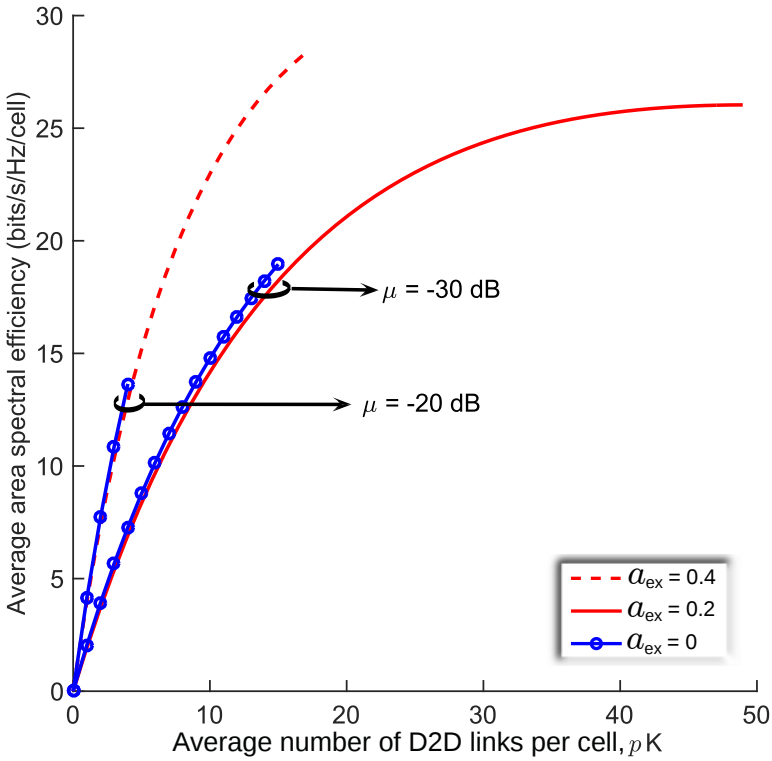

Figure 4.5: With $\nu = 0.8$, achievable average area spectral efficiency of the underlay D2D links with $\mathsf{a}_\mathrm{d} = 0.12$ and $\beta = 0$, parameterized by μ and a_{ex}.

4.2.6 Summary

Clearly, the exclusion regions alleviate the surge in D2D interference seen at the BS, as seen from the CDFs of C_c in Fig. 4.3. Note that this is at the expense of a sparser reuse of the available D2D links, thereby compromising the area spectral efficiency. All the same, for a given degradation of the average uplink performance (if that can be accepted), the exclusion regions allow packing more D2D links per cell, thereby achieving a higher area spectral efficiency, as evidenced by the results plotted in Fig. 4.5.

While the underlay D2D may seem less appealing due to the degradation engendered on the legacy cellular uplink, the emergence of massive MIMO BSs is expected to render it more manageable [29].

4.3 Overlay D2D with Exclusion Regions

4.3.1 Background

Recall the CDFs of spectral efficiency from Example 3.6 and the area spectral efficiency from Example 3.7. A significant share of D2D links has very low spectral efficiency due to close-by interferers; this is more pronounced when $\beta < 1/2$, i.e., when the desired link distance shrinks slower with the user density λ_d than the interferer link distances. Also, (with $\beta < 1/2$) the network progressively gets clogged with interference as λ_d increases (cf. Fig. 3.9).

Exclusion regions have been studied in the context of wireless ad-hoc networks [124–129], cognitive networks [130, 131] and D2D networks [32, 132–134]. The existing works on ad-hoc networks explore this possibility in terms of transmission capacity [124, 125], defined as the maximum permissible density of simultaneous transmissions that satisfies a target receiver SIR with a specified outage probability, or else in terms of interference statistics [126, 127]. In this chapter, instead, we focus on the ergodic spectral efficiency.

4.3.2 Network Geometry

The co-channel links are selected from a pool of available links such that there are no co-channel interferers within circular exclusion regions around each receiver. The locations of the available transmitters—recall—belongs to a homogeneous PPP $\Phi_d \subset \mathbb{R}^2$ of density λ_d, implying that on average there are λ_d available links per unit area. Each available transmitter has its intended receiver at a fixed distance $r_{d,0} = \mathsf{r}_d$, and at a random angle uniformly distributed in $[0, 2\pi)$.[1] The exclusion regions around the receivers have a radius $\delta \cdot \mathsf{r}_d$ where $\delta \geq 0$ is the ratio of the exclusion radius to the intended link length r_d.

The average number of co-channel links per unit area, denoted by $\tilde{\lambda}_d$, depends on the exclusion radius $\delta\,\mathsf{r}_d$ and on the type of channelization scheme as explained in the next section. The establishment of exclusion regions results in dependent thinning of the initial PPP Φ_d. Consequently, the locations of the co-channel transmitters no longer conform to a homogeneous PPP.

[1] Hereafter, the intended D2D link distance, defined as $r_{d,0} = \frac{\mathsf{r}_d}{K^{\beta}}$ in Chapter 3, is set independent of the link density with $\beta = 0$.

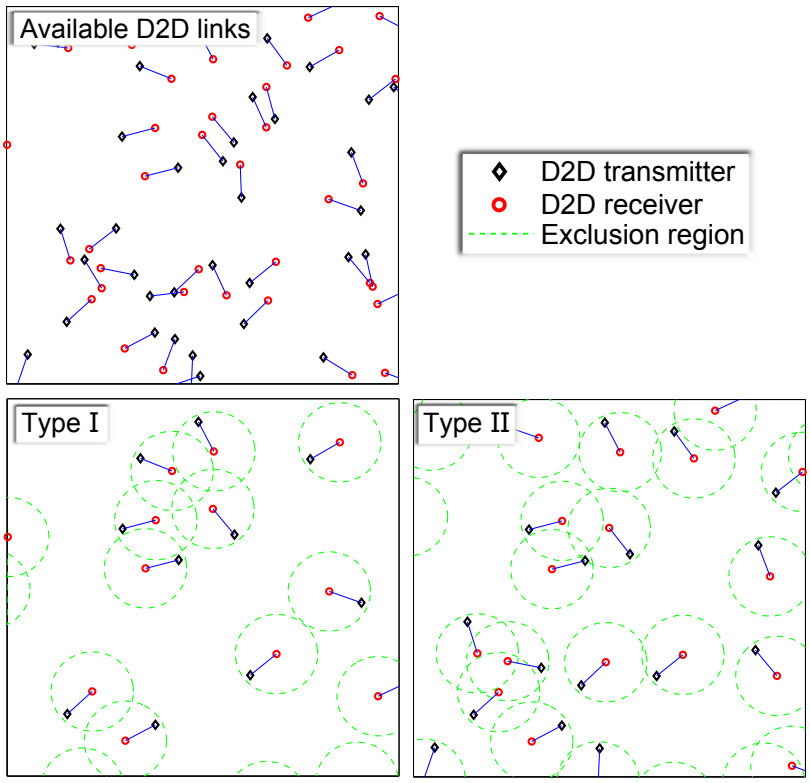

Figure 4.6: Co-channel links under type I and type II channelization schemes performed on the same pool of available links.

4.3.3 Channelization Schemes

To make the analysis as inclusive as possible, we consider two types of channelization schemes motivated by the Matérn hard core models type I and type II [135] commonly employed in the analysis of wireless ad-hoc networks [124, 125, 127, 133]. Though both types can achieve circular exclusion regions around the receivers as depicted in Fig. 4.6, for the same exclusion radius $\delta\, r_d$ they result in a different $\tilde{\lambda}_d$.

Type I

In type I, an available link is allowed on the channel under consideration only when there is no interfering transmitter present inside the circle of radius $\delta\, r_d$ centered at its receiver. The link is thus allowed with probability

$$p_d = e^{-\lambda_d \pi \delta^2 r_d^2},$$

which is the void probability of the PPP Φ_{d} (the probability that within a given area there exists no point of the PPP [41]) in the area $\pi\delta^2\mathsf{r}_{\mathrm{d}}^2$. Then, the average number of co-channel links per unit area becomes

$$\tilde{\lambda}_{\mathrm{d}} = \lambda_{\mathrm{d}}\, e^{-\lambda_{\mathrm{d}}\pi\delta^2\mathsf{r}_{\mathrm{d}}^2}, \tag{4.15}$$

which is unimodal in λ_{d}, i.e, it has only one maximum over any $\lambda_{\mathrm{d}} \in \mathbb{R}^+$. For a given δ, $\tilde{\lambda}_{\mathrm{d}} \to 0$ as $\lambda_{\mathrm{d}} \to \infty$. The maximum value of (4.15) is $\tilde{\lambda}_{\mathrm{d}} = \frac{1}{e\pi\delta^2\mathsf{r}_{\mathrm{d}}^2}$, achieved at $\lambda_{\mathrm{d}} = \frac{1}{\pi\delta^2\mathsf{r}_{\mathrm{d}}^2}$.

Type II

In type II, each available link is endowed with a random mark, uniformly distributed in $[0, 1]$, which may represent the time stamp or the priority of that link. An available link is allowed on the channel under consideration only when the following two conditions are met:

1. No transmitter with a lower mark is present inside a circle of radius $\delta\,\mathsf{r}_{\mathrm{d}}$ around the link receiver.
2. No receiver with a lower mark is present inside a circle of radius $\delta\,\mathsf{r}_{\mathrm{d}}$ around the link transmitter.

Inspired by existing work on scheduling/channelization for randomly distributed transceiver pairs [125, 127, 129, 133], we adopt the following approach to compute $\tilde{\lambda}_{\mathrm{d}}$: consider a link with mark m. Since the marks are uniformly distributed in $[0, 1]$, the density of links with a mark lower than m is $m\lambda_{\mathrm{d}}$ [41]. Condition 1 is based on the interfering transmitter locations relative to the given link, and Condition 2 is based on the interfered receiver locations, which also depend on the corresponding transmitter locations through the link distance r_{d}. Combining all that, we identify the transmitter locations that would violate Condition 2 and construct a resultant area, denoted by A_{II}, where no other transmitters must be present for both conditions to be satisfied.

Lemma 4.3. The resultant area is

$$A_{\mathrm{II}} = \pi\,\xi(\delta)\,\mathsf{r}_{\mathrm{d}}^2 \tag{4.16}$$

where

$$\xi(\delta) = \delta(\delta+1) - \frac{2}{\pi^2}\int_{|\delta-1|}^{\delta+1} r \arcsin^2\left(\frac{r^2+1-\delta^2}{2r}\right) \mathrm{d}r \tag{4.17}$$

Proof. See Appendix C.3. ■

The probability of allowing a link with random mark m is

$$p_{\mathrm{d}} = e^{-m\lambda_{\mathrm{d}} A_{\mathrm{II}}}$$

which is the void probability of a PPP [41] with density $m\lambda_{\mathrm{d}}$ in the area A_{II}. Then, the average number of co-channel links per unit area equals

$$\tilde{\lambda}_{\mathrm{d}} = \lambda_{\mathrm{d}} \int_0^1 e^{-m\lambda_{\mathrm{d}} A_{\mathrm{II}}} \mathrm{d}m \tag{4.18}$$

$$= \frac{1 - e^{-\lambda_{\mathrm{d}} \pi \xi(\delta) \mathsf{r}_{\mathrm{d}}^2}}{\pi\, \xi(\delta)\, \mathsf{r}_{\mathrm{d}}^2} \tag{4.19}$$

where (4.19) follows from integration via (4.16). As per (4.19), $\tilde{\lambda}_{\mathrm{d}}$ is monotonically increasing in $\lambda_{\mathrm{d}}\mathrm{L}$ and, as $\lambda_{\mathrm{d}} \to \infty$,

$$\tilde{\lambda}_{\mathrm{d}} \to \frac{1}{\pi\, \xi(\delta)\, \mathsf{r}_{\mathrm{d}}^2} \tag{4.20}$$

(Recall that, in contrast, in type I we observed that $\tilde{\lambda}_{\mathrm{d}} \to 0$ for $\lambda_{\mathrm{d}} \to \infty$.).

Next, we develop an analytical model to characterize the spectral efficiency of a given link in a system with exclusion regions of radius $\delta\, \mathsf{r}_{\mathrm{d}}$ and with the ensuing average number of co-channel links per unit area, $\tilde{\lambda}_{\mathrm{d}}$.

4.3.4 Interference Modeling

Local Distribution

Again, following the approach in Section (3.3.1), the distribution of z_{d}, conditioned on $\{r_{\mathrm{d},j}\}_{k=1}^{\infty}$, is modeled $z_{\mathrm{d}} \sim \mathcal{N}_{\mathbb{C}}(0, \sigma_{\mathrm{d}}^2)$ with

$$\sigma_{\mathrm{d}}^2 = \sum_{j=1}^{\infty} P_{\mathrm{d}}\, r_{\mathrm{d},j}^{-\eta_{\mathrm{d}}}. \tag{4.21}$$

Interferer Locations

As mentioned, the locations of the interfering transmitters do not conform to a PPP once exclusion regions are introduced. Even though the mean interference at the receiver could be computed exactly [126, 127], doing the same with the spectral efficiency appears

unwieldy. Thus, we approximate the interferer locations with the points of a PPP $\tilde{\Phi}_{\mathrm{d}}$ of density $\tilde{\lambda}_{\mathrm{d}}$ present outside $\mathcal{B}(0, \delta \mathsf{r}_{\mathrm{d}})$, an approach that has been successfully applied to obtain the distribution of instantaneous SIR [124, 125] and whose goodness for our purposes is validated later in the chapter.

Note that, with the PPP modeling of the locations, the additional step of introducing an averaging circle could be effected as in the previous cases, which we do not do in this context, as it does not aid the particular analysis that is presented next.

4.3.5 SIR

Applying the interference model, and recalling the intended signal term from (3.3), the instantaneous SIR enjoyed by the receiver at origin is

$$\mathsf{SIR}_{\mathrm{d}} = \rho_{\mathrm{d}} |H_{\mathrm{d},0}|^2 \tag{4.22}$$

with

$$\rho_{\mathrm{d}} = \frac{\mathsf{r}_{\mathrm{d}}^{-\eta_{\mathrm{d}}}}{\sum_{j=1}^{\infty} r_{\mathrm{d},j}^{-\eta_{\mathrm{d}}}} \tag{4.23}$$

being the local-average SIR at the intended receiver.

Local-Average SIR Distribution

Under the foregoing PPP approximation for the interferer locations, the distribution of the local-average SIR is characterized in the Laplace domain as follows.

Lemma 4.4. In overlay, with exclusion region radius $\delta \mathsf{r}_{\mathrm{d}}$ around each co-channel receiver, the CDF $F_{1/\rho_{\mathrm{d}}}(\cdot)$ in the Laplace domain is

$$\mathcal{L}_{F_{1/\rho_{\mathrm{d}}}}(\mathsf{s}) \approx \frac{1}{\mathsf{s}} e^{\pi \tilde{\lambda}_{\mathrm{d}} \mathsf{r}_{\mathrm{d}}^2 \left[\delta^2 + \mathsf{s}^{2/\eta_{\mathrm{d}}} \frac{2}{\eta_{\mathrm{d}}} \bar{\Gamma}(-2/\eta_{\mathrm{d}}, \mathsf{s}/\delta^{\eta_{\mathrm{d}}})\right]} \tag{4.24}$$

where $\tilde{\lambda}_{\mathrm{d}}$ depends on λ_{d} and δ as per (4.15) for type I and (4.19) for type II.

Proof. The result follows from the derivation of (2.38) in Example 2.7. ∎

Recall again, that $F_{\rho_{\mathrm{d}}}(\cdot)$ can be computed via the application of $\mathcal{L}_{F_{1/\rho_{\mathrm{d}}}}(\cdot)$ in Lemma 2.1.

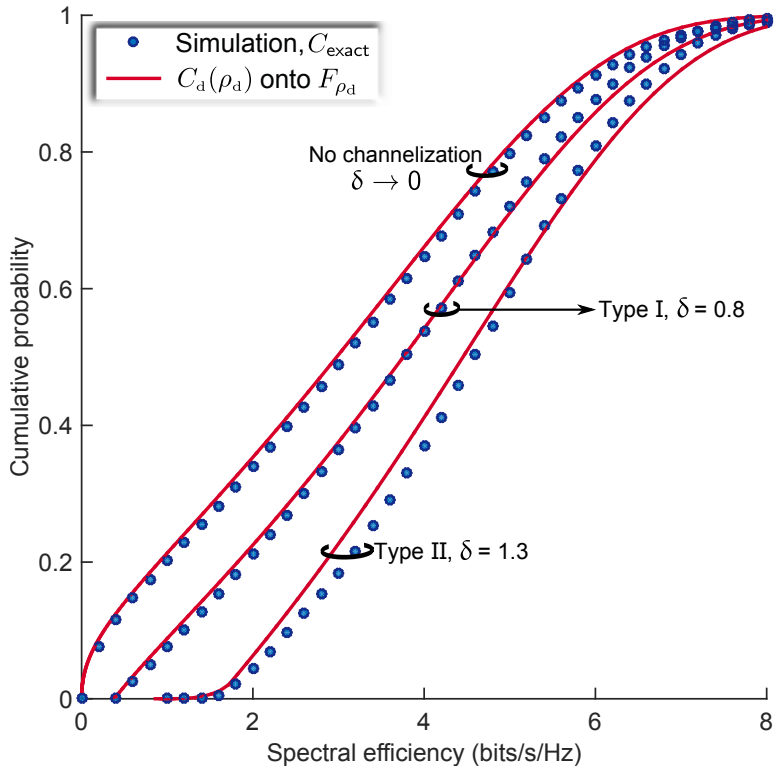

Figure 4.7: CDF of spectral efficiency for $\lambda_{\text{d}} = 40$ links/km^2, $\mathsf{r}_{\text{d}} = 40$ m and path loss exponent $\eta_{\text{d}} = 4.5$.

4.3.6 Ergodic Spectral Efficiency

Specific Network Geometry

Once again, recall that the ergodic spectral efficiency for given ρ_{d} is

$$C_{\text{d}}(\rho_{\text{d}}) = e^{1/\rho_{\text{d}}} E_1\left(\frac{1}{\rho_{\text{d}}}\right) \log_2 e. \tag{4.25}$$

Distribution over All Geometries

The CDF $F_{C_{\text{d}}}(\cdot)$ is evaluated via the mapping of $C_{\text{d}}(\rho_{\text{d}})$ onto $F_{\rho_{\text{d}}}(\cdot)$.

The following example validates the goodness of our interference model (Gaussian modeling of the local distribution and the Poisson approximation of the locations).

Example 4.4. Let $\lambda_{\text{d}} = 40$ links/km^2 with an intended link length of $\mathsf{r}_{\text{d}} = 40$ m and with a path loss exponent $\eta_{\text{d}} = 4.5$. In Fig. 4.7, the spectral efficiency CDFs obtained by mapping $C_{\text{d}}(\rho_{\text{d}})$ onto the $F_{\rho_{\text{d}}}(\cdot)$

computed via Lemma 2.1 are contrasted against their *exact* counterparts obtained via Monte-Carlo. Note that, C_{exact} is computed under the non-Gaussian interference (cf. Appendix A.1) and with the locations of the interferers realized exactly under the respective channelization schemes, without the Poisson approximation. Very good agreements are observed for type I with $\delta = 0.8$ and for type II with $\delta = 1.3$.

Similarly good agreements are observed for a variety of other settings, supporting our interference modeling approach.

Spatial Average

Next, let us average the D2D link spectral efficiency over all possible geometries.

Proposition 4.3. For given λ_{d} and δ, the D2D link spectral efficiency averaged over all network geometries is

$$\bar{C}_{\mathrm{d}}(\lambda_{\mathrm{d}}, \delta) \approx \log_2(e) \int_0^{\infty} \frac{1}{\gamma + 1} e^{\pi \tilde{\lambda}_{\mathrm{d}} \, \mathsf{r}_{\mathrm{d}}^2 \left[\delta^2 + \gamma^{2/\eta_{\mathrm{d}}} \frac{2}{\eta_{\mathrm{d}}} \bar{\Gamma}(-2/\eta_{\mathrm{d}}, \gamma/\delta^{\eta_{\mathrm{d}}})\right]} \mathrm{d}\gamma \tag{4.26}$$

where $\tilde{\lambda}_{\mathrm{d}}$ depends on λ and δ as per (4.15) for type I and (4.19) for type II.

Proof. The result follows from the application of $\mathcal{L}_{F_{1/\rho_{\mathrm{d}}}}(\cdot)$ from Lemma 4.4, in Lemma 2.2. ∎

For $\delta = 0$, i.e., when there is no channelization and all available links are co-channel, taking $\lim_{\delta \to 0} \bar{C}_{\mathrm{d}}(\lambda_{\mathrm{d}}, \delta)$ in (4.26) gives

$$\bar{C}_{\mathrm{d}}(\lambda_{\mathrm{d}}, 0) = \log_2(e) \int_0^{\infty} \frac{1}{\gamma + 1} \, e^{-\gamma^{2/\eta_{\mathrm{d}}} \, \pi \, \mathsf{r}_{\mathrm{d}}^2 \, \lambda_{\mathrm{d}} \, \Gamma\left(1 - \frac{2}{\eta_{\mathrm{d}}}\right)} \mathrm{d}\gamma \tag{4.27}$$

which conforms to the result in Prop. 3.6, with overlay $\varkappa = 0$, from the previous chapter. Also, note that the approximation becomes an equality in this case, as the actual interferer locations belong to the PPP Φ_{d}.

Simplified versions of Prop. 4.3 and (4.27) can be obtained by utilizing the approximation [136]

$$E_1(x) \approx 4\sqrt{2\pi} \, \mathsf{a}_{\bar{N}} \mathsf{a}_{\bar{M}} \sum_{n=1}^{\bar{N}+1} \sum_{i=1}^{\bar{M}+1} \sqrt{\mathsf{b}_n} e^{-4\mathsf{b}_n \mathsf{b}_i x} \tag{4.28}$$

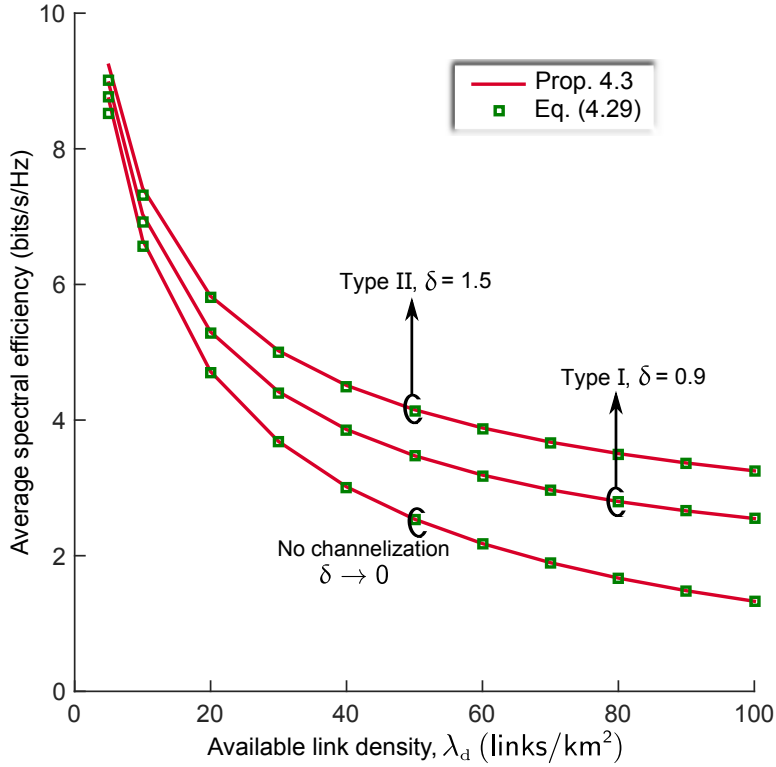

Figure 4.8: Average spectral efficiency as function of λ_{d} with $\mathsf{r}_{\mathrm{d}} = 40$ m and $\eta_{\mathrm{d}} = 4.5$.

where $\bar{N}$ and $\bar{M}$ are positive integers that control the accuracy while the coefficients $\mathsf{a}_{\bar{N}}$, $\mathsf{a}_{\bar{M}}$, b_n and b_i are computed as described in [136, Sec. II]. Plugging this approximation into (4.25) and averaging over all geometries via ρ_{d}, we obtain

$$\bar{C}_{\mathrm{d}}(\lambda_{\mathrm{d}}, \delta) \approx 4\sqrt{2}\pi\, \mathsf{a}_{\bar{N}} \mathsf{a}_{\bar{N}} \log_2(e) \sum_{n=1}^{\bar{N}+1} \sum_{i=1}^{\bar{M}+1} \sqrt{\mathsf{b}_n}$$
$$\cdot \exp\left\{ \pi \tilde{\lambda}_{\mathrm{d}}\, \mathsf{r}_{\mathrm{d}}^2 \left[\delta^2 + (4\mathsf{b}_n \mathsf{b}_i - 1)^{\frac{2}{\eta_{\mathrm{d}}}} \frac{2}{\eta_{\mathrm{d}}} \bar{\Gamma}\left(-\frac{2}{\eta_{\mathrm{d}}}, \frac{4\mathsf{b}_n \mathsf{b}_i - 1}{\delta^{\eta_{\mathrm{d}}}} \right) \right] \right\} \quad (4.29)$$

where we again recall that $\tilde{\lambda}_{\mathrm{d}}$ is a function of λ_{d} and δ, as given in (4.15) for type I and in (4.19) for type II. Similarly, for $\delta = 0$,

$$\bar{C}_{\mathrm{d}}(\lambda_{\mathrm{d}}, 0) \approx 4\sqrt{2}\pi\, \mathsf{a}_{\bar{N}} \mathsf{a}_{\bar{M}} \log_2(e)$$
$$\cdot \sum_{n=1}^{\bar{N}+1} \sum_{i=1}^{\bar{M}+1} \sqrt{\mathsf{b}_n}\, e^{-(4\mathsf{b}_n \mathsf{b}_i - 1)^{2/\eta_{\mathrm{d}}}\, \pi\, \mathsf{r}_{\mathrm{d}}^2\, \lambda_{\mathrm{d}}\, \Gamma\left(1 - \frac{2}{\eta_{\mathrm{d}}}\right)}. \quad (4.30)$$

These closed forms, validated next, shall come handy in further analyses.

Example 4.5. Fig. 4.8 compares the spatially averaged spectral efficiency in Prop. 4.3 with its approximation in (4.29), computed with $\bar{N} = \bar{M} = 50$. The average spectral efficiencies are plotted for the case of no channelization ($\delta = 0$), for type I channelization with $\delta = 0.9$ and for type II channelization with $\delta = 1.5$.

4.3.7 Area Spectral Efficiency

The average area spectral efficiency (in bits/s/Hz/unit area) is obtained by scaling the spatially averaged spectral efficiency by the average number of co-channel links per unit area, $\tilde{\lambda}_{\mathrm{d}}$, giving

$$\bar{\mathcal{C}}_{\mathrm{d}}(\lambda_{\mathrm{d}}, \delta) \approx \tilde{\lambda}_{\mathrm{d}} \log_2(e) \int_0^{\infty} \frac{1}{\gamma + 1} e^{\pi \tilde{\lambda}_{\mathrm{d}} \mathsf{r}_{\mathrm{d}}^2 \left[\delta^2 + \gamma^{2/\eta_{\mathrm{d}}} \frac{2}{\eta_{\mathrm{d}}} \bar{\Gamma}(-2/\eta_{\mathrm{d}}, \gamma/\delta^{\eta_{\mathrm{d}}})\right]} \mathrm{d}\gamma \tag{4.31}$$

where, once more, $\tilde{\lambda}_{\mathrm{d}}$ depends on λ_{d} and δ as per (4.15) for type I and (4.19) for type II.

4.3.8 Exclusion Region Size Optimization

To maximize the average area spectral efficiency for a given λ_{d}, the exclusion regions have to be optimally sized. This optimization returns

$$\bar{\mathcal{C}}_{\mathrm{d}}^{\star}(\lambda_{\mathrm{d}}) = \max_{\delta} \bar{\mathcal{C}}_{\mathrm{d}}(\lambda_{\mathrm{d}}, \delta) \tag{4.32}$$

and the argument that maximizes (4.32) is denoted by $\delta^{\star}(\lambda_{\mathrm{d}})$ while the value of $\tilde{\lambda}_{\mathrm{d}}$ that ensues is $\tilde{\lambda}_{\mathrm{d}}^{\star}(\lambda_{\mathrm{d}})$.

Example 4.6. Consider an overlay D2D network with $\mathsf{r}_{\mathrm{d}} = 40$ m and path loss exponent $\eta_{\mathrm{d}} = 4.5$. Figure 4.9 plots $\bar{\mathcal{C}}_{\mathrm{d}}^{\star}(\lambda_{\mathrm{d}})$ obtained numerically for both type I and type II channelizations. The figure also shows the average area spectral efficiency without channelization, $\bar{\mathcal{C}}_{\mathrm{d}}(\lambda_{\mathrm{d}}, 0)$. The $\delta^{\star}(\lambda_{\mathrm{d}})$ and $\tilde{\lambda}_{\mathrm{d}}^{\star}(\lambda_{\mathrm{d}})$ that indicate the correspondingly optimal exclusion size and average number of co-channel links per km^2 are respectively plotted in Figs. 4.10 and 4.11.

Example 4.6 has been repeated for other values of r_{d} and η_{d} to verify that the qualitative behavior does not change. This prompts the following observations:

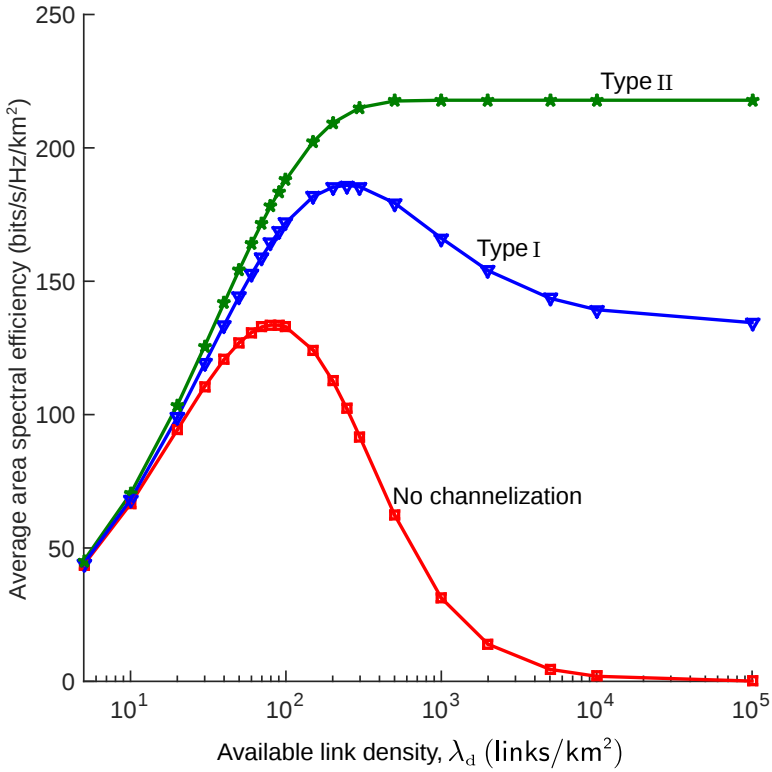

Figure 4.9: Average area spectral efficiency (bits/s/Hz/km^2) as function of λ_d, for $r_d = 40$ m and $\eta_d = 4.5$, with optimized δ.

- Both types of channelization dramatically outperform the no-channelization baseline in terms of the optimized area spectral efficiency, with type II markedly superior and monotonically improving in λ_d.

- The exclusion radius of type I diminishes with increasing λ_d, while type II maintains it at a value greater than the intended link distance, thereby protecting the links from close-by interferers.

- Though type I achieves higher $\tilde{\lambda}_d^\star(\lambda_d)$ than type II for many values of λ_d, it is inferior in terms of both link and area spectral efficiencies.

Next, we characterize the peak values of the optimized area spectral efficiency under both types of channelization.

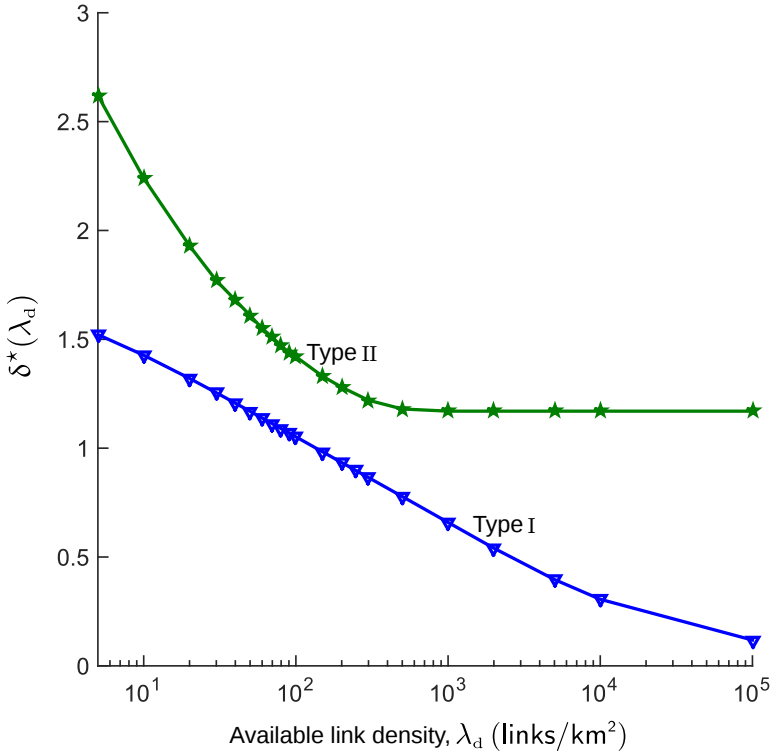

Figure 4.10: Optimum δ as function of λ_d for $r_d = 40$ m and $\eta_d = 4.5$.

Type I

In this case, the peak value of the optimized area spectral efficiency is

$$\bar{\mathcal{C}}_d^{\star\star} = \max_{\lambda_d,\delta} \bar{\mathcal{C}}_d(\lambda_d, \delta) \tag{4.33}$$

and the arguments that maximize (4.33) are denoted by $\lambda_d^\star$ and $\delta_I = \delta^\star(\lambda_d^\star)$. In light of the transmission-capacity findings in [124], we conjecture that

$$\lambda_d^\star = \frac{1}{\pi \delta_I^2 r_d^2}.$$

We further conjecture that δ_I is independent of the intended link distance r_d.

To validate these conjectures, we observe that $\bar{\mathcal{C}}_d(\lambda_d, \delta)$ is unimodal in both λ_d and δ and, utilizing the approximation in (4.29), we differentiate $\bar{\mathcal{C}}_d(\lambda_d, \delta)$ with respect to λ_d and δ for arbitrary r_d. Armed with the resulting expression we analytically verify that, indeed, for

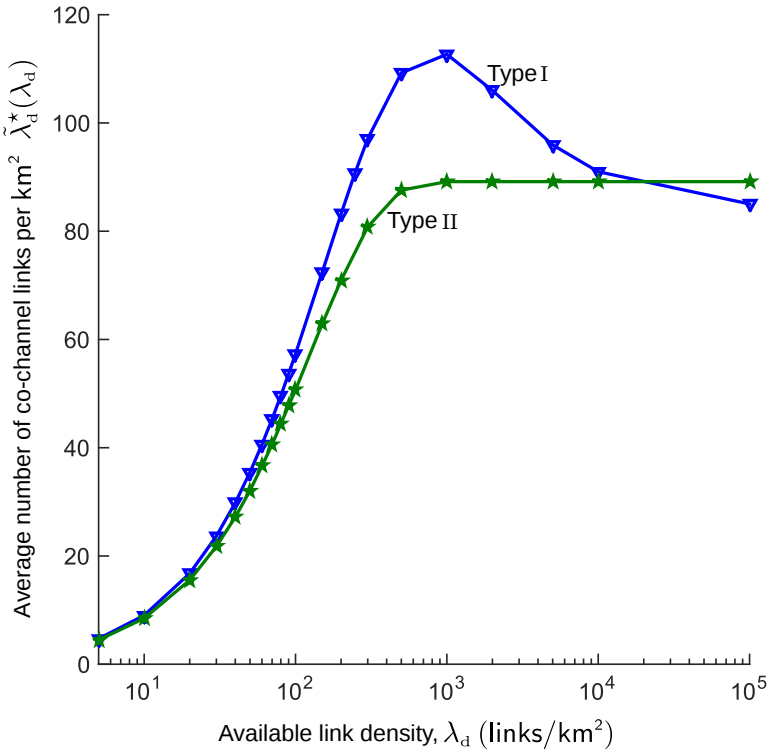

Figure 4.11: Average number of co-channel links per km^2 as function of λ_{d}, for $\mathsf{r}_{\mathrm{d}} = 40$ m and $\eta_{\mathrm{d}} = 4.5$, with optimized δ.

specific values of η_{d} and the corresponding δ_{I} obtained numerically,

$$\frac{\partial \bar{\mathcal{C}}_{\mathrm{d}}(\lambda_{\mathrm{d}}, \delta)}{\partial \lambda_{\mathrm{d}}}\Big|_{\delta=\delta_{\mathrm{I}}, \lambda_{\mathrm{d}}=\frac{1}{\pi \delta_{\mathrm{I}}^2 \mathsf{r}_{\mathrm{d}}^2}} \approx 0 \tag{4.34}$$

$$\frac{\partial \bar{\mathcal{C}}_{\mathrm{d}}(\lambda_{\mathrm{d}}, \delta)}{\partial \delta}\Big|_{\delta=\delta_{\mathrm{I}}, \lambda_{\mathrm{d}}=\frac{1}{\pi \delta_{\mathrm{I}}^2 \mathsf{r}_{\mathrm{d}}^2}} \approx 0 \tag{4.35}$$

where both zeroes are progressively approached as the accuracy of (4.29) is increased. For $\eta_{\mathrm{d}} = 4.5$ and $\bar{N} = \bar{M} = 50$, e.g., the derivatives are within $10^{-16}/\mathsf{r}_{\mathrm{d}}^2$ and $10^{-4}/\mathsf{r}_{\mathrm{d}}^2$ of zero, respectively.

Substituting $\delta = \delta_{\mathrm{I}}$ and

$$\lambda_{\mathrm{d}} = \frac{1}{\pi \delta_{\mathrm{I}}^2 \mathsf{r}_{\mathrm{d}}^2}$$

in (4.31), we can express the peak area spectral efficiency in the simple form

$$\bar{\mathcal{C}}_{\mathrm{d}}^{\star\star} = \frac{\kappa_{\mathrm{I}}(\eta_{\mathrm{d}})}{\mathsf{r}_{\mathrm{d}}^2} \tag{4.36}$$

Table 4.1: Typical values of δ_{I} and $\kappa_{\mathrm{I}}(\eta_{\mathrm{d}})$ for type I

η_{d}	δ_{I}	$\kappa_{\mathrm{I}}(\eta_{\mathrm{d}})$
3.8	0.8744	0.2282
4	0.8827	0.2482
4.5	0.8984	0.2976

where

$$\kappa_{\mathrm{I}}(\eta_{\mathrm{d}}) = \frac{\log_2(e)}{e\,\pi\,\delta_{\mathrm{I}}^2} \int_0^\infty \frac{1}{\gamma+1} e^{\frac{1}{e}\left[1+\frac{\gamma^{2/\eta_{\mathrm{d}}}}{\delta_{\mathrm{I}}^2}\frac{2}{\eta_{\mathrm{d}}}\bar{\Gamma}\left(-\frac{2}{\eta_{\mathrm{d}}},\frac{\gamma}{\delta_{\mathrm{I}}^{\eta_{\mathrm{d}}}}\right)\right]} \mathrm{d}\gamma \tag{4.37}$$

depends only on η_{d}. Values for δ_{I} and the corresponding $\kappa_{\mathrm{I}}(\eta_{\mathrm{d}})$ for path loss exponents spanning the entire range of interest for D2D are given in Table. 4.1.

Plugging $\delta = \delta_{\mathrm{I}}$ and

$$\lambda_{\mathrm{d}} = \frac{1}{\pi\delta_{\mathrm{I}}^2\mathsf{r}_{\mathrm{d}}^2}$$

into (4.15), the average number of co-channel links per unit area corresponding to the peak is obtained as

$$\tilde{\lambda}_{\mathrm{d}}^{\star}(\lambda_{\mathrm{d}}^{\star}) = \frac{1}{e\pi\delta_{\mathrm{I}}^2\mathsf{r}_{\mathrm{d}}^2}. \tag{4.38}$$

Thus, the average spectral efficiency at the peak of the optimized area spectral efficiency equals

$$\frac{\bar{\mathcal{C}}_{\mathrm{d}}^{\star\star}}{\tilde{\lambda}_{\mathrm{d}}^{\star}(\lambda_{\mathrm{d}}^{\star})} = e\,\pi\,\delta_{\mathrm{I}}^2\,\kappa_{\mathrm{I}}(\eta_{\mathrm{d}}) \tag{4.39}$$

which is independent of the link distance r_{d} and a function of only the path loss.

Another interesting observation is that the share of system area occupied by exclusion regions at the peak of the optimized area spectral efficiency equals, on average

$$\tilde{\lambda}_{\mathrm{d}}^{\star}(\lambda_{\mathrm{d}}^{\star})\,\pi\delta_{\mathrm{I}}^2\mathsf{r}_{\mathrm{d}}^2 = 1/e. \tag{4.40}$$

Type II

In the case of type II, the optimized area spectral efficiency is bounded but monotonically increasing and thus its peak value is

$$\bar{\mathcal{C}}_{\mathrm{d}}^{\star\star} = \max_{\delta} \lim_{\lambda_{\mathrm{d}}\to\infty} \bar{\mathcal{C}}_{\mathrm{d}}(\lambda_{\mathrm{d}},\delta) \tag{4.41}$$

where

$$\lim_{\lambda_{\mathrm{d}}\to\infty} \bar{\mathcal{C}}_{\mathrm{d}}(\lambda_{\mathrm{d}},\delta) = \frac{\log_2(e)}{\pi\,\xi(\delta)\,\mathsf{r}_{\mathrm{d}}^2}\int_0^\infty \frac{1}{\gamma+1}\, e^{\frac{1}{\xi(\delta)}\left[\delta^2+\gamma^{2/\eta_{\mathrm{d}}}\,\frac{2}{\eta_{\mathrm{d}}}\,\bar{\Gamma}\left(-\frac{2}{\eta_{\mathrm{d}}},\frac{\gamma}{\delta^{\eta_{\mathrm{d}}}}\right)\right]}\,\mathrm{d}\gamma \tag{4.42}$$

which follows from (4.26) and from the fact that

$$\tilde{\lambda}_{\mathrm{d}} \to \frac{1}{\pi\xi(\delta)\mathsf{r}_{\mathrm{d}}^2}$$

as $\lambda_{\mathrm{d}} \to \infty$. We again conjecture that the δ that solves (4.41) is independent of r_{d}, and denote it by $\delta_{\mathrm{II}} = \delta^\star(\infty)$.

Since we observe that (4.42) is unimodal in δ, for specific values of η_{d} and arbitrary r_{d} we verify analytically that the corresponding numerically obtained values of δ_{II} satisfy

$$\frac{\partial\bar{\mathcal{C}}_{\mathrm{d}}(\infty,\delta)}{\partial\delta}|_{\delta=\delta_{\mathrm{II}}} \approx 0. \tag{4.43}$$

The differentiation is performed utilizing (4.29) with

$$\tilde{\lambda}_{\mathrm{d}} = \frac{1}{\pi\,\xi(\delta)\,\mathsf{r}_{\mathrm{d}}^2}$$

and with the lower limit of the integral in (4.17) relaxed from $r = |\delta-1|$ to $r = \delta-1$ in light of the fact that $\delta_{\mathrm{II}} > 1$ for the entire range of path loss exponents relevant to D2D (cf. Table. 4.2). The left side of (4.43) approaches zero as the accuracy of (4.29) is increased. For $\eta_{\mathrm{d}} = 4.5$ and $\bar{N} = \bar{M} = 50$, e.g., zero is approached to within $10^{-5}/\mathsf{r}_{\mathrm{d}}^2$.

Rewriting (4.42) with $\delta = \delta_{\mathrm{II}}$, we can express $\bar{\mathcal{C}}_{\mathrm{d}}^{\star\star}$ as

$$\bar{\mathcal{C}}_{\mathrm{d}}^{\star\star} = \frac{\kappa_{\mathrm{II}}(\eta_{\mathrm{d}})}{\mathsf{r}_{\mathrm{d}}^2} \tag{4.44}$$

where

$$\kappa_{\mathrm{II}}(\eta_{\mathrm{d}}) = \frac{\log_2(e)}{\pi\,\xi(\delta_{\mathrm{II}})}\int_0^\infty \frac{1}{\gamma+1} e^{\frac{1}{\xi(\delta_{\mathrm{II}})}\left[\delta_{\mathrm{II}}^2+\gamma^{2/\eta_{\mathrm{d}}}\,\frac{2}{\eta_{\mathrm{d}}}\,\bar{\Gamma}\left(-\frac{2}{\eta_{\mathrm{d}}},\frac{\gamma}{\delta_{\mathrm{II}}^{\eta_{\mathrm{d}}}}\right)\right]}\,\mathrm{d}\gamma \tag{4.45}$$

which depends only on η_{d}. Values for δ_{II} and the corresponding $\kappa_{\mathrm{II}}(\eta_{\mathrm{d}})$ for typical path loss exponents are given in Table 4.2.

Table 4.2: Typical values of δ_{II} and $\kappa_{\text{II}}(\eta_{\text{d}})$ for type II

η_{d}	δ_{II}	$\kappa_{\text{II}}(\eta_{\text{d}})$
3.8	1.1455	0.2625
4	1.1556	0.2873
4.5	1.1738	0.3486

Letting $\lambda_{\text{d}} \to \infty$ and substituting $\delta = \delta_{\text{II}}$ in (4.19), we obtain the average number of co-channel links per unit area at the peak area spectral efficiency,

$$\tilde{\lambda}_{\text{d}}^{\star}(\infty) = \frac{1}{\pi\, \xi(\delta_{\text{II}})\, \mathsf{r}_{\text{d}}^2}.$$

Then, the average spectral efficiency corresponding to the peak area spectral efficiency can be expressed as

$$\frac{\bar{\mathcal{C}}_{\text{d}}^{\star\star}}{\tilde{\lambda}_{\text{d}}^{\star}(\infty)} = \pi\, \xi(\delta_{\text{II}})\, \kappa_{\text{II}}(\eta_{\text{d}}) \tag{4.46}$$

which, interestingly enough, is independent of the link length r_{d}. The share of system area occupied by the exclusion regions equals, on average,

$$\tilde{\lambda}_{\text{d}}^{\star}(\infty)\, \pi\, \delta_{\text{II}}^2\, \mathsf{r}_{\text{d}}^2 = \frac{\delta_{\text{II}}^2}{\xi(\delta_{\text{II}})}$$

which depends only on the path loss exponent.

Before wrapping up the chapter, let us take a look at how the individual D2D links perform with optimized exclusion region sizes, by contrasting the CDFs of spectral efficiency for the two channelization schemes, via a final example.

Example 4.7. Consider again a D2D network with $\mathsf{r}_{\text{d}} = 40$ m and path loss exponent $\eta_{\text{d}} = 4.5$, and let the available link density be

$$\lambda_{\text{d}} = \frac{1}{\pi \delta_{\text{I}}^2 \mathsf{r}_{\text{d}}^2} = 246.46 \text{ links/km}^2,$$

recalling—from Table 4.1—that $\delta_{\text{I}} = 0.8984$, i.e., the value corresponding to $\bar{\mathcal{C}}_{\text{d}}^{\star\star}$ in (4.33). Then, with the exclusion region size optimization as per (4.32), we have: (*i*) in type I, $\delta^{\star} = \delta_{\text{I}}$ and consequently $\tilde{\lambda}_{\text{d}}^{\star} = 90.67$ links/km^2; meanwhile (*ii*) in type II, $\delta^{\star} = 1.247$ and thereby $\tilde{\lambda}_{\text{d}}^{\star} = 76.32$ links/km^2. Under these settings, the CDFs of spectral efficiency, obtained by mapping $C_{\text{d}}(\rho_{\text{d}})$ onto the $F_{\rho_{\text{d}}}(\cdot)$ computed via Lemma 2.1, are plotted in Fig. 4.12.

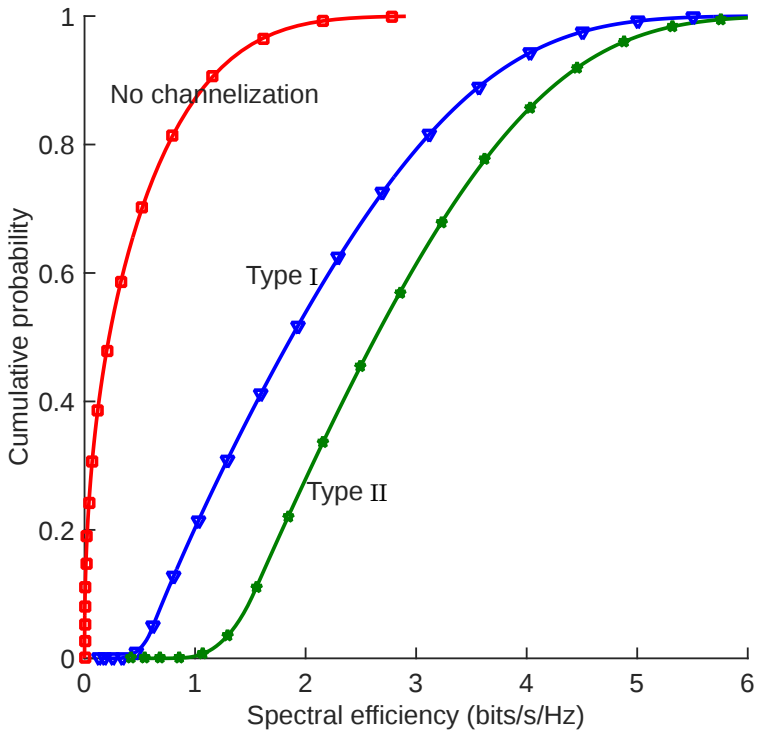

Figure 4.12: CDF of spectral efficiency for $\lambda_{\mathrm{d}} = 246.46$ links/km^2, $\mathsf{r}_{\mathrm{d}} = 40$ m, path loss exponent $\eta_{\mathrm{d}} = 4.5$ and optimized exclusion regions as per (4.32).

4.3.9 Summary

As evidenced by Fig. 3.4, without a careful channelization the performance of a D2D network progressively collapses—because of interference—once the link density exceeds a certain value that depends on the length of the links. With properly sized exclusion regions, though, this phenomenon is avoided. Although both types of channelization exhibit a satisfactory behavior in that respect, type II is able to find a markedly better tradeoff between the density of co-channel links and their individual spectral efficiencies. Conveniently, with type II the area spectral efficiency is monotonic in λ and thus there is no need to curb the system load at some fine-tuned value.

Compact forms for the optimum size of the exclusion regions and for the resulting area spectral efficiencies have been obtained as function of the key network parameters, facilitating intuition as to the effect of altering quantities such as the path loss exponent or the length of the links.

Chapter 5

Enclosed mmWave Wearable Networks

5.1 Background

In this chapter, we investigate the impact of reflections and blockages on the fundamental performance limits of enclosed mmWave wearable networks equipped with directional antennas, with emphasis on dense deployments.

Related work on this topic [85, 86, 100] employed propagation models that accounted for reflections in a coarse way, by fitting different path loss parameters for the LOS (line-of-sight) and the NLOS (non-line-of-sight) links. Although these existing models are more amenable to analysis, recognizing that the path loss parameter values reported by different indoor measurements vary significantly [137], we set out to pursue a different path by modeling reflections explicitly. The ensuing multipath propagation environment involving surface reflections is modeled via geometric optics, surface reflectivity and free space path loss, similar to the models in [93, 94].

As our propagation model incorporates reflections off interior surfaces, we account for the blockages in both direct and reflected propagation paths, building on the approach propounded by [85, 86], where human body blockages in direct links were modeled explicitly, but reflections were not. Based on measurements, [90] has indicated that the characteristics of mmWave indoor propagation that determine radio link performance are mainly dictated by the reflections off the superstructure—i.e., walls, ceiling, and floor—while details

such as tables and cabinets have only insignificant influence. Nevertheless, considering the crowded scenarios of our interest, we acknowledge that incorporating reflections off the human bodies [138] might be a necessary follow-up to our work.

A stochastic model for the body blockages in the direct propagation paths was devised in [86], based on the application of stochastic geometry and random shape theory, demonstrated earlier by [139, 140] for analyzing the building blockage effects in outdoor cellular networks. We adopt this stochastic blockage modeling approach and expand it by incorporating blockages in the reflected paths as well, so as to obtain results without the need to exhaustively test whether each individual link is blocked.

Eventually, our endeavor is to discern whether reflections are beneficial or detrimental and whether satisfactory performance is possible in relevant enclosed settings. We provide several examples of the performance of a reference transmitter-receiver pair in the network, taking the additional signal and interference contributions due to reflections into account, and considering the potential for directional beamforming. Based on these examples, we try to answer questions such as:

- How do surface reflectivity and signal blockages impact the performance?
- In denser environments, there are more sources of interference, but also more interference blockages. With surface reflections incorporated, what is the net effect?
- High-bandwidth mmWave applications result in increased noise levels. Is the performance limited by interference or by noise?
- How does the relative location, within the enclosed space, of the reference transmitter-receiver pair affect the performance?
- Do the reflections contribute enough useful signal for satisfactory operation in the absence of a strong direct signal path? If so, what range of beamforming gains are needed?

5.2 Network Modeling

Consider people within an enclosed space with reflective interior surfaces and no signal penetration from outside. Each individual wears

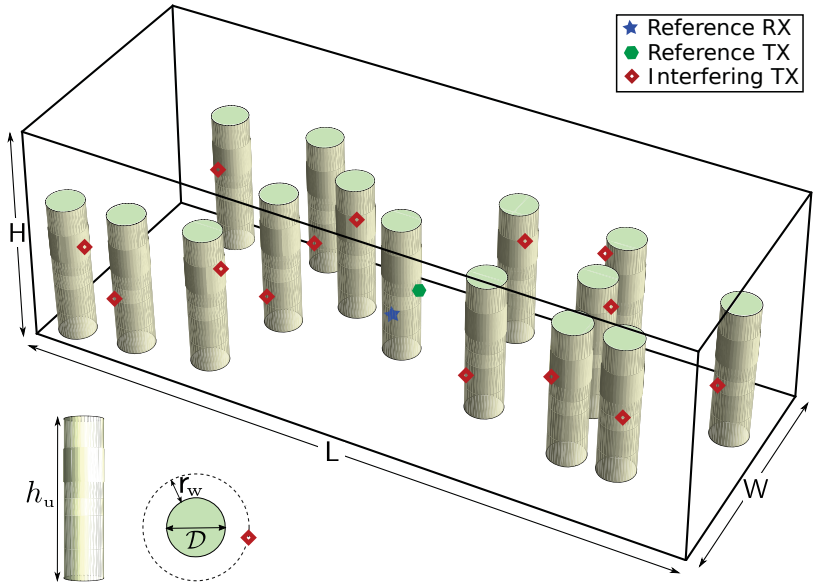

Figure 5.1: Co-channel wearable devices on people—modeled as circular cylinders of diameter $\mathcal{D}$ and height $h_u < \mathsf{H}$—within an enclosed space. Each wearable is located below height h_u and at a horizontal distance $r_w \geq 0$ from its body.

multiple communication devices and the intended transmissions are always between devices on a same person. Those transmissions are assumed to be orthogonal as they can be coordinated via a hub. Therefore, interfering transmissions are always from wearables on different people.

As indicated, we focus on a time-frequency channel occupied by a reference transmitter-receiver pair on a reference person. There are K other people on which the interfering transmitters reusing the same channel are located. Each person has one transmitter on the time-frequency channel under consideration.

5.2.1 Network Geometry

We consider an enclosed space shaped as an $\mathsf{L} \times \mathsf{W} \times \mathsf{H}$ cuboid (cf. Fig. 5.1) with people modeled as circular cylinders of diameter $\mathcal{D}$, height $h_u < \mathsf{H}$ and axis perpendicular to the floor. Each wearable is located below height h_u, at a perpendicular distance $\mathcal{D}/2 + r_w$ from the axis of its cylinder and with an azimuth orientation random in $[0, 2\pi)$. In effect, $r_w \geq 0$ is the distance of each wearable from its body. The reference receiver is located at X_0^r while the $K+1$ transmitters are located at $\{X_k\}_{k=0}^K$, with X_0 being the intended

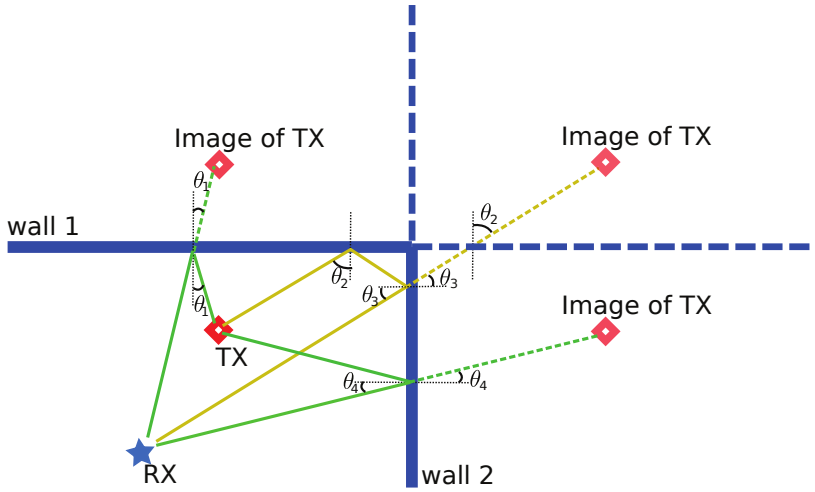

Figure 5.2: Reflected links from a transmitter to a receiver, off two walls. There are two first order reflections and one second order reflection.

(reference) transmitter. With L along the x-axis, W along the y-axis, H along the z-axis, and fixing the origin at the center of the enclosed space, let the coordinates of X_0^{r} and X_k be respectively $(\mathsf{x}_0^{\mathrm{r}}, \mathsf{y}_0^{\mathrm{r}}, \mathsf{z}_0^{\mathrm{r}})$ and $(\mathsf{x}_k, \mathsf{y}_k, \mathsf{z}_k)$, while the distance between X_0^{r} and X_k is $r_k = \|X_k - X_0^{\mathrm{r}}\|$.

5.2.2 Surface Reflections

The transmission from X_k reaches X_0^{r} via a direct propagation link and via reflections off the surfaces. To model these reflections, we need the lengths of the reflected links as well as the angles of incidence and the ensuing reflection coefficients.

Geometry of the Reflections

Adding extra (phantom) transmitters at the mirror image locations across each surface (cf. Fig. 5.2) facilitates the reflection modeling [141]. In this dissertation, we consider only first-order reflections, i.e., single bounces off each surface.[1] From each transmitter X_k there are six such reflections reaching X_0^{r}, which are incorporated by adding six phantom transmitters. The four walls are indexed with $i = 1, \ldots, 4$, the ceiling with $i = 5$, and the floor with $i = 6$. For

[1] We have numerically verified that higher-order reflections, which can be incorporated by placing phantom transmitters at the corresponding image locations (cf. Fig. 5.2), have a minor effect on the results.

$i = 1, \ldots, 6$, the images of X_k are located at $X_{i,k}$, the corresponding angles of incidence are $\theta_{i,k}$, and the reflected link distances are $r_{i,k} = \|X_{i,k} - X_0^{\mathrm{r}}\|$. The coordinates of the image locations and the angles of incidence can be easily obtained as functions of the coordinates of X_k and X_0^{r}, as detailed in Appendix D.1.

Note that the links emanating from $\{X_{i,0}\}_{i=1}^{6}$ correspond to the reflections of the intended transmission from X_0. While the intended transmission has a direct *on-body* link and six reflected *off-body* links, all the interfering links (both direct and reflected) are off-body.

Reflection Coefficient

The reflectivity of a surface depends on the properties of the material, the angle of incidence, and the polarization of the incident wave. We apply the model in [142], which provides reflection coefficients $\Gamma_\perp$ and $\Gamma_\parallel$ for a homogeneous dielectric plate with a smooth surface, thickness Δ and complex refractive index n.

These coefficients are

$$\Gamma_\ell = \frac{1 - e^{-\mathrm{j}\,2\,\delta}}{1 - \gamma_\ell^2\, e^{-\mathrm{j}\,2\,\delta}}\,\gamma_\ell \qquad \ell \in \{\perp, \parallel\} \tag{5.1}$$

with

$$\begin{aligned} \delta &= \frac{2\pi\Delta}{\lambda}\sqrt{n^2 - \sin^2\theta} \\ \gamma_\perp &= \frac{\cos\theta - \sqrt{n^2 - \sin^2\theta}}{\cos\theta + \sqrt{n^2 - \sin^2\theta}} \\ \gamma_\parallel &= \frac{n\cos\theta - \sqrt{n^2 - \sin^2\theta}}{n\cos\theta + \sqrt{n^2 - \sin^2\theta}} \end{aligned} \tag{5.2}$$

where λ is the wavelength and θ is the angle of incidence. The coefficients $\Gamma_\perp$ and $\Gamma_\parallel$ relate the reflected and incident electric fields when the polarization is respectively perpendicular and parallel to the plane of incidence (defined as the plane containing the incident and reflected rays and the surface normal).

According to the Rayleigh criterion [88], the shorter wavelength of mmWave signals renders surfaces *rougher* than at microwave frequencies. While many indoor surfaces might still be deemed smooth, the effect of roughness—when it is significant—features as an extra

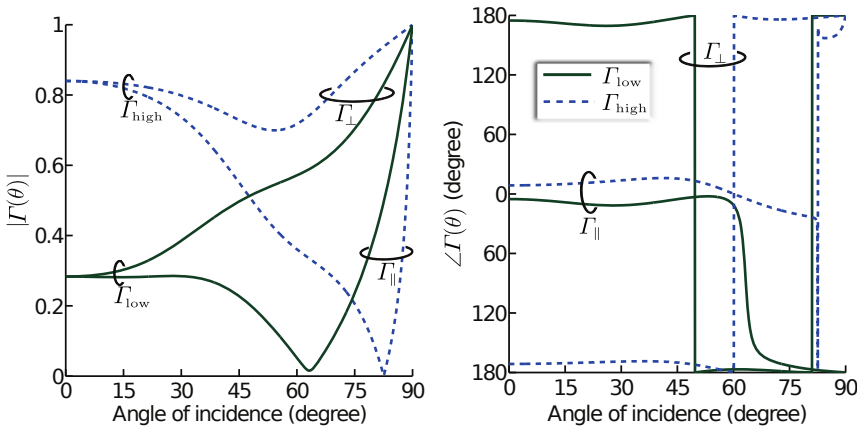

(a) Magnitude (b) Phase

Figure 5.3: Low (Γ_{low}) and high (Γ_{high}) reflection coefficients as functions of the angle of incidence.

loss factor in the reflection coefficient, which can either be modeled based on the standard deviation of surface roughness or be incorporated implicitly when the reflectivity is measured [88–90]. Importantly, at mmWave frequencies, the ensuing diffuse scattering off rough surfaces has been observed to not contribute significantly to the total received power, such that the propagation remains effectively specular [88–90].

The following example presents two extreme reflectivity settings, low reflectivity (Γ_{low}) and high reflectivity (Γ_{high}), which will be employed throughout the paper to gauge the impact of surface reflectivity on the performance.

Example 5.1. Fig. 5.3 depicts the reflection coefficients at 60 GHz (i.e., $\lambda = 5\,\text{mm}$) obtained with the following values of Δ and n:

1. Low reflectivity (Γ_{low}): $\Delta = 8.8\,\text{mm}$ and $n = 7.62 - \text{j}\,0.02$
2. High reflectivity (Γ_{high}): $\Delta = 14.2\,\text{mm}$ and $n = 1.85 - \text{j}\,0.086$

To account for the random orientation of the wearables, the polarization of the electric field is regarded as random. The direction of the electric field vector—perpendicular to the direction of propagation by definition—in each propagation path from X_k is abstracted by an angle (cf. Appendix D.2), which is denoted by α_k for the

direct path and by $\alpha_{i,k}$ for the ith reflected path. Let us define the corresponding polarization unit vectors

$$\boldsymbol{p}_k = [\cos\alpha_k \quad \sin\alpha_k]^{\mathrm{T}} \tag{5.3}$$

$$\boldsymbol{p}_{i,k} = [\cos\alpha_{i,k} \quad \sin\alpha_{i,k}]^{\mathrm{T}} \tag{5.4}$$

which shall come handy later, in expressing the propagation model in Section 5.4. Upon reflection on a surface, the field is projected with reference to the plane of incidence, the appropriate reflection coefficient ($\Gamma_{\parallel}$ or $\Gamma_{\perp}$) is applied to each projected component, and the field is subsequently reconstructed [93, 94]. Specifically, assuming that all surfaces have the same Δ and n, the horizontally and vertically polarized components of each transmission are respectively subject to $\Gamma_{\parallel}$ and $\Gamma_{\perp}$ when bouncing off walls ($i = 1, \ldots, 4$), and vice versa when bouncing off ceiling or floor ($i = 5, 6$). Correspondingly, we define the reflection coefficient matrix

$$\boldsymbol{\Gamma}_{i,k} = \begin{cases} \boldsymbol{\Gamma}(\theta_{i,k}) & i = 1, \ldots, 4 \\ \boldsymbol{\Gamma}^{\mathrm{T}}(\theta_{i,k}) & i = 5, 6 \end{cases} \tag{5.5}$$

with

$$\boldsymbol{\Gamma}(\theta) = \begin{bmatrix} \Gamma_{\parallel}(\theta) & 0 \\ 0 & \Gamma_{\perp}(\theta) \end{bmatrix},$$

also to be applied in the expressions in Section 5.4. Readers interested in further details on how reflections affect polarization are referred to [143].

5.2.3 Body Blockages

The links—both direct and reflected—among the wearables can get blocked by people's bodies. Since the reflections are modeled explicitly, and the penetration losses at mmWave frequencies are very high (typically in excess of 40 dB) we assume that no signal traverses such blockages. The blocking of the direct link from X_k is indicated by a binary variable β_k, which equals 1 if unblocked and 0 if blocked. Likewise, the blocking of the link from X_k reflected off the ith surface is indicated by another binary variable $\beta_{i,k}$.

Interference Path

The direct interference path between X_k and X_0^{r} is blocked if it cuts through any of the cylinders. Such blockages include self-body blockages [98], i.e., the link between X_k and X_0^{r} can get blocked

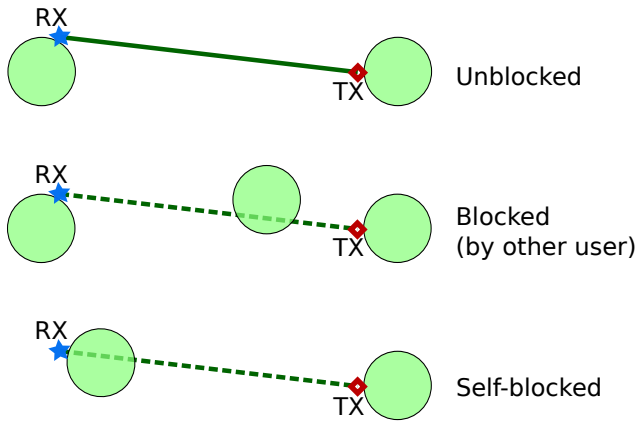

Figure 5.4: Illustrations of unblocked and blocked propagation paths; a path is blocked when a circle—projection of a cylinder onto the horizontal plane ($\mathcal{X}_0$) containing RX—gets intersected by the it.

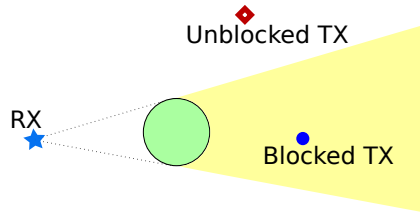

Figure 5.5: A cone shaped blockage zone (shaded), formed by a circular blockage, from the vantage of the receiver (RX); transmitters (TX) falling inside such blockage zone are blocked.

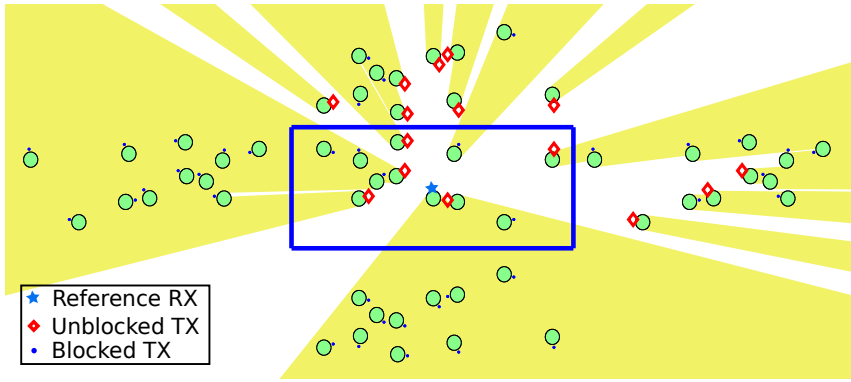

Figure 5.6: An instance of the interferers (unblocked/blocked) to the reference receiver located at the center of $\mathcal{X}_0$. The phantom transmitters across each wall correspond to the reflections while the blockage regions caused by the circles (people's bodies) are the shaded areas.

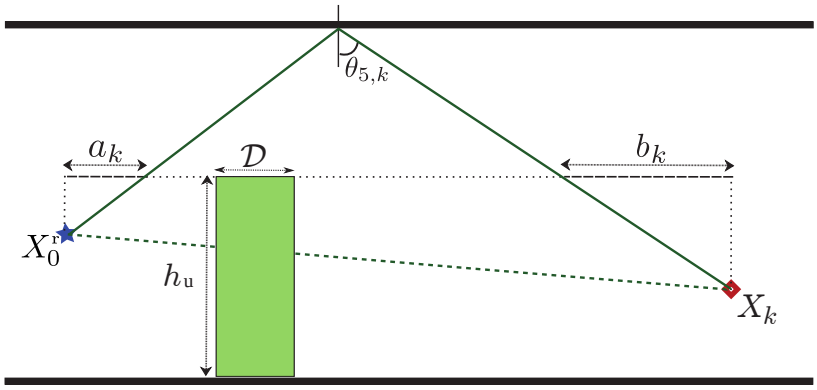

Figure 5.7: Ceiling-reflected link from transmitter X_k to receiver X_0^{r}. Bodies within the horizontal distances a_k and b_k block the ceiling reflection.

by the people on which transmitter or receiver are located. Since everybody has the same height h_{u} and the wearables are located below that height, the blockages in the direct interfering links are independent of the heights of the wearable locations. Therefore, the blockages can be determined from the projections of the wearable locations and the cylinders onto the horizontal plane, which we denote by $\boldsymbol{\mathcal{X}}_0$, that contains X_0^{r}. Noting that the projections of the cylinders are circles on $\boldsymbol{\mathcal{X}}_0$, we denote the projection of X_k by X_k'. Then, the blockages are determined by checking whether the direct path between X_k' and X_0^{r} intersects any of the circles (cf. Fig. 5.4), which, as propounded in [85, 86, 144], can be effected via finding the transmitters falling inside cone shaped blockage zones formed by circular blockages from the vantage of the reference receiver (cf. Fig. 5.5). Applied to the corresponding phantom transmitters, this blockage model further extends to the reflected links off the four walls and an algorithm for determining such blockages is given in Appendix D.3. An instance of the (unblocked/blocked) interferers to the reference receiver located at the center of $\boldsymbol{\mathcal{X}}_0$ is depicted Fig. 5.6, where the phantom transmitters across each wall correspond to the reflections and the transmitters which fall in the shaded blockage regions are blocked.

Given the gap between the ceiling and people's heads, a ceiling reflection is blocked only if someone is close enough to the transmitter or receiver, specifically closer than

$$a_k = (h_{\mathrm{u}} - \mathsf{H}/2 - \mathsf{z}_0^{\mathrm{r}}) \tan\theta_{5,k} \tag{5.6}$$

from the receiver at X_0^{r} or closer than

$$b_k = (h_{\mathrm{u}} - \mathsf{H}/2 - \mathsf{z}_k)\, \tan\theta_{5,k} \tag{5.7}$$

from the transmitter at X_k' (cf. Fig. 5.7). Further details on how to determine the ceiling blockages are given in Appendix D.3.

Since bodies touch the floor, each reflection off the floor gets blocked only if the corresponding direct path is blocked, i.e., $\beta_{6,k} = \beta_k$.

Intended Signal Path

The foregoing blockage model for the wall reflections is applicable to all the off-body links, including the wall-reflected paths of the intended transmission from X_0. The coefficients $\beta_{i,0}$, for $i = 1, \ldots, 4$, are determined via the algorithm in Appendix D.3.

As for the on-body intended link, since it is between wearables on the same individual, it should have an independent blockage/shadowing model. In the absence of a good model for on-body shadowing, we consider specific values for β_0 in the range $[0, 1]$. Two values of special interest are: (*unblocked on-body link*) $\beta_0 = 1$ and (*blocked on-body link*) $\beta_0 = 0$. When the on-body link is blocked, transmission from X_0 reaches X_0^{r} only via the reflected links.

The intended signal reflections off the ceiling and the floor are assumed to be unblocked ($\beta_{5,0} = \beta_{6,0} = 1$). A possible future refinement for $\beta_{5,0}$ and $\beta_{6,0}$ would be to model them based on specific wearable applications.

5.3 Antenna Arrays

Devices operating at mmWave frequencies are expected to incorporate polarization-diverse antennas so as to circumvent polarization mismatch losses; this is in fact rather critical given the limited scattering, and thus the reduced depolarization, experienced at these frequencies [145–147]. We therefore postulate that polarization diversity is in place, providing immunity from polarization mismatch losses. The antennas most likely to be featured by wearables are patches, dual-polarized versions of which have been implemented lately [148, 149]. An array of such patches produces a beam that can be steered by physically titling the array or else through beamforming coefficients. We model this beam as having rotational symmetry with two defining parameters: the main-lobe gain, G, and its

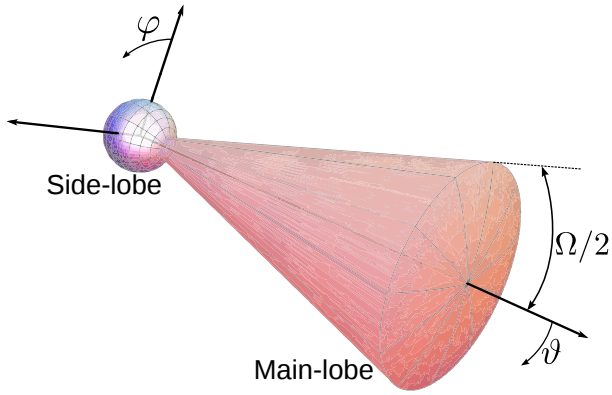

Figure 5.8: Antenna gain pattern, rotationally symmetric about the broadside direction.

beamwidth, Ω (cf. Fig. 5.8). Expressed as a function of ϑ (off the beam axis) and φ (on the plane perpendicular to the beam axis),

$$\mathcal{G}(\vartheta,\varphi) = \begin{cases} \mathsf{G} & 0 \le \vartheta \le \Omega/2,\ 0 \le \varphi < 2\pi \\ \mathsf{g} & \Omega/2 < \vartheta \le \pi,\ 0 \le \varphi < 2\pi \end{cases} \tag{5.8}$$

with g the side-lobe gain and with

$$\int_0^{2\pi}\int_0^{\pi} \mathcal{G}(\vartheta,\varphi)\,\frac{\sin\vartheta}{4\pi}\,\mathrm{d}\vartheta\,\mathrm{d}\varphi = 1 \tag{5.9}$$

to ensure that the total radiated power is preserved [150]. While simple, (5.8) captures the key features very effectively, approximating well the pattern of an N-element uniform planar square array (UPA), i.e., a $(\sqrt{\mathsf{N}} \times \sqrt{\mathsf{N}})$ UPA with main-lobe gain $\mathsf{G} = \mathsf{N}$ and beamwidth $\Omega = \sqrt{3/\mathsf{N}}$, and consequently with

$$\mathsf{g} = \mathsf{N} + (1-\mathsf{N})\,\sec^2\!\left(\sqrt{3/\mathsf{N}}/4\right). \tag{5.10}$$

Example 5.2. Listed in Table 5.1 are the antenna array parameters for different values of N that are used in later examples in this paper. Note that $\mathsf{N} = 1$ corresponds to omnidirectional antennas.

To incorporate the transmit and receive antenna gains to the propagation from transmitter X_k to the reference receiver X_0^{r} via the direct and the reflected paths, we introduce (i) the transmit antenna gains $\mathcal{G}_k^{\mathrm{t}}$ and $\mathcal{G}_{i,k}^{\mathrm{t}}$, respectively from X_k and $X_{i,k}$ in the direction of X_0^{r}, and (ii) the receive antenna gains $\mathcal{G}_k^{\mathrm{r}}$ and $\mathcal{G}_{i,k}^{\mathrm{r}}$, respectively in the direction of X_k and $X_{i,k}$.

Table 5.1: Array Settings

N	G (dBi)	g (dBi)	Ω
1	0	0	
4	6	-0.68	49.6°
9	9.54	-0.80	33°
16	12	-0.85	24.6°

By virtue of the rotationally symmetric pattern, the receive antenna gains can be obtained by evaluating (5.8) for ϑ equal to the angle between the main-lobe direction of X_0^{r} and the orientation of the transmitter relative to X_0^{r}. Similarly, the transmit antenna gains can be determined by evaluating (5.8) for ϑ equal to the angle between the main-lobe direction of transmitter and the orientation of X_0^{r} relative to the transmitter. We specify the main-lobe directions of the wearables with the azimuth and the elevation angles with respect to the x, y and z axes as defined in Section 5.2.1: the main-lobe of X_0^{r} is directed at azimuth ψ_0^{a} and elevation ψ_0^{e}, while X_k has its main-lobe directed at azimuth ψ_k^{a} and elevation ψ_k^{e}.

Further details on the determination of the gain parameters and the main-lobe directions of the phantom transmitters are given in Appendix B.5.

5.4 Propagation Model

All transmissions have (fixed) power P and each wearable is assumed to have its main-lobe oriented towards its intended signal link (direct on-body or reflected off-body).

5.4.1 Intended Signal Power

The signal power received at X_0^{r} from X_0 is $P\,G_0$, with the large-scale gain modeled as

$$G_0 = \left(\frac{\lambda}{4\pi}\right)^2 \left\| \beta_0 \frac{\sqrt{\mathcal{G}_0^{\mathrm{r}}\,\mathcal{G}_0^{\mathrm{t}}}}{r_0} \boldsymbol{p}_0 + \sum_{i=1}^{6} \beta_{i,0} \frac{\sqrt{\mathcal{G}_{i,0}^{\mathrm{r}}\,\mathcal{G}_{i,0}^{\mathrm{t}}}}{r_{i,0}} e^{-\mathrm{j}\,\Delta\phi_{i,0}}\, \boldsymbol{\Gamma}_{i,0}\, \boldsymbol{p}_{i,0} \right\|^2 \tag{5.11}$$

where $\Delta\phi_{i,0} = 2\pi(r_{i,0} - r_0)/\lambda$ is the phase difference between the direct link and the ith reflected link. Given the locations X_0^{r} and

X_0, their respective main-lobe directions ($\{\psi_0^{\mathrm{a}}, \psi_0^{\mathrm{e}}\}$ and $\{\psi_0^{\mathrm{a}}, \psi_0^{\mathrm{e}}\}$) and subsequently all the antenna gain parameters in (5.11) become determined (cf. Appendix B.5).

Recall that the vectors $\boldsymbol{p}_0$ and $\boldsymbol{p}_{i,0}$, respectively given in (5.3) and (5.4), abstract the polarization, while the reflection coefficient matrix $\boldsymbol{\Gamma}_{i,0}$ is determined via (5.5). Also recall, from Section 5.2.3, that the blocking coefficient β_0 is specified independently of the relative locations of the wearables while $\{\beta_{i,0}\}_{i=1}^4$ are determined as per the algorithm in Appendix D.3 and $\beta_{5,0} = \beta_{6,0} = 1$.

5.4.2 Interference Power

The interference power received at X_0^{r} from X_k, for $k = 1, \ldots, K$, is $P\, G_k$ with the large-scale gain modeled as

$$G_k = \left(\frac{\lambda}{4\pi}\right)^2 \left\| \beta_k \frac{\sqrt{\mathcal{G}_k^{\mathrm{r}}\, \mathcal{G}_k^{\mathrm{t}}}}{r_k} \boldsymbol{p}_k + \sum_{i=1}^{6} \beta_{i,k} \frac{\sqrt{\mathcal{G}_{i,k}^{\mathrm{r}}\, \mathcal{G}_{i,k}^{\mathrm{t}}}}{r_{i,k}} e^{-\mathrm{j}\,\Delta\phi_{i,k}}\, \boldsymbol{\Gamma}_{i,k}\, \boldsymbol{p}_{i,k} \right\|^2 \tag{5.12}$$

where $\Delta\phi_{i,k} = 2\pi(r_{i,k} - r_k)/\lambda$ is the phase difference between the direct and the ith reflected links. Given the locations X_k and X_0^{r}, and the receiver main-lobe direction $\{\psi_0^{\mathrm{a}}, \psi_0^{\mathrm{e}}\}$, the receive antenna gains in (5.12) are determined, as detailed in Appendix B.5. The transmit antenna gains depend on the main-lobe direction of X_k, which is assumed to be uniformly distributed, i.e., ψ_k^{a} is uniform in $[0, 2\pi)$, and ψ_k^{e} is distributed with PDF (probability density function) [151]

$$f_{\psi_k^{\mathrm{e}}}(\nu) = \frac{\sin \nu}{2} \qquad 0 \le \nu \le \pi. \tag{5.13}$$

Again, recall that $\boldsymbol{p}_k$, $\boldsymbol{p}_{i,k}$ and $\boldsymbol{\Gamma}_{i,k}$ are respectively as given in (5.3), (5.4) and (5.5), while β_k and $\{\beta_{i,k}\}_{i=0}^5$ are determined as per Appendix D.3 and $\beta_{6,k} = \beta_k$.

5.5 SINR

On account of the minimal fading at mmWave frequencies, we disregard the small-scale effects and model the SINR seen at the reference receiver as

$$\mathsf{SINR} = \frac{G_0}{\sum_{k=1}^{K} G_k + \sigma_{\mathrm{N}}^2/P} \tag{5.14}$$

where the AWGN power $\sigma_{\mathrm{N}}^2 = F_{\mathrm{N}} N_0 B$, with F_{N} the receiver noise figure, N_0 the noise power spectral density and B the bandwidth.

For a specific network geometry (i.e., given the positions of people and wearables) and specific orientations and polarization angles, SINR in (5.14) becomes determined. A randomized network geometry and a distribution for the orientation of people and the polarization angles induce a distribution for SINR. In the next section, we introduce a random network geometry model—specified by the distribution of wearables and blockages within the enclosure—and stochastically model the concomitant propagation parameters so as to simplify the computation of the SINR distribution.

5.6 Stochastic Modeling

Stochastic geometry analyses of unbounded wireless networks, modeled via appropriate point processes—recall from Section 2.7—are usually conducted from the perspective of the typical receiver (randomly chosen and held fixed), over all possible network geometries. Differently, for the finite-size space under consideration, we evaluate the performance of a reference link with given receiver location X_0^{r}, when the interfering transmitters $\{X_k\}_{k=1}^K$ and the blockages (people) are distributed randomly. Such an evaluation is arguably more informative than a complete averaging over all possible locations of the reference link, as the performance does depend on such location: a link in the center of the space, for instance, will generally perform differently than a link near one of the corners.

5.6.1 Random Network Geometry

The reference individual, represented by the corresponding circle on $\boldsymbol{\mathcal{X}}_0$, has its center $\mathcal{D}/2 + \mathsf{r}_{\mathrm{w}}$ away from X_0^{r} with a uniformly random orientation in $[0, 2\pi)$. The corresponding transmitter X_0 is another wearable on the reference individual at a distance r_0 away from X_0^{r}. The coordinates of X_0 are

$$\begin{aligned} \mathsf{x}_0 &= \mathsf{x}_0^{\mathrm{r}} + r_0 \sin\varsigma_0^e \cos\varsigma_0^a \\ \mathsf{y}_0 &= \mathsf{y}_0^{\mathrm{r}} + r_0 \sin\varsigma_0^e \sin\varsigma_0^a \\ \mathsf{z}_0 &= \mathsf{z}_0^{\mathrm{r}} + r_0 \cos\varsigma_0^e \end{aligned} \tag{5.15}$$

where $\varsigma_0^a \in [0, 2\pi)$ and ς_0^e has the PDF

$$f_{\varsigma_0^e}(\nu) = \frac{\sin\nu}{2} \qquad 0 \le \nu \le \pi \tag{5.16}$$

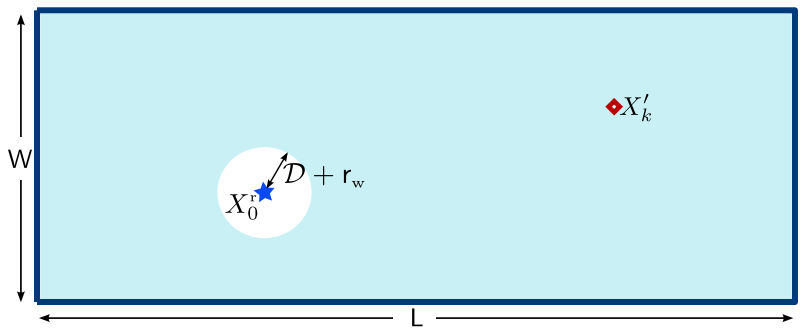

Figure 5.9: The horizontal plane $\boldsymbol{\mathcal{X}}_0$ containing the reference receiver X_0^r. Projections of the interfering wearables $\{X'_k\}$ are assumed to be distributed independently and uniformly within the shaded area.

meaning that the direction of X_0 from X_0^r is uniformly distributed.

The interfering wearables, $\{X_k\}_{k=1}^K$, are distributed independently as follows. Each projection X'_k, specified by the coordinates x_k and y_k, is uniformly distributed on $\boldsymbol{\mathcal{X}}_0$ excluding a circular region centered at X_0^r with area $\mathsf{A} = \pi(\mathcal{D} + \mathsf{r}_\mathrm{w})^2$ (cf. Fig. 5.9).[2] As the center of $\boldsymbol{\mathcal{X}}_0$ is at $(0, 0, \mathsf{z}_0^\mathrm{r})$, the joint PDF of x_k and y_k is

$$f_{\mathsf{x}_k,\mathsf{y}_k}(\mathsf{x},\mathsf{y}) = \frac{1}{\mathsf{L}\,\mathsf{W} - \mathsf{A}} \qquad \begin{array}{l} |\mathsf{x}| < \mathsf{L}/2,\ |\mathsf{y}| < \mathsf{W}/2 \\ (\mathsf{x} - \mathsf{x}_0^\mathrm{r})^2 + (\mathsf{y} - \mathsf{y}_0^\mathrm{r})^2 > \mathsf{A}/\pi \end{array} \tag{5.17}$$

while z_k, which specifies the kth interfering wearable's height, varies independently and uniformly in $[\mathcal{H}_\mathrm{up}, \mathcal{H}_\mathrm{dw}]$, with $\mathcal{H}_\mathrm{up} < h_\mathrm{u} - \mathsf{H}/2$ and $\mathcal{H}_\mathrm{dw} > -\mathsf{H}/2$.

Similarly, the individual wearing the interferer at X_k, represented by the corresponding circle on $\boldsymbol{\mathcal{X}}_0$, has its center $\mathcal{D}/2 + \mathsf{r}_\mathrm{w}$ away from the projection X'_k, at an angle uniform in $[0, 2\pi)$. The distribution of such circle center on $\boldsymbol{\mathcal{X}}_0$, while not exactly uniform, can be approximated by the uniform distribution in (5.17)—tighter as $\mathcal{D}/2 + \mathsf{r}_\mathrm{w}$ gets smaller compared to L and W—so as to derive (cf. Appendix B.4) the approximate blockage probabilities presented next. The accuracy of these approximations will be validated, for practically relevant settings, in Examples 5.4 and 5.5.

[2] This small exclusion region, consistent with the impossibility of two people occupying the same physical space, is introduced to avoid circles overlapping with the reference receiver and thereby blocking all the links. Interfering wearables overlapped by circles are considered blocked (cf. Appendix D.3).

Table 5.2: Settings

Parameter	Value
$\mathsf{L} \times \mathsf{W} \times \mathsf{H}$	20 m × 4 m × 2.5 m
r_0	25 cm
λ	5 mm
$\mathcal{D}$	50 cm
h_{u}	175 cm
$\mathcal{H}_{\mathrm{up}}$	25 cm
$\mathcal{H}_{\mathrm{dw}}$	-75 cm
P	0 dBm
F_{N}	9 dB
N_0	-174 dBm/Hz

Interlude: Significance of the Propagation Model

Before proceeding further, let us halt to examine the propagation model under the foregoing random network geometry, specifically to glimpse the possibility of an abstraction that fits a stochastic model involving a distance-dependent path loss function and shadowing.

Example 5.3. Under the settings in Table 5.2, high reflectivity (Γ_{high}) surfaces and omnidirectional ($\mathsf{N} = 1$) antennas, the plots in Fig. 5.10 show the realizations—obatianed via Monte-Carlo, with the blockages determined as per the algorithm in Appendix D.3—of the large-scale gain G_k as per (5.12) vs. (direct) link distance r_k in log scale. The values for the cases of unblocked direct link ($\beta_k = 1$) and blocked direct link ($\beta_k = 0$) are plotted separately.

The preceding example indicates that a more involved model than a simple single-slope path loss function coupled with a distance-independent shadowing variance would be required to abstract the indoor propagation at these frequencies. Instead of pursuing this path further, we try to simplify the blockage model and continue to work with the propagation model in Section 5.4, as our primary focus is to investigate the impact of reflections.

5.6.2 Stochastic Blockage Model

We now set out to devise, by means of random shape theory [86, 139], a stochastic alternative to the algorithm presented in Appendix

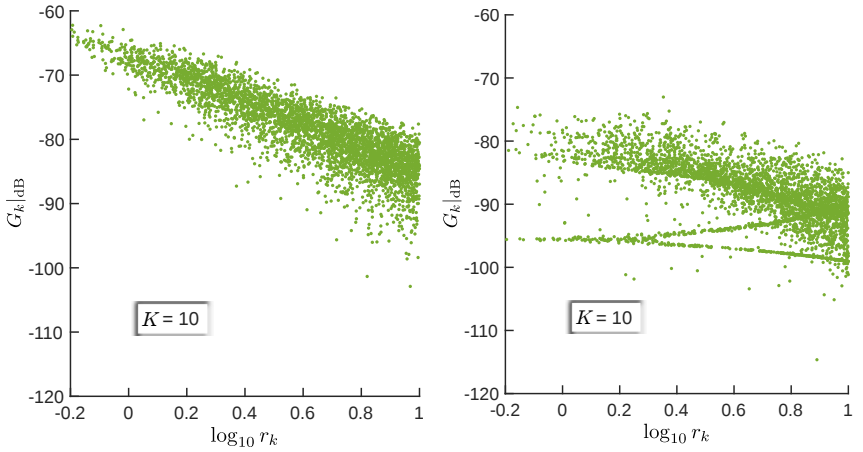

(a) Unblocked direct link ($\beta_k = 1$) (b) Blocked direct link ($\beta_k = 0$)

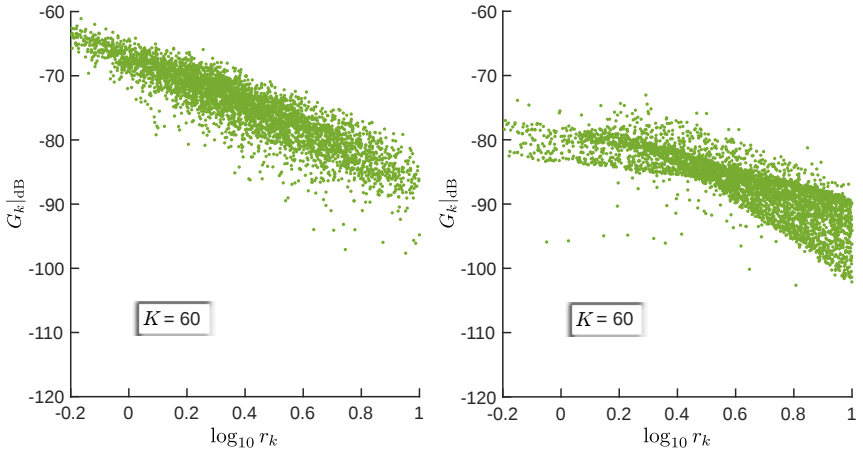

(c) Unblocked direct link ($\beta_k = 1$) (d) Blocked direct link ($\beta_k = 0$)

Figure 5.10: Large-scale gain G_k vs. (direct) link distance r_k, under high reflectivity (Γ_{high}) surfaces and omnidirectional ($\mathsf{N} = 1$) antennas.

D.3 to determine blockages.

Direct Interference Paths

For the direct interference link from a given transmitter X_k to X_0^{r}, considering the potential blockages by the $K-1$ other people and the potential self-body blocking by the link's own individuals (the reference one and the one wearing X_k), the probability of blockage satisfies (cf. Appendix D.5)

$$\mathbb{P}[\beta_k = 0] \approx 1 - \left(1 - \frac{r_k' \mathcal{D} - \tilde{\mathsf{A}}}{\mathsf{L}\mathsf{W} - \mathsf{A}}\right)^{K-1} \left(1 - \frac{\arcsin \frac{\mathcal{D}}{2\,\mathsf{r}_{\mathrm{w}} + \mathcal{D}}}{\pi}\right)^2 \tag{5.18}$$

where $r_k' = \|X_k' - X_0^{\mathrm{r}}\|$ and

$$\tilde{\mathsf{A}} = \frac{\mathsf{A}}{\pi} \arcsin \frac{\mathcal{D}/2}{\mathcal{D} + \mathsf{r}_{\mathrm{w}}} + \frac{\mathcal{D}(\mathcal{D} + \mathsf{r}_{\mathrm{w}})}{2} \cos\left(\arcsin \frac{\mathcal{D}/2}{\mathcal{D} + \mathsf{r}_{\mathrm{w}}}\right) - \frac{\pi \mathcal{D}^2}{8}. \tag{5.19}$$

Then, β_k for each given X_k is a Bernoulli random variable with $\mathbb{P}[\beta_k = 0]$ given by (5.18).

The self-body blockage probability, obtained by evaluating (5.18) with $K = 1$, increases with shrinking r_{w} for given $\mathcal{D}$, while being independent of the transmitter location. When $\mathsf{r}_{\mathrm{w}} = 0$, a given link can get blocked by its own individuals with probability 3/4. Quite naturally, blocking by other people occurs with higher probability for longer links and higher densities.

Wall-Reflected Interference Paths

As shown in Appendix D.5, the probability of blockage of the reflected interfering links off the walls, i.e., the links from $\{X_{i,k}\}_{i=1}^4$, can also be approximated by (5.18). Thus, for $i = 1, \ldots, 4$, $\beta_{i,k}$ is Bernoulli with

$$\mathbb{P}[\beta_{i,k} = 0] \approx 1 - \left(1 - \frac{r_{i,k}' \mathcal{D} - \tilde{\mathsf{A}}}{\mathsf{L}\mathsf{W} - \mathsf{A}}\right)^{K-1} \left(1 - \frac{\arcsin \frac{\mathcal{D}}{2\,\mathsf{r}_{\mathrm{w}} + \mathcal{D}}}{\pi}\right)^2 \tag{5.20}$$

where $r_{i,k}' = \|X_{i,k}' - X_0^{\mathrm{r}}\|$.

Ceiling-Reflected Interference Paths

To characterize the blockage probability of the ceiling reflection from X_k, we express

$$\beta_{5,k} = \beta_{5,k}^{\mathrm{sb}0}\, \beta_{5,k}^{\mathrm{sb}k}\, \beta_{5,k}^{\mathrm{ob}} \tag{5.21}$$

where the independent Bernoulli variables $\beta_{5,k}^{\mathrm{sb}0}$, $\beta_{5,k}^{\mathrm{sb}k}$ and $\beta_{5,k}^{\mathrm{ob}}$ respectively capture the self-body blocking by the reference individual, self-body blocking by the person wearing X_k, and blocking by the $K-1$ other people. Recalling $a_k = (h_{\mathrm{u}} - H/2 - \mathsf{z}_0^{\mathrm{r}}) \tan\theta_{5,k}$ and $b_k = (h_{\mathrm{u}} - H/2 - \mathsf{z}_k) \tan\theta_{5,k}$ from Section 5.2.3, with a modicum of trigonometry (cf. Appendix D.5) we obtain

$$\mathbb{P}[\beta_{5,k}^{\mathrm{sb}0} = 0] = \begin{cases} \frac{\arcsin \frac{\mathcal{D}}{2\,\mathsf{r}_{\mathrm{w}}+\mathcal{D}}}{\pi} & a_k \geq \sqrt{\mathsf{r}_{\mathrm{w}}(\mathcal{D}+\mathsf{r}_{\mathrm{w}})} \\ \frac{\arccos \frac{a_k^2+\mathsf{r}_{\mathrm{w}}\mathcal{D}+\mathsf{r}_{\mathrm{w}}^2}{a_k(2\,\mathsf{r}_{\mathrm{w}}+\mathcal{D})}}{\pi} & \sqrt{\mathsf{r}_{\mathrm{w}}(\mathcal{D}+\mathsf{r}_{\mathrm{w}})} > a_k \geq \mathsf{r}_{\mathrm{w}} \\ 0 & a_k < \mathsf{r}_{\mathrm{w}} \end{cases} \tag{5.22}$$

$$\mathbb{P}[\beta_{5,k}^{\mathrm{sb}k} = 0] = \begin{cases} \frac{\arcsin \frac{\mathcal{D}}{2\,\mathsf{r}_{\mathrm{w}}+\mathcal{D}}}{\pi} & b_k \geq \sqrt{\mathsf{r}_{\mathrm{w}}(\mathcal{D}+\mathsf{r}_{\mathrm{w}})} \\ \frac{\arccos \frac{b_k^2+\mathsf{r}_{\mathrm{w}}\mathcal{D}+\mathsf{r}_{\mathrm{w}}^2}{b_k(2\,\mathsf{r}_{\mathrm{w}}+\mathcal{D})}}{\pi} & \sqrt{\mathsf{r}_{\mathrm{w}}(\mathcal{D}+\mathsf{r}_{\mathrm{w}})} > b_k \geq \mathsf{r}_{\mathrm{w}} \\ 0 & b_k < \mathsf{r}_{\mathrm{w}} \end{cases} \tag{5.23}$$

$$\mathbb{P}[\beta_{5,k}^{\mathrm{ob}} = 0] \approx 1 - \left(1 - \frac{(a_k + b_k)\,\mathcal{D} - \tilde{\mathsf{A}} + \pi\,\mathcal{D}^2/2}{\mathsf{L}\,\mathsf{W} - \mathsf{A}}\right)^{K-1}. \tag{5.24}$$

Note that, unlike for direct path and wall reflections, the blockage probability of the ceiling reflection depends on the wearable heights (via z_k for the transmitter and $\mathsf{z}_0^{\mathrm{r}}$ for the receiver).

Blocking of a ceiling reflection implies that the corresponding direct path is also blocked, i.e, $\beta_{5,k}$ and β_k are dependent and

$$\begin{aligned} \mathbb{P}[\beta_k = 0] &= \mathbb{P}[\beta_k = 0 | \beta_{5,k} = 0]\, \mathbb{P}[\beta_{5,k} = 0] \\ &\quad + \mathbb{P}[\beta_k = 0 | \beta_{5,k} = 1]\, \mathbb{P}[\beta_{5,k} = 1] \qquad (5.25) \\ &= \mathbb{P}[\beta_{5,k} = 0] + \mathbb{P}[\beta_k = 0 | \beta_{5,k} = 1]\, \mathbb{P}[\beta_{5,k} = 1]. \qquad (5.26) \end{aligned}$$

This dependence can be captured in the stochastic model by introducing an auxiliary random variable, as explained in Appendix D.5.

Wall-Reflected Signal Paths

As for the intended signal reflections off the walls, i.e., the links from $\{X_{i,0}\}_{i=1}^{4}$, only the reference individual can effect self-body blockage on them while the other K people can potentially intersect the links. Then, as argued in Appendix D.5, the probability of blockage for the link from $\{X_{i,0}\}_{i=1}^{4}$ satisfies

$$\mathbb{P}[\beta_{i,0}=0] \approx 1-\left(1-\frac{r'_{i,0}\,\mathcal{D}-\tilde{\mathsf{A}}}{2\,(\mathsf{L}\,\mathsf{W}-\mathsf{A})}\right)^{K} \cdot\left(1-\frac{\arcsin\frac{r'_0}{2\,\mathsf{r}_{\mathrm{w}}+\mathcal{D}}+\arcsin\frac{\mathcal{D}}{2\,\mathsf{r}_{\mathrm{w}}+\mathcal{D}}}{\pi}\right) \tag{5.27}$$

with $r'_{i,0}=\|X'_{i,0}-X_0^{\mathrm{r}}\|$ and $r'_0=\|X'_0-X_0^{\mathrm{r}}\|$. For $i=1,\ldots,4$, the coefficient $\beta_{i,0}$ is Bernoulli with $\mathbb{P}[\beta_{i,0}=0]$ given by (5.27).

Note that the self-body blocking of the wall-reflected signal paths (by the reference individual) depends on the intended transmitter location X_0, in addition to r_{w} and $\mathcal{D}$.

The following example validates, for the settings in Table 5.2, the blockage probabilities that we have established throughout this section.

Example 5.4. Consider a reference receiver X_0^{r} at the center of the enclosed space. Depicted with markers in the plots in Fig. 5.11, are the average blockage probabilities, computed via the expectations of the location-dependent blockage random variables over the locations distributed as per Section 5.6.1, for different values of K and r_{w}. Their exact counterparts, obtained via Monte-Carlo (by establishing each individual blockage deterministically as detailed in Appendix D.3), are the solid curves plotted alongside.

Very good matches in support of our stochastic model can be observed. As can be seen, the blockage probability increases significantly with decreasing r_{w} (self-body blockage) and with increasing densities (other-body blockage).

From the marginal distributions established for $\{\beta_k\}$ and $\{\beta_{i,k}\}$, a stochastic blockage model can be constructed by regarding these variables as independent, functions only of their respective transmitter locations. This ignores potential dependences across links due to common blockages and related reflections, and thus some validation

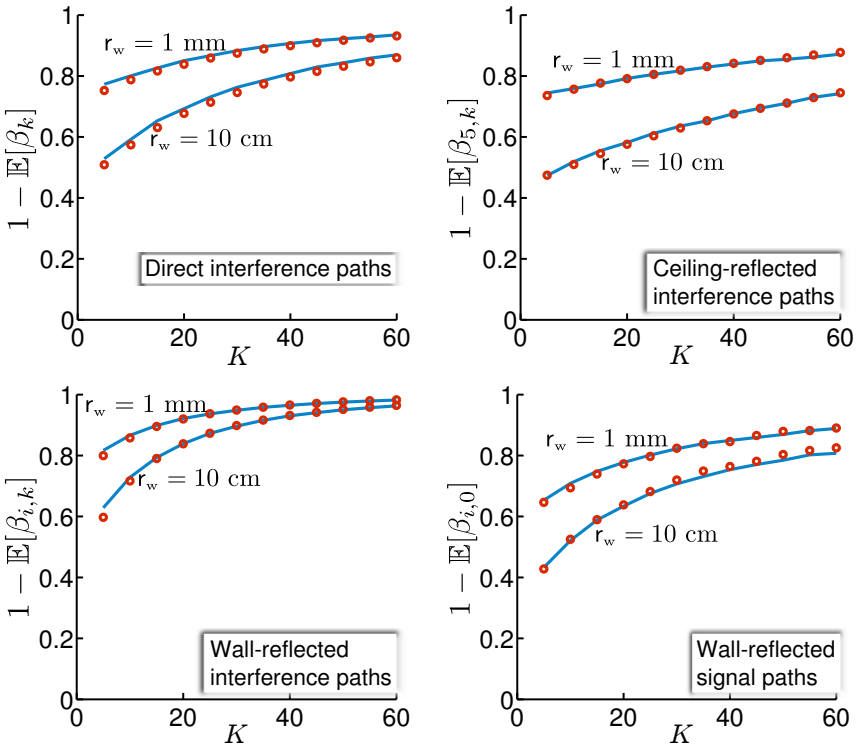

Figure 5.11: Average blockage probabilities of the direct interference path and the reflected paths.

of whether significant such dependences do exist is needed before we can confidently apply the model. This validation is provided in Example 5.5.

5.6.3 Stochastic Model for the Antenna Gains

Since the main-lobe directions of the interfering transmitters are distributed independently and uniformly, the receiver X_0^{r} is in the main-lobe of X_k with probability

$$p_{\mathrm{t}} = \int_0^{2\pi} \int_0^{\frac{\sqrt{3/N}}{2}} \frac{\sin\vartheta}{4\,\pi}\,\mathrm{d}\vartheta\,\mathrm{d}\varphi \tag{5.28}$$

$$= \sin^2\left(\sqrt{3/\mathsf{N}}/4\right). \tag{5.29}$$

Then, the transmit antenna gain $\mathcal{G}_k^{\mathrm{t}}$, for $k = 1, \ldots, K$, satisfies

$$\mathcal{G}_k^{\mathrm{t}} = \begin{cases} \mathsf{G} & \text{with prob.} \quad p_{\mathrm{t}} \\ \mathsf{g} & \text{with prob.} \quad 1 - p_{\mathrm{t}} \end{cases} \tag{5.30}$$

where $\mathsf{G} = \mathsf{N}$ and g is as in (5.10). The transmit antenna gains for the reflected links, $\mathcal{G}^{\mathrm{t}}_{i,k}$, have the same distribution. The dependence between $\mathcal{G}^{\mathrm{t}}_{k}$ and $\mathcal{G}^{\mathrm{t}}_{i,k}$ is ignored, with the accuracy of this assumption validated in Example 5.8.

Recall, from Section 5.3 and Appendix B.5, that all the receive antenna gains $\{\mathcal{G}^{\mathrm{r}}_{k}\}$ and $\{\mathcal{G}^{\mathrm{r}}_{i,k}\}$ are functions of the main-lobe direction of X^{r}_{0}. Consequently, they are mutually dependent for $k = 1, \ldots, K$, unlike the transmit antenna gains. In this paper, we intend to study the network performance under specific cases of the receiver main-lobe direction (cf. Section 5.8). Nonetheless, over a uniform distribution of the receiver main-lobe direction, each $\mathcal{G}^{\mathrm{r}}_{k}$ and $\mathcal{G}^{\mathrm{r}}_{i,k}$ would also abide by (5.30).

5.7 Impact of Reflections and Blockages

This section provides examples, for the settings in Table 5.2, to test the accuracy of the stochastic blockage model proposed in Section 5.6.2 and to gauge the impact of reflections and blockages on the communication performance with isotropic antennas ($\mathsf{N} = 1$). The results presented hereafter are obtained for two specific locations for the reference receiver X^{r}_{0}:

- *Center* of the space, whereby X^{r}_{0} is at the origin
- *Corner* of the space, whereby

$$(\mathsf{x}^{\mathrm{r}}_{0}, \mathsf{y}^{\mathrm{r}}_{0}, \mathsf{z}^{\mathrm{r}}_{0}) = (8.5 \text{ m}, 1.5 \text{ m}, 0.25 \text{ m})$$

Also, recall the two reflectivity settings (Γ_{low} and Γ_{high}) from Fig. 5.3. Unless otherwise specified, the bandwidth B, which determines the noise power σ^2_{N}, is set to $B = 1$ GHz.

Example 5.5. For a reference receiver located at the center, the CDFs of SINR are plotted in Fig. 5.12, with $\mathsf{r}_{\mathrm{w}} = 10$ cm and $N = 1$. The CDFs obtained by independently realizing $\{\beta_k\}$ and $\{\beta_{i,k}\}$ via the probabilities given in Section 5.6.2, ignoring their dependences, are contrasted against the exact ones obtained by establishing each individual blockage deterministically as detailed in Appendix D.3.

Very good agreements are observed, supporting the stochastic model under these settings and indicating that the distribution of SINR

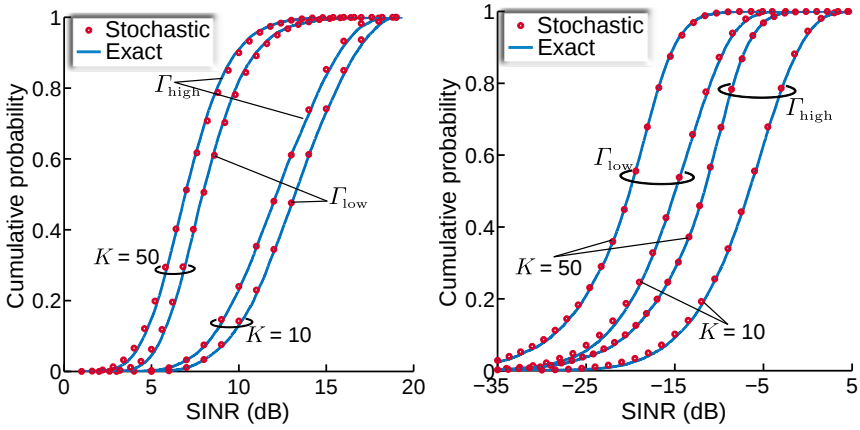

(a) Unblocked on-body link ($\beta_0 = 1$) (b) Blocked on-body link ($\beta_0 = 0$)

Figure 5.12: CDFs of SINR with the reference receiver located at the center, $\mathsf{r}_{\mathsf{w}} = 10$ cm and isotropic antennas ($\mathsf{N} = 1$).

computed over all possible geometries is not sensitive to potential dependences caused by common blockages and related reflections.

Given the minimal fading at mmWave frequencies and under the premise of Gaussian signaling, the spectral efficiency can be obtained from SINR as $C(\mathsf{SINR}) = \log_2(1 + \mathsf{SINR})$, which can then be spatially averaged over the distribution of SINR (dictated by all possible locations of people and wearables, orientations and polarization angles) to obtain the average performance for a given reference receiver location

$$\bar{C} = \mathbb{E}[\log_2(1 + \mathsf{SINR})]. \tag{5.31}$$

Example 5.6. For a reference receiver located at the center, $\bar{C}$ as function of bandwidth B is plotted in Fig. 5.13a, with $\mathsf{r}_{\mathsf{w}} = 10$ cm, high reflectivity surfaces (Γ_{high}) and isotropic antennas ($\mathsf{N} = 1$). Multiples curves, obtained with different values for K for both unblocked on-body link ($\beta_0 = 1$) and blocked on-body link ($\beta_0 = 0$), are contrasted.

Example 5.7. With the bandwidth fixed again at $B = 1$ GHz, Fig. 5.13b shows $\bar{C}$ as function of K for high reflectivity surfaces (Γ_{high}), blocked on-body link ($\beta_0 = 0$) and isotropic antennas ($\mathsf{N} = 1$). The contrast is between center and corner receiver locations, and between two different values of r_{w}.

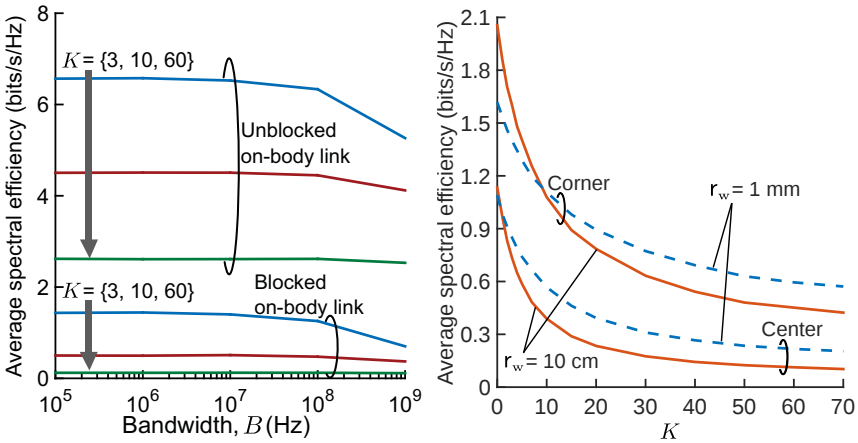

(a) Receiver at center; $\mathsf{r}_\mathrm{w} = 10$ cm. (b) Blocked on-body link ($\beta_0 = 0$).

Figure 5.13: Spatially averaged spectral efficiency (bits/s/Hz) with high-reflectivity surfaces (Γ_high) and isotropic antennas ($\mathsf{N} = 1$).

The examples above lead to the following observations, in terms of the impact of reflections and blockages:

- When the direct on-body signal is unblocked, reflections are overall detrimental. The increase in interference dominates the increase in useful signal, as indicated by the degradation in performance with increasing reflectivity (cf. Fig. 5.12). Given the short range of the on-body link, efficient communication is possible even without antenna gains.
- When the direct on-body signal is blocked and the intended signal is received only via reflections, increased reflectivity improves the performance (by as much as 10 dB), yet the SINR is very low and operation might not be feasible at all without strong antenna gains.
- As far as interference blockages are concerned, their probability increases with the density of people and with shrinking r_w, but not fast enough to fully shield receivers and hence the cumulative interference grows with the density.
- Noise is not negligible for high-bandwidth applications (cf. Fig 5.13a), yet, even with very few interferers, the performance is on-average interference-limited. This is revealed by the steep decline in Fig. 5.13b, when going from $K = 0$ (no interference) to $K > 0$.

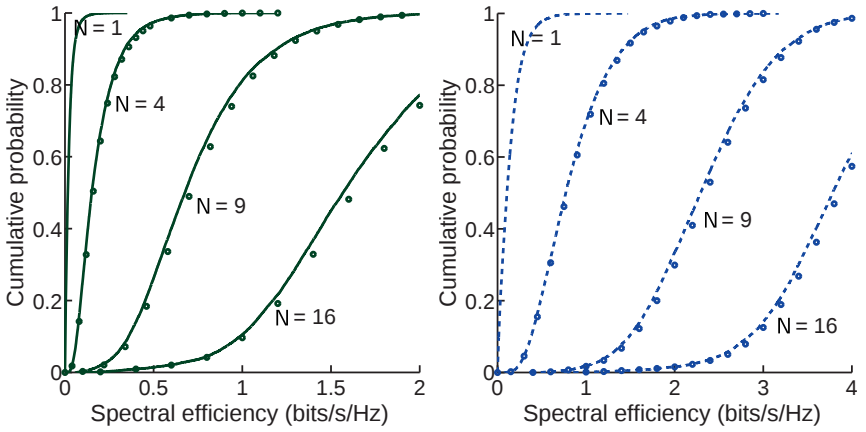

(a) Low reflectivity surfaces, Γ_{low}. (b) High reflectivity surfaces, Γ_{high}.

Figure 5.14: CDFs of spectral efficiency (bits/s/Hz) with the reference receiver located at the center, blocked on-body link ($\beta_0 = 0$), $K = 40$ and $\mathsf{r}_{\text{w}} = 10$ cm.

- At corner locations, there are stronger signal reflections and a natural protection from direct interference. With very low K, even the effect of self-blocking in the wall-reflected signal (effected via r_{w}) becomes noticeable, as evidenced by the cross-over of the curves in Fig. 5.13b.

Recognizing the necessity of antenna gains in the absence of a strong on-body link, the focus of the next section is on evaluating the performance improvement brought about by steering the beams towards strong signal reflections in such situations.

5.8 Impact of Antenna Arrays

For a reference receiver located at the center, the closest surfaces are the ceiling and the floor. Therefore, when the on-body link is blocked, the main-lobes of the reference wearables are steered towards the signal reflection off the ceiling, which is assumed unblocked. Specifically, the main-lobe of the receiver X_0^{r} is pointed to the phantom transmitter $X_{5,0}$, while the main-lobe of the intended transmitter X_0 points to the phantom image of X_0^{r} across the ceiling (cf. Appendix D.1). The azimuth and the elevation angles of these main-lobes are computed following the steps in Appendix D.4.

Example 5.8. Plotted in Fig. 5.14 are the CDFs of spectral efficiency, $C(\mathsf{SINR})$, for a reference receiver located at the center with

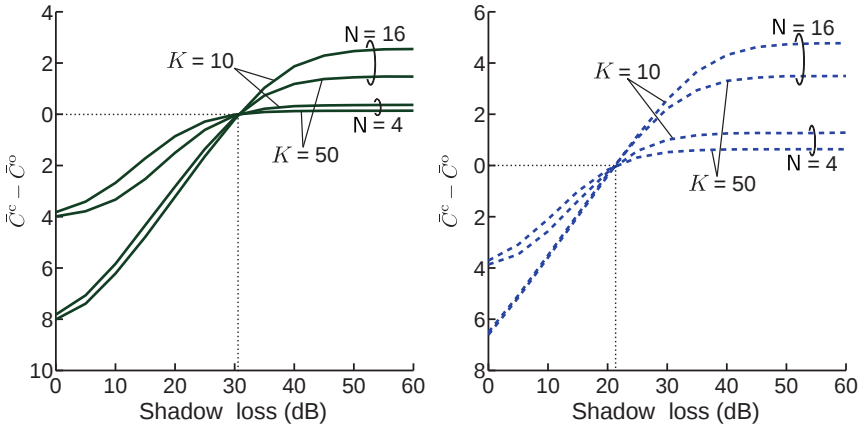

(a) Low reflectivity surfaces, Γ_{low}. (b) High reflectivity surfaces, Γ_{high}.

Figure 5.15: Difference between the average spectral efficiencies considered in Example 5.9, for varying shadow-loss in the on-body link, when the reference receiver is located at the center and $\mathsf{r}_{\text{w}} = 10$ cm.

blocked on-body link ($\beta_0 = 0$), $K = 40$ and $\mathsf{r}_{\text{w}} = 10$ cm, under different antenna settings and the two reflectivity scenarios. For $\mathsf{N} > 1$, there are two results per case: the one in markers, obtained by applying the stochastic model for the transmit antenna parameters (cf. Section 5.6.3), and the one in solid/dashed, obtained as per Appendix B.5.

The performance improves steadily with N and communication becomes feasible with high probability beyond $\mathsf{N} \approx 9$ antennas per wearable, provided the beams are well pointed. Again, note that the dependence on surface reflectivity is significant, as much as 2 bits/s/Hz for the settings we have considered.

Next, instead of a complete blockage of the on-body link ($\beta_0 = 0$), we vary $\beta_0 \in (0, 1]$ so as to quantify the shadow loss $1/\beta_0$ that would render reflection a better communication mechanism than the direct on-body link. Consider two main-lobe directions for the reference wearables: (*i*) towards the direct on-body link, and (*ii*) towards the ceiling reflection. We denote by $\bar{C}^{\text{o}}$ and $\bar{C}^{\text{c}}$ the spatially averaged spectral efficiency (5.31) in the first and second cases, respectively.

Example 5.9. For a reference receiver at the center, Fig. 5.15 shows $\bar{C}^{\text{c}} - \bar{C}^{\text{o}}$ as function of $1/\beta_0$ with $\mathsf{r}_{\text{w}} = 10$ cm and parameterized by N and K.

As can be seen, steering the main-lobe to a strong signal reflection becomes preferable to the direct on-body link under relatively moderate shadowing (20 to 30 dB for the settings considered), which could be rather common for on-body communication links.

Another interesting observation from Example 5.9 is that the shadow loss at the points where $\bar{C}^{\mathrm{c}} = \bar{C}^{\mathrm{o}}$ is roughly the same, irrespective of N and K, for each reflectivity. This is because, in our model, the ceiling reflection of the intended signal is always available, and thus the shadow loss that renders $\bar{C}^{\mathrm{c}}$ and $\bar{C}^{\mathrm{o}}$ equal is the difference between the propagation losses of the on-body and ceiling-reflected paths.

5.9 Summary

The performance of enclosed mmWave wearable networks is influenced decidedly by blockages, reflections and directional beamforming. We have proposed a simple stochastic model that incorporates these effects, and validated the satisfactory behavior of this model under relevant settings.

Indoor wearable networks may be feasible at mmWave frequencies with antenna arrays of reasonable size, even in the absence of a strong direct signal path and in high-density environments, relying on the plausible availability of signal reflections. On the order of 10 antenna elements per transceiver suffices to ensure comfortable spectral efficiencies—and thus very high bit rates given the volumes of available bandwidth—in most situations, provided the beams are well-pointed.

Chapter 6

Conclusion

6.1 Summary of Conclusions

6.1.1 Application of Stochastic Geometry to Wireless Network Analysis

The dissertation has set forth a novel approach for the spectral efficiency analysis of wireless networks, which, by decoupling the small- and large-scale channel features and abstracting out the former via local ergodicity, focus crisply on the large-scale features. Jointly with a Gaussian model for the aggregate interference that recognizes that the fading of each term therein is unknown, this is shown to enrich the stochastic geometry based analysis by circumventing analytical roadblocks and yielding expressions that are more precise and more open to generalizations. Further, we have demonstrated that simpler characterizations can be obtained by judiciously introducing approximations that are tailored to the specific network scenarios. The potency and versatility offered by these modeling principles were elucidated via the analytical framework for D2D in cellular networks, presented in Chapter 3, and via the extensibility thereof in accommodating the changes in network geometry ensuing from the incorporation of exclusion regions, presented in Chapter 4.

6.1.2 Benefits of D2D in Cellular Networks

D2D communication offers a prime opportunity for network densification in the face of local traffic. The increase in area spectral efficiency that it can bring about is very high, even if no attempt is made to optimize the scheduling of D2D transmissions. While

a large share of the D2D links is observed to have better spectral efficiency than the cellular uplink, strong interference does arise as a problem for a share of the D2D links and more severely for the cellular uplink in underlay networks. Additionally, depending on whether and how the length of the D2D links vary with the user density—empirical data on which is yet to be gathered based on the user behavior in specific D2D applications [13]—the network may get clogged with interference.

The aforesaid performance degradation resulting from the surge of D2D interference is shown to be alleviated via smart channelization schemes, two instances of which were analyzed in the dissertation. Namely, (*i*) establishing exclusion regions around each BS to avoid close-by D2D interference in underlay networks and (*ii*) ensuring that all co-channel D2D links respect certain exclusion regions in overlay networks. Under different criteria for the two cases—i.e., (*i*) maintaining minimum cellular uplink performance and (*ii*) maximizing the area spectral efficiency—we have demonstrated that interference protection can be achieved while boosting the aggregate network performance, despite the ensuing sparser spectral reuse.

6.1.3 Enclosed mmWave Wearable Networks: Feasibility and Performance

Chapter 5 established that mmWave propagation and thereby the network performance are impacted distinctly by blockages and surface reflections in crowded indoor settings. We have evidenced the significance of a propagation model that adequately incorporates these mechanisms and directional beamforming, in assessing the performance of indoor wearable networks.

The results of our investigation indicated that a genuinely challenging situation in wearable networks operating at these frequencies is the possible blocking of the on-body signal, which is aggravated by the interference from high-density environments. However, such networks may function in enclosed settings, relying on the likely availability of signal reflections that can be gathered via antenna arrays of reasonable size. Provided the beams are well-pointed, we have demonstrated that on the order of 10 antenna elements per transceiver can provide spectral efficiencies that are adequate to enable high bit rate wearable applications, leveraging the availability of bandwidth.

6.2 Future Research

6.2.1 D2D in Cellular Networks

The analytical framework presented in the dissertation was extended by the authors of [152] to encompass ITLinQ [33]: an advanced channelization scheme for D2D based on information theoretical optimality, whose implementable version was shown to be effectively realizing exclusion regions, around co-channel receivers and transmitters, that can be tuned more efficiently. In this direction, the framework may be employed to analyze the benefits of ITLinQ+ [38]: a more recent and smarter scheme that combines D2D channelization with transmit power control.

The optimization problems addressed in this dissertation and by the extension of our framework in [152] mainly dealt with the spatially averaged spectral efficiency. All the same, as the framework also offers the distribution of spectral efficiency, avenues are open for optimizations involving the same, which might be of great interest; for instance, to base the optimization of a channelization scheme on the edge-rate (recall from the 5G requirements in Section 1.1.1).

The framework has been developed for single-antenna transmitters and receivers, and hence a generalization to multiantenna setups would be a logical follow-up. With multiple antennas per transceiver, even denser spectrum reuse and/or higher-rate links would be possible. Recall that our modeling approach renders extensions to incorporate MIMO rather straight forward—indicated by Example 2.4 and evidenced in detail by [101]—which were intractable under the conventional approach.

Many recent investigations on D2D networks that apply stochastic geometry [66–68] follow the conventional modeling approach that unnecessarily limits the scope and makes the analysis rather cumbersome. For instance, the extensions to fading distributions other than Rayleigh [66] can be rendered much easier using our framework, as we have indicated in Example 2.3. It is our hope that the framework put forth in this dissertation can serve other researchers as they further explore the potential and the challenges associated with D2D.

6.2.2 Enclosed mmWave Wearable Networks

Incorporation of a more refined model for the blockage/shadowing in the intended signal paths (direct on-body and ceiling/floor reflected off-body) would be key for a more comprehensive performance evaluation of wearable applications.

In scenarios that warrant inclusion of diffuse scattering effects, our model for the specular-dominant large-scale effects could be combined with stochastic small-scale fading models, similar to the quasi-deterministic approach proposed in [153, 154].

Other potential follow-up work could include assessing the impact of body reflectivity [138] (which was ignored in our models) and power control to comply with appropriate regulatory requirements for safety (e.g., the temperature-based safety compliance proposed by [138]), and quantifying the degree of beam-pointing accuracy that is required, as well as devising algorithms to effect the beam pointing and tracking.

Further work is needed to generalize the model to nonrectangular spaces and to include blocking/reflecting partitions within such spaces and to extend its validation. Also, further abstraction of the propagation model, possibly by devising a simpler stochastic model involving a distance dependent path loss function and shadowing, is much desirable; however, care must be exercised not to abstract out key features that impact the performance.

Appendix A

Appendix to Chapter 2

A.1 Computation of C_{exact} in Eq. (2.6)

For given $\{G_k\}_{k=1}^K$ and H_0, the exact mutual information under the non-Gaussian z in (2.2) is

$$I\Big(s_0; \sqrt{P\,G_0}\,H_0\,s_0 + z\Big) = \mathfrak{h}\Big(\sqrt{P\,G_0}\,H_0\,s_0 + z\Big) \tag{A.1}$$

$$- \mathfrak{h}\Big(\sqrt{P\,G_0}\,H_0\,s_0 + z\,\Big|s_0\Big)$$

$$= \mathfrak{h}\Big(\sqrt{P\,G_0}\,H_0\,s_0 + z\Big) - \mathfrak{h}(z) \tag{A.2}$$

where we have introduced the differential entropy

$$\mathfrak{h}(x) = -\mathbb{E}\left[\log f_x(x)\right]$$

with $x \in \mathbb{C}$. The expectations are evaluated via Monte-Carlo over the random variables $\{s_0\}_{k=0}^K$ and $\{H_k\}_{k=1}^K$, and averaged over multiple realizations of H_0 to obtain C_{exact} in (2.6). Specifically, we employ Monte-Carlo histograms to numerically evaluate

$$\mathfrak{h}(x) = -\int_{\mathbb{R}^2} f_{\boldsymbol{x}'}(\boldsymbol{\zeta})\,\log\left[f_{\boldsymbol{x}'}(\boldsymbol{\zeta})\right]\,\mathrm{d}\boldsymbol{\zeta} \tag{A.3}$$

with $\boldsymbol{x}' = [\Re(x)\ \Im(x)]^{\mathrm{T}}$.

The large-scale distribution of C_{exact}, and its average $\bar{C}_{\mathsf{exact}}$, are obtained via multiple realizations of $\{G_k\}_{k=0}^K$.

In MIMO, the foregoing computation involves channel matrices and signal vectors, with the differential entropy of a vector $\boldsymbol{x} \in \mathbb{C}^n$ being

$$\mathfrak{h}(\boldsymbol{x}) = -\mathbb{E}\left[\log f_{\boldsymbol{x}}(\boldsymbol{x})\right].$$

A.2 Derivation of Eq. (2.9)

With SINR given by (2.3),

$$\mathbb{E}\big[\log_2(1+\mathsf{SINR}\,|\{G_k\})\big] = \int_0^\infty \mathbb{P}\big[\log_2(1+\mathsf{SINR}\,|\{G_k\}) > y\big]\,\mathrm{d}y \tag{A.4}$$

$$= \int_0^\infty \frac{\log_2 e}{1+x}\, F^{\mathrm{c}}_{\mathsf{SINR}|\{G_k\}}(x)\,\mathrm{d}x \tag{A.5}$$

where (A.5) follows from the variable change $y = \log_2(1+x)$ and the CCDF $F^{\mathrm{c}}_{\mathsf{SINR}|\{G_k\}}(\cdot)$ can be computed as

$$F^{\mathrm{c}}_{\mathsf{SINR}|\{r_k\}}(x) = \mathbb{P}\left[\frac{P\,G_0|H_0|^2}{P\sum_{k=1}^K G_k|H_k|^2+\sigma_{\mathrm{N}}^2} > x \,\middle|\, \{G_k\}\right] \tag{A.6}$$

$$= \mathbb{E}_{\{H_k\}}\left[e^{-x\,G_0^{-1}\left(\sum_{k=1}^K G_k|H_k|^2+\sigma_{\mathrm{N}}^2/P\right)} \,\middle|\, \{G_k\}\right] \tag{A.7}$$

$$= e^{-x\,\frac{\sigma_{\mathrm{N}}^2}{P\,G_0}}\;\mathbb{E}_{\{H_k\}}\left[\prod_{k=1}^K e^{-x\,\frac{G_k}{G_0}|H_k|^2} \,\middle|\, \{G_k\}\right] \tag{A.8}$$

$$= e^{-x\,\frac{\sigma_{\mathrm{N}}^2}{P\,G_0}} \prod_{k=1}^\infty \frac{1}{1+x\,G_k/G_0} \tag{A.9}$$

where (A.7) follows from the exponential distribution of $|H_0|^2$ and the expectation is over $\{H_k\}_{k=1}^K$. In turn, (A.9) follows from the fact that $\{H_k\}_{k=1}^K$ are IID.

Appendix B

Appendix to Chapter 3

B.1 Proof of Proposition 3.1

Recall, from (3.19), that the local-average SIR in the presence of an averaging circle is

$$\rho_{\mathrm{c}} = \frac{P_{\mathrm{c}}\, r_{\mathrm{c},0}^{-\eta_{\mathrm{c}}}}{\sigma^2_{\mathrm{c,in}} + \overline{\sigma^2}_{\mathrm{c,out}}} \tag{B.1}$$

where $\overline{\sigma^2}_{\mathrm{c,out}}$ is the spatial average of $\sigma^2_{\mathrm{c,out}}$. For this computation though, it is more convenient to retain an averaging circle (equal to a cell size) only for the cellular interferers, while not applying it to D2D interferers (or, equivalently, taking its size to infinity, which can only sharpen the model). With it, the local-average SIR with underlay ($\varkappa = 1$) becomes

$$\rho_{\mathrm{c}} = \frac{r_{\mathrm{c},0}^{-\eta_{\mathrm{c}}}}{\mu \sum_{j=1}^{\infty} r_{\mathrm{d},j}^{-\eta_{\mathrm{c}}} + \frac{2}{(\eta_{\mathrm{c}}-2)R^{\eta_{\mathrm{c}}}}}. \tag{B.2}$$

Conditioned on the summation in the denominator of (B.2), denoted hereafter by $\mathcal{Y} = \sum_{j=1}^{\infty} r_{\mathrm{d},j}^{-\eta_{\mathrm{c}}}$, the CDF of ρ_{c} can be expressed as

$$F_{\rho_{\mathrm{c}}\,|\,\mathcal{Y}}(x) = \mathbb{P}\left[\frac{r_{\mathrm{c},0}^{-\eta_{\mathrm{c}}}}{\mu\,\mathcal{Y} + \frac{2}{(\eta_{\mathrm{c}}-2)R^{\eta_{\mathrm{c}}}}} < x\right] \tag{B.3}$$

$$= \mathbb{P}\left[a_{\mathrm{c},0} > x^{-\frac{1}{\eta_{\mathrm{c}}}} \left(\mu\,\mathcal{Y} R^{\eta_{\mathrm{c}}} + \frac{2}{\eta_{\mathrm{c}}-2}\right)^{-\frac{1}{\eta_{\mathrm{c}}}}\right]. \tag{B.4}$$

For a user uniformly located in the cell, we can write the CDF of $a_{\mathrm{c},0}$ as

$$F_{a_{\mathrm{c},0}}(a) = \begin{cases} a^2 & 0 \le a \le 1 \\ 1 & a > 1 \end{cases} \tag{B.5}$$

and thus (B.4) becomes

$$F_{\rho_\mathrm{c}\,|\,\mathcal{Y}}(x) = 1 - F_{a_{\mathrm{c},0}}\left[x^{-\frac{1}{\eta_\mathrm{c}}}\left(\mu\,\mathcal{Y} R^{\eta_\mathrm{c}} + \frac{2}{\eta_\mathrm{c}-2}\right)^{-\frac{1}{\eta_\mathrm{c}}}\right] \tag{B.6}$$

$$= 1 - x^{-\frac{2}{\eta_\mathrm{c}}}\left(\mu\,\mathcal{Y} R^{\eta_\mathrm{c}} + \frac{2}{\eta_\mathrm{c}-2}\right)^{-\frac{2}{\eta_\mathrm{c}}} \quad \text{for} \quad x \ge \frac{\eta_\mathrm{c}-2}{\mu\,\mathcal{Y} R^{\eta_\mathrm{c}}(\eta_\mathrm{c}-2)+2}. \tag{B.7}$$

Expecting $F_{\rho_\mathrm{c}\,|\,\mathcal{Y}}(x)$ over $\mathcal{Y}$, the unconditional CDF of ρ_c can be obtained. Since the resulting form is unwieldy for general η_c, we restrict ourselves to $\eta_\mathrm{c} = 4$ for which the PDF of $\mathcal{Y}$ is [155, Sec. V]

$$f_\mathcal{Y}(\nu) = \frac{\pi}{2}\,\lambda_\mathrm{d}\,\nu^{\frac{-3}{2}}\,e^{\frac{-\pi^3\lambda_\mathrm{d}^2}{4\nu}} \qquad \nu > 0. \tag{B.8}$$

Averaging $F_{\rho_\mathrm{c}\,|\,\mathcal{Y}}(\cdot)$ over $\mathcal{Y}$, we obtain the CDF of ρ_c

$$F_{\rho_\mathrm{c}}(x) = \begin{cases} \int\limits_{\frac{1-x}{R^4\mu x}}^{\infty} \left(f_\mathcal{Y}(\nu) - \frac{f_\mathcal{Y}(\nu)}{\sqrt{x(\mu\,\nu R^4+1)}}\right)\mathrm{d}\nu & 0 < x < 1 \\ 1 - \int\limits_0^{\infty} \frac{f_\mathcal{Y}(\nu)}{\sqrt{x(\mu\,\nu R^4+1)}}\,\mathrm{d}\nu & x \ge 1 \end{cases} \tag{B.9}$$

where the limits of the integrals follow from $\nu \ge \frac{1-x}{R^4\mu x}$ and $\nu > 0$. The claim of the proposition follows from inserting (B.8) into (B.9), substituting $\lambda_\mathrm{d} = \frac{\mathsf{K}}{\pi R^2}$ and solving the integrals.

B.2 Proof of Proposition 3.2

With overlay ($\varkappa = 0$), the cellular link is not subject to D2D interference and the local-average SIR

$$\rho_\mathrm{c} = \frac{\eta_\mathrm{c}-2}{2\,a_{\mathrm{c},0}^{\eta_\mathrm{c}}}$$

depends only on $a_{\mathrm{c},0}$. Thus, the CDF of ρ_c can be expressed as

$$F_{\rho_\mathrm{c}}(x) = 1 - F_{a_{\mathrm{c},0}}\left[\left(\frac{\eta_\mathrm{c}-2}{2\,x}\right)^{\frac{1}{\eta_\mathrm{c}}}\right]. \tag{B.10}$$

Applying (B.5) to (B.10) yields the claimed result.

B.3 Proof of Proposition 3.3

The distribution of ρ_{d} can be computed over the spatial locations of all interferers in the network, which is tantamount to taking the size of the averaging circle to infinity. Thereby, from (3.24)

$$\rho_{\mathrm{d}} = \frac{r_{\mathrm{d},0}^{-\eta_{\mathrm{d}}}}{\sum_{j=1}^{\infty} r_{\mathrm{d},j}^{-\eta_{\mathrm{d}}} + \frac{\varkappa}{\mu} \sum_{k=1}^{\infty} r_{\mathrm{c},k}^{-\eta_{\mathrm{d}}}}. \tag{B.11}$$

The denominator of (B.11), denoted hereafter by

$$\mathcal{I} = \sum_{j=1}^{\infty} r_{\mathrm{d},j}^{-\eta_{\mathrm{d}}} + \frac{\varkappa}{\mu} \sum_{k=1}^{\infty} r_{\mathrm{c},k}^{-\eta_{\mathrm{d}}}$$

, has the characteristic function

$$\phi_{\mathcal{I}}(\omega) = \mathbb{E}\left[e^{\mathrm{j}\,\omega\,\mathcal{I}}\right] \tag{B.12}$$

$$= e^{-\pi\left(\lambda_{\mathrm{d}} + \frac{\varkappa}{\mu^{2/\eta_{\mathrm{d}}}}\lambda_{\mathrm{c}}\right)\Gamma\left(1-\frac{2}{\eta_{\mathrm{d}}}\right) e^{-\frac{\mathrm{j}\pi}{\eta_{\mathrm{d}}}}\,\omega^{\frac{2}{\eta_{\mathrm{d}}}}} \qquad \omega \geq 0 \tag{B.13}$$

where j is the imaginary unit and $\phi_{\mathcal{I}}(\omega) = \phi_{\mathcal{I}}^{*}(-\omega)$. The expression for $\phi_{\mathcal{I}}(\omega)$ in (B.13) is obtained as the product of the characteristic functions of the first and second summations in $\mathcal{I}$, which are computed as illustrated in [155, Sec. V]. Then, the density of $\mathcal{I}$ can be obtained by taking the inverse Fourier transform of $\phi_{\mathcal{I}}(\omega)$ and the corresponding CDF is

$$F_{\mathcal{I}}(\nu) = 1 - \frac{1}{\pi} \sum_{k=1}^{\infty} \left[\pi\left(\lambda_{\mathrm{d}} + \frac{\varkappa}{\mu^{2/\eta_{\mathrm{d}}}}\lambda_{\mathrm{c}}\right)\Gamma\left(1-\frac{2}{\eta_{\mathrm{d}}}\right)\nu^{\frac{-2}{\eta_{\mathrm{d}}}}\right]^{k} \cdot \frac{\Gamma\left(\frac{2\,k}{\eta_{\mathrm{d}}}\right)}{k!} \sin\left[k\pi\left(1-\frac{2}{\eta_{\mathrm{d}}}\right)\right] \tag{B.14}$$

which, for $\eta_{\mathrm{d}} = 4$, equals

$$F_{\mathcal{I}}(\nu) = 1 - \operatorname{erf}\left[\frac{\pi^{3/2}\left(\lambda_{\mathrm{d}} + \frac{\varkappa}{\sqrt{\mu}}\lambda_{\mathrm{c}}\right)}{2\sqrt{\nu}}\right]. \tag{B.15}$$

The CDF of ρ_{d} is given by

$$F_{\rho_{\mathrm{d}}}(x) = 1 - F_{\mathcal{I}}\left(\frac{r_{\mathrm{d},0}^{-\eta_{\mathrm{d}}}}{x}\right). \tag{B.16}$$

Using (B.14) and (B.15) in (B.16), and substituting $r_{\mathrm{d},0} = \mathsf{r}_{\mathrm{d}}/\mathsf{K}^{\beta}$ and $\lambda_{\mathrm{d}} = \frac{\mathsf{K}}{\pi R^2}$, we obtain the claim of Prop. 3.3.

B.4 Proof of Proposition 3.4

The uplink spectral efficiency averaged over all geometries is

$$\bar{C}_{\mathrm{c}} = \mathbb{E}[C_{\mathrm{c}}(\rho_{\mathrm{c}})]$$

with expectation over ρ. Expanding this expectation,

$$\bar{C}_{\mathrm{c}} = \mathbb{E}\left[\mathbb{E}\left[\log_2(1+\mathsf{SIR}_{\mathrm{c}}|\rho_{\mathrm{c}})\right]\right] \tag{B.17}$$

$$= \mathbb{E}\left[\int_0^\infty \frac{\log_2 e}{\gamma+1}(1-F_{\mathsf{SIR}_{\mathrm{c}}|\rho_{\mathrm{c}}}(\gamma))\,\mathrm{d}\gamma\right] \tag{B.18}$$

$$= \int_0^\infty \frac{\log_2 e}{\gamma+1}\left(1-\mathbb{E}\left[F_{\mathsf{SIR}_{\mathrm{c}}|\rho_{\mathrm{c}}}(\gamma)\right]\right)\,\mathrm{d}\gamma \tag{B.19}$$

$$= \int_0^\infty \frac{\log_2 e}{\gamma+1}\left(1-F_{\mathsf{SIR}_{\mathrm{c}}}(\gamma)\right)\,\mathrm{d}\gamma \tag{B.20}$$

where the outer and inner expectations in (B.17) are over ρ_{c} and over the fading, respectively. We next compute $F_{\mathsf{SIR}_{\mathrm{c}}}(\cdot)$ and then use it to evaluate (B.20). For this computation, we employ the approach in Appendix B.1 and utilize (B.2) to expand the conditional CDF of the SIR

$$F_{\mathsf{SIR}_{\mathrm{c}}|\rho_{\mathrm{c}}}(\gamma) = 1-e^{-\gamma\,\frac{r_{\mathrm{c},0}^{\eta_{\mathrm{c}}}}{R^{\eta_{\mathrm{c}}}}\,\frac{2}{\eta_{\mathrm{c}}-2}}\prod_{j=1}^{\infty} e^{-\gamma\,\varkappa_\mu\, r_{\mathrm{c},0}^{\eta_{\mathrm{c}}}\, r_{\mathrm{d},j}^{-\eta_{\mathrm{c}}}}. \tag{B.21}$$

Conditioning on $r_{\mathrm{c},0}$ and averaging over the interference locations

$$F_{\mathsf{SIR}_{\mathrm{c}}|r_{\mathrm{c},0}}(\gamma) = 1-e^{-\gamma\,\frac{r_{\mathrm{c},0}^{\eta_{\mathrm{c}}}}{R^{\eta_{\mathrm{c}}}}\,\frac{2}{\eta_{\mathrm{c}}-2}}\,\mathbb{E}\left[\prod_{j=1}^{\infty} e^{-\gamma\,\varkappa_\mu\, r_{\mathrm{c},0}^{\eta_{\mathrm{c}}}\, r_{\mathrm{d},j}^{-\eta_{\mathrm{c}}}}\right] \tag{B.22}$$

$$= 1-e^{-\gamma\,\frac{r_{\mathrm{c},0}^{\eta_{\mathrm{c}}}}{R^{\eta_{\mathrm{c}}}}\,\frac{2}{\eta_{\mathrm{c}}-2}}\,e^{-2\pi\lambda_{\mathrm{d}}\int_0^\infty\left(1-e^{-\gamma\,\varkappa_\mu\, r_{\mathrm{c},0}^{\eta_{\mathrm{c}}}\, x^{-\eta_{\mathrm{c}}}}\right)x\mathrm{d}x} \tag{B.23}$$

$$= 1-e^{-\gamma\,\frac{r_{\mathrm{c},0}^{\eta_{\mathrm{c}}}}{R^{\eta_{\mathrm{c}}}}\,\frac{2}{\eta_{\mathrm{c}}-2}}\,e^{-\gamma^{\frac{2}{\eta_{\mathrm{c}}}}\,\frac{r_{\mathrm{c},0}^2}{R^2}\,\mathsf{K}\,\frac{2}{\eta_{\mathrm{c}}}\int_0^\infty\left(1-e^{-\varkappa_\mu u}\right)\frac{1}{u^{1+2/\eta_{\mathrm{c}}}}\mathrm{d}u} \tag{B.24}$$

where the expectation in (B.22) is over the PPP Φ_{d}, (B.23) follows from the definition of the probability generating functional (PGFL) of the PPP [41], and (B.24) follows from the variable change $\gamma\, r_{\mathrm{c},0}^{\eta_{\mathrm{c}}}\, x^{-\eta_{\mathrm{c}}} = u$ and the relation $\pi\lambda_{\mathrm{d}} = \mathsf{K}/R^2$. Employing integration by parts in (B.24) and invoking $a_{\mathrm{c},0} = r_{\mathrm{c},0}/R$, we obtain

$$F_{\mathsf{SIR}_{\mathrm{c}}|a_{\mathrm{c},0}}(\gamma) = 1-e^{-\gamma\, a_{\mathrm{c},0}^{\eta_{\mathrm{c}}}\,\frac{2}{\eta_{\mathrm{c}}-2}\,-\varkappa\,(\gamma\mu)^{\frac{2}{\eta_{\mathrm{c}}}}\,a_{\mathrm{c},0}^2\,\mathsf{K}\,\Gamma\left(1-\frac{2}{\eta_{\mathrm{c}}}\right)}. \tag{B.25}$$

Further averaging $F_{\mathsf{SIR}_{\mathrm{c}}|a_{\mathrm{c},0}}(\cdot)$ over $a_{\mathrm{c},0}$ via the distribution in (B.5) we obtain $F_{\mathsf{SIR}_{\mathrm{c}}}(\cdot)$, which plugged into (B.20) yields (3.34).

B.5 Proof of Proposition 3.5

Again, with overlay ($\varkappa = 0$), the local-average SIR of the cellular uplink is

$$\rho_{\mathrm{c}} = \frac{\eta_{\mathrm{c}} - 2}{2\, a_{\mathrm{c},0}^{\eta_{\mathrm{c}}}}$$

and the expectation is only over $a_{\mathrm{c},0}$. Averaging $C_{\mathrm{c}}(\rho_{\mathrm{c}})$ over $a_{\mathrm{c},0}$ via the distribution in (B.5) yields

$$\bar{C}_{\mathrm{c}} = \log_2(e) \int_0^1 e^{\frac{2\, a^{\eta_{\mathrm{c}}}}{\eta_{\mathrm{c}} - 2}} E_1\!\left(\frac{2\, a^{\eta_{\mathrm{c}}}}{\eta_{\mathrm{c}} - 2}\right) \mathrm{d}F_{a_{\mathrm{c},0}}(a). \tag{B.26}$$

When x is positive and real, $E_1(x) = -E_{\mathrm{i}}(-x)$ where

$$E_{\mathrm{i}}(x) = \int_{-x}^{\infty} \frac{-e^{-t}}{t}\, \mathrm{d}t.$$

Utilizing this relation in (B.26) and then evaluating the integral by virtue of the identity given in [156], we obtain (3.36).

B.6 Proof of Proposition 3.6

Here we can directly average the link spectral efficiency over the spatial locations of all cellular and D2D interferers in the network, without invoking any a-priori averaging circle, using (B.11). Thus, the conditional CDF of $\mathsf{SIR}_{\mathrm{d}}$ is expanded as

$$F_{\mathsf{SIR}_{\mathrm{d}}|\rho_{\mathrm{d}}}(\gamma) = 1 - \prod_{j=1}^{\infty} e^{-\gamma\, r_{\mathrm{d},0}^{\eta_{\mathrm{d}}}\, r_{\mathrm{d},j}^{-\eta_{\mathrm{d}}}} \prod_{k=1}^{\infty} e^{-\gamma\, \frac{\varkappa}{\mu}\, r_{\mathrm{d},0}^{\eta_{\mathrm{d}}}\, r_{\mathrm{c},k}^{-\eta_{\mathrm{d}}}}. \tag{B.27}$$

Maintaining the conditioning on the desired link distance $r_{\mathrm{d},0}$, we average (B.27) over the PPPs Φ_{d} and Φ_{c} to obtain

$$F_{\mathsf{SIR}_{\mathrm{d}}|a_{\mathrm{d},0}}(\gamma) = 1 - \mathbb{E}_{\Phi_{\mathrm{d}}}\!\left[\prod_{j=1}^{\infty} e^{-\gamma\, r_{\mathrm{d},0}^{\eta_{\mathrm{d}}}\, r_{\mathrm{d},j}^{-\eta_{\mathrm{d}}}}\right] \mathbb{E}_{\Phi_{\mathrm{c}}}\!\left[\prod_{k=1}^{\infty} e^{-\gamma\, \frac{\varkappa}{\mu}\, r_{\mathrm{d},0}^{\eta_{\mathrm{d}}}\, r_{\mathrm{c},k}^{-\eta_{\mathrm{d}}}}\right] \tag{B.28}$$

$$= 1 - e^{-\gamma^{\frac{2}{\eta_{\mathrm{d}}}} \frac{\mathsf{a}_{\mathrm{d}}^2}{\mathsf{K}^{2\beta}} \Gamma\left(1 - \frac{2}{\eta_{\mathrm{d}}}\right) \left(\mathsf{K} + \varkappa\, \mu^{\frac{-2}{\eta_{\mathrm{d}}}}\right)} \tag{B.29}$$

where the expectations in (B.29) are computed as in Appendix B.4 with the substitution $a_{\mathrm{d},0} = \frac{\mathsf{a}_{\mathrm{d}}}{\mathsf{K}^{\beta}}$. Thus, the average spectral effi-

ciency of the D2D links becomes

$$\bar{C}_{\mathrm{d}} = \int_0^\infty \frac{\log_2 e}{\gamma+1}(1 - F_{\mathsf{SIR}_{\mathrm{d}}|a_{\mathrm{d},0}}(\gamma))\,\mathrm{d}\gamma \tag{B.30}$$

$$= \log_2(e) \int_0^\infty \frac{e^{-\gamma^{\frac{2}{\eta_{\mathrm{d}}}} \frac{\mathsf{a}_{\mathrm{d}}^2}{\mathsf{K}^{2\beta}} \Gamma\left(1-\frac{2}{\eta_{\mathrm{d}}}\right)\left(\mathsf{K}+\frac{\varkappa}{\mu^{2/\eta_{\mathrm{d}}}}\right)}}{\gamma+1}\,\mathrm{d}\gamma \tag{B.31}$$

which is unwieldy for general η_{d}. However, for $\eta_{\mathrm{d}} = 4$, (B.31) reduces to

$$\bar{C}_{\mathrm{d}} = 2\log_2(e) \int_0^\infty \frac{x\, e^{-x\,\mathcal{K}\mathsf{a}_{\mathrm{d}}^2}}{x^2+1}\,\mathrm{d}x \tag{B.32}$$

which follows from the variable change $\sqrt{\gamma} = x$ in (B.30) with

$$\mathcal{K} = \frac{\sqrt{\pi}}{\mathsf{K}^{2\beta}}\left(\mathsf{K} + \frac{\varkappa}{\sqrt{\mu}}\right).$$

By virtue of [157, 3.354.2], (B.32) turns into the claimed expression in (3.38).

Appendix C

Appendix to Chapter 4

C.1 Proof of Lemma 4.1

With ρ_{c} as in (4.7), the Laplace transform of $1/\rho_{\mathrm{c}}$ is

$$\mathcal{L}_{F_{1/\rho_{\mathrm{c}}}}(\mathsf{s}) = \mathbb{E}_{r_{\mathrm{c},0}}\left\{ e^{-\mathsf{s}\, r_{\mathrm{c},0}^{\eta_{\mathrm{c}}}\, \overline{\sigma^2}_{\mathrm{c,out}}}\, \mathbb{E}_{\Phi_{\mathrm{d}}}\left[\prod_{j=1}^{\mathcal{K}'} e^{-\mathsf{s}\,\mu\, r_{\mathrm{c},0}^{\eta_{\mathrm{c}}}\, r_{\mathrm{d},j}^{-\eta_{\mathrm{c}}}} \middle| r_{\mathrm{c},0} \right] \right\} \tag{C.1}$$

$$= \mathbb{E}_{a_{\mathrm{c},0}}\Bigg\{ e^{-p\mathsf{K}-\mathsf{s}\, a_{\mathrm{c},0}^{\eta_{\mathrm{c}}}\, \frac{2(\mu p \mathsf{K}+1)}{\eta_{\mathrm{c}}-2}} \cdot e^{-\frac{2\mathsf{K}}{\eta_{\mathrm{c}}}\left[a_{\mathrm{ex}}^2 E_{\frac{2+\eta_{\mathrm{c}}}{\eta_{\mathrm{c}}}}\left(\mathsf{s}\,\mu\, \frac{a_{\mathrm{c},0}^{\eta_{\mathrm{c}}}}{a_{\mathrm{ex}}^{\eta_{\mathrm{c}}}} \right) - E_{\frac{2+\eta_{\mathrm{c}}}{\eta_{\mathrm{c}}}}\left(\mathsf{s}\,\mu\, a_{\mathrm{c},0}^{\eta_{\mathrm{c}}} \right) \right]} \Bigg\} \tag{C.2}$$

where the expectation over the PPP Φ_{d} is computed following steps in Example 2.7. The expatiation over $a_{\mathrm{c},0}$ in (C.2) via the its PDF in (B.5) completes the proof.

C.2 Proof of Lemma 4.2

With ρ_{d} as in (4.8), the Laplace transform of $1/\rho_{\mathrm{d}}$ is

$$\mathcal{L}_{F_{1/\rho_{\mathrm{d}}}}(\mathsf{s}) = e^{-\gamma\, r_{\mathrm{d},0}^{\eta_{\mathrm{d}}}\, \overline{\sigma^2}_{\mathrm{d,out}}} \mathbb{E}_{\Phi_{\mathrm{d}}}\left[\prod_{j=1}^{\mathsf{K}''} e^{-\gamma\, r_{\mathrm{d},0}^{\eta_{\mathrm{d}}} r_{\mathrm{d},j}^{-\eta_{\mathrm{d}}}}\right] \mathbb{E}_{\Phi_{\mathrm{c}}}\left[\prod_{k=1}^{\mathsf{K}''} e^{-\frac{\gamma}{\mu} r_{\mathrm{d},0}^{\eta_{\mathrm{d}}}\, r_{\mathrm{c},k}^{-\eta_{\mathrm{d}}}}\right] \tag{C.3}$$

$$= e^{-\gamma\, a_{\mathrm{d},0}^{\eta_{\mathrm{d}}} \frac{2}{\eta_{\mathrm{d}}-2}\left(p\mathsf{K}+\frac{1}{\mu}\right)} e^{-(\mathsf{K}+1)} \cdot e^{\frac{2}{\eta_{\mathrm{d}}}\left[\mathsf{K}\, E_{\frac{2+\eta_{\mathrm{d}}}{\eta_{\mathrm{d}}}}\left(\gamma \frac{\mathsf{a}_{\mathrm{d}}^{\eta_{\mathrm{d}}}}{\mathsf{K}^{\eta_{\mathrm{d}}}\beta}\right) + E_{\frac{2+\eta_{\mathrm{d}}}{\eta_{\mathrm{d}}}}\left(\frac{\gamma}{\mu}\frac{\mathsf{a}_{\mathrm{d}}^{\eta_{\mathrm{d}}}}{\mathsf{K}^{\eta_{\mathrm{d}}}\beta}\right)\right]} \tag{C.4}$$

where the expectations over the PPPs Φ_{c} and Φ_{d} are computed following steps in Example 2.7 to obtain the desired result.

C.3 Proof of Lemma 4.3

Consider the D2D link represented by the segment AB in Fig. C.1, where A and B indicate the transmitter and the receiver locations, respectively. Let us identify the possible locations of other transmitters (with mark lower than AB) that could violate the conditions in Sec. 4.3.3. Condition 1 is violated by the presence of other transmitters within the shaded circular region of radius $\delta \mathsf{r}_{\mathrm{d}}$ around B, denoted by $\mathcal{B}_{\mathrm{B}}$. As for Condition 2, which is violated by the presence of other receivers within a circle of radius $\delta \mathsf{r}_{\mathrm{d}}$ centered at A, the corresponding transmitter locations (r_{d} away from each receiver at a uniformly distributed random angle) cannot be farther than $\delta \mathsf{r}_{\mathrm{d}} + \mathsf{r}_{\mathrm{d}}$ from A. Hence, the D2D link AB could fail to satisfy the conditions only by the presence of lower-mark transmitters within the circle of radius $\delta \mathsf{r}_{\mathrm{d}} + \mathsf{r}_{\mathrm{d}}$ centered at A and denoted by $\mathcal{B}_{\mathrm{A}}$.

Since the presence of a lower-mark transmitter within $\mathcal{B}_{\mathrm{B}}$ will certainly violate the Condition 1, $\mathcal{B}_{\mathrm{B}}$ is part of A_{II}.

The presence of a lower-mark transmitter in the unshaded region within $\mathcal{B}_{\mathrm{A}}$ would violate Condition 2 only if the distance between its intended receiver and A is less than $\delta \mathsf{r}_{\mathrm{d}}$. Consider a lower-mark transmitter denoted by D at a distance r and angle θ from A, as shown in Fig. C.1. The presence of D can violate Condition 2 for

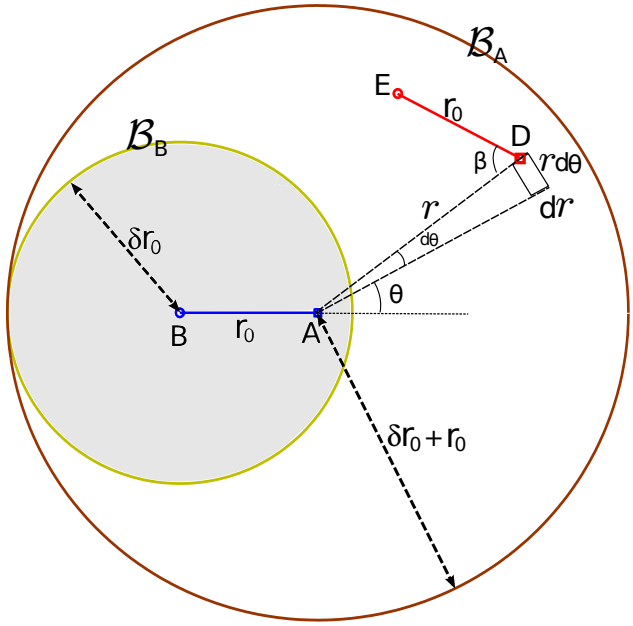

Figure C.1: Two neighboring D2D links under type II channelization scheme.

AB with probability

$$p_1(r) = \frac{1}{\pi} \arccos\left(\frac{r^2 + \mathsf{r}_\mathrm{d}^2(1-\delta^2)}{2r\mathsf{r}_\mathrm{d}}\right) \tag{C.5}$$

which is the probability that the distance between its intended receiver E and A is less than $\delta \mathsf{r}_\mathrm{d}$. This follows from the law of cosines and the fact that the angle β formed at D, between A and the D2D link DE, is uniformly distributed in $[0, \pi]$. Thus, the integration of $r\mathrm{d}\theta\,\mathrm{d}r$ scaled by $p_1(r)$ within the unshaded region is also part of A_{II}.

For the transmitter D to be within the unshaded region, the distance between B and D must be greater than $\delta \mathsf{r}_\mathrm{d}$. Thus, when $\delta > 1$ as in the figure and D is within the unshaded region, r varies in $[\delta \mathsf{r}_\mathrm{d} - \mathsf{r}_\mathrm{d}, \delta \mathsf{r}_\mathrm{d} + \mathsf{r}_\mathrm{d}]$ while the angle θ, within the upper half of the unshaded region, varies in $[0, \theta']$ where

$$\theta' = \pi - \arccos\left(\frac{r^2 + \mathsf{r}_\mathrm{d}^2(1-\delta^2)}{2r\mathsf{r}_\mathrm{d}}\right).$$

Then, A_{II} can be computed as

$$A_{\mathrm{II}} = \pi\delta^2\mathsf{r}_{\mathrm{d}}^2 + 2\int_{\delta\mathsf{r}_{\mathrm{d}}-\mathsf{r}_{\mathrm{d}}}^{\delta\mathsf{r}_{\mathrm{d}}+\mathsf{r}_{\mathrm{d}}}\int_{0}^{\theta'} p_1(r) r \mathrm{d}r\mathrm{d}\theta \tag{C.6}$$

$$= \pi\delta^2\mathsf{r}_{\mathrm{d}}^2 + \int_{\delta\mathsf{r}_{\mathrm{d}}-\mathsf{r}_{\mathrm{d}}}^{\delta\mathsf{r}_{\mathrm{d}}+\mathsf{r}_{\mathrm{d}}} \frac{\pi r}{2} - \frac{2r}{\pi}\arcsin^2\left(\frac{r^2+\mathsf{r}_{\mathrm{d}}^2(1-\delta^2)}{2r\mathsf{r}_{\mathrm{d}}}\right)\mathrm{d}r \tag{C.7}$$

$$= \pi\mathsf{r}_{\mathrm{d}}^2\delta(\delta+1) - \frac{2\mathsf{r}_{\mathrm{d}}^2}{\pi}\int_{\delta-1}^{\delta+1} r\arcsin^2\left(\frac{r^2+1-\delta^2}{2r}\right)\mathrm{d}r \tag{C.8}$$

where the first term in (C.6) is the area of $\mathcal{B}_{\mathrm{B}}$ and the second term corresponds to the resultant area computed based on the transmitter locations within the unshaded region in $\mathcal{B}_{\mathrm{A}}$ that would violate Condition 2. Note that (C.8) is valid only for $\delta > 1$ as in Fig. C.1. The result is generalized by replacing the lower limit of the integral with $|\delta-1|$, which is the result in Lemma 4.3. This is because, when $0 < \delta < 1$, a transmitter present inside a circle of radius $\mathsf{r}_{\mathrm{d}} - \delta\mathsf{r}_{\mathrm{d}}$ centered at A will always have its intended receiver located at a distance farther than $\delta\mathsf{r}_{\mathrm{d}}$ from A and thereby cannot violate the second condition.

Appendix D

Appendix to Chapter 5

D.1 Coordinates of Image Transmitters and Angles of Incidence

Recall that the origin is at the center of the enclosed space. Thus, the coordinates of the phantom transmitter $X_{i,k}$ for $i = 1, \ldots, 6$ are

$$\begin{aligned}
(\mathsf{x}_{1,k}, \mathsf{y}_{1,k}, \mathsf{z}_{1,k}) &= (\mathsf{L} - \mathsf{x}_k, \mathsf{y}_k, \mathsf{z}_k) \\
(\mathsf{x}_{2,k}, \mathsf{y}_{2,k}, \mathsf{z}_{2,k}) &= (-\mathsf{L} - \mathsf{x}_k, \mathsf{y}_k, \mathsf{z}_k) \\
(\mathsf{x}_{3,k}, \mathsf{y}_{3,k}, \mathsf{z}_{3,k}) &= (\mathsf{x}_k, \mathsf{W} - \mathsf{y}_k, \mathsf{z}_k) \\
(\mathsf{x}_{4,k}, \mathsf{y}_{4,k}, \mathsf{z}_{4,k}) &= (\mathsf{x}_k, -\mathsf{W} - \mathsf{y}_k, \mathsf{z}_k) \\
(\mathsf{x}_{5,k}, \mathsf{y}_{5,k}, \mathsf{z}_{5,k}) &= (\mathsf{x}_k, \mathsf{y}_k, \mathsf{H} - \mathsf{z}_k) \\
(\mathsf{x}_{6,k}, \mathsf{y}_{6,k}, \mathsf{z}_{6,k}) &= (\mathsf{x}_k, \mathsf{y}_k, -\mathsf{H} - \mathsf{z}_k)
\end{aligned}$$

and the angles of incidence are

$$\begin{aligned}
\theta_{1,k} &= \arccos\left(|\mathsf{L} - \mathsf{x}_k - \mathsf{x}_0^{\mathrm{r}}|/r_{1,k}\right) \\
\theta_{2,k} &= \arccos\left(|-\mathsf{L} - \mathsf{x}_k - \mathsf{x}_0^{\mathrm{r}}|/r_{2,k}\right) \\
\theta_{3,k} &= \arccos\left(|\mathsf{W} - \mathsf{y}_k - \mathsf{y}_0^{\mathrm{r}}|/r_{3,k}\right) \\
\theta_{4,k} &= \arccos\left(|-\mathsf{W} - \mathsf{y}_k - \mathsf{y}_0^{\mathrm{r}}|/r_{4,k}\right) \\
\theta_{5,k} &= \arccos\left(|\mathsf{H} - \mathsf{z}_k - \mathsf{z}_0^{\mathrm{r}}|/r_{5,k}\right) \\
\theta_{6,k} &= \arccos\left(|-\mathsf{H} - \mathsf{z}_k - \mathsf{z}_0^{\mathrm{r}}|/r_{6,k}\right).
\end{aligned}$$

The phantom image of the reference receiver X_0^{r} across the ceiling, mentioned in Section 5.8, has coordinates $(\mathsf{x}_0^{\mathrm{r}}, \mathsf{y}_0^{\mathrm{r}}, \mathsf{H} - \mathsf{z}_0^{\mathrm{r}})$.

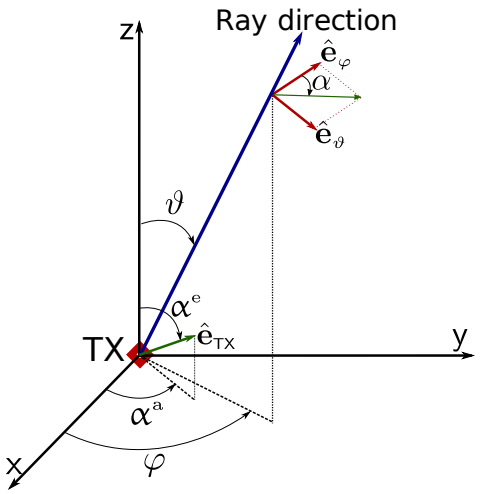

Figure D.1: Polarization of a ray from a transmitter (TX).

D.2 Polarization Angles

Consider a transmitter (cf. Fig. D.1) whose antenna polarization is defined by the azimuth angle α^{a} and the elevation angle α^{e}, i.e., along the unit vector

$$\hat{\mathbf{e}}_{\mathsf{TX}} = \sin \alpha_k^{\mathrm{e}} \cos \alpha_k^{\mathrm{a}} \, \hat{\boldsymbol{x}} + \sin \alpha_k^{\mathrm{e}} \sin \alpha_k^{\mathrm{a}} \, \hat{\boldsymbol{y}} + \cos \alpha_k^{\mathrm{e}} \, \hat{\boldsymbol{z}}. \tag{D.1}$$

Then, the polarization in a ray propagating from the transmitter in a direction specified by azimuth φ and elevation ϑ is abstracted by the angle

$$\alpha(\vartheta, \varphi) = \arctan\left(\frac{|\langle \hat{\mathbf{e}}_{\mathsf{TX}}, \hat{\mathbf{e}}_\vartheta \rangle|}{|\langle \hat{\mathbf{e}}_{\mathsf{TX}}, \hat{\mathbf{e}}_\varphi \rangle|} \right) \tag{D.2}$$

where $\langle \cdot, \cdot \rangle$ denotes the inner product and the unit normal vectors perpendicular to the ray direction (cf. Fig. D.1) are

$$\hat{\mathbf{e}}_\vartheta = \cos \vartheta \cos \varphi \, \hat{\boldsymbol{x}} + \cos \vartheta \sin \varphi \, \hat{\boldsymbol{y}} - \sin \vartheta \, \hat{\boldsymbol{z}} \tag{D.3}$$

$$\hat{\mathbf{e}}_\varphi = \sin \varphi \, \hat{\boldsymbol{x}} - \cos \varphi \, \hat{\boldsymbol{y}}. \tag{D.4}$$

Namely, the electric field vector is in the direction of $\hat{\mathbf{e}}_\varphi \cos[\alpha(\vartheta, \varphi)] + \hat{\mathbf{e}}_\vartheta \sin[\alpha(\vartheta, \varphi)]$.

Let the orientation of the transmitter location X_k with respect to the reference receiver X_0^{r} be specified by the elevation and azimuth

angles

$$\varsigma_k^{\mathrm{e}} = \arccos \frac{\mathsf{z}_k - \mathsf{z}_0^{\mathrm{r}}}{r_k} \tag{D.5}$$

$$\varsigma_k^{\mathrm{a}} = \arg[(\mathsf{x}_k - \mathsf{x}_0^{\mathrm{r}}) + \mathsf{j}\,(\mathsf{y}_k - \mathsf{y}_0^{\mathrm{r}})]. \tag{D.6}$$

Similarly, let the orientation of the image location $X_{i,k}$ with respect to X_0^{r} be

$$\varsigma_{i,k}^{\mathrm{e}} = \arccos \frac{\mathsf{z}_{i,k} - \mathsf{z}_0^{\mathrm{r}}}{r_{i,k}} \tag{D.7}$$

$$\varsigma_{i,k}^{\mathrm{a}} = \arg[(\mathsf{x}_{i,k} - \mathsf{x}_0^{\mathrm{r}}) + \mathsf{j}\,(\mathsf{y}_{i,k} - \mathsf{y}_0^{\mathrm{r}})]. \tag{D.8}$$

We model the antenna polarization of the transmitter X_k by a uniformly distributed azimuth angle $\alpha_k^{\mathrm{a}} \in [0, 2\pi)$, and an elevation angle α_k^{e} distributed with PDF $f_{\alpha_k^{\mathrm{e}}}(\nu) = \frac{\sin \nu}{2}\, 0 \leq \nu \leq \pi$. Then, following (D.2), the polarization angles (in each propagation path) are computed as

$$\alpha_k = \arctan(\rho_k) \tag{D.9}$$

$$\alpha_{i,k} = \arctan(\rho_{i,k}) \tag{D.10}$$

where

$$\rho_k = \frac{|\cos(\varsigma_k^{\mathrm{e}})\cos(\alpha_k^{\mathrm{a}} - \varsigma_k^{\mathrm{a}})\sin(\alpha_k^{\mathrm{e}}) - \cos(\alpha_k^{\mathrm{a}})\sin(\varsigma_k^{\mathrm{e}})|}{|\sin(\alpha_k^{\mathrm{e}})\sin(\alpha_k^{\mathrm{a}} - \varsigma_k^{\mathrm{a}})|}$$

$$\rho_{i,k} = \frac{|\cos(\varsigma_{i,k}^{\mathrm{e}})\cos(\alpha_k^{\mathrm{a}} - \varsigma_{i,k}^{\mathrm{a}})\sin(\alpha_k^{\mathrm{e}}) - \cos(\alpha_k^{\mathrm{a}})\sin(\varsigma_{i,k}^{\mathrm{e}})|}{|\sin(\alpha_k^{\mathrm{e}})\sin(\alpha_k^{\mathrm{a}} - \varsigma_{i,k}^{\mathrm{a}})|}.$$

D.3 Algorithm to Determine Blockages

D.3.1 Direct Interference Paths and Wall Reflections

This is a modified version of the algorithm presented in [85, 86] that includes blocking of the wall reflections. Let the circles (people), and more precisely the locations of their centers on $\boldsymbol{\mathcal{X}}_0$, be denoted by $\{X_k^{\mathrm{c}}\}_{k=0}^{K}$. The phantom images of X_k^{c}, across the four walls, are denoted by $\{X_{i,k}^{\mathrm{c}}\}_{i=1}^{4}$. Given X_0^{r}, $\{X_k\}$ and $\{X_k^{\mathrm{c}}\}$, the blockages in the direct interfering paths and the paths reflected off the walls can be determined using the following algorithm:

1. Let $\mathcal{S}_{X^{\mathrm{c}}} = \{X_k^{\mathrm{c}}\} \cup \{X_{i,k}^{\mathrm{c}}\}_{i=1}^{4}$ be the set of circles on the horizontal plane $\boldsymbol{\mathcal{X}}_0$. For each $X_\ell^{\mathrm{c}} \in \mathcal{S}_{X^{\mathrm{c}}}$, compute the distance $\|X_\ell^{\mathrm{c}} - X_0^{\mathrm{r}}\|$ and the corresponding angle $\angle(X_\ell^{\mathrm{c}} - X_0^{\mathrm{r}})$

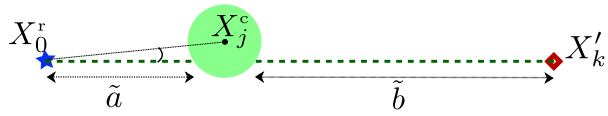

Figure D.2: A blockage (X_j^{c}) in the direct path between X_k' and X_0^{r}.

2. Compute the blocking cones formed by each circle X_ℓ^{c} as [85, 86]

$$B_{\mathrm{C}_\ell} = \angle(X_\ell^{\mathrm{c}} - X_0^{\mathrm{r}}) \pm \arcsin \frac{\mathcal{D}}{2\,\|X_\ell^{\mathrm{c}} - X_0^{\mathrm{r}}\|} \tag{D.11}$$

3. Determine $\mathcal{S}_X = \{X_k\} \cup \{X_{i,k}\}_{i=1}^4$, the set of all the transmitters and their phantom images across the walls.

4. A transmitter $X_m \in \mathcal{S}_X$ is blocked when either of the following two conditions are true:

   - X_m', the projection of X_m on $\boldsymbol{\mathcal{X}}_0$, lies within the blockage cones of the circles with $\|X_\ell^{\mathrm{c}} - X_0^{\mathrm{r}}\| < \|X_m' - X_0^{\mathrm{r}}\|$, i.e.,

$$\angle(X_m' - X_0^{\mathrm{r}}) \in \bigcup_{\{\ell:\, \|X_\ell^{\mathrm{c}} - X_0^{\mathrm{r}}\| < \|X_m' - X_0^{\mathrm{r}}\|\}} B_{\mathrm{C}_\ell} \tag{D.12}$$

   - X_m' has any $X_\ell^{\mathrm{c}} \in \mathcal{S}_{X^{\mathrm{c}}}$ within a distance $\mathcal{D}/2$.

D.3.2 Ceiling-Reflected Interference Path

For each blockage in the direct path with circle center X_j^{c}, compute (cf. Fig. D.2)

$$\tilde{a} = d\cos\xi - (\mathcal{D}/2)\cos\big(\arcsin[(2d/\mathcal{D})\sin\xi]\big) \tag{D.13}$$

$$\tilde{b} = r_k' - d\cos\xi - (\mathcal{D}/2)\cos\big(\arcsin[(2d/\mathcal{D})\sin\xi]\big) \tag{D.14}$$

where $d = \|X_j^{\mathrm{c}} - X_0^{\mathrm{r}}\|$ and $\xi = \angle(X_j^{\mathrm{c}} - X_0^{\mathrm{r}})$. The ceiling reflection from X_k is blocked ($\beta_{5,k} = 0$) by the user circle X_j^{c} if $\tilde{a} < a_k$ or $\tilde{b} < b_k$.

D.4 Antenna Gains

Recall the orientations given in (D.5), (D.6), (D.7) and (D.8). Then, the receive antenna gains are obtained via (5.8) as

$$\mathcal{G}_k^{\mathrm{r}} = \mathcal{G}(\vartheta)|_{\vartheta=\arccos[\cos\psi_0^{\mathrm{e}}\,\cos\varsigma_k^{\mathrm{e}}+\sin\psi_0^{\mathrm{e}}\,\sin\varsigma_k^{\mathrm{e}}\,\cos(\varsigma_k^{\mathrm{a}}-\psi_0^{\mathrm{a}})]} \tag{D.15}$$

$$\mathcal{G}_{i,k}^{\mathrm{r}} = \mathcal{G}(\vartheta)|_{\vartheta=\arccos[\cos\psi_0^{\mathrm{e}}\,\cos\varsigma_{i,k}^{\mathrm{e}}+\sin\psi_0^{\mathrm{e}}\,\sin\varsigma_{i,k}^{\mathrm{e}}\,\cos(\varsigma_{i,k}^{\mathrm{a}}-\psi_0^{\mathrm{a}})]} \tag{D.16}$$

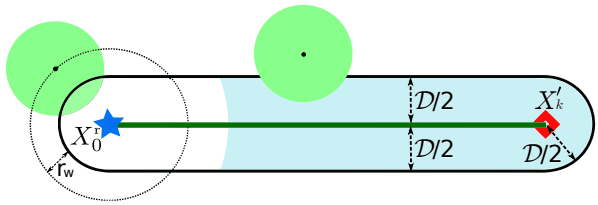

Figure D.3: A direct interferer path. The link intersects any circle with center inside the 2-D capsule.

and the transmit antenna gains become

$$\mathcal{G}_k^{\mathrm{t}} = \mathcal{G}(\vartheta)\big|_{\vartheta=\arccos[-\cos\psi_k^{\mathrm{e}}\,\cos\varsigma_k^{\mathrm{e}}-\sin\psi_k^{\mathrm{e}}\,\sin\varsigma_k^{\mathrm{e}}\,\cos(\varsigma_k^{\mathrm{a}}-\psi_k^{\mathrm{a}})]} \tag{D.17}$$

$$\mathcal{G}_{i,k}^{\mathrm{t}} = \mathcal{G}(\vartheta)\big|_{\vartheta=\arccos[-\cos\psi_k^{\mathrm{e}}\,\cos\varsigma_{i,k}^{\mathrm{e}}-\sin\psi_k^{\mathrm{e}}\,\sin\varsigma_{i,k}^{\mathrm{e}}\,\cos(\varsigma_{i,k}^{\mathrm{a}}-\psi_k^{\mathrm{a}})]} \tag{D.18}$$

where

$$\begin{aligned}
\psi_{i,k}^{\mathrm{e}} &= \psi_k^{\mathrm{e}} && i = 1,\ldots,4\\
\psi_{i,k}^{\mathrm{e}} &= \pi - \psi_k^{\mathrm{e}} && i = 5,6\\
\psi_{i,k}^{\mathrm{a}} &= \pi - \psi_k^{\mathrm{a}} && i = 1,2\\
\psi_{i,k}^{\mathrm{a}} &= -\psi_k^{\mathrm{a}} && i = 3,4\\
\psi_{i,k}^{\mathrm{a}} &= \psi_k^{\mathrm{a}} && i = 5,6.
\end{aligned} \tag{D.19}$$

specify the main-lobe directions of the phantom transmitters.

D.5 Derivation of Blockage Probability

D.5.1 Direct Interference Paths

Consider the projection of a direct interference link from X_k to X_0^{r} on $\boldsymbol{\mathcal{X}}_0$, as depicted in Fig. D.3. A circle of diameter $\mathcal{D}$ is intersected by the link if and only if its center falls inside the 2-D capsule of radius $\mathcal{D}/2$ and length $r'_k = \|X'_k - X_0^{\mathrm{r}}\|$ drawn around the link. The circle centers, X_0^{c} and X_k^{c}, each fall independently inside the capsule (self-body blocking) with probability

$$p_{\mathrm{sb}} = \frac{\arcsin\frac{\mathcal{D}}{2\,\mathsf{r}_{\mathrm{w}}+\mathcal{D}}}{\pi}. \tag{D.20}$$

Each of the $K-1$ other circle centers in $\{X_j^{\mathrm{c}}\}_{j\notin\{0,k\}}$ is located at a distance $\mathcal{D}/2+\mathsf{r}_{\mathrm{w}}$ away from the corresponding wearable X_j, at an angle ϱ_j independently and uniformly distributed in $[0,2\pi)$, with

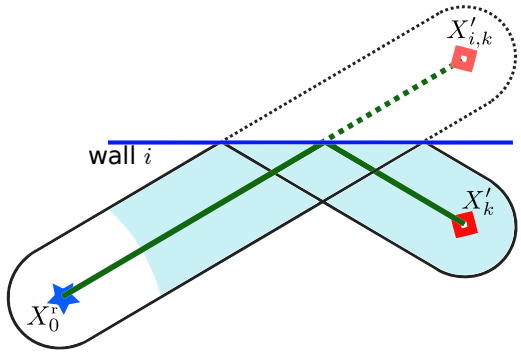

Figure D.4: A reflected interferer link off a wall. The link intersects any circle with center inside the folded 2-D capsule depicted with solid lines.

coordinates $\mathsf{x}_j^{\mathrm{c}} = x_j + (\mathcal{D}/2 + \mathsf{r}_{\mathrm{w}}) \cos \varrho_j$ and $\mathsf{y}_j^{\mathrm{c}} = y_j + (\mathcal{D}/2 + \mathsf{r}_{\mathrm{w}}) \sin \varrho_j$. Then, $\{X_j^{\mathrm{c}}\}_{j \notin \{0,k\}}$ are independently distributed on $\boldsymbol{\mathcal{X}}_0$, with PDF

$$f_{\mathsf{x}_j^{\mathrm{c}}, \mathsf{y}_j^{\mathrm{c}}}(x, y) = \int_0^{2\pi} f_{\mathsf{x}_k, \mathsf{y}_k} \left[x - (\mathcal{D}/2 + \mathsf{r}_{\mathrm{w}}) \cos \varrho, y - (\mathcal{D}/2 + \mathsf{r}_{\mathrm{w}}) \sin \varrho \right] \mathrm{d}\varrho \tag{D.21}$$

which we approximate as

$$f_{\mathsf{x}_j^{\mathrm{c}}, \mathsf{y}_j^{\mathrm{c}}}(x, y) \approx f_{\mathsf{x}_k, \mathsf{y}_k}(x, y) \tag{D.22}$$

the accuracy of which is validated in Examples 5.4 and 5.5. Each circle center in $\{X_j^{\mathrm{c}}\}_{j \notin \{0,k\}}$ independently fall inside the capsule with probability

$$p_{\mathrm{ob}}(r'_k) \approx \frac{r'_k \mathcal{D} - \tilde{\mathsf{A}}}{\mathsf{L}\mathsf{W} - \mathsf{A}} \tag{D.23}$$

where $\tilde{\mathsf{A}} + \pi \mathcal{D}^2/4$ is the area of the intersection of the capsule and the exclusion circle, i.e., the unshaded part of the capsule in Fig. D.3. Thus, the probability of the link being blocked satisfies

$$\mathbb{P}[\beta_k = 0] \approx 1 - \left(1 - p_{\mathrm{ob}}(r'_k)\right)^{K-1} \left(1 - p_{\mathrm{sb}}\right)^2 . \tag{D.24}$$

The result in (5.18) is obtained by plugging (D.20) and (D.23) into (D.24).

D.5.2 Wall-Reflected Interference Paths

The link from a phantom transmitter across the walls, $\{X_{i,k}\}_{i=1}^4$, is blocked by circles with center falling inside the folded 2-D capsule in Fig. D.4. Then, (D.24) can be used as a close approximation

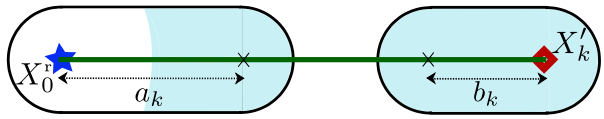

Figure D.5: A direct interferer link. The corresponding ceiling reflection intersects any circle with center inside any of the two 2-D capsules.

for the blockage probability of the wall reflections, not exact only because of the folded capsule having slightly lesser area than the unfolded capsule (cf. Fig. D.4).

D.5.3 Ceiling-Reflected Interference Paths

Those blockages in the direct path from X_k that block the ceiling reflection as per Section 5.2.3 will have their circle centers inside one of the two 2-D capsules depicted in Fig. D.5. Recall from Section 5.2.3 that

$$a_k = (h_{\mathrm{u}} - \mathsf{H}/2 - \mathsf{z}_0^{\mathrm{r}}) \tan\theta_{5,k}$$

and

$$b_k = (h_{\mathrm{u}} - \mathsf{H}/2 - \mathsf{z}_k) \tan\theta_{5,k}$$

depend on the wearable heights. Consider the self-body blocking by the reference user X_0^{c}, which is located $\mathcal{D}/2 + \mathsf{r}_{\mathrm{w}}$ away from X_0^{r} and at a uniformly random angle in $[0, 2\pi)$. The probability for X_0^{c} falling in the capsule of length a_k becomes the self-body blocking probability in (5.22). Similarly, X_k^{c}, located $\mathcal{D}/2 + \mathsf{r}_{\mathrm{w}}$ away from X_k and at a uniformly random angle in $[0, 2\pi)$, effects self-body blocking with probability (5.23). Again, the probability of any of the other $K-1$ users falling in either of the two capsules, given by (5.24), is obtained via the density in (D.22).

To capture the dependence between $\beta_{5,k}$ and β_k, we introduce an auxiliary random variable $\tilde{\beta}_k$, which is Bernoulli with

$$\mathbb{P}[\tilde{\beta}_k = 0] = \mathbb{P}[\beta_k = 0 | \beta_{5,k} = 1] \tag{D.25}$$

which is essentially the probability for the direct link being blocked, given that no circle center is present inside the two capsules in Fig. D.5. Then, β_k computed as

$$\beta_k = \tilde{\beta}_k \, \beta_{5,k} \tag{D.26}$$

by independently generating $\beta_{5,k}$ and $\tilde{\beta}_k$, satisfies

$$\begin{aligned}\mathbb{P}[\beta_k = 0] &= \mathbb{P}[\tilde{\beta}_k = 0]\,\mathbb{P}[\beta_{5,k} = 0] + \mathbb{P}[\tilde{\beta}_k = 1]\,\mathbb{P}[\beta_{5,k} = 0] \\ &\qquad + \mathbb{P}[\tilde{\beta}_k = 0]\,\mathbb{P}[\beta_{5,k} = 1] \qquad \text{(D.27)} \\ &= \mathbb{P}[\beta_{5,k} = 0] + \mathbb{P}[\tilde{\beta}_k = 0]\,\mathbb{P}[\beta_{5,k} = 1] \qquad \text{(D.28)}\end{aligned}$$

complying with (5.25). Explicitly, $\tilde{\beta}_k$ as per (D.25) can be modeled as

$$\tilde{\beta}_k = \tilde{\beta}_k^{\mathrm{sb0}}\, \tilde{\beta}_k^{\mathrm{sb}k}\, \tilde{\beta}_k^{\mathrm{ob}} \qquad \text{(D.29)}$$

where the factors are independent Bernoulli random variables with probabilities

$$\mathbb{P}[\tilde{\beta}_k^{\mathrm{sb0}} = 0] = \begin{cases} 0 & a_k \geq \sqrt{\mathsf{r}_{\mathrm{w}}(\mathcal{D} + \mathsf{r}_{\mathrm{w}})} \\ \dfrac{\arcsin \frac{\mathcal{D}}{2\,\mathsf{r}_{\mathrm{w}} + \mathcal{D}} - \arccos \frac{a_k^2 + \mathsf{r}_{\mathrm{w}}\mathcal{D} + \mathsf{r}_{\mathrm{w}}^2}{a_k(2\,\mathsf{r}_{\mathrm{w}} + \mathcal{D})}}{\pi - \arccos \frac{a_k^2 + \mathsf{r}_{\mathrm{w}}\mathcal{D} + \mathsf{r}_{\mathrm{w}}^2}{a_k(2\,\mathsf{r}_{\mathrm{w}} + \mathcal{D})}} & \sqrt{\mathsf{r}_{\mathrm{w}}(\mathcal{D} + \mathsf{r}_{\mathrm{w}})} > a_k \geq \mathsf{r}_{\mathrm{w}} \\ \dfrac{\arcsin \frac{\mathcal{D}}{2\,\mathsf{r}_{\mathrm{w}} + \mathcal{D}}}{\pi} & a_k < \mathsf{r}_{\mathrm{w}} \end{cases} \qquad \text{(D.30)}$$

$$\mathbb{P}[\tilde{\beta}_k^{\mathrm{sb}k} = 0] = \begin{cases} 0 & b_k \geq \sqrt{\mathsf{r}_{\mathrm{w}}(\mathcal{D} + \mathsf{r}_{\mathrm{w}})} \\ \dfrac{\arcsin \frac{\mathcal{D}}{2\,\mathsf{r}_{\mathrm{w}} + \mathcal{D}} - \arccos \frac{b_k^2 + \mathsf{r}_{\mathrm{w}}\mathcal{D} + \mathsf{r}_{\mathrm{w}}^2}{b_k(2\,\mathsf{r}_{\mathrm{w}} + \mathcal{D})}}{\pi - \arccos \frac{b_k^2 + \mathsf{r}_{\mathrm{w}}\mathcal{D} + \mathsf{r}_{\mathrm{w}}^2}{b_k(2\,\mathsf{r}_{\mathrm{w}} + \mathcal{D})}} & \sqrt{\mathsf{r}_{\mathrm{w}}(\mathcal{D} + \mathsf{r}_{\mathrm{w}})} > b_k \geq \mathsf{r}_{\mathrm{w}} \\ \dfrac{\arcsin \frac{\mathcal{D}}{2\,\mathsf{r}_{\mathrm{w}} + \mathcal{D}}}{\pi} & b_k < \mathsf{r}_{\mathrm{w}} \end{cases} \qquad \text{(D.31)}$$

$$\mathbb{P}[\tilde{\beta}_k^{\mathrm{ob}} = 0] \approx 1 - \left(\frac{\mathsf{Area} - r'_{i,k}\mathcal{D} + \tilde{\mathsf{A}}}{\mathsf{Area} - (a_k + b_k)\,\mathcal{D} + \tilde{\mathsf{A}} - \pi\,\mathcal{D}^2/2} \right)^{K-1} \qquad \text{(D.32)}$$

where $\mathsf{Area} = \mathsf{L}\,\mathsf{W} - \mathsf{A}$.

D.5.4 Wall-Reflected Signal Path

For the signal reflections off the walls, i.e., the links from $\{X_{i,0}\}_{i=1}^4$, only the reference user X_0^{c} can cause self-body blocking and the other K users can potentially block the link if any circle center falls within the folded capsule depicted in Fig. D.6. Specifically, self-body blocking of the ith reflection happens when it falls in the angle ζ depicted in Fig. D.6 and computed as

$$\zeta = 2\left(\arcsin \frac{r'_0}{2\,\mathsf{r}_{\mathrm{w}} + \mathcal{D}} + \arcsin \frac{\mathcal{D}}{2\,\mathsf{r}_{\mathrm{w}} + \mathcal{D}} \right). \qquad \text{(D.33)}$$

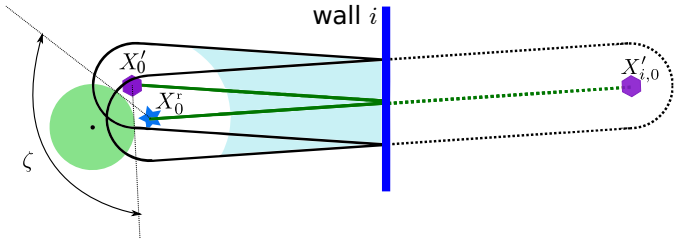

Figure D.6: A reflected signal link off a wall. The link intersects any circle with center inside the folded 2-D capsule depicted with solid lines.

Then, we approximate the folded capsule area with half the area of the unfolded capsule (cf. Fig. D.6) and an approximation of the blockage probability of the reflected signal link off the ith wall can be obtained as in (5.27).

Bibliography

Each reference indicates the pages where it appears.

[1] A. Gupta and R. K. Jha. A survey of 5G network: Architecture and emerging technologies. *IEEE Access*, 3:1206–1232, 2015. 1

[2] S. Mumtaz, K. M. Saidul Huq, and J. Rodriguez. Direct mobile-to-mobile communication: Paradigm for 5G. *IEEE Wireless Commun. Mag.*, 21(5):14–23, October 2014. 1

[3] X. Shen. Device-to-device communication in 5G cellular networks. *IEEE Network*, 29(2):2–3, March 2015.

[4] S. Ray, J. Park, and S. Bhunia. Wearables, implants, and internet of things: The technology needs in the evolving landscape. *IEEE Trans. Multi-Scale Compu. Syst.*, 2(2):123–128, April 2016.

[5] S. H. Sun, J. L. Hu, Y. Peng, X. M. Pan, L. Zhao, and J. Y. Fang. Support for vehicle-to-everything services based on LTE. *IEEE Wireless Commun. Mag.*, 23(3):4–8, June 2016.

[6] E. Soltanmohammadi, K. Ghavami, and M. Naraghi-Pour. A survey of traffic issues in machine-to-machine communications over LTE. *IEEE Internet of Things Journal*, 3(6):865–884, December 2016. 1

[7] J. G. Andrews, S. Shakkottai, R. W. Heath Jr., N. Jindal, M. Haenggi, R. Berry, D. Guo, M. Neely, S. Weber, S. Jafar, and A. Yener. Rethinking information theory for mobile ad hoc networks. *IEEE Commun. Mag.*, 46(12):94–101, December 2008. 1, 4

[8] C. Park and T. S. Rappaport. Short-range wireless communications for next-generation networks: UWB, 60 GHz millimeter-wave WPAN, and ZigBee. *IEEE Wireless Commun. Mag.*, 14(4):70–78, August 2007. 2, 10

[9] F. Boccardi, R. W. Heath Jr., A. Lozano, T. Marzetta, and P. Popovski. Five disruptive technology directions for 5G. *IEEE Commun. Mag.*, 52(2):74–80, February 2014. 2, 3, 11

[10] J. G. Andrews, S. Buzzi, W. Choi, S. Hanly, A. Lozano, A. C. K. Soong, and J. C. Zhang. What will 5G be? *IEEE Journal on Sel. Areas in Communications*, 32(7), July 2014. 2, 3, 11

[11] B. Bangerter, S. Talwar, R. Arefi, and K. Stewart. Networks and devices for the 5G era. *IEEE Commun. Mag.*, 52(2):90–96, February 2014.

[12] S. Andreev, A. Pyattaev, K. Johnsson, O. Galinina, and Y. Koucheryavy. Cellular traffic offloading onto network-assisted device-to-device connections. *IEEE Commun. Mag.*, 52(4):20–31, April 2014.

[13] Y. Li, T. Wu, P. Hui, D. Jin, and S. Chen. *IEEE Commun. Mag.* 3, 126

[14] 3GPP TR 22.803 V1.0.0. Feasibility study for proximity services. Technical report, 3rd Generation Partnership Project 3GPP, www.3gpp.org, 2012. 3

[15] L. Lei, Z. Zhong, C. Lin, and X. Shen. Operator controlled device-to-device communications in LTE-advanced networks. *IEEE Wireless Commun. Mag.*, 19(3):96–104, June 2012.

[16] X. Lin, J.G. Andrews, A. Ghosh, and R. Ratasuk. An overview of 3GPP device-to-device proximity services. *IEEE Commun. Mag.*, 52(4):40–48, April 2014. 3, 4

[17] K. Doppler, C. Yu, C. B. Ribeiro, and P. Janis. Mode selection for device-to-device communication underlaying an LTE-advanced network. In *Proc. IEEE Wireless Commun. and Networking Conf.*, April 2010. 4, 7, 47

[18] G. Fodor and N. Reider. A distributed power control scheme for cellular network assisted D2D communications. In *Proc. IEEE Global Telecommun. Conf.*, pages 1–6, December 2011.

[19] H. Min, W. Seo, J. Lee, S. Park, and D. Hong. Reliability improvement using receive mode selection in the device-to-device uplink period underlaying cellular networks. *IEEE Trans. Wireless Commun.*, 10(2):413–418, February 2011. 47

[20] G. Fodor, E. Dahlman, G. Mildh, S. Parkvall, N. Reider, G. Miklós, and Z. Turányi. Design aspects of network assisted device-to-device communications. *IEEE Trans. Commun.*, 50 (3):170–177, March 2012.

[21] Y. Pei and Y-C Liang. Resource allocation for device-to-device communications overlaying two-way cellular networks. *IEEE Trans. Wireless Commun.*, 12(7):3611–3621, July 2013. 47

[22] C. Yu, K. Doppler, C. B. Ribeiro, and O. Tirkkonen. Resource sharing optimization for device-to-device communication underlaying cellular networks. *IEEE Trans. Wireless Commun.*, 10(8):2752–2763, August 2011.

[23] D. Feng, L. Lu, Y. Yuan-Wu, G.Y. Li, G. Feng, and S. Li. Device-to-device communications underlaying cellular networks. *IEEE Trans. Commun.*, 61(8):3541–3551, August 2013.

[24] S. Shalmashi, G. Miao, and S. B. Slimane. Interference management for multiple device-to-device communications underlaying cellular networks. In *Proc. IEEE Int. Symp. Pers., Indoor, Mobile Radio Commun.*, pages 223–227, September 2013.

[25] H. Tang, C. Zhu, and Z. Ding. Cooperative MIMO precoding for D2D underlay in cellular networks. In *Proc. IEEE Int. Conf. Commun.*, pages 5517–5521, June 2013.

[26] W. Xu, L. Liang, H. Zhang, S. Jin, J.C.F. Li, and M. Lei. Performance enhanced transmission in device-to-device communications: beamforming or interference cancellation? In *Proc. IEEE Global Telecommun. Conf.*, pages 4296–4301, Dec 2012. 47

[27] A. Asadi and V. Mancuso Q. Wang. A survey on device-to-device communication in cellular networks. Available online: http://arxiv.org/abs/1310.0720v6, 2014.

[28] B. Kaufman, J. Lilleberg, and B. Aazhang. Spectrum sharing scheme between cellular users and ad-hoc device-to-device users. *IEEE Trans. Wireless Commun.*, 12(3):1038–1049, March 2013. 4, 7, 47

[29] X. Lin, R. W. Heath Jr., and J. G. Andrews. The interplay between massive MIMO and underlaid D2D networking. *IEEE Trans. Wireless Commun.*, 14(6):3337–3351, June 2015. 5, 80

[30] N. Lee, X. Lin, J. G. Andrews, and R. W. Heath Jr. Power control for D2D underlaid cellular networks:

Modeling, algorithms and analysis. Available online: http://arxiv.org/abs/1305.6161, 2013. 5, 8

[31] H. ElSawy, E. Hossain, and M. -S. Alouini. Analytical modeling of mode selection and power control for underlay D2D communication in cellular networks. *IEEE Trans. Commun.*, 62(11):4147–4161, November 2014. 5, 8

[32] X. Wu, S. Tavildar, S. Shakkottai, T. Richardson, J. Li, R. Laroia, and A. Jovicic. FlashLinQ: A synchronous distributed scheduler for peer-to-peer ad hoc networks. *IEEE/ACM Trans. Networking*, 21(4):1215–1228, August 2013. 5, 7, 81

[33] N. Naderializadeh and A.S. Avestimehr. ITLinQ: A new approach for spectrum sharing in device-to-device communication systems. *IEEE Journal on Sel. Areas in Communications, to appear*, 2014. 5, 7, 127

[34] N. Lee and R. W. Heath Jr. Advanced interference management technique: potentials and limitations. 23(3):30–38, June 2016. 6

[35] N. Lee, R. Tandon, and R. W. Heath. Distributed space-time interference alignment with moderately delayed CSIT. *IEEE Trans. Wireless Commun.*, 14(2):1048–1059, February 2015.

[36] N. Lee and R. W. Heath. Space-time physical-layer network coding. *IEEE J. Select. Areas Commun.*, 33(2):323–336, February 2015. 6

[37] R. K. Mungara, G. George, and A. Lozano. Overhead and spectral efficiency of pilot-assisted interference alignment in time-selective fading channels. *IEEE Trans. Wireless Commun.*, 13(9):4884–4895, September 2014. 6

[38] X. Yi and G. Caire. ITLinQ+: An improved spectrum sharing mechanism for device-to-device communications. In *Proc. Annual Asilomar Conf. Signals, Syst., Comp.*, pages 1310–1314, November 2015. 7, 127

[39] H. S. Dhillon, R. K. Ganti, F. Baccelli, and J. G. Andrews. Modeling and analysis of k-tier downlink heterogeneous cellular networks. *IEEE J. Select. Areas Commun.*, 30(3):550–560, April 2012. 7

[40] D. Ramasamy, R. Ganti, and U. Madhow. On the capacity of picocellular networks. In *Proc. IEEE Int. Symp. Inform. Theory*, pages 241–245, July 2013. 7

[41] M. Haenggi. *Stochastic Geometry for Wirelss Networks*. Cam-

bridge University Press, Cambridge, UK, 2012. 8, 34, 44, 45, 54, 83, 84, 134

[42] M. Haenggi, J. G. Andrews, F. Baccelli, O. Dousse, and M. Franceschetti. Stochastic geometry and random graphs for the analysis and design of wireless networks. *IEEE J. Select. Areas Commun.*, 27(7):1029–1046, May 2009. 8, 19

[43] J. G. Andrews, F. Baccelli, and R. K. Ganti. A tractable approach to coverage and rate in cellular networks. *IEEE Trans. Commun.*, 59(11):3122–3134, November 2011. 40, 42

[44] N. Deng, W. Zhou, and M. Haenggi. The Ginibre point process as a model for wireless networks with repulsion. *IEEE Trans. Wireless Commun.*, 14(1):107–121, January 2015.

[45] J. S. Gomez, A. Vasseur, A. Vergne, P. Martins, L. Decreusefond, and W. Chen. A case study on regularity in cellular network deployment. *IEEE Wireless Commun. Lett.*, 4:421–424, August 2015.

[46] A. Guo and M. Haenggi. Joint spatial and propagation models for cellular networks. In *Proc. IEEE Global Telecommun. Conf.*, pages 1–6, December 2015.

[47] J. G. Andrews, R. K. Ganti, M. Haenggi, N. Jindal, and S. Weber. A primer on spatial modeling and analysis in wireless networks. *IEEE Commun. Mag.*, 48:156–163, November 2010.

[48] H. S. Dhillon, R. K. Ganti, F. Baccelli, and J. G. Andrews. Modeling and analysis of K-tier downlink heterogeneous cellular networks. *IEEE J. Select. Areas Commun.*, 30(3):550–560, April 2012.

[49] S. Mukherjee. Distribution of downlink SINR in heterogeneous cellular networks. *IEEE J. Select. Areas Commun.*, 30(3):575–585, April 2012.

[50] S. Singh, H. S. Dhillon, and J. G. Andrews. Offloading in heterogeneous networks: Modeling, analysis, and design insights. *IEEE Trans. Wireless Commun.*, 12(5):2484–2497, May 2013.

[51] H. ElSawy, E. Hossain, and M. Haenggi. Stochastic geometry for modeling, analysis, and design of multi-tier and cognitive cellular wireless networks: A survey. *IEEE Commun. Surveys Tuts.*, 15(3):996–1019, Third Quarter 2013. 42

[52] H. ElSawy, A. Sultan-Salem, M.-S. Alouini, and M. Z. Win. Modeling and analysis of cellular networks using stochastic geometry: A tutorial. *IEEE Commun. Surveys Tuts.*, PP, 2016. URL `http://ieeexplore.ieee.org/stamp/stamp.`

jsp?arnumber=7733098. 39, 40

[53] C. H. Lee and M. Haenggi. Interference and outage in Poisson cognitive networks. *IEEE Trans. Wireless Commun.*, 11(4): 1392–1401, April 2012.

[54] A. Guo and M. Haenggi. Asymptotic deployment gain: A simple approach to characterize the SINR distribution in general cellular networks. *IEEE Trans. Commun.*, 63:962–976, March 2015.

[55] M. D. Renzo and P. Guan. Stochastic geometry modeling and system-level analysis of uplink heterogeneous cellular networks with multi-antenna base stations. *IEEE Trans. Commun.*, 64: 2453–2476, June 2016.

[56] M. D. Renzo and W. Lu. Stochastic geometry modeling and performance evaluation of MIMO cellular networks using the equivalent-in-distribution (EiD)-based approach. *IEEE Trans. Commun.*, 63:977–996, March 2015.

[57] H. S. Dhillon, M. Kountouris, and J. G. Andrews. Downlink MIMO HetNets: Modeling, ordering results and performance analysis. *IEEE Trans. Wireless Commun.*, 12:5208–5222, October 2013.

[58] L. H. Afify, H. ElSawy, T. Y. Al-Naffouri, and M.-S. Alouini. A unified stochastic geometry model for MIMO cellular networks with retransmissions. *IEEE Trans. Wireless Commun.*, 15 (12):8595–8609, December 2016.

[59] C. Li, J. Zhang, J. G. Andrews, and K. B. Letaief. Success probability and area spectral efficiency in multiuser MIMO HetNets. *IEEE Trans. Commun.*, 64(4):1544–1556, April 2016.

[60] R. Tanbourgi, H. S. Dhillon, and F. K. Jondral. Analysis of joint transmit–receive diversity in downlink MIMO heterogeneous cellular networks. *IEEE Trans. Wireless Commun.*, 14 (12):6695–6709, December 2015.

[61] R. Tanbourgi, S. Singh, J. G. Andrews, and F. K. Jondral. A tractable model for noncoherent joint-transmission base station cooperation. *IEEE Trans. Wireless Commun.*, 13(9): 4959–4973, September 2014. 8, 19

[62] B. Błaszczyszyn and M. K. Karray. Spatial distribution of the SINR in Poisson cellular networks with sector antennas. *IEEE Trans. Wireless Commun.*, 15:581–593, Jan. 2016. 26

[63] P. C. Pinto and M. Z. Win. Communication in a Poisson

field of interferers–part I: Interference distribution and error probability. *IEEE Trans. Wireless Commun.*, 9(7):2176–2186, July 2010. 8, 26

[64] X. Lin, J. G. Andrews, and A. Ghosh. Spectrum sharing for device-to-device communication in cellular networks. *IEEE Trans. Wireless Commun.*, 13(12):6727–6740, December 2014. 8, 40, 47, 49

[65] Q. Ye, M. Al-Shalash, C. Caramanis, and J. G. Andrews. Resource optimization in device-to-device cellular systems using time-frequency hopping. Available online: http://arxiv.org/abs/1309.4062/, 2013. 47

[66] Y. J. Chun, S. L. Cotton, H. S. Dhillon, A. Ghrayeb, and M. O. Hasna. A stochastic geometric analysis of device-to-device communications operating over generalized fading channels. 2016. URL http://arxiv.org/abs/1605.03244. 127

[67] M. A. Kishk and H. S. Dhillon. Stochastic geometry-based comparison of secrecy enhancement techniques in D2D networks. 2017. URL http://arxiv.org/abs/1701.00298.

[68] K. S. Ali, H. ElSawy, and M. -S. Alouini. Modeling cellular networks with full duplex D2D communication: A stochastic geometry approach. *IEEE Trans. Commun.*, 64(10):4409–4424, October 2016. 8, 127

[69] A. Lozano and N. Jindal. Transmit diversity vs. spatial multiplexing in modern MIMO systems. *IEEE Trans. Wireless Commun.*, 9(1):186–197, January 2010. 8, 19, 21

[70] A. Lozano and N. Jindal. Are yesterday's information-theoretic fading models and performance metrics adequate for the analysis of today's wireless systems? *IEEE Commun. Mag.*, 50(11):210–217, November 2012. 8, 19, 21

[71] Juniper Research. Smart wearable devices: Fitness, healthcare, entertainment & enterprise 2013-2018. 2013. 9

[72] T. Starner. How wearables worked their way into the mainstream. *IEEE Pervasive Computing*, 13(4):10–15, October 2014. 9

[73] J. Wei. How wearables intersect with the cloud and the internet of things : Considerations for the developers of wearables. *IEEE Consumer Electron. Mag.*, 3(3):53–56, July 2014. 9

[74] B. Fong, P. B. Rapajic, G. Y. Hong, and A. C. M. Fong. Factors causing uncertainties in outdoor wireless wearable communications. *IEEE Pervasive Computing*, 2(2):16–19, April

2003.

[75] S. K. Feiner. The importance of being mobile: some social consequences of wearable augmented reality systems. In *in Proc. 2nd IEEE and ACM IWAR*, pages 145–148, 1999. 9

[76] S. Byford. Oculus founder says cables are a 'major obstacle' to VR's success on PC. *The Verge* [Online]. Available: http://www.theverge.com/2015/11/1/9656756/oculus-rift-wireless-cables-mobile, November 2015. 9

[77] R. Cavallari, F. Martelli, R. Rosini, C. Buratti, and R. Verdone. A survey on wireless body area networks: Technologies and design challenges. *IEEE Commun. Surveys Tuts.*, 16(3): 1635–1657, Third 2014. 9

[78] A. Pyattaev, K. Johnsson, S. Andreev, and Y. Koucheryavy. Communication challenges in high-density deployments of wearable wireless devices. *IEEE Wireless Commun. Mag.*, 22:12–18, February 2015. 10, 11, 12

[79] T. S. Rappaport, S. Sun, R. Mayzus, H. Zhao, Y. Azar, K. Wang, G. N. Wong, J. K. Schulz, M. Samimi, and F. Gutierrez. Millimeter wave mobile communications for 5G cellular: It will work! *IEEE Access*, 1:335–349, May 2013. 10

[80] T. S. Rappaport, R. W. Heath Jr., R. Daniels, and J. N. Murdock. *Millimeter Wave Wireless Communications*. Prentice Hall, Upper Saddle River, NJ, USA, 2014. 10, 12

[81] WirelessHD. WirelessHD specification overview. 2010. URL http://www.wirelesshd.org. 11

[82] E. Perahia, C. Cordeiro, M. Park, and L. L. Yang. IEEE 802.11ad: Defining the next generation multi-Gbps Wi-Fi. In *Proc. IEEE Consumer Communications and Networking Conference*, pages 1–5, January 2010. 11

[83] G. George, R. K. Mungara, and A. Lozano. An analytical framework for device-to-device communication in cellular networks. *IEEE Trans. Wireless Commun.*, 14(11):6297–6310, November 2015. 11

[84] O. Galinina, A. Pyattaev, K. Johnsson, A. Turlikov, S. Andreev, and Y. Koucheryavy. Assessing system-level energy efficiency of mmWave-based wearable networks. *IEEE J. Select. Areas Commun.*, 34(4):923–937, April 2016. 11

[85] K. Venugopal, M. C. Valenti, and R. W. Heath Jr. Interference in finite-sized highly dense millimeter wave networks. In *Proc. IEEE Int. Symp. Inform. Theory and its Applications*, pages

175–180, February 2015. 12, 97, 105, 143, 144

[86] K. Venugopal, M. C. Valenti, and R. W. Heath Jr. Device-to-device millimeter wave communications: Interference, coverage, rate, and finite topologies. *IEEE Trans. Wireless Commun.*, 15(9):6175–6188, September 2016. 12, 97, 98, 105, 112, 143, 144

[87] K. Venugopal and R. W. Heath Jr. Millimeter wave networked wearables in dense indoor environments. *IEEE Access*, 4:1205–1221, April 2016. 11

[88] P. F. M. Smulders. Deterministic modelling of indoor radio propagation at 40–60 GHz. *Wireless Pers. Commun., Kluwer*, 1(2):127–135, 1994. 11, 101, 102

[89] J. J. G. Fernandes, J. C. Neves, and P. F. M. Smulders. Mm-wave indoor radio channel modelling vs. measurements. *Wireless Pers. Commun., Kluwer*, 1(3):211–219, 1994.

[90] P. F. M. Smulders and L. M. Correia. Characterisation of propagation in 60 GHz radio channels. *Electron. Commun. Eng. J.*, 9(2):73–80, Apr 1997. 11, 97, 102

[91] H. Xu, V. Kukshya, and T. S. Rappaport. Spatial and temporal characteristics of 60-GHz indoor channels. *IEEE J. Select. Areas Commun.*, 20(3):620–630, April 2002.

[92] A. Maltsev, R. Maslennikov, A. Sevastyanov, A. Khoryaev, and A. Lomayev. Experimental investigations of 60 GHz WLAN systems in office environment. *IEEE J. Select. Areas Commun.*, 27(8):1488–1499, October 2009.

[93] E. Torkildson, H. Zhang, and U. Madhow. Channel modeling for millimeter wave MIMO. In *Proc. IEEE Int. Symp. Inform. Theory and its Applications*, pages 1–8, January 2010. 97, 103

[94] E. Torkildson, U. Madhow, and M. Rodwell. Indoor millimeter wave MIMO: Feasibility and performance. *IEEE Trans. Wireless Commun.*, 10(12):4150–4160, December 2011. 97, 103

[95] Y. Niu, Y. Li, D. Jin, L. Su, and A. V. Vasilakos. A survey of millimeter wave (mmWave) communications for 5G: Opportunities and challenges. *Wireless Networks*, 21(8):2657–2676, 2015. 11

[96] P. Karadimas, B. Allen, and P. Smith. Human body shadowing characterization for 60-GHz indoor short-range wireless links. *IEEE Antennas Wireless Propagat. Lett.*, 12:1650–1653, December 2013.

[97] S. Collonge, G. Zaharia, and G. E. Zein. Influence of the human activity on wide-band characteristics of the 60 GHz indoor radio channel. *IEEE Trans. Wireless Commun.*, 3(6): 2396–2406, November 2004. 11

[98] T. Bai and R. W. Heath Jr. Analysis of self-body blocking effects in millimeter wave cellular networks. In *Proc. Annual Asilomar Conf. Signals, Syst., Comp.*, pages 1921–1925, Nov 2014. 11, 103

[99] K. Zhao, J. Helander, Z. Ying, D. Sjoberg, M. Gustafsson, and S. He. mmWave phased array in mobile terminal for 5G mobile system with consideration of hand effect. In *Proc. IEEE Veh. Technol. Conf.*, pages 1–4, May 2015. 12

[100] K. Venugopal, M. C. Valenti, and R. W. Heath Jr. Analysis of millimeter-wave networked wearables in crowded environment. In *Proc. Annual Asilomar Conf. Signals, Syst., Comp.*, November 2015. 12, 97

[101] G. George, R. K. Mungara, A. Lozano, and M. Haenggi. Ergodic spectral efficiency in MIMO cellular networks. *IEEE Trans. Wireless Commun.*, 16(5):1–1, April 2017. 20, 26, 127

[102] W. C. Jakes. *Microwave mobile communications*. Wiley-IEEE Press, 1994. 20

[103] A. Lapidoth and S. Shamai. Fading channels: how perfect need "perfect side information" be? *IEEE Trans. on Inform. Theory*, 48(5):1118–1134, May 2002. 25

[104] A. Giorgetti and M. Chiani. Influence of fading on the Gaussian approximation for BPSK and QPSK with asynchronous cochannel interference. *IEEE Trans. Wireless Commun.*, 4: 384–389, Mar. 2005. 26

[105] S. Ak, H. Inaltekin, and H. V. Poor. Gaussian approximation for the downlink interference in heterogeneous cellular networks. 2016. URL `http://arxiv.org/abs/1601.06023`. 26

[106] R. K. Mungara, D. Morales-Jiménez, and A. Lozano. System-level performance of interference alignment. *IEEE Trans. Wireless Commun., submitted*, 2014. 26

[107] S. N. Diggavi and T. M. Cover. The worst additive noise under a covariance constraint. *IEEE Trans. Inform. Theory*, 47(7): 3072–3081, 2001. 26

[108] M. S. Alouini and A. Goldsmith. Capacity of Nakagami multipath fading channels. In *Proc. IEEE Veh. Technol. Conf.*,

volume 1, pages 358–362, May 1997. 28

[109] H. Shin and J. H. Lee. Capacity of multiple-antenna fading channels: spatial fading correlation, double scattering, and keyhole. *IEEE Trans. Inform. Theory*, 49(10):2636–2647, October 2003. 28

[110] J. Abate and W. Whitt. Numerical inversion of Laplace transforms of probability distributions. *ORSA J. Compt.*, 7(1): 36–43, 1995. 31, 32

[111] C. A. O'cinneide. Euler summation for Fourier series and Laplace transform inversion. *Commun. Statist. -Stochastic Models*, 13(2):315–337, 1997. 32

[112] J. Guo, S. Durrani, and X. Zhou. Outage probability in arbitrarily-shaped finite wireless networks. *IEEE Trans. Commun.*, 62(2):699–712, February 2014. 37

[113] A. K. Gupta, H. S. Dhillon, S. Vishwanath, and J. G. Andrews. Downlink multi-antenna heterogeneous cellular network with load balancing. *IEEE Trans. Commun.*, 62:4052–4067, November 2014. 39

[114] M. Haenggi. On distances in uniformly random networks. *IEEE Trans. Inform. Theory*, 51(10):3584–3586, October 2005. 40, 42, 64, 65

[115] N. Lee, X. Lin, J. G. Andrews, and R. W. Heath Jr. Power control for D2D underlaid cellular networks: Modeling, algorithms and analysis. *IEEE J. Select. Areas Commun.*, 33(1): 1–13, January 2015. 47

[116] T. D. Novlan, H. S. Dhillon, and J. G. Andrews. Analytical modeling of uplink cellular networks. *IEEE Trans. Commun.*, 12(6):2669–2679, June 2013. 49

[117] P. Madhusudhanan, J. G. Restrepo, Y. E. Liu, and T. X. Brown. Carrier to Interference ratio analysis for the shotgun cellular system. In *Proc. IEEE Global Telecommun. Conf.*, pages 1–6, Honolulu, USA, November 2009. 50

[118] J. G. Andrews, A. K. Gupta, and H. S. Dhillon. A primer on cellular network analysis using stochastic geometry. 2016. URL `http://arxiv.org/abs/1604.03183`. 51

[119] B. Błaszczyszyn, M. K. Karray, and H. P. Keeler. Wireless networks appear Poissonian due to strong shadowing. *IEEE Trans. Wireless Commun.*, 14(8):4379–4390, August 2015. 51

[120] H. P. Keeler, N. Ross, and A. Xia. When do wireless network signals appear Poisson? 2014. URL `http://arxiv.org/abs/`

1411.3757. 51

[121] S. Catreux, P. F. Driessen, and L. J. Greenstein. Data throughputs using multiple-input multiple-output (MIMO) techniques in a noise-limited cellular environment. *IEEE Trans. Wireless Commun.*, 1(2):226–235, April 2002. 61

[122] M. Ni, L. Zheng, F. Tong, J. Pan, and L. Cai. A geometrical-based throughput bound analysis for device-to-device communications in cellular networks. Available online: http://arxiv.org/abs/1404.2366v1, 2014. 72

[123] Z. Syu and C. Lee. Spatial constraints of device-to-device communications. In *IEEE First Int. Black Sea Conf. on Commun. and Networking (BlackSeaCom)*, pages 94–98, July 2013. 72

[124] A. Hasan and J. G. Andrews. The guard zone in wireless ad hoc networks. *IEEE Trans. Wireless Commun.*, 2(3):897–906, March 2007. 81, 82, 85, 91

[125] F. Baccelli, J. Li, T. Richardson, S. Shakkottai, S. Subramanian, and X. Wu. On optimizing CSMA for wide area ad-hoc networks. In *Proc. Int. Symp. on Modelling and Opt. in Mobile, Ad-hoc and Wireless Networks*, pages 354–359, May 2011. 81, 82, 83, 85

[126] M. Haenggi. Mean interference in hard-core wireless networks. *IEEE Commun. Lett.*, 15(8):792–794, August 2011. 81, 84

[127] Y. Zhong, W. Zhang, and M. Haenggi. Stochastic analysis of the mean interference for the RTS/CTS mechanism. In *Proc. IEEE Int. Conf. Commun.*, pages 1996–2001, June 2014. 81, 82, 83, 84

[128] D. Torrieri and M. C. Valenti. Exclusion and guard zones in DS-CDMA ad hoc networks. *IEEE Trans. Commun.*, 61(6): 2468–2476, June 2013.

[129] G. Alfano, M. Garetto, and E. Leonardi. New directions into the stochastic geometry analysis of dense CSMA networks. *IEEE Trans. Mobile Comput.*, 13(2):324–336, February 2014. 81, 83

[130] S. Cho and W. Choi. Relay cooperation with guard zone to combat interference from an underlaid network. In *Proc. IEEE Global Telecommun. Conf.*, pages 1–5, December 2011. 81

[131] C. H. Lee and M. Haenggi. Interference and outage in Poisson cognitive networks. *IEEE Trans. Wireless Commun.*, 11(4): 1392–1401, April 2012. 81

[132] N. Naderializadeh and A. S. Avestimehr. ITLinQ: A new ap-

proach for spectrum sharing in device-to-device communication systems. *IEEE J. Select. Areas Commun.*, 32(6):1139–1151, June 2014. 81

[133] R. K. Mungara, X. Zhang, A. Lozano, and R. W. Heath Jr. On the spatial spectral efficiency of ITLinQ. In *Proc. Annual Asilomar Conf. Signals, Syst., Comp.*, November 2014. 82, 83

[134] R. K. Mungara, X. Zhang, A. Lozano, and R. W. Heath Jr. Performance evaluation of ITLinQ and FlashLinQ for overlaid device-to-device communication. In *Proc. IEEE ICC Workshop on Device-to-Device Communication for Cellular and Wireless Networks (ICC'15)*, June 2015. 81

[135] B. Matérn. Spatial variation. *Lecture Notes in Statistics*, 36, 1986. 82

[136] A. A. Alkheir and M. Ibnkahla. An accurate approximation of the exponential integral function using a sum of exponentials. *IEEE Commun. Lett.*, 17(7):1364–1367, July 2013. 87, 88

[137] P. F. M. Smulders. Statistical characterization of 60-GHz indoor radio channels. *IEEE Trans. Antennas Propagat.*, 57 (10):2820–2829, October 2009. 97

[138] T. Wu, T. S. Rappaport, and C. M. Collins. The human body and millimeter-wave wireless communication systems: Interactions and implications. In *Proc. IEEE Int. Conf. Commun.*, pages 2423–2429, June 2015. 98, 128

[139] T. Bai, R. Vaze, and R. W. Heath Jr. Analysis of blockage effects on urban cellular networks. *IEEE Trans. Wireless Commun.*, 13(9):5070–5083, September 2014. 98, 112

[140] T. Bai and R. W. Heath Jr. Coverage and rate analysis for millimeter-wave cellular networks. *IEEE Trans. Wireless Commun.*, 14(2):1100–1114, February 2015. 98

[141] R.A. Valenzuela. A ray tracing approach to predicting indoor wireless transmission. In *Proc. IEEE Veh. Technol. Conf.*, pages 214–218, May 1993. 100

[142] K. Sato, H. Kozima, H. Masuzawa, T. Manabe, T. Ihara, Y. Kasashima, and K. Yamaki. Measurements of reflection characteristics and refractive indices of interior construction materials in millimeter-wave bands. In *Proc. IEEE Veh. Technol. Conf.*, volume 1, pages 449–453, Jul 1995. 101

[143] P. F. M. Smulders and J. J. G. Fernandes. Wide-band simulations and measurements of MM-wave indoor radio channels. In *Proc. IEEE Int. Symp. Pers., Indoor, Mobile Radio Com-*

mun., pages 501–504 vol.2, September 1994. 103

[144] G. George and A. Lozano. Impact of reflections in enclosed mmWave wearable networks. In *Proc. IEEE Int. Workshop on Computational Advances in Multi-Sensor Adaptive Processing (CAMSAP)*, pages 201–204, December 2015. 105

[145] J. Song, J. Choi, S. G. Larew, D. J. Love, T. A. Thomas, and A. A. Ghosh. Adaptive millimeter wave beam alignment for dual-polarized MIMO systems. *IEEE Trans. Wireless Commun.*, 14(11):6283–6296, November 2015. 106

[146] N. P. Lawrence, Brian W.-H. Ng, H. J. Hansen, and D. Abbott. Analysis of millimetre-wave polarization diverse multiple-input multiple-output capacity. *Royal Society Open Science*, 2(12), December 2015. doi: 10.1098/rsos.150322. URL http://rsos.royalsocietypublishing.org/content/2/12/150322.

[147] N. P. Lawrence, H. J. Hansen, and D. Abbott. Tri-orthogonal polarization diversity for 5G networks. *Trans. Emerging Tel. Tech.*, March 2016. ISSN 2161-3915. doi: 10.1002/ett.3042. URL http://dx.doi.org/10.1002/ett.3042. 106

[148] A. Valdes-Garcia, A. Natarajan, D. Liu, M. Sanduleanu, X. Gu, M. Ferriss, B. Parker, C. Baks, J. O. Plouchart, H. Ainspan, B. Sadhu, M. Islam, and S. Reynolds. A fully-integrated dual-polarization 16-element W-band phased-array transceiver in SiGe BiCMOS. In *IEEE Radio Frequency Integrated Circuits Symposium (RFIC)*, pages 375–378, June 2013. 106

[149] X. Gu, A. Valdes-Garcia, A. Natarajan, B. Sadhu, D. Liu, and S. K. Reynolds. W-band scalable phased arrays for imaging and communications. *IEEE Commun. Mag.*, 53(4):196–204, 2015. 106

[150] Constantine A Balanis. *Antenna Theory: Analysis and Design, Third Edition*. Wiley-Interscience, 2012. 107

[151] E. W. Weisstein. Sphere point picking. *MathWorld – A Wolfram Web Resource.* [Online]. Available: http://www.mathworld.wolfram.com. 109

[152] R. K. Mungara, X. Zhang, A. Lozano, and R. W. Heath. Analytical characterization of ITLinQ: Channel allocation for device-to-device communication networks. *IEEE Trans. Wireless Commun.*, 15(5):3603–3615, May 2016. 127

[153] A. Maltsev, A. Pudeyev, I. Karls, I. Bolotin, G. Morozov,

R. Weiler, M. Peter, and W. Keusgen. Quasi-deterministic approach to mmWave channel modeling in a non-stationary environment. In *Proc. IEEE Global Telecommun. Conf.*, pages 966–971, December 2014. 128

[154] A. Maltsev, A. Pudeyev, A. Lomayev, and I. Bolotin. Channel modeling in the next generation mmWave Wi-Fi: IEEE 802.11ay standard. In *Proc. European Wireless Conf.*, pages 1–8, May 2016. 128

[155] E. S. Sousa and J. A. Silvester. Optimum transmission ranges in a direct-sequence spread-spectrum multihop packet radio network. *IEEE J. Select. Areas Commun.*, 8(5):762–771, June 1990. 132, 133

[156] Wolfram Research. The Wolfram functions website. Available online: http://functions.wolfram.com/06.35.21.0015.01, 2001. 135

[157] I. S. Gradshteyn and I. M. Ryzhik. *Table of Integrals, Series, and Products*. Academic Press, San Diego, 7th edition, 2007. 136